



**UCGE Reports
Number 20331**

Department of Geomatics Engineering

**Polarimetric and Interferometric SAR Statistical
Analysis and Signal Processing**

(URL: <http://www.geomatics.ucalgary.ca/graduatetheses>)

by

Yong Bian

June 2011



UNIVERSITY OF CALGARY

Polarimetric and Interferometric SAR Statistical Analysis and Signal Processing

by

Yong Bian

A THESIS

SUBMITTED TO THE FACULTY OF GRADUATE STUDIES
IN PARTIAL FULFILMENT OF THE REQUIREMENTS FOR THE
DEGREE OF DOCTOR OF PHILOSOPHY

DEPARTMENT OF GEOMATICS ENGINEERING

CALGARY, ALBERTA

JUNE 2011

© Yong Bian 2011

Abstract

Polarimetric and interferometric synthetic aperture radar (SAR) (PolInSAR) is a technology combining elements of polarimetric SAR (PolSAR) and interferometric SAR (InSAR). In this thesis, we approach PolInSAR as a system comprised of its PolSAR and InSAR subsystems. The information extraction from a PolInSAR system depends on the application of many signal processing methods. Most signal processing methods require a data statistical model as the *a priori* knowledge. This thesis addresses certain statistical analysis issues and signal processing methods of a non-specific PolInSAR system.

First, the statistical model describing PolSAR data is studied. From this analysis, the covariance matrix based on fractional lower order statistics (FLOS) is proposed. Finally, an optimal despeckling method based on this statistical analysis is proposed.

Coherence is one of the most important measurements of the InSAR subsystem. However, the traditional sample coherence estimation suffers from statistical and sample biases. In order to reduce these biases, in this thesis, a coherence definition based on FLOS is proposed. The proposed method can reduce the statistical bias in the sample coherence estimation.

Phase filtering is an important signal processing technique in the InSAR subsystem. In this thesis, two new wavelet domain phase filtering methods using a simultaneous detection and estimation technique are proposed. In the first method, simultaneous detection and estimation is applied in the wavelet-packet domain, while in the second method, it is applied in the undecimated wavelet domain.

Phase unwrapping is another important InSAR signal processing requirement. In this thesis, a weighted regularized preconditioned conjugate gradient (PCG) phase

unwrapping method is proposed. This proposed method applies the regularization and weights in one unwrapping method. The regularization operation can interpolate the phase map at the areas that are missing valid phase data while the weights are used to suppress the noise. Therefore, the proposed method not only obtains a smooth surface in areas missing valid data but also suppresses the noise of other areas.

A phase quality map is an important component of many existing “quality-guided” phase unwrapping methods. In this thesis, the concept of residue is extended to the second order, which is proposed as the phase quality measurement. It can be used as the quality map for related phase unwrapping methods.

Finally, this thesis addresses the statistical analysis and coherence formulation of the whole PolInSAR system. First, the PolInSAR data is modeled using the alpha-stable distribution rather than the widely used but more restrictive Gaussian distribution. Then, a vector coherence definition based on FLOS is proposed. Finally, FLOS-based coherence optimization is proposed, which obtains a better separation of the underlying scattering mechanisms when the PolInSAR data are non-Gaussian distributed.

Acknowledgements

First and foremost, I would like to express my deep gratitude to my supervisor Dr. Bryan Mercer for his support and encouragement during my Ph.D. study and thesis research.

I would also like to thank the members of my supervisory committee, Dr. Michael Collins, Dr. Derek Lichti, for their encouragements during my Ph.D. study.

I am grateful to the staffs at the Library of the University of Calgary for helping me find part of the references used in this research.

I would like to thank Intermap Technologies Corporation for the provision of part of the SAR data used in this thesis and for financial support applied through the University of Calgary.

I would like to thank the editor, associate editor, and the anonymous reviewers for their suggestions and comments, and JAXA for providing the ALOS PALSAR data used in this thesis.

I am partly supported by the following awards and scholarships during my Ph.D. study: Special Award (2006), GRS Award (2007), L. R. (Dick) Newby Memorial Award (2008, 2009), Eratosthenes Award (2009), C. F. Gauss Award (2009), Queen Elizabeth II Graduate Scholarships (Doctoral) (2009, 2010), and FGS Scholarship (2010). I would like to thank the individuals and agencies that made these awards and scholarships available.

Special thank goes to my wife who spend much of her time in taking care of my son.

Table of Contents

Abstract	ii
Acknowledgements	iv
Table of Contents	v
List of Tables	ix
List of Figures	x
List of Abbreviations	xvi
CHAPTER 1: INTRODUCTION	1
1.1 Review of Related Studies and Problem Statement.....	2
1.1.1 PolSAR	2
1.1.1.1 General Review	2
1.1.1.2 Problem Statement.....	12
1.1.2 InSAR	15
1.1.2.1 General Review	15
1.1.2.2 Problem Statement.....	22
1.1.3. Polarimetric and Interferometric SAR.....	29
1.1.3.1 General Review	29
1.1.3.2 Problem Statement.....	31
1.2 Research Objectives.....	33
1.3 Thesis Overview	37
1.4 SAR Data Used in this Thesis.....	40
1.5 Research Contributions of this Thesis	41
1.6 List of Publications and Further Notes	43
CHAPTER 2: POLARIMETRIC SAR STATISTICAL ANALYSIS USING ALPHA-STABLE DISTRIBUTION AND ITS APPLICATION IN OPTIMAL DESPECKLING	46
2.1 Introduction.....	46
2.2 Polarimetric SAR Image Statistical Analysis Using Alpha-Stable Distribution	48
2.2.1 Review of Polarimetric SAR Statistical Analysis	48
2.2.2 Alpha-Stable Distribution in Complex Polarimetric SAR Data.....	49
2.2.3 Model Analysis Using Real Polarimetric SAR Data.....	55
2.2.4 The Relationship Between the Characteristic Exponents of In-phase, Quadrature and Complex SAR Data	58
2.2.5 Goodness-of-Fit Tests between the Proposed Model and Real Polarimetric SAR Data	59
2.2.5.1 Experiments of Different Polarizations	62
2.2.5.2 Experiments of Different Types of Targets:.....	63
2.2.5.3 Experiments of Different Wavelengths:.....	68
2.3 Covariance Matrix Based on FLOS.....	70
2.3.1 Review of Covariance Matrix.....	70
2.3.2 Covariance Matrix Based on FLOS	71
2.3.3 Analysis of the Covariance Matrix Based on FLOS	76
2.3.4 pdf of the Covairance Matrix using FLOS	79

2.4 Polarimetric SAR Optimal Despeckling Using FLOS	80
2.4.1 Original Optimal Despeckling Method	80
2.4.2 Despeckling Based on FLOS.....	80
2.4.3 Adaptive Despeckling Algorithm.....	81
2.4.4 Parameter Estimation.....	83
2.4.5 Computational Times	85
2.4.6 Experiments of the Optimal Despeckling Method Using Alpha-Stable Distribution.....	88
2.5 Conclusion	91
 CHAPTER 3: INTERFEROMETRIC SAR EXTENDED COHERENCE CALCULATION BASED ON FRACTIONAL LOWER ORDER STATISTICS..93	
3.1 Introduction.....	93
3.2 Review of Alpha-Stable Distribution	95
3.3 Coherence Calculation Based on FLOS	95
3.3.1 Review of Standard Coherence Estimation	95
3.3.2 Coherence Based on FLOS	96
3.3.3 Discussion.....	97
3.3.4 Bias Removal.....	98
3.4 Implementations and Experiments.....	101
3.4.1 Adaptive Sample Coherence Estimation	101
3.4.2 Sampled Estimate of the FLOS-Based Coherence	101
3.4.3 Experimental Results.....	103
3.4.4 Experiments Using Averaged Complex Sample Coherence	105
3.5 Conclusion	106
3.6 Appendix.....	106
 CHAPTER 4: INTERFEROMETRIC SAR PHASE FILTERING IN THE WAVELET DOMAIN USING SIMULTANEOUS DETECTION AND ESTIMATION	
4.1 Introduction.....	109
4.2 Simultaneous Detection and Estimation for Phase Filtering in the Wavelet Domain.....	112
4.2.1 Model.....	112
4.2.2 Simultaneous Detection and Estimation in the Wavelet Domain.....	115
4.2.3 Estimator in the Wavelet Domain	117
4.2.4 Detection in the Wavelet Domain	122
4.2.5 Summary of the Proposed Simultaneous Detection and Estimation Algorithm.....	124
4.3 Phase Filtering Using Wavelet Packet and Simultaneous Detection and Estimation	125
4.3.1 Simultaneous Detection and Estimation Using Wavelet Packet	125
4.3.2 Processing Steps	126
4.4 Phase Filtering in the Undecimated Wavelet Domain Using Simultaneous Detection and Estimation.....	133
4.4.1 Detection and Estimation in the Undecimated Wavelet Domain.....	133
4.4.2 Processing Steps	133

4.5 Implementation Issues	136
4.5.1 Function Calculation	136
4.5.2 Wavelet Decomposition Level	138
4.6 Experimental Results Using Simulated Data.....	139
4.6.1 Methods Used in the Experiments.....	139
4.6.2 Parameter Selection in Simultaneous Detection and Estimation	140
4.6.3 Experimental Results of Simulated Data I	141
4.6.4 Experimental Results of Simulated Data II	146
4.6.5 Experimental Results of Simulated Data III.....	152
4.6.6 Processing Speeds of the Algorithms	153
4.7 Experimental Results Using Real InSAR Data.....	154
4.8 Conclusion	160
4.9 Appendix A.....	162
4.10 Appendix B.....	162
CHAPTER 5: WEIGHTED REGULARIZED PRECONDITIONED CONJUGATE GRADIENT (PCG) PHASE UNWRAPPING METHOD	164
5.1 Introduction.....	164
5.2 Weighted Regularized PCG Method	166
5.2.1 Review of Least Squares Method.....	166
5.2.2 Weighted Regularized PCG Method	167
5.2.3 Valid and Invalid Data Areas	170
5.3 Implementation of the WRPCG Method	171
5.3.1 Border Manipulation	171
5.3.2 PCG Method.....	174
5.3.3 Weight Selection	176
5.4 Unwrapping Experiments on Simulated Data	178
5.4.1 Simulated Data	178
5.4.2 Unwrapping Experiment on Simulated Data.....	178
5.4.3 Evaluation and Discussion of the Unwrapping Results	181
5.4.4 Memory Requirement and CPU Time.....	185
5.5 Unwrapping Method and Experiments on Real SAR Data	187
5.5.1 Unwrapping Method for Real SAR Data	187
5.5.2 Unwrapping Experiment on Real SAR Data.....	188
5.6 Discussion and Conclusion.....	189
CHAPTER 6: USING SECOND ORDER RESIDUE IN POLINSAR PHASE UNWRAPPING.....	191
6.1 Introduction.....	191
6.2 Second Order Residue	193
6.2.1 Review of First Order Residue	193
6.2.2 Second Order Residue	193
6.3 Phase Unwrapping Using Second Order Residue.....	196
6.3.1 Unwrapping Method Using Second Order Residue	196
6.3.2 Unwrapping Experiment and Result	199
6.4 Conclusion	202

CHAPTER 7: POLINSAR STATISTICAL ANALYSIS AND COHERENCE	
OPTIMIZATION USING FRACTIONAL LOWER ORDER STATISTICS	203
7.1 Introduction.....	203
7.2 PolInSAR Statistical Analysis Using Alpha-stable Distribution.....	205
7.2.1 Review of Alpha-Stable Distribution	205
7.2.2 PolInSAR Statistical Analysis Using Isotropic Symmetric Alpha-Stable	
Distribution.....	206
7.3 Vector Coherence Based on FLOS	207
7.3.1 Review of Vector Coherence.....	207
7.3.2 Vector Coherence Based on FLOS.....	208
7.4 Coherence Optimization Based on FLOS.....	211
7.4.1 Definition.....	211
7.4.2 Implementation.....	212
7.5 Experimental Results	214
7.6 Conclusion	216
CHAPTER 8: SUMMERY AND OUTLOOK OF FUTURE RESEARCH	218
8.1 Summary.....	218
8.2 Outlook of Future Studies.....	223
BIBLIOGRAPHY	226

List of Tables

Table 2.1: Estimated Parameters of Polarimetric SAR data.....	54
Table 2.2: Estimated Parameters of Polarimetric SAR data.....	55
Table 2.3: Hellinger Distance of Polarimetric SAR data.....	63
Table 2.4: Estimated Parameters of Polarimetric SAR data.....	64
Table 2.5: Estimated Parameters of Polarimetric SAR data.....	64
Table 2.6: Estimated Parameters of Polarimetric SAR data.....	64
Table 2.7: Hellinger Distance of Polarimetric SAR data.....	67
Table 2.8: Estimated Parameters of Polarimetric SAR data.....	68
Table 2.9: Hellinger Distance of Polarimetric SAR data.....	69
Table 2.10: Estimated Parameters of Polarimetric SAR data After the Scaled Operation	76
Table 2.11: ENL of Despeckled and Original Image (Delta Fraser Area).....	89
Table 4.1: Residual Errors (RMSEs) of the Filtered Results of Data I.....	142
Table 4.2: Residual Errors (RMSEs) of the Filtered Results of Data II.....	142
Table 4.3: Residual Errors (RMSEs) of the Filtered Results of Data III.....	142
Table 4.4: Percentage of Residues Left in the Filtered Results.....	160
Table 5.1: Mean Relative Error, Standard Deviation of Unwrapping Error, and RMSE of the Unwrapping Result.....	180

List of Figures

Figure 1.1. PolInSAR system. As defined in this thesis, the PolInSAR system includes two PolSAR subsystems and four InSAR subsystems providing a total of eight input data channels	34
Figure 2.1. The amplitude images of polarimetric SAR data, Edson area. (a) HH, (b) HV, (c) VV, (d) VH.....	53
Figure 2.2. The amplitude images of polarimetric SAR data, Delta Fraser area. (a) HH, (b) HV, (c) VV, (d) VH.....	53
Figure 2.3. The histograms of the amplitudes of polarimetric SAR images, Delta area. (a) HH. (b) HV. (c) VV. (d) VH.....	54
Figure 2.4. The goodness-of-fit experiment of L-band Edson area data. (a) HH. (b) HV. (c) VV. (d) VH.....	61
Figure 2.5. The goodness-of-fit experiment of L-band Delta area data. (a) HH. (b) HV. (c) VV. (d) VH.....	61
Figure 2.6. Three areas in the goodness-of-fit tests. The areas from left to right are (c), (b), and (a), respectively.....	63
Figure 2.7. The goodness-of-fit experiment of L-band delta data, for area A,. (a) HH. (b) HV. (c) VV. (d) VH.....	65
Figure 2.8. The goodness-of-fit experiment of L-band delta data, for area B. (a) HH. (b) HV. (c) VV. (d) VH.....	66
Figure 2.9. The goodness-of-fit experiment of L-band delta data, for area C. (a) HH. (b) HV. (c) VV. (d) VH.....	66
Figure 2.10. The goodness-of-fit experiment of Intermap P-band Edson data. (a) HH. (b) HV. (c) VV. (d) VH.....	69
Figure 2.11. Estimated $\hat{\alpha}$ values from Delta data. Window size is 11×11 . (a) HH, (b) HV, (c) VV, (d) VH.....	86
Figure 2.12. Despeckling results using the original despeckling method in [144] and the proposed non-adaptive and adaptive method. (a) Image after despeckling using the original despeckling method in [144], window size= 11×11 . (b) Image after despeckling using the proposed non-adaptive method (Equation (20),	

$p_{HH} = p_{HV} = p_{VV} = 0.5$, window size= 11×11). (c) Image after despeckling using the proposed non-adaptive method ($p_{HH} = p_{HV} = p_{VV} = 0.2$, window size= 11×11). (d) Image after despeckling using the proposed adaptive method (window size in alpha estimation and despeckling are 11×11).....	87
Figure 2.13. Profiles in some areas. Area A is left, Area B is the right. (a) Profile of area A. (b) Profile of area B. (c) The two areas.....	90
Figure 3.1. Single-look images and estimated alpha values (the value of α is from high to low is denoted from white to black; 11×11 window) from InSAR data. (a) Master image. (b) Estimated alpha values of master image. (c) Slave image. (d) Estimated alpha values of slave image.....	97
Figure 3.2. Experimental results of InSAR data. (a1)-(d1) Coherence maps before sample-bias removal. (a2)-(d2) Coherence maps after sample-bias removal. (a1) and (a2) Coherence maps using the standard coherence estimation method. (a3)-(d3) Difference maps between the coherence before and after sample-bias removal. (b1) and (b2) ((c1) and (c2)) Coherence maps using the non-adaptive FLOS-based coherence estimation method when $t=0.6$ (when $t=0.25$). (d1) and (d2) Coherence maps using the adaptive FLOS-based coherence estimation method. (A1), (B1), (A2), and (B2) are zoomed-in looks of (a1), (d1), (a2), and (d2), respectively.....	100
Figure 3.3. Coherence histograms of the results in Figure 3.2. (a) Before sample-bias removal. (b) After sample-bias removal.....	102
Figure 3.4. Coherence maps of the average of complex sample estimation (5×5 window). (a) Standard method. (b) FLOS-based adaptive method.....	103
Figure 4.1. Flowchart of the proposed PFWPSDE method. The dotted lines denote the parameter flow, while the solid lines describe the data flow.....	129
Figure 4.2. Flowchart of the proposed PFUWSDE method. The dotted lines denote the parameter flow, while the solid lines describe the data flow.....	132
Figure 4.3. “Clean” (noise-free) simulated phase.....	141
Figure 4.4. Simulated input data contaminated by noise: Data I. (a), (b), and (c) are Data I-1, Data I-2, and Data I-3, respectively.....	143

Figure 4.5. Phase-filtering results using simulated Data I. First row: (A-I)-(E-I) includes the filtered results of Data I-1; second row: (A-II)-(E-II) includes the filtered results of Data I-2; third row: (A-III)-(E-III) includes the filtered results of Data I-3. Fourth row: (A-V)-(E-V) includes difference maps between the filtering results of Data I-3 and the original clean phase. Column (A): Filtering results of the method in [218]. Column (B): Filtering results of the method in [217]. Column (C): Filtering results of the method in [219]. Column (D): Filtering results of the proposed PFWPSDE method. Column (E): Filtering results of the proposed PFUWSDE method.....144

Figure 4.6. Simulated input data contaminated by noise: Data II. (a), (b), and (c) are Data II-1, Data II-2, and Data II-3, respectively.....146

Figure 4.7. Phase-filtering results using simulated Data II. First row: (A-I)-(E-I) are the experimental results of Data II-1; Second row: (A-II)-(E-II) are the experimental results of Data II-2; Third row: (A-III)-(E-III) are the experimental results of Data II-3; Fourth row: (A-V)-(E-V) are difference maps between the filtered results of Data II-3 and the clean phase. Column (A): Filtering results of the method in [218]. Column (B): Filtering results of the method in [217]. Column (C): Filtering results of the method in [219]. Column (D): Filtering results of the proposed PFWPSDE method. Column (E): Filtering results of the proposed PFUWSDE method.....147

Figure 4.8. Simulated input data contaminated by noise: Data III. (A1), (B1), and (C1) are Data III-1, Data III-2, and Data III-3, respectively. (A2), (B2), and (C2) are the coherence levels of Data III-1, Data III-2, and Data III-3, respectively.....150

Figure 4.9. Phase-filtering results using simulated Data III. First row: (A-I)-(E-I) are the experimental results of Data III-1; Second row: (A-II)-(E-II) are the experimental results of Data III-2; Third row: (A-III)-(E-III) are the experimental results of Data III-3; Fourth row: (A-V)-(E-V) are difference maps between the filtering results of Data III-1 and the clean phase. Column (A): Filtering results of the method in [218]. Column (B): Filtering results of the method in [217]. Column (C): Filtering results of the method in [219]. Column (D): Filtering results of the proposed PFWPSDE method. Column (E): Filtering results of the proposed PFUWSDE method.....151

Figure 4.10. (a) Coherence of the Intermap InSAR data. (b) Histogram of the coherence.....153

Figure 4.11. Original interferometric phase and the filtering results of Intermap InSAR data (1024*1024). (a) Interferometric phase of real InSAR data. (b) Filtering result of the method in [218]. (c) Filtering result of the method in [217]. (d) Filtering result of the method in [219]. (e) Filtering result of the proposed PFWPSDE method. (f) Filtering result of the proposed PFUWSDE method.....156

Figure 4.12. Original interferometric phase and the filtering results of ALOS PALSAR data (512*512). (a) Interferometric phase of real InSAR data. (b) Filtering result of the method in [218]. (c) Filtering result of the method in [217]. (d) Filtering result of the method in [219]. (e) Filtering result of the proposed PFWPSDE method. (f) Filtering result of the proposed PFUWSDE method.....157

Figure 5.1. The original phase before wrapping and the wrapped phase. (a) Correct unwrapped phase. (b)-(d) are the wrapped phases contaminated by Gaussian noise when the noise variance is 0.5, 0.7, and 0.9, respectively.....176

Figure 5.2. The unwrapped phase results for the simulated data in Figure 5.1. In these experiments, we use the PDV as a quality map. The first, second, and third rows are the unwrapping results using different methods when the noise variance of the input data is 0.5 (Figure 5.1 (b)), 0.7 (Figure 5.1 (c)), and 0.9 (Figure 5.1 (d)), respectively. (a1)-(a3) are the unwrapping results using the multigrid method in [268] [127], with weights; the quality map is thresholded. (b1)-(b3) are the unwrapping results using the multigrid method in [268] [127], with weights, but the quality map is not thresholded. (c1)-(c3) are the unwrapping results using the original PCG method in [264] [127], with weights; the quality map is thresholded. (d1)-(d3) are the unwrapping results using the original PCG method in [264] [127], with weights, but the quality map is not thresholded. (e1)-(e3) are the unwrapping results using the WRPCG method, $\delta = 1200$, $\varepsilon = 0.015$, no weights, and boundary condition one. (f1)-(f3) are the unwrapping results using the WRPCG method, $\delta = 1200$, $\varepsilon = 0.015$, with weights, and boundary condition one; the quality map is not thresholded.....177

Figure 5.3. The flowchart of the WRPCG method when unwrapping the real SAR data.....186

Figure 5.4. The wrapped phase and unwrapping result of the PolInSAR data. In this experiment, PDV is used as a quality map; the quality map is thresholded and fattened by two pixels using the method in [127]. (a) Wrapped phase (we use the same phase data as [255]). (b) Unwrapping result using the original PCG method in [264], with weight. (c) Unwrapping result using the WRPCG method, $\delta = 9000$, $\varepsilon = 0.0002$, with weight, and boundary condition one; the unwrapping result is inverted. (d) Unwrapping result using the WRPCG Method, $\delta = 9000$, $\varepsilon = 0.0002$, with weight, and boundary condition two.....188

Figure 6.1. The first and second order residue. (a) The computation of first order residue [276]. (b) The definition of second order residue. (c) The second order residue of the spiral data, this data is distributed with [127].....195

Figure 6.2. Unwrapping result of the QGPF method using the coherence and second order residue as quality map, the data is the third optimization data. (a) Wrapped phase of the third optimization. (b) Unwrapping result of QGPF method using coherence as quality map. (c) Unwrapping result of QGPF method using second order residue as quality map (Method One). (d) Unwrapping result of QGPF method using second order residue as quality map (Method Two).....197

Figure 6.3. Unwrapping result of the QGPF method using the coherence and second order residue as quality map, the data is the second optimization data. (a) Wrapped phase of the second optimization. (b) Unwrapping result of QGPF method using coherence as quality map. (c) Unwrapping result of QGPF method using second order residue as quality map (Method One). (d) Unwrapping result of QGPF method using second order residue as quality map (Method Two).....197

Figure 6.4. Unwrapping result of the QGPF method using the coherence and second order residue as quality map, the data is the first optimization data. (a) Wrapped phase of the first optimization. (b) Unwrapping result of QGPF method using coherence as quality map. (c) Unwrapping result of QGPF method using second order residue as quality map (Method One). (d) Unwrapping result of QGPF method using second order residue as quality map (Method Two).....199

Figure 7.1. L-band PolInSAR image. Master image of HH.....207

Figure 7.2. (a1)-(a3) are the optimized coherences of the first, second, and third optimizations of the standard method in [16], respectively. (b1)-(b3) are the optimized coherences of the first, second, and third optimizations of the proposed method, respectively. (a4) is the mask of (a1) shown in white when the optimized coherence is higher than 0.9. (b4) is the mask of (b1) shown in white when the optimized coherence is higher than 0.9.....210

Figure 7.3. Coherence magnitude histograms of the results in Figure 7.2. Histograms represent the first, second, and third optimized coherences using (thick lines) the standard method in [16] and (thin lines) the proposed method.....211

Figure 7.4. (a1)-(a3) are the optimized phases of the first, second, and third optimizations of the standard method in [16], respectively. (b1)-(b3) are the optimized phases of the first, second, and third optimizations of the proposed method, respectively.....213

Figure 7.5. Phase histogram of the result in Figure 7.4. Phase histogram of the first optimized coherence using the method in [16] and the proposed method. The histogram of solid line is from the standard method, and the dotted line is from the proposed method. The horizontal axis is the phase in radians.....214

List of Abbreviations

DEM	Digital elevation model
ENL	Equivalent Number of Looks
FFT	Fast Fourier Transform
FLOS	Fractional Lower Order Statistics
FLOM	Fractional Lower Order Moments
GHF	Generalized Hypergeometric Function
InSAR	Interferometric SAR
JAXA	Japan Aerospace Exploration Agency
LiDAR	Light Detection and Ranging
MPG	Maximum Phase Gradient
PCG	Preconditioned Conjugate Gradient
pdf	Probability Density Function
PDV	Phase Derivative Variance
PFUWSDE	Phase Filtering in the Undecimated Wavelet Domain Using Simultaneous Detection and Estimation
PFWPSDE	Phase Filtering Using Wavelet Packet and Simultaneous Detection and Estimation
PolSAR	Polarimetric SAR
PolInSAR	Polarimetric and Interferometric SAR
QGPf	Quality Guided Path Following
RMSE	Root Mean Square Error
SAR	Synthetic aperture radar
SOM	Second Order Moment
WRPCG	Weighted Regularized Preconditioned Conjugate Gradient

CHAPTER 1: INTRODUCTION

Synthetic aperture radar (SAR) is an active remote sensing technology which has been widely used in various aspects of Earth observation from both airborne and satellite platforms. Polarimetric SAR (PolSAR) uses different polarizations in the transmitting and receiving antennas to obtain polarization characteristics of the imaged targets [1][2][3]. Interferometric SAR (InSAR) uses two or more antennas separated spatially to obtain a three-dimensional measurement of the Earth surface [7]. Polarimetric and interferometric SAR is the combination of PolSAR and InSAR. In this thesis, we use the term “polarimetric and interferometric SAR” (PolInSAR) to represent the whole system which includes the PolSAR and InSAR as its subsystems.

PolInSAR technology is evolved from the SAR technologies that have been developed during the past few decades and incorporates wide areas of SAR technology. Information extraction using a PolInSAR system requires signal processing. Moreover, most of the signal processing methods (such as filtering, detection, and estimation) requires statistical modeling of the PolInSAR data. Therefore, in this thesis, we try to discuss signal processing and statistical modeling together where possible. This gives two advantages. First, the study of statistical models will lead to the better understanding of data characteristics and provide the *a priori* knowledge for the development of a signal processing method. Second, the study of signal processing provides a verification tool for the study of statistical modeling. This thesis focuses on the statistical analysis and some of the major signal processing issues of the PolInSAR system.

In the following sections, we first give a review of SAR, PolSAR, InSAR, and polarimetric SAR interferometry techniques and applications, and then provide the background and problem statement of the thesis research.

1.1 Review of Related Studies and Problem Statement

1.1.1 PolSAR

1.1.1.1 General Review

Basics of SAR:

The resolution of traditional real aperture radar is limited by the physical size of the antenna [319][321][322]. SAR uses a synthetic aperture technique to obtain a high azimuth resolution that cannot be obtained by the real aperture radar [319][321][322].

The raw data obtained in the SAR system is not focused and must be focused before usage [319]. A focused image can be obtained using optical or digital processing methods [319][321]. Digital methods are widely used now due to the fast development of digital computer technique. Nowadays, SAR image focusing methods generally refer to digital processing methods, which apply complex signal processing techniques to compress the unfocused signal energy and obtain a well focused image. There are many image focusing methods in the literature, such as the well-known range Doppler [332] and chirp scaling algorithms [333]. The azimuth resolution is half of the antenna length [319][321][322]. The range resolution is $c/2B_W$ [321][319], where B_W is the bandwidth and c is the velocity of light [321][319].

For distributed targets, a resolution cell involves the energy from a number of different scatterers; therefore, the focused amplitude image has a noisy, “salt and pepper” appearance called speckles [320][324]. The properties of speckle are as follows:

- (a) Speckle can be described by a random process and need to be studied using statistical methods [325].
- (b) Speckle is signal dependent [326]. Therefore, useful information of SAR image may be removed during speckle filtering.
- (c) Speckle is spatially correlated and the degree of correlation is determined by sampling distance and resolution [326][327][331]. Therefore, speckle filtering methods need to consider the correlation of speckle.

Speckle needs to be reduced to obtain a better understanding of the SAR image. In order to reduce speckle, three ways can be used [323][331]: First one performs incoherent averaging during image focusing [324][331], which is called multi-look processing [320]. However, it is well-known that multi-look processing reduces spatial resolution [331]. The second and third ways are both conducted on the focused image. The second way performs the speckle removal in the image domain [323] while the third way is the speckle removal in the wavelet domain [328].

Speckle can be described by a multiplicative model [323],

$$S_v(m,n) = S_c(m,n)v(m,n) \quad (1.1)$$

where $S_v(m,n)$, $S_c(m,n)$, and $v(m,n)$ are the noisy signal, clean signal, and noise component due to speckle, respectively. This model is proved to be accurate only in the areas of distributed scatterers [329]. However, it is still widely used due to its simplicity.

When we use logarithm to transform the SAR image, the speckle noise model is converted to an additive model [330],

$$\log S_n(i, j) = \log S_c(i, j) + \log n(i, j) \quad (1.2)$$

Therefore, the speckle removal can be conducted on the original data using a multiplicative model or on the logarithm of the data using an additive model.

Basics of Polarimetric SAR:

PolSAR uses information from the different transmit/receive signal polarizations to obtain target polarization characteristics [1][2][3]. Since different polarizations are applied, both in the transmitting and receiving antennas, more measurements can be obtained by a fully polarimetric SAR than for single polarization SAR [4]. PolSAR is a vector (i.e., multichannel) measurement system, and information regarding target polarization characteristics can be obtained from this vector measurement [4].

The electric fields of the incident and scattered waves can be described by the following Jones vectors [305],

$$\mathbf{E}_t = \begin{bmatrix} E_H^t \\ E_V^t \end{bmatrix}, \quad \mathbf{E}_s = \begin{bmatrix} E_H^s \\ E_V^s \end{bmatrix} \quad (1.3)$$

where H and V refer to horizontal and vertical polarized components. Defining k as the radar wavenumber and r as the distance between the target and the antenna, the relationship between these two vectors can be described as [1][305][304]

$$\mathbf{E}_t = \frac{\exp(jkr)}{kr} \mathbf{S} \mathbf{E}_s \quad (1.4)$$

where \mathbf{S} is a 2×2 complex matrix called the scattering matrix [2][304][306][307], which determines the scatterer characteristics observed by a calibrated polarimetric SAR,

$$\mathbf{S} = \begin{bmatrix} S_{HH} & S_{HV} \\ S_{VH} & S_{VV} \end{bmatrix} \quad (1.5)$$

where S_{HH} , S_{HV} , S_{VH} , S_{VV} are the complex polarimetric SAR data of the horizontal transmit and horizontal receive, horizontal transmit and vertical receive, vertical transmit and horizontal receive, and vertical transmit and vertical receive, respectively. S_{HH} and S_{VV} are the co-polarized terms, while S_{HV} and S_{VH} are the cross-polarized terms [95]. There are at most seven independent parameters in the scattering matrix and can be reduced to five for the reciprocal case [95] where the HV and VH terms are equal. The scattering matrix has its limitations, and is insufficient for the description of distributed targets [307][305].

The scattering matrix can be transformed into a vector form using the basis matrices such as the lexicographic and Pauli basis [311][38][26],

$$\Psi_l = \left\{ 2 \begin{bmatrix} 1 & 0 \\ 0 & 0 \end{bmatrix}, 2 \begin{bmatrix} 0 & 1 \\ 0 & 0 \end{bmatrix}, 2 \begin{bmatrix} 0 & 0 \\ 1 & 0 \end{bmatrix}, 2 \begin{bmatrix} 0 & 0 \\ 0 & 1 \end{bmatrix} \right\} \quad (1.6)$$

$$\Psi_{Pauli} = \left\{ \sqrt{2} \begin{bmatrix} 1 & 0 \\ 0 & 1 \end{bmatrix}, \sqrt{2} \begin{bmatrix} 1 & 0 \\ 0 & -1 \end{bmatrix}, \sqrt{2} \begin{bmatrix} 0 & 1 \\ 1 & 0 \end{bmatrix}, \sqrt{2} \begin{bmatrix} 0 & -i \\ i & 0 \end{bmatrix} \right\} \quad (1.7)$$

Using lexicographic and Pauli basis, the scattering matrix can be transformed into lexicographic and Pauli scattering vectors [311][38][26]

$$k_l = [S_{HH} \quad S_{HH} \quad S_{HH} \quad S_{HH}]^T \quad (1.8)$$

$$k_{Pauli} = [S_{HH} + S_{VV} \quad S_{VV} - S_{HH} \quad S_{HV} + S_{VH} \quad i(S_{HV} - S_{VH})]^T \quad (1.9)$$

The lexicographic and Pauli scattering vectors can be used to construct the covariance and coherency matrices, respectively. The coherency matrix has a clearer physical

meaning than the covariance matrix because the terms of Pauli basis are related to different scattering mechanisms [55].

For distributed scatters, we need to use other representations other than scattering matrix to describe the scattering characteristics, such as a 4×4 real matrix called the Mueller matrix [304][305][308][311]

$$[\mathbf{M}] = \langle \mathbf{P} \mathbf{W} \mathbf{P}^{-1} \rangle \quad (1.10)$$

where

$$[\mathbf{W}] = \begin{bmatrix} S_{HH} S_{HH}^* & S_{HH} S_{HV}^* & S_{HV} S_{HH}^* & S_{HV} S_{HV}^* \\ S_{HH} S_{VH}^* & S_{HH} S_{VV}^* & S_{HV} S_{VH}^* & S_{HV} S_{VV}^* \\ S_{VH} S_{HH}^* & S_{VH} S_{HV}^* & S_{VV} S_{HH}^* & S_{VV} S_{HV}^* \\ S_{VH} S_{VH}^* & S_{VH} S_{VV}^* & S_{VV} S_{VH}^* & S_{VV} S_{VV}^* \end{bmatrix} \quad (1.11)$$

$$[\mathbf{P}] = \begin{bmatrix} 1 & 0 & 0 & 1 \\ 1 & 0 & 0 & -1 \\ 0 & 1 & 1 & 0 \\ 0 & j & -j & 0 \end{bmatrix} \quad (1.12)$$

where $\langle \rangle$ denotes the ensemble average operation. The Mueller matrix can describe more types of scattering than those of the scattering matrix [305][308]. For some special cases such as a deterministic scatterer [307], the scattering matrix and Mueller matrix are equivalent [305].

Another representation for the distributed scatterers is the covariance matrix [311], which is derived by performing the ensemble average on the outer product operation of the lexicographic scattering vectors [311][145] (see Section 2.3.1 for the definition of covariance matrix, which is not repeated here). There are up to sixteen independent parameters in the covariance matrix, and for scattering media with different type of symmetry properties, the number of independent parameters will be reduced differently

[313]. The symmetry property of a specific type of media can be used in the polarimetric SAR calibration [313].

Similarly, performing the ensemble average on the outer product of the Pauli scattering vectors, the coherency matrix can be defined as [145][311][26][312],

$$\begin{aligned} \langle [\mathbf{T}] \rangle &= \left\langle \sum_{m=1}^M k_{Pauli}(m) k_{Pauli}^{*T}(m) \right\rangle \\ &= \left\langle \frac{1}{2} \begin{bmatrix} S_{HH} + S_{VV} \\ S_{HH} - S_{VV} \\ S_{HV} + S_{VH} \\ i(S_{HV} - S_{VH}) \end{bmatrix} \begin{bmatrix} (S_{HH} + S_{VV})^* & (S_{HH} - S_{VV})^* & (S_{HV} + S_{VH})^* & -i(S_{HV} - S_{VH})^* \end{bmatrix} \right\rangle \end{aligned} \quad (1.13)$$

The coherency matrix and covariance matrix represent the second order statistics of the polarimetric SAR data [312].

Using the Mueller matrix, we can provide another definition to describe polarization characteristics, called the polarization signature [304][309]. Letting ϕ_t , ϕ_r , θ_t , and θ_r be the transmitting ellipticity, receiving ellipticity, transmitting orientation, and receiving orientation angles of the polarization ellipse, respectively, the definition of polarization signature is [304][309]

$$\sigma = \frac{4\pi}{k^2} \begin{bmatrix} 1 \\ \cos(2\phi_t)\cos(2\theta_t) \\ \cos(2\phi_t)\sin(2\theta_t) \\ \sin(2\phi_t) \end{bmatrix}^T [\mathbf{M}] \begin{bmatrix} 1 \\ \cos(2\phi_r)\cos(2\theta_r) \\ \cos(2\phi_r)\sin(2\theta_r) \\ \sin(2\phi_r) \end{bmatrix} \quad (1.14)$$

where the limitations of ϕ_t , ϕ_r , θ_t , and θ_r are $-\pi/4 \leq \phi_t \leq \pi/4$, $-\pi/4 \leq \phi_r \leq \pi/4$, $-\pi/4 \leq \theta_t \leq \pi/4$, and $-\pi/4 \leq \theta_r \leq \pi/4$ [306]. The polarization signature σ describes the radar cross section of scatter for different transmit and receive polarization status [304][309][310], which can be displayed using a three-dimensional graph [304][58].

However, there is a limitation of this representation: different type of scatters may have the same polarization signature [304]. The polarization signature can be used to estimate the orientation angle which can be used to estimate the digital elevation model [38][58], although this is seldom used in practice, InSAR being the preferred approach.

In the following, some of the major research areas of PolSAR are summarized.

Target Decomposition:

In order to identify the type of scatterers in the observed scene, we need to understand the scattering mechanisms observed by the PolSAR data. The modeling that determines the underlying scattering mechanisms of the observed fully polarimetric SAR data has been one of the most important research topics. These models are generally called target decomposition techniques [26], which are summarized as follows:

- a) *Coherent Decomposition:* Most of the early target decomposition methods are based on the analysis of the scattering matrix, which is classified as coherent decomposition [38][311]. The typical example of coherent decomposition is the Krogager decomposition [74] and Cameron decomposition [80]. Since the scattering matrix is only good at describing the deterministic scatters, the coherent decomposition is only suitable for the application of few dominated scatters [95], it can not be used for the decomposition of distributed scatters.
- b) *Incoherent Decomposition:* The second class of target decomposition methods is called incoherent decomposition, which depends on the analysis of the second-order statistics such as the covariance matrix (see Equation (2.5) for the definition

of covariance matrix) or the coherency matrix [95]. The incoherent decomposition is suitable for the application for distributed targets.

- c) Currently, many widely used target decomposition methods use second-order statistics such as covariance matrix or coherency matrix to perform the decomposition. 1) *The following methods use the coherency matrix to perform target decomposition:* The most recognized target decomposition method that uses the coherency matrix is Cloude and Pottier's method [26], which uses eigendecomposition to separate the scattering mechanisms. Based on this method, several improved methods have been proposed [51][29], and the bias due to multilook processing has been studied in [82]. 2) *The following methods use covariance matrix to do the target decomposition:* These methods include the three-component method [5] and its revision [24], four-component method [36], and two-component method [35]. In order to incorporate more types of scatterers in the decomposition, a five-component method which includes the wire scattering in the urban areas has recently been proposed in [45][64].
- d) Recently, a target decomposition method that uses quaternion formalism [75] and both scattering matrix and coherency matrix has been proposed in [75].
- e) Some target decomposition methods have been designed to tailor to the specified applications. The following are some examples: In [25], a two-component model is designed for Earth surface roughness estimation; In order to improve the performance in soil moisture estimation, the three-component method in [5] has been revised in [57]; Recently, a coherent target decomposition method has been applied in wetland characterization and presented in [49].

- f) Target decomposition techniques have been widely applied in many areas of the PolSAR applications, such as the biogenic slicks [65] and oil slick observation [66].

PolSAR Applications:

A lot of research has been done regarding the specific applications of PolSAR data. Since PolSAR data contains the information of target scattering characteristics, we can obtain much more accurate target separation from the fully polarimetric SAR data than from single polarization data. Therefore, it is not surprising that one of the most successful applications of PolSAR data is classification, which is mostly implemented through the application of the target decomposition technique. For instance, the method in [89] applies Cloude and Pottier's decomposition [26] while the method in [140] applies Freeman and Durden's decomposition [5] to perform land classification. Besides target decomposition, a variety of other techniques have been applied to do the classification, such as the neural network method [102] and the method that applies the deorientation parameters from the coherency matrix [88].

Another important application of PolSAR is image segmentation. Target decomposition technique can be also used to help the segmentation, such as the method in [101]. Besides target decomposition, a broad range of image processing techniques have been applied to perform the segmentation, such as the maximum likelihood method [100] and the Markov random field method [30].

Another important application of PolSAR is target detection. PolSAR can be used for general target detection [27] or the detection of specified type of targets, such as ship

detection [46][70] and coastline detection [98]. It even has the potential of detecting and classifying targets at the same time [28].

PolSAR data can be used to extract the slopes of the observed objects. Through the extraction of slope information, fully polarimetric SAR data can be used to extract the digital elevation model [58][59][60], although it is not as popular as generating digital elevation model from InSAR data. Using its slope measurement ability, the object angles of urban areas have been extracted in [69] and ocean wave slopes have been measured in [99].

Besides these aforementioned major applications, PolSAR has also been applied to numerous other applications, such as vegetation parameter estimation [34], biophysical parameter estimation [47], Earth surface roughness estimation [54][25][52][53], wetland characterization [48], sea ice thickness estimation [92], characterization of manmade targets [81], and target detection in urban areas [72].

Other Major Research Areas:

One of the major research areas is PolSAR calibration, which is to reduce the cross talk, amplitude imbalance, and phase imbalance between different polarizations [84][85][86]. Calibration techniques can be also used to reduce the Faraday rotation [96][97]. One recent study is focused on reducing the calibration errors using an *a posteriori* method [87].

Another major research area is compact PolSAR [62][63][68]. The fully polarimetric SAR mode has to sacrifice the swath width due to the limitations of other system parameters [62][63][68]. Some studies have focused on designing a compact PolSAR [62][63][68] which can not only extend the swath width and reduce the data rate,

but also maintain the basic observation ability of fully polarimetric SAR. The application of compact PolSAR to soil moisture estimation has been presented in [71].

1.1.1.2 Problem Statement

In Section 1.1.1.1, a brief, general review of PolSAR technique has been provided. As mentioned before, the information extraction of PolSAR requires the application of signal processing, such as filtering, detection, and estimation. Most of the signal processing methods requires the accurate modeling of the fully polarimetric SAR data. Polarimetric statistical models are important *a priori* information for many signal processing methods. Therefore, in this thesis, we study the PolSAR statistical modeling, covariance matrix formulation, and optimal despeckling.

Limitations of Previous Research:

1) PolSAR Statistical Model:

Appropriate statistical models are very important for PolSAR signal processing and information estimation [146]. However, there are many difficulties to obtain an appropriate statistical model:

- (a) In order to obtain a useful statistical signal processing method (for example, the PolSAR optimal despeckling in [144]), we need to establish an accurate statistical model for the PolSAR data. In order to adequately model the PolSAR data, generally we need to develop a statistical model with a higher level of complexity, hence requiring more parameters. Since single- or multi-look complex PolSAR data are multichannel, this improves the model complexity as well.

- (b) On the other hand, the more complex the statistical model, the more difficult it is to obtain a closed-form signal processing method. Therefore, in order to develop a closed-form signal processing method, sometimes we need to simplify a specified statistical model while maintaining its accuracy as much as possible.
- (c) The complex statistical model with more parameters generally increases the difficulty of parameter estimation. In this case, we need to develop more accurate parameter estimation methods.

All in all, we need to develop a statistical model which not only fits well with the fully polarimetric SAR data but also is easy to be implemented in signal processing.

The existing PolSAR statistical models are mostly based on the complex multivariate Gaussian [143] assumption and/or the product model [144][149] (see Section 2.2.1 for the details). However, these models have their limitations (Section 2.2.1). Therefore, we need to develop a statistical model which can completely or partly overcome these limitations. In Chapter 2, we study the alpha-stable model, and try to find an appropriate form of it which is suitable for the modeling of multichannel fully polarimetric SAR data. In Chapter 2, a new PolSAR statistical model is proposed using the alpha-stable distribution. In this study, we model the multichannel fully polarimetric SAR data as following a multichannel isotropic symmetric alpha-stable distribution. The goodness-of-fit of the proposed model is examined by experiments using real PolSAR data.

2) PolSAR Data Formulation:

PolSAR information extraction and signal processing significantly depends on the data formulation. For example, existing PolSAR information extraction (such as the target decomposition techniques that reviewed in Section 1.1.1.1) and signal processing (such as despeckling [144], detection [27], and estimation) techniques are mostly implemented through the analysis of the second-order models such as the covariance matrix [145]. However, these second-order models are based on the assumption that the fully polarimetric SAR data follows a multivariate Gaussian distribution. Therefore, the traditional covariance matrix has its limitations (see Section 2.3.2 for details). For non-Gaussian data, these second-order models may be inappropriate since sometimes the second-order moments do not exist [179]. In this case, model deviation introduces errors in the final results of information extraction or signal processing (Chapter 2 gives an example associated with despeckling). In Chapter 2, we study the covariance matrix definition based on the proposed PolSAR statistical model. The objective of this study is to develop a covariance matrix definition which can be applied to PolSAR data with a wide range of statistical characteristics of which the Gaussian assumption represents a sub-set. Based on some theoretical results from the alpha-stable model analysis, the covariance matrix based on fractional lower order statistics is proposed.

3) PolSAR Optimal Despeckling:

Existing PolSAR despeckling methods are mostly based on the covariance matrix [147][148], and are developed assuming the PolSAR data follows a Gaussian or product model [144][149]. In this thesis, we study the PolSAR optimal despeckling method in [144]. The existing optimal despeckling methods are derived using the Gaussian-based covariance matrix as well. Therefore, they have their limitations (see Section 2.4.1 for the

detailed comments). When there are strong reflectors in the scene, most of the existing filtering algorithms obtain blurred filtering results around these areas (Section 2.4.6). In this thesis, we study the PolSAR optimal despeckling method and propose an improved method which can reduce the artifacts around strong scatterers (Chapter 2). This proposed method is based on the application of the proposed covariance matrix definition.

1.1.2 InSAR

1.1.2.1 General Review

InSAR uses two or more spatially separated antennas to obtain the multichannel (usually two channels) SAR measurements [7]. The multichannel measurements of InSAR are different than those of the PolSAR since both the master and slave images are of the same polarization. Since the two antennas are separated spatially by a baseline [6], there is a path difference and hence a phase difference between the common pixels of the two images from the antennas. A 2-dimensional map of the phase differences across the target area is called the interferogram. The interferogram contains information about the topographic elevation or target movement. Depending on the different measuring geometry, we can obtain either elevation [9] or movement information [8][14] by properly interpreting and processing the interferogram. Digital elevation model extraction is one of the most important applications of InSAR [12], and its measurement sensitivity is determined by the system and geometric parameters [10][11].

Basics of InSAR:

The fundamental measurement of InSAR is the interferogram, which is the complex product of the master image $S_1(m,n)$, multiplied by the complex conjugate of the slave image $S_2(m,n)$ [7][311][6]

$$\begin{aligned}
 I &= S_1(m,n)S_2^*(m,n) = \left| S_1(m,n)S_2^*(m,n) \right| \exp\left(-j\frac{4\pi}{\lambda}(d_1(m,n) - d_2(m,n))\right) \\
 &= \left| S_1(m,n)S_2^*(m,n) \right| \exp\left(-j\frac{4\pi}{\lambda}(\Delta d(m,n))\right) \\
 &= \left| S_1(m,n)S_2^*(m,n) \right| \exp(j\phi(m,n))
 \end{aligned} \tag{1.15}$$

where $d_1(m,n)$ and $d_2(m,n)$ are the distances from the master and slave antenna to the target, respectively; λ is the wavelength of the radar system. The phase in the interferogram is the most important observable, however, this phase is only within the range of $(-\pi, \pi]$, which needs to be unwrapped to obtain its original value.

From interferometric phase, we can obtain the height, $h(m,n)$, of the target through the following relationship [141] [314],

$$\phi(m,n) = \frac{4\pi G}{\lambda} h(m,n) \tag{1.16}$$

where G is a parameter that relates to the baseline and the other geometric parameters [311]. Therefore, if we can obtain a correct estimation of the interferometric phase, the height of target may be obtained. However, the observation of $\phi(m,n)$ is in its principle value and contaminated by noise, which is [212]

$$\begin{aligned}
 \phi(m,n) &= W[\varphi(m,n) + \varepsilon(m,n)] \\
 &= \varphi(m,n) + \varepsilon(m,n) \pm k(m,n) \cdot 2\pi \in (-\pi, \pi] \\
 &= \psi(m,n) + \varepsilon(m,n) \in (-\pi, \pi]
 \end{aligned} \tag{1.17}$$

where $\phi(m,n)$ is the observed phase value, $\varphi(m,n)$ is the clean phase value before modulo 2π , $\psi(m,n)$ is the wrapped clean phase value, and $w[\]$ is the modulo operation. We need to perform phase filtering and unwrapping to restore its original value. Phase filtering is to estimate $\psi(m,n)$ from $\phi(m,n)$; phase unwrapping is to restore $\varphi(m,n)$ from $\psi(m,n)$.

Phase Filtering of InSAR:

It is obvious that phase filtering is a signal estimation problem, and the Cramer-Rao lower bound of this estimation problem has been derived as [193][10]

$$E[(\phi - \psi)^2] = \frac{1 - \gamma^2}{2N\gamma^2} \quad (1.18)$$

where N is the number of samples used in the estimation. The phase filtering problem has been solved by a maximum a posteriori estimation [141].

Phase Statistics:

Phase statistics are important knowledge for the phase filtering and phase unwrapping. Assuming Gaussian statistics, the pdf of the interferometric phase is [298][150][110]

$$f(\psi) = \frac{\Gamma(n+0.5)(1-|\gamma|^2)^n |\gamma| \cos(\phi - \psi)}{2\sqrt{\pi}\Gamma(n)(1-[\gamma|\cos(\phi - \psi)]^2)^{n+0.5}} + \frac{(1+|\gamma|^2)^n}{2\pi} {}_2F_1\left(n, 1; 0.5; [\gamma|\cos(\phi - \psi)]^2\right) \quad (1.19)$$

where ${}_2F_1$ is the Gauss hypergeometric function [237], ϕ and ψ are the observed interferometric phase and the clean wrapped phase, respectively; γ is the coherence, and $-\pi < \phi \leq \pi$. The single look form of (1.19) has been applied in the phase filtering [141].

The variance of the phase is a function of coherence [7],

$$\sigma_{\phi}^2 = E[(\phi - \psi)^2] = \frac{\pi^2}{3} - \pi \arcsin(|\gamma|) + \arcsin^2(|\gamma|) - Li_2(|\gamma|^2) / 2 \quad (1.20)$$

where Li_2 is the Euler's dilogarithm defined as [216]

$$Li_2(|\gamma|^2) = \sum_{n=1}^{\infty} \frac{|\gamma|^{2n}}{n^2} \quad (1.21)$$

This equation means that the noise standard deviation is related to coherence [318]. Since the value of coherence varies spatially, the noise standard deviation varies spatially, too.

Phase Unwrapping of InSAR:

Phase unwrapping is an ill-posed problem which needs some *a priori* information [315]. From (1.17), we know that the phase unwrapping is to restore $\phi(m, n)$ from $\psi(m, n)$, i.e., to obtain the value of $k(m, n)$.

The two-dimensional phase gradient of the wrapped phase can be defined as [127]

$$\begin{aligned} \Delta_x(m, n) &= W\{\psi(m+1, n) - \psi(m, n)\} \quad m=1, 2, \dots, M-1, n=1, 2, \dots, N \\ \Delta_x(m, n) &= 0 \quad \text{otherwise} \end{aligned} \quad (1.22)$$

$$\begin{aligned} \Delta_y(m, n) &= W\{\psi(m, n+1) - \psi(m, n)\} \quad m=1, 2, \dots, M-1, n=1, 2, \dots, N \\ \Delta_y(m, n) &= 0 \quad \text{otherwise} \end{aligned} \quad (1.23)$$

Itoh's theory [316] means that when $-\pi < \Delta_x(m, n) \leq \pi$, $-\pi < \Delta_y(m, n) \leq \pi$, the unwrapping can be correctly performed by simply integrating the phase gradient of the wrapped phase [127]. This is the fundamental theory of InSAR phase unwrapping, and most existing phase unwrapping algorithms can be considered as an implementation of this theory.

However, in the real InSAR case, the condition that $-\pi < \Delta_x(m, n) \leq \pi$, $-\pi < \Delta_y(m, n) \leq \pi$ is not always satisfied due to the noise and other factors [315][127]. When this occurs,

phase unwrapping can be formulated as a signal estimation problem. Phase unwrapping has been formulated as a maximum *a posteriori* estimation which is implemented using the statistical information of the wrapped phase [134][317], and also has been formulated as a maximum *a posteriori* estimation problem and solved by the implementation of Kalman filtering [211]. Recent research showed that the weighted least squares method is equivalent to maximum likelihood and maximum *a posteriori* method under some conditions [211].

Coherence and Decorrelation:

Coherence γ is one of the most important observables derived from InSAR because it can describe InSAR decorrelation effects. The detailed definition of coherence can be found in (3.2). Coherence can be decomposed into several sources [6][311][94]:

$$\gamma = \gamma_B \gamma_T \gamma_N \gamma_V \quad (1.24)$$

where

1) γ_B is the spatial decorrelation (also known as baseline decorrelation), which is due to the different measuring geometry of the two antennas [311].

2) $\gamma_N = \frac{1}{\sqrt{1+1/\nu_1} \sqrt{1+1/\nu_2}}$ is the thermal noise decorrelation [6], which is caused by the

thermal noise in the radar system, where ν_1 and ν_2 are the signal to noise ratio of the master and slave image channels, respectively.

3) γ_T is the temporal decorrelation [311], which is due to the time difference between the two observations.

4) γ_V is the volume decorrelation [6], which is due to the volume scattering existing in three-dimensional situations such as forest canopy and urban built-up areas [94].

Major Research Areas of InSAR:

According to the directions of the baseline with respect to the flying track, it is well-known that InSAR can be classified into across-track and along-track modes. In this thesis, we are mainly concerned with the signal processing methods of across-track interferometry. Along-track interferometry is mentioned here only for completeness.

In this thesis, we define the across-track interferometry as the InSAR mode that has antenna separation across the flying track for the single-pass mode or the different passes have spatial separation across the flying track for the repeat-pass mode [6]. Therefore, its most popular application is to measure the topography of the Earth, by deriving digital elevation models, digital surface models, and digital terrain models. When the temporal decorrelation can be neglected (for most of the cases, when use one single flying pass over the imaging area, the temporal decorrelation can be neglected), it is called single-pass InSAR; otherwise, when the temporal decorrelation cannot be neglected, it is called multi-pass InSAR (Note: In [6], repeat-pass InSAR is defined as the mode outside of along-track or across-track interferometry, which is different to the definition here). Several of the major research and application areas for across-track InSAR are listed below:

- a) One important research area is to accurately extract digital terrain model from the measured digital surface model [78][79].
- b) It can also be used in the forest height estimation [119][151].
- c) It has also been applied in the digital surface model mapping in urban areas:

Because layover and shadow frequently occurs in urban areas, it is difficult to

conduct the urban mapping using InSAR [121][122]. Therefore, some studies are focused on the relative complex processing in urban areas [121][122].

- d) It also has the potential for ocean wave imaging [129].
- e) The application of multi-pass across-track SAR for the digital elevation model generation has been studied in [137].
- f) The most popular application of multi-pass InSAR is change detection [125], such as the measurement of subsidence in urban areas [126], and the observation of the water level change in flood plains [108] or wetlands [109].
- g) The multi-pass data may be collected during a long period of time and from which we obtain the displacement information of objects from multiple interferograms. This technique is generally called differential interferometry [114][115][103]. One important research area related to differential interferometry is how to apply the permanent scatterers technique [83] in order to reduce the impact of temporal decorrelation. Applying the permanent scatterers technique can remove the errors due to atmospheric phase screen [83], improve the measurement accuracy of differential interferometry [103], improve the height measurement accuracy of urban areas [114], and measure the ground deformation over interested areas [115].

Along-track interferometry generally denotes the InSAR mode that has an antenna separation along the flying track [6]. In this thesis, we define along-track interferometry as the InSAR mode that is mainly sensitive to target movement information such as ocean currents or vehicle traffic. Along-track interferometry also includes the single- and multi-pass modes. To list a few, along-track InSAR has the following major research areas:

- a) One of the most popular applications is to measure the ocean current velocity [123][124].
- b) Another popular application of along-track InSAR is moving target detection [110] and velocity estimation [111]. When the baseline component exists in both the along- and across-track direction, the special processing methods for the moving target detection has been studied in [112].

Single baseline InSAR can only obtain the gross height of all the scatterers, cannot obtain the distribution of the scatterers along the height direction [40]. Therefore, another important research area is to use multibaseline InSAR technique to achieve tomography [40].

There are various sources of errors in InSAR, which has been discussed in [10][113]. The errors of the measured digital elevation model include the geometric errors such as baseline errors [10], signal processing errors such as phase filtering errors and phase unwrapping errors [113], and other errors such as the errors due to the penetration of radar signal into the different part of volume for different wavelengths [116] and the height measurement errors induced by the inappropriate selection of look angle [120]. In the following, we will give a more detailed introduction about the signal processing errors in the InSAR subsystem.

1.1.2.2 Problem Statement

The successful extraction of digital elevation model depends on the development of many signal processing procedures. In this thesis, we study some of the signal processing methods that relate to digital elevation model extraction.

Signal Processing Methods: After image formation, the InSAR data need to go through a series of signal processing steps in order to extract a digital elevation model. These steps generally include: coregistration [13], range spectral filtering [93], flat-Earth phase removal [15], phase filtering [150], phase unwrapping [142], geocoding, and digital elevation model generation. The steps addressed in this thesis include phase filtering and phase unwrapping.

Although image coregistration is not the major concern of this thesis, for the sake of completeness, we give it a brief introduction here. Image coregistration (also called registration) is an important research area of InSAR. The coregistration accuracy is one of the factors that impact the quality of interferometric phase [128][104]. Some coregistration methods are performed during the image focusing [104], while most are performed after the image focusing step. Most of the coregistration methods need to conduct interpolation during the coregistration. The comparison of different types of interpolations has been presented in [105]. Most of the existing interpolation methods are time consuming. Therefore, it is important to develop a fast interpolation method, such as the method proposed in [117]. Coregistration accuracy largely depends on the interpolation accuracy. Therefore, a lot of research has been focused on developing an accurate interpolation method, such as the interpolation kernel proposed in [118]. Other studies use ancillary information to improve the coregistration accuracy [106]. Recently, the coregistration method that applies the analytic search instead of discrete search has been proposed in [107]. In this thesis, we do not discuss coregistration but consider two other InSAR signal processing methods: phase filtering and phase unwrapping.

Phase Filtering:

Phase filtering is one of the most important signal processing steps in InSAR for the following reasons:

1) Phase quality directly impacts the accuracy of height measurements in the InSAR system [132] and thus influences the error level in the digital elevation model generation [10].

2) Most InSAR suffers from the types of decorrelations noted in equation (1.22), which ultimately impact the phase quality [10][131][133]: baseline decorrelation, thermal noise decorrelation, temporal decorrelation, miscoregistration decorrelation, and topography decorrelation. In one form or another, these decorrelations create noisy and/or biased phase. Topography decorrelation is most eminent in the areas with foreshortening and layover [131]. Interferometric phase can be of very low quality due to the decorrelation effects in the InSAR subsystem [130]. When the decorrelation is severe, the signal to noise ratio is low [150]. In this case, phase filtering is an obvious way of reducing the noise in the InSAR system. There is another technique called range spectral filtering [93] which can be used to reduce decorrelation and improve coherence. However, range spectral filtering method can only remove part of the phase noise and is mostly applied when the topography is relatively flat [133][93]. After range spectral filtering, there will be noise remaining in the interferometric phase in most cases. Therefore, for most of the InSAR applications, phase filtering becomes the only effective way to reduce the phase noise and improve the phase quality.

3) Additionally, the subsequent phase unwrapping may develop errors due to phase noise.

4) Due to layover and shadow, some areas of the phase image may be dominated by noise and difficult to interpret [131]. In this case, we need to apply phase filtering to reduce the noise inside these areas.

However, there are many difficulties in developing a successful phase filtering method:

- 1) When the noise level is very high, the phase fringes may easily be destroyed during the noise removal.
- 2) During the phase filtering (especially wavelet-domain filtering, also see Chapter 4 for details), we generally consider the high frequency information as noise [141]. However, when the phase fringes are dense, the high frequency information may contain phase information (see Section 4.5.2 for details). In this case, it is very difficult to separate the noise from the high frequency phase information.
- 3) When there are shadow areas in the mapped scene of the phase image, the phase data may be dominated by noise inside these areas. This increases the difficulty of phase filtering.
- 4) Phase filtering largely depends on the statistical analysis of phase data. For the transform-domain phase filtering, we need to establish the statistical models of the phase data in the transform domain. However, there are not many studies in the literature about this matter (see Chapter 4 for details). Therefore, a lot of research needs to be done for the transform-domain phase filtering.

- 5) The computational complexity may be very high for the filtering of large areas.
- 6) The memory requirement may be very high for some phase filtering methods.

Phase Unwrapping:

The original interferometric phase obtained from the focused SAR images is wrapped to $[-\pi, \pi)$ and needs to be unwrapped to restore its original value. Generally speaking, phase unwrapping includes global and local methods [127]. Global methods are implemented by the formulation of the phase unwrapping problem as a mathematical problem [127][135]. The typical global methods include the least squares method [266] and the minimum L_p norm method [270]. Local methods are implemented by setting up the optimized integration path and unwrap the phase through the simple addition or subtraction of 2π for the specific pixels [127][135]. The typical local method is the Goldstein's branch-cut method [142][135]. There are many difficulties and challenges in phase unwrapping [134][135][136][138][139]:

- 1) When the integration of the pixels in the 2×2 moving window inside the wrapped phase map is not zero, there is a discontinuity in these pixels [127][301] (For the definition of discontinuity, also see Section 6.2.1 for details). The discontinuity of the phase leads to phase unwrapping errors and when there are large numbers of discontinuities in the phase map, it is difficult to perform the unwrapping correctly. Phase discontinuities can be

described by the presence of residues [142][135] (The definition of residue is very similar to that of discontinuities, for the definition of residues, see Section 6.2.1 for details). By the proper arrangement of the unwrapping around the residues, we can reduce the phase unwrapping errors.

- 2) In areas with mountains or urban objects, shadow and layover may cause large numbers of residues in the interferogram [134][136][139]. In the shadow areas, the interferometric phase is dominated by noise [138][139]. In these shadow areas, most of the local unwrapping methods cannot obtain an unwrapping result. Inside the shadow areas, the residues are very dense, which causes large numbers of global errors for the global unwrapping method. Layover may also cause large number of residues in the wrapped phase. More importantly, due to layover, the radar echoes from different topography positions may be received at the same resolution cell, which increase the difficulty of phase unwrapping [134][138][139].
- 3) Decorrelation leads to phase noise and thus large numbers of residues. When the coherence level is very low, it is difficult to identify and separate the phase fringes from the noise. In this case, most existing phase unwrapping algorithms cannot obtain a satisfactory unwrapping result.
- 4) For large area phase unwrapping, sometimes the memory and computational requirements remain a challenge even for the fastest computers [135].

Because of the importance and challenges of phase unwrapping, much research tends to be focused on developing robust phase unwrapping methods.

Limitations of previous research:

1) Existing phase filtering methods are mostly time domain methods, and existing wavelet-domain methods are mostly simple filtering methods (see Section 4.1 for details). When the value of coherence is very low, most of the existing methods cannot obtain a satisfactory residue reduction result and at the same time maintain the phase fringes (see Chapter 4). Therefore, in this thesis, we try to develop more advanced phase filtering methods. In Chapter 4, the wavelet-domain phase-filtering method is studied. Based on the statistical analysis of the wavelet coefficients of the phase data, two new wavelet-domain phase-filtering methods are proposed (Chapter 4).

2) The existing phase unwrapping methods mostly cannot perform the unwrapping at the areas missing valid data due to shadow. In this thesis, we research the robust phase unwrapping methods which can perform a smooth unwrapping at the areas with invalid data. A phase unwrapping method which applies both the regularization and weighting techniques is proposed to solve this problem (Chapter 5).

3) The “quality-guided” phase-unwrapping methods use a phase-quality map to direct the selection of the integration path to reduce phase unwrapping errors [127]. Weighted phase unwrapping methods use a phase quality map to assign weights to specific pixels in order to suppress the influence of noise [264][268][127]. Therefore, the phase quality map is an important input component for both quality-guided and weighted phase unwrapping methods (see Chapter 6). Residue is an important measurement of phase quality for the branch-cut method [142]. However, residue cannot be directly used as a

quality map for quality-guided methods [136] because it is not a quantitative representation of the noise levels. A new phase quality measurement called second-order residue is proposed in this thesis and applied in PolInSAR phase unwrapping (Chapter 6).

1.1.3. Polarimetric and Interferometric SAR

1.1.3.1 General Review

The combination of PolSAR and InSAR is called polarimetric and interferometric SAR (PolInSAR) (also called polarimetric SAR interferometry) [16]. InSAR is mainly sensitive to height information of the scatterers, while PolSAR is mainly sensitive to their shape and orientation [17][39]. Therefore, PolInSAR is sensitive to both height and shape information [17]. Since both the magnitude and interferometric phase information of PolInSAR data can be used to obtain the scattering characteristics of targets [21], PolInSAR provides more information than either PolSAR or InSAR [22] independently. The question is how to correctly extract the respective information for each designated application.

Basics of PolInSAR:

The Pauli scattering vectors of the master and slave images (indices 1 and 2 respectively) are

$$k_{1,Pauli} = [S_{HH1} + S_{VV1} \quad S_{VV1} - S_{HH1} \quad S_{HV1} + S_{VH1} \quad i(S_{HV1} - S_{VH1})]^T \quad (1.25)$$

$$k_{2,Pauli} = [S_{HH2} + S_{VV2} \quad S_{VV2} - S_{HH2} \quad S_{HV2} + S_{VH2} \quad i(S_{HV2} - S_{VH2})]^T \quad (1.26)$$

Assuming $\omega = \omega_1 = \omega_2$, the interferogram of PolInSAR can be calculated as [19][38]

$$I_1 I_2^* = (\omega k_1)(\omega k_2)^{*T} = \omega^{*T} [\Omega_{12}] \omega \quad (1.27)$$

where $\Omega_{12} = \langle k_1 k_2^{*T} \rangle$, ω is a parameter that defines the scattering mechanisms [16]. The interferometric phase of PolInSAR is [38][19]

$$\psi = \arg\{I_1 I_2^*\} = \arg\{\omega^T [\Omega_{12}] \omega\} \quad (1.28)$$

The vector coherence can be obtained as [23][38]

$$\gamma = \frac{\omega^{*T} [\Omega_{12}] \omega}{\omega^{*T} [T] \omega} \quad (1.29)$$

where $T = \frac{T_{11} + T_{22}}{2}$, and $T_{11} = \langle k_1 k_1^{*T} \rangle$, $T_{22} = \langle k_2 k_2^{*T} \rangle$ [19]. The definition in (1.29) is the special case of (7.3).

Review of PolInSAR:

Currently, the most promising application of PolInSAR is vegetation height and structure measurement [18][19][20]. Although PolSAR can be used for vegetation parameter inversion [34], PolInSAR provides more accurate estimation results in many circumstances. However, without appropriate modeling, it is difficult to retrieve information from PolInSAR data. Therefore, the modeling of PolInSAR data is an important research topic. For example, the two well known models of tree height estimation are the orientated volume over ground [17][91] and random volume over ground [23] models. A comparison of these two models has been presented in [43] using the experimental results of agricultural applications. The experiments on applying these models have been demonstrated using L-band [19][76], P-band [20], and X-band [73][77] PolInSAR systems. However, these two models [23][91][43][19] are implemented by the inversion of the vector coherence (or coherency matrix) proposed in [16] (See equation (7.3) for the definition of the vector coherence in [16]. Also see the definition of (1.28)

and (1.29)). In Chapter 7, we will study the definition of vector coherence and propose a revised vector coherence definition.

Besides the application in agriculture and forest monitoring, the potentials of PolInSAR have also been demonstrated in urban mapping [31][32] and building height estimation [50][77].

Another promising application is PolInSAR tomography, which is to obtain the distribution information in the vertical dimension [41][42].

Besides these applications, PolInSAR demonstrates its advantages in land classification by using the phase information [33], coherence optimization [67], and volume decorrelation [94][95]. PolInSAR can be also applied in ship classification [55][56], detecting the target hidden under forest canopies [61], and the observation of glaciers [90].

1.1.3.2 Problem Statement

In this portion of the thesis, we are mainly concerned with statistical modeling, data formulation, and the related signal processing methods (such as coherence optimization) of PolInSAR.

PolInSAR Data Formulation: Generally speaking, there are eight input data channels (the four polarimetric channels for each of the two InSAR antennas). If we apply the reciprocal assumption [180][295], $HV_1=VH_1$, $HV_2=VH_2$, it is simplified to six independent PolInSAR channels (as in the example of Chapter 7). The information extraction generally needs to be applied on a specified formulation which organizes the multichannel PolInSAR data together. There are several ways to organize these data:

1) The most popular way is to arrange them as a coherence formulation, such as the vector coherence definition in [16], which has been widely accepted and extended to the so-called PolInSAR coherence set [38]. Similar to InSAR, one of the most important PolInSAR observables is coherence. The eight (or six) channels of PolInSAR data can be used to obtain the coherences for all the combinations of polarizations, these coherences can be formulated by the so called vector coherence [16]. Recently, a PolInSAR coherence formulation which includes polarimetric decomposition and the coherences of ground and volume has been proposed in [39].

2) The second way is to design the PolInSAR formulation as a structure of parameter estimation [37].

3) The third way is the PolInSAR formulation that uses the matrix analysis method [44].

The second and third ways are included for the sake of completeness and will not be addressed further.

Limitations of previous research:

1) In previous research, much work concerns the statistical analysis and modeling of PolInSAR data and similar to the PolSAR and InSAR cases noted earlier, the data are mostly modeled as multivariate complex Gaussian distributions [143][38] for simplicity [16]. However, when there are strong scatterers in the SAR image, which mostly (but do not have to) occur in urban areas, the SAR clutter may be impulsive in character. In this case, the SAR image may be represented better by a heavy-tailed distribution rather than a Gaussian distribution [179][183][184] (Here heavy-tailed means that the two ending parts of the probability density function (pdf) approach zero more slowly than the Gaussian distribution [179] while the central part is more strongly peaked than the

Gaussian distribution). Therefore, when the PolInSAR data are non-Gaussian (heavy-tailed distributed), the existing Gaussian-based PolInSAR processing methods may introduce errors due to model deviation (see Chapter 7 for details). The objective in this thesis is to propose a PolInSAR statistical model which can accurately describe the data of a wide range of distributions.

2) The PolInSAR formulation (i.e. vector coherence, see Section 7.3.1) is developed based on the assumption that the multichannel PolInSAR data is multivariate Gaussian distributed [143][38]. This formulation is not accurate when the PolInSAR data includes heterogeneous areas. Therefore, in this thesis, the coherence formulation of PolInSAR data is studied under the assumption of a wide range of data distributions (Chapter 7).

3) A widely accepted PolInSAR coherence optimization scheme is that proposed in [16]. However, this method is also derived using the Gaussian-based PolInSAR formulation, i.e., the vector coherence in [16]. Since the vector coherence in [16] assumes the PolInSAR data as Gaussian distributed, which is inaccurate when the PolInSAR data include heterogeneous areas and/or heavy-tailed distributions. This leads to the errors in the results of coherence optimization (see Chapter 7 for details). In order to reduce these errors due to statistical model deviation, we study the PolInSAR coherence optimization when the PolInSAR data is non-Gaussian (heavy-tailed) distributed (Chapter 7).

1.2 Research Objectives

In this thesis, three major issues are studied. First the statistical analysis and signal processing of the PolSAR subsystem are studied. Second, the signal processing (coherence estimation, phase filtering, and phase unwrapping) of the InSAR subsystem is

studied. Third, the statistical analysis and signal processing of the PolInSAR system are studied.

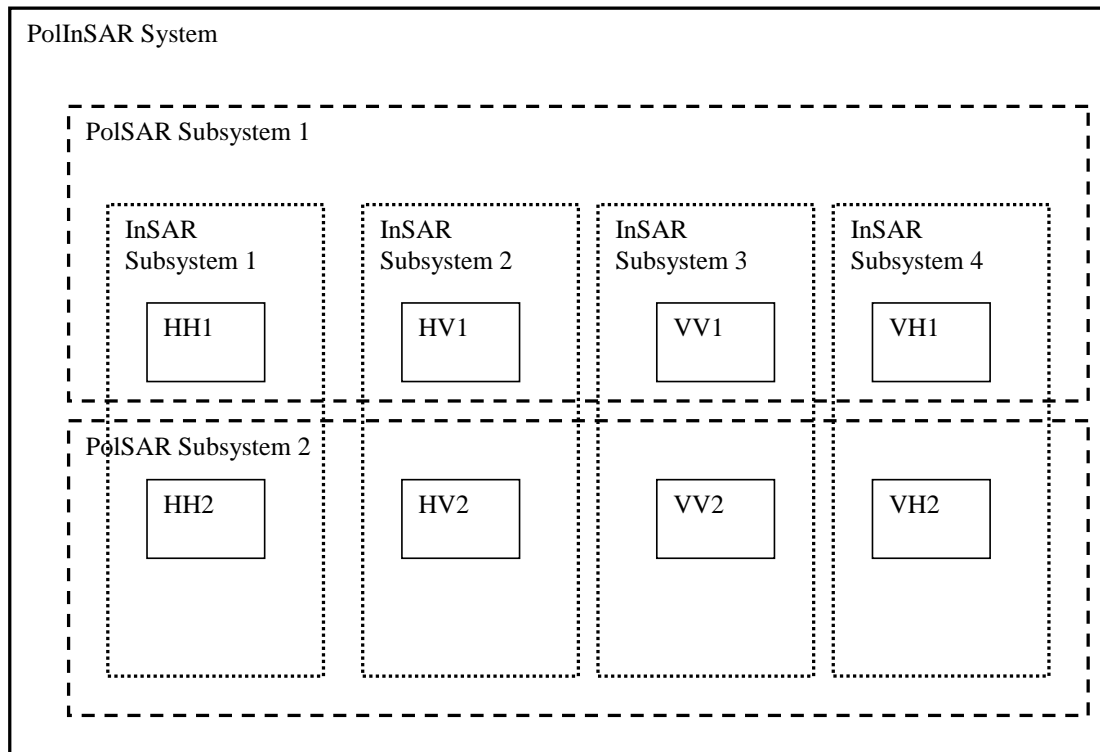


Figure 1.1. PolInSAR system. As defined in this thesis, the PolInSAR system includes two PolSAR subsystems and four InSAR subsystems providing a total of eight input data channels.

Most of the problems in the PolSAR subsystem and InSAR subsystem will be inherited by the whole PolInSAR system. Therefore, most of the signal processing methods of PolSAR and InSAR subsystems can be used in PolInSAR (For example, the coherence estimation, phase filtering method, and phase unwrapping method used in InSAR subsystem can be applied to the PolInSAR system as well). A typical PolInSAR

system which includes the PolSAR and InSAR as its subsystems has been illustrated in Figure 1.1.

The PolInSAR system in Figure 1.1 includes two PolSAR subsystems and four InSAR subsystems (When we apply the reciprocal assumption [180][295], $HV_1=VH_1$, $HV_2=VH_2$, the PolInSAR system can be simplified to six channels of SAR data, which includes two PolSAR systems and three InSAR subsystems). The observations of the PolSAR subsystem are the four channels of single-look or multilook complex SAR data.

The PolInSAR system in Figure 1.1 includes two PolSAR subsystems, which are:

- (a) HH1, HV1, VV1, and VH1;
- (b) HH2, HV2, VV2, and VH2.

The fundamental observations of the InSAR subsystem are the single-look complex master and slave images. The PolInSAR system in Figure 1.1 includes four InSAR subsystems, which are:

- (a) HH1 and HH2;
- (b) HV1 and HV2;
- (c) VV1 and VV2;
- (d) VH1 and VH2.

The observations of the PolInSAR system in Figure 1.1 include eight channels: HH1, HV1, VV1, and VH1 are the master images; HH2, HV2, VV2, and VH2 are the slave images.

This thesis will first study the statistical characteristics of the PolSAR data, and select an appropriate model to describe these data. The validity of the proposed model is

tested by goodness-of-fit experiments. Using the proposed statistical model, some signal processing methods will be developed.

Since phase filtering and phase unwrapping are fundamental to accurate phase determination in InSAR, and ultimately determine the accuracy of digital elevation model generation, we therefore, research phase filtering and phase unwrapping methods in this thesis, developing new algorithms for both.

Finally, this thesis addresses a PolInSAR formulation which is suitable for the representation of PolInSAR data with a wide range of statistical characteristics.

The specific research objectives of this thesis are as follows:

- 1) To study the statistical characteristics of PolSAR data; to propose a PolSAR statistical model (specifically, the alpha-stable model) which can represent the PolSAR data of not only non-heavy tailed but also heavy-tailed distributions (The PolSAR data include the scenes of both homogeneous and heterogeneous areas).
- 2) Based on statistical analysis of PolSAR data, to develop a PolSAR formulation which reflects its statistical information content.
- 3) Based on the proposed PolSAR formulation, study the related PolSAR signal processing methods.
- 4) To study the InSAR coherence estimation method.
- 5) To research phase filtering methods of the InSAR subsystem; to propose a phase filtering method which can not only significantly reduce the number of residues, but also maintain most of the phase fringes even when the phase quality is poor.

- 6) To research phase unwrapping methods of the InSAR subsystem; to propose a phase unwrapping method which can obtain a robust unwrapping result when some areas of the phase data that are missing valid data and other areas are of low coherence.
- 7) To study the statistical characteristics of PolInSAR data; to propose a PolInSAR statistical model which can accurately describe the statistical characteristics of multichannel PolInSAR data.
- 8) To research PolInSAR coherence formulation, and propose an accurate PolInSAR formulation which considers the underlying statistical characteristics of PolInSAR data.
- 9) Based on the statistical analysis, to study the PolInSAR signal processing methods (such as coherence optimization) in order to improve the processing accuracy and to reduce the processing errors.

1.3 Thesis Overview

This thesis contains eight chapters. Chapter 1 (current chapter) is the literature review and thesis overview which provides the background to the thesis research and introduces the problem statement and research objectives. Chapter 2 to Chapter 7 are the chapters containing original research. Most of this research work has been presented in separate papers (see Section 1.5 for details) that have either been published, accepted for publication or are currently under review. Each of the Chapters (Chapter 2 to Chapter 7) consists of a single paper. Chapter 8 is the summary of the thesis and introduces topics for future research.

Chapter 2 concerns the statistical analysis of PolSAR data and its signal processing methods. In Chapter 2, we first study the statistical distribution of complex fully polarimetric SAR data. Based on the statistical analysis, we propose to use the multichannel alpha-stable model to describe the multichannel PolSAR data (see Section 2.2.2 for the details). This statistical model has many advantages with respect to the traditional Gaussian model. From the review of Section 1.1.1.1, the traditional PolSAR information extraction is largely based on the covariance matrix. Therefore, we study the covariance matrix in Chapter 2 as well. Using the proposed statistical model, the covariance matrix based on fractional lower order statistics (FLOS) is developed. Using this FLOS-based covariance matrix, a revised optimal despeckling method is proposed. The proposed optimal despeckling method is not only an improved method, but also validates the proposed statistical model and covariance matrix definition.

Chapter 3 addresses the coherence estimation of an InSAR subsystem. Although the coherence estimation is discussed using InSAR as an example, it can be applied to the PolSAR subsystem and the whole PolInSAR system as well. Using the alpha-stable model, a new coherence definition has been proposed in this chapter.

Chapter 4 concerns the phase filtering of the InSAR subsystem (Note: Although phase filtering is discussed using the context of InSAR, it is obvious that it can be applied to the PolSAR subsystem and the whole PolInSAR system as well). First, the wavelet-domain phase filtering is formulated as a signal detection and estimation problem. Second, a wavelet-domain phase filtering scheme using simultaneous detection and estimation has been established. Third, the closed-form estimator and detector are derived based on the statistical modeling of wavelet coefficients. Fourth, two wavelet-domain

phase-filtering methods using simultaneous detection and estimation are proposed. The first one is performed in the wavelet-packet domain while the second one is performed using undecimated wavelet.

Chapter 5 and Chapter 6 addresses the phase unwrapping and the phase quality map. The phase quality map can be used as an input parameter during the phase unwrapping. Therefore, Chapter 5 and Chapter 6 are related because the research in Chapter 6 can be used in Chapter 5.

Chapter 5 proposes a new phase unwrapping method called weighted regularized preconditioned conjugate gradient (PCG) phase unwrapping. Through the combination of regularization and weights, the proposed method reduces not only the phase unwrapping errors in the areas missing valid phase data, but also those of the noise contaminated areas.

Chapter 6 studies the phase quality map which is an important input parameter for many phase unwrapping methods. A phase quality map is important for the quality-guided methods and also serves as the weights for many weighted phase unwrapping methods. In Chapter 6, we propose a new phase quality indicator which is called second order residue. The second order residue can be directly used as a quality map after simple arrangements. Finally, the proposed phase quality map is applied in PolInSAR phase unwrapping.

Similar to Chapter 2 and Chapter 3, Chapter 7 also address the statistical analysis based upon the alpha-stable model. Chapter 7 addresses PolInSAR coherence formulation and coherence optimization. First, the PolInSAR statistical model is studied using the alpha-stable model. Based on this study, a new PolInSAR coherence formulation based

on fractional lower order statistics is proposed. Finally, the proposed coherence formulation is verified using the coherence optimization technique.

Chapter 8 provides a summary and concluding remarks to the thesis and suggests topics for future research. First, the major results of this thesis will be summarized. Then the outlook of future studies will be provided.

The link between the separate chapters:

1. Chapters 2, 3, and 7 are concerned with the statistical analysis using the alpha-stable distribution for PolSAR, InSAR, and PolInSAR, respectively. The statistical analysis is related to the single look complex SAR image.
2. Chapters 5 and 6 are, respectively, about phase unwrapping and the quality map. The phase quality map can be used as the input parameters for some phase unwrapping methods, and therefore these topics are related.
3. Chapter 4 and 5, and 6 are about the statistical analysis and signal processing of InSAR subsystem.
4. Chapter 2 deals with specifically with PolSAR, Chapters 3, 4, 5, and 6 address issues with InSAR, while Chapter 7 is concerned with PolInSAR as a whole. All the Chapters 2-7 are concerned with statistical analysis and signal processing. They are just different subtopics of the PolInSAR system.

1.4 SAR Data Used in this Thesis

The SAR data used in this thesis include P-band and L-band data:

P-band: The fully polarimetric P-band repeat-pass InSAR data were acquired by Intermap Technologies Corporation using their airborne InSAR system [336][337]. This InSAR system operates at the wavelength of 72 cm [336]. The azimuth and range resolution are both approximately 3 meters [338].

L-band: The L-band SAR data were also acquired by the Intermap Technologies Corporation. This single-pass InSAR system was developed using an upgraded platform from the TOPOSAR system [334]. The TOPOSAR L-band system has a range and azimuth resolution of about 1.1 and 0.25 meters (single-look), respectively [335].

1.5 Research Contributions of this Thesis

The major contributions of this thesis are as follows:

- 1) Chapter 2: In this chapter, a new PolSAR statistical model is proposed. In this study, the complex, multipolarization PolSAR images are modeled as a multichannel isotropic complex symmetric alpha-stable distribution. Based on this statistical model, a new covariance matrix based on the fractional lower order statistics has been proposed. Finally, a revised optimal despeckling method using the proposed covariance matrix is proposed.
- 2) Chapter 3: A new coherence estimation method is proposed for InSAR data. Assuming the InSAR data follow an alpha-stable distribution, this new coherence definition is derived using the concept of fractional lower order statistics. The proposed coherence estimation reduces the statistical bias that exists in the results of the original, Gaussian-based sample coherence calculation. The statistical bias

due to the difference of the alpha-stable model relative to Gaussian is studied for the first time in the literature. The coherence estimation based on fractional lower order statistics can be applied whether the InSAR data is Gaussian or non-Gaussian distributed.

- 3) Chapter 4: The wavelet-domain InSAR phase filtering is for the first time formulated as a signal detection and estimation problem. The simultaneous detection and estimation technique is for the first time applied in the wavelet domain and applied in InSAR phase filtering. The new closed-form detector and estimator are derived based on the statistical analysis of the wavelet coefficients of the InSAR phase data. Based on this theoretical analysis, two new wavelet-domain phase-filtering methods using simultaneous detection and estimation are proposed. First, the phase filtering method using wavelet-packet and simultaneous detection and estimation is developed. Second, the phase filtering method in the undecimated wavelet domain and using simultaneous and detection is developed. To the best of the author's knowledge, InSAR phase filtering is studied in the undecimated wavelet domain for the first time.
- 4) Chapter 5: A new phase unwrapping method called weighted regularized PCG phase unwrapping method is proposed. This method applies both the regularization and weights during unwrapping. Therefore, this method not only can obtain an interpolated unwrapping result at the areas with missing phase data, but also obtain a more robust unwrapping result in areas of noisy data. The border conditions and implementation methods are proposed as well. The combination of

regularization and weights in one phase unwrapping method is presented in the literature for the first time.

- 5) Chapter 6: A new concept called second order residue is proposed for phase quality maps and demonstrated in standard existing phase unwrapping methods. A new phase quality map is proposed using the second order residue. The second order residue can be directly used as quality map after some arrangements and used in the phase unwrapping.
- 6) Chapter 7: Multichannel PolInSAR images are for the first time modeled as multichannel complex isotropic symmetric alpha-stable distribution. Based on this statistical model, the vector coherence based on fractional lower order statistics has been proposed. This FLOS-based vector coherence combines the statistical information in the vector coherence definition for the first time.

1.6 List of Publications and Further Notes

Chapter 2 ~ Chapter 7 are presented using [199][302][303][253][255][192], respectively. Chapter 3 ~ Chapter 7 includes the reuse of the papers in [302][303][253][255][192], respectively, with the kind permission of the publishers. The reference numbers in the papers have been revised for this thesis to provide a single consistent numbering system.

Contributions of the authors: In Chapter 2 (reference [199]), I am the sole author. In the papers associated with Chapters 3-7 (references [302][303][253][255][192]), I am the first author, my supervisor is the second author. For the papers in Chapters 3-7, I initiated

and performed the research work and wrote the papers. My supervisor contributed mainly as an editor, improving the clarity of the presentations as well as critiquing the contents.

Redundancies: There are some redundancies among Chapters 2-7 because they were composed as stand-alone papers.

This thesis includes the following publications:

Chapter 2 is from:

[199] Yong Bian, "Polarimetric SAR statistical analysis using alpha-stable distribution and its application in optimal despeckling," *International Journal of Remote Sensing*, Submitted for publication.

Chapter 3 is reprinted, with permission, from:

[302] Yong Bian and Bryan Mercer, "Interferometric SAR extended coherence calculation based on fractional lower order statistics," *IEEE Geoscience and Remote Sensing Letters*, vol. 7, no. 4, pp. 841-845, October 2010.

Chapter 4 is reprinted, with permission, from:

[303] Yong Bian and Bryan Mercer, "Interferometric SAR phase filtering in the wavelet domain using simultaneous detection and estimation," *IEEE Transactions on Geoscience and Remote Sensing*, vol. 49, no. 4, pp. 1396-1416, April 2011.

Chapter 5 is reprinted, with permission, from:

[253] Yong Bian and Bryan Mercer, "Weighted regularized preconditioned conjugate gradient (PCG) phase unwrapping method," *Journal of Optics: A: Pure and Applied*

Optics, vol. 11, issue 1, article number: 015504, 11pp, 2009. doi:10.1088/1464-4258/11/1/015504.

Chapter 6 is reprinted, with permission, from:

[255] Yong Bian and Bryan Mercer, “Using second order residue in PolInSAR phase unwrapping,” *Proceedings of the 2008 IEEE Radar Conference*, Rome, Italy, May 26-30, 2008, pp. 1-5.

Chapter 7 is reprinted, with permission, from:

[192] Yong Bian and Bryan Mercer, “PolInSAR statistical analysis and coherence optimization using fractional lower order statistics,” *IEEE Geoscience and Remote Sensing Letters*, vol. 7, no. 2, pp. 314-318, April 2010.

CHAPTER 2: POLARIMETRIC SAR STATISTICAL ANALYSIS USING ALPHA-STABLE DISTRIBUTION AND ITS APPLICATION IN OPTIMAL DESPECKLING¹

In this chapter, the statistical model of the polarimetric SAR single look complex image is analyzed using the alpha-stable distribution. It is better to use the alpha-stable distribution to represent statistical characteristics of the polarimetric SAR image than the Gaussian distribution. The polarimetric SAR covariance matrix estimation method based on fractional lower order statistics (FLOS) is proposed. Based on this model, an adaptive polarimetric SAR optimal despeckling method based on FLOS is developed. This algorithm adaptively estimates the characteristic exponents of each channel and uses these estimated alphas to adaptively calculate the parameters for the optimal despeckling. The experiments using the polarimetric SAR data demonstrate that the proposed method not only reduces the blurs which occur in the area of impulsive reflectors in the result of the original optimal despeckling method, but also maintains the speckle reduction ability (equivalent number of looks (ENL)).

2.1 Introduction

Polarimetric synthetic aperture radar (SAR) uses multi-polarization data to acquire the different polarization characteristics from different targets in order to obtain strong

¹ This chapter is from [199].

target classification ability [1]. The statistical characteristics of single channel SAR images have originally been represented using a Gaussian model. However, previous research shows that it is more accurate to analyze the statistical characteristics of SAR images using a non-Gaussian model [160]. Recently, the alpha-stable distribution was used to model the SAR imagery [183] because it is more accurate in modeling SAR images than the traditional Gaussian model and it considers the Gaussian model as a special case.

To the best of our knowledge, the multi-channel polarimetric SAR data is not yet studied using the alpha-stable distribution. The alpha-stable distribution is mostly used in signal processing for the impulsive noise modeling [167]. For the SAR image modeling, the impulsive signal may come from the strong scatterers which mostly exist in urban areas. Therefore, when we process the SAR image with strong reflectors, the alpha-stable distribution is a method that needs to be considered. In this paper, the statistical model of polarimetric SAR images will be studied using the alpha-stable distribution.

Polarimetric SAR applications are largely based on the analysis of the covariance matrix of the different polarization data. The covariance matrix of polarimetric SAR data is an important concept which is widely used in polarimetric SAR processing, especially in despeckling [144], target detection [172], and contrast enhancement [180]. However, the covariance matrix estimation is based on the Gaussian noise assumption which is not suitable for the non-Gaussian case [144]. In the applications of the traditional covariance matrix in the non-Gaussian distribution environment, most previous research was focused on using the product model [162][144]. However, the product model does not work well for urban areas [181][146][162], or long wavelength SAR data [146][149].

The complex SAR data can be modeled with the complex alpha-stable distribution [183]. Therefore, it is useful to generalize the polarimetric covariance matrix into a formulation which is suitable for the alpha-stable model. In this paper, the covariance matrix estimation using the complex symmetric alpha-stable ($S\alpha S$) distribution [182] model is proposed.

Using this generalized covariance matrix, an optimal despeckling method which is suitable for the application under the stable distribution environment is proposed and used for the polarimetric SAR image despeckling. This adaptive method is the generalization of the method in [144].

The organization of this chapter is as follows. In Section 2.2, the polarimetric SAR statistical analysis using alpha-stable distribution is introduced. In Section 2.3, the covariance matrix estimation using alpha-stable distribution is presented. The polarimetric SAR optimal despeckling method based on FLOS is presented in Section 2.4. The final section draws the conclusion.

2.2 Polarimetric SAR Image Statistical Analysis Using Alpha-Stable Distribution

2.2.1 Review of Polarimetric SAR Statistical Analysis

There is a lot of research related to the polarimetric SAR statistical model. Quegan and Rhodes [146] discussed the statistical model of different wavelength polarimetric SAR data using K-distribution. The polarimetric SAR data are widely modeled with the multivariate Gaussian distribution [181][143] in the homogeneous areas and multivariate

K-distribution [181][162][187][186] in the heterogeneous areas. In the heterogeneous areas, the SAR image can be modeled as a scalar product model [181][162][144][149]:

$$\mathbf{X} = \sqrt{\varepsilon} \mathbf{G} \quad (2.1)$$

where ε is a scalar that represents the texture, and \mathbf{G} is the vector that conforms to the Gaussian distribution. Although the product model is widely used in the modeling of the non-Gaussian case, there are some performance limitations in: areas with impulsive reflectors such as urban areas [181][146][162], long wavelength data [146][149], or single look data [162].

2.2.2 Alpha-Stable Distribution in Complex Polarimetric SAR Data

The research of polarimetric SAR is mostly based on the assumption that SAR data conforms to the Gaussian distribution. However, this assumption is only valid in homogeneous areas [181]. In real applications, sometimes the in-phase, quadrature, and amplitude of the SAR image are better modeled with a heavy-tailed model. In previous research, the single channel SAR data was modeled using the alpha-stable distribution [183]. The in-phase, quadrature, and amplitude of the SAR data can be modeled with the univariate alpha-stable distribution. The characteristic function of univariate alpha-stable distribution is [176][179]:

(a) when $\alpha \neq 1$,

$$E(\exp(j\omega X)) = \exp \left[j\mu\omega - \gamma|\omega|^\alpha \left(1 - j\beta(\text{sign}\omega)\tan\frac{\pi\alpha}{2} \right) \right], \quad (2.2a)$$

(b) when $\alpha = 1$,

$$E(\exp(j\omega X)) = \exp \left[j\mu\omega - \gamma|\omega| \left(1 + j\frac{2}{\pi}\beta(\text{sign}\omega)\ln|\omega| \right) \right], \quad (2.2b)$$

where

$$\text{sign}(x) = \begin{cases} 1 & \text{while } x > 0 \\ 0 & \text{while } x = 0. \\ -1 & \text{while } x < 0 \end{cases}$$

In this definition, α (characteristic exponent), β , γ , and μ are the parameters that control the heavy-tailed characteristic, skewness, dispersion, and position of the center of the spectral density function, respectively. The valid range limitations of these parameters are $0 < \alpha \leq 2$, $-1 \leq \beta \leq 1$, $\gamma > 0$, $-\infty < \mu < \infty$ [179]. The smaller the α , the more impulsive the data and the heavier the tails in the probability density function (pdf). β controls the skewness of the pdf, when $1 \geq \beta > 0$, the pdf is skewed to the left; otherwise, when $-1 \leq \beta < 0$, the pdf is skewed to the right. γ is similar to the variance of the Gaussian distribution, the larger the γ , the more heavily the data deviates from the mean value.

The single channel complex polarimetric SAR image can be modeled with the bivariate alpha-stable distribution with in-phase and quadrature as the two variables. Assuming the single look complex SAR data is $X = X_1 + jX_2$, for the stable non-symmetric complex stable distribution, when $0 < \alpha < 2$, the characteristic function is [176] pp. 65:

(1) when $\alpha \neq 1$

$$\begin{aligned} \varphi(\boldsymbol{\omega}) &= E \left\{ \exp \left[- \int_{S_2} |(\boldsymbol{\omega}, \mathbf{x})|^\alpha \left(1 - j \text{sign}[(\boldsymbol{\omega}, \mathbf{x})] \tan \frac{\alpha\pi}{2} \right) \Gamma(d\mathbf{x}) + j(\boldsymbol{\omega}, \boldsymbol{\mu}^0) \right] \right\} \\ &= \exp \left[- \int_{S_2} |\omega_1 x_1 + \omega_2 x_2|^\alpha \left(1 - j \text{sign}[\omega_1 x_1 + \omega_2 x_2] \tan \frac{\alpha\pi}{2} \right) d\Gamma(x_1, x_2) \right] \cdot \exp \left[j[\omega_1 \mu_1^0 + \omega_2 \mu_2^0] \right], \end{aligned}$$

(2) when $\alpha = 1$

$$\begin{aligned}\varphi(\boldsymbol{\omega}) &= E \left\{ \exp \left[- \int_{S_2} |(\boldsymbol{\omega}, \mathbf{x})|^\alpha \left(1 + j \frac{2}{\pi} \text{sign}[(\boldsymbol{\omega}, \mathbf{x})] \ln |(\boldsymbol{\omega}, \mathbf{x})| \right) \Gamma(d\mathbf{x}) + j(\boldsymbol{\omega}, \boldsymbol{\mu}^0) \right] \right\} \\ &= \exp \left[- \int_{S_2} |\omega_1 x_1 + \omega_2 x_2|^\alpha \left(1 + j \frac{2}{\pi} \text{sign}[\omega_1 x_1 + \omega_2 x_2] \ln |\omega_1 x_1 + \omega_2 x_2| \right) d\Gamma(x_1, x_2) \right] \cdot \exp \left[j[\omega_1 \mu_1^0 + \omega_2 \mu_2^0] \right],\end{aligned}$$

where Γ is the spectral measure, S_2 is the unit sphere, and $\boldsymbol{\mu}^0$ is the vector of shift [176].

For the SAR image amplitude, the value of α is typically higher than 1 [160], therefore the case $1 < \alpha < 2$ is good enough for most of the SAR applications.

Tsakalides and Nikias [183] propose to use the complex $S\alpha S$ distribution to model the range focused SAR signal. In the study of Tsakalides and Nikias [182], they model the radar clutter as complex isotropic $S\alpha S$ distribution. Since the distribution of focused single-look complex image is heavy-tailed, in this paper, we assume the focused single-look complex SAR image as a complex isotropic $S\alpha S$ distribution [182]. Therefore, the fully polarimetric SAR data can be modeled as a multi-channel isotropic complex $S\alpha S$ distribution. The validity of applying this model will be discussed in the follows through a series of experiments. In order to assume that the single channel SAR data conforms to the isotropic symmetric alpha-stable distribution, the following must be satisfied [176]: (1) for being symmetric, the imagery part of the characteristics function is zero and the $\exp[j[\omega_1 \mu_1^0 + \omega_2 \mu_2^0]]$ term is one; (2) for being isotropic, the distribution is translation invariant. For the symmetric isotropic alpha-stable distribution, the characteristic function of single channel complex SAR data can be simplified as [182][156][183][176] pp. 86:

$$\begin{aligned}\varphi(\boldsymbol{\omega}) &= \exp \left[- \int_{S_2} |\omega_1 x_1 + \omega_2 x_2|^\alpha d\Gamma(x_1, x_2) \right] \\ &= \exp \left[- \left(\frac{1}{2\pi} \int_0^{2\pi} |\cos \xi|^\alpha d\xi \right) \Gamma(S_2) |\boldsymbol{\omega}|^\alpha \right] = \exp \left[- \gamma |\boldsymbol{\omega}|^\alpha \right],\end{aligned}$$

where ξ are the variables in \mathbf{x} [176], S_2 is the unit circle [176], and γ is the dispersion parameter like the univariate case.

The multi-channel SAR data can be modeled as the multi-channel isotropic complex $S\alpha S$ distribution. The existing polarimetric SAR statistical models are mostly based on the multivariate complex Gaussian distribution [143]. Here we generalize this model to the multi-channel isotropic complex $S\alpha S$ distribution. The direct generalization of multi-channel polarimetric SAR data is to model them with a multivariate alpha-stable distribution. However, it is very difficult to model the multivariate alpha-stable distribution using the complex data as each variable. Here, we use a simplified model, which is to model the multi-channel polarimetric SAR data as multi-channel data where each channel data conforms to the complex rotationally invariant $S\alpha S$ distribution. The statistical distribution of multi-channel polarimetric SAR single look complex data can be modeled with the multi-channel isotropic $S\alpha S$ distribution:

$$\mathbf{k}_4 = \begin{bmatrix} HH \\ HV \\ VV \\ VH \end{bmatrix} \sim \begin{bmatrix} S(\alpha_{HH}, 0, \gamma_{HH}, 0) \\ S(\alpha_{HV}, 0, \gamma_{HV}, 0) \\ S(\alpha_{VV}, 0, \gamma_{VV}, 0) \\ S(\alpha_{VH}, 0, \gamma_{VH}, 0) \end{bmatrix}, \quad (2.3)$$

where HH , HV , VV , and VH denote the single look complex images of HH, HV, VV, and VH polarizations, respectively; the symbol of $S(*, *, *, *)$ means $S(\alpha, \beta, \gamma, \mu)$. This model means that each channel of the polarimetric SAR data follows the isotropic $S\alpha S$ distribution, i.e., $\beta_{HH} = \beta_{HV} = \beta_{VV} = \beta_{VH} = 0$ and $\mu_{HH} = \mu_{HV} = \mu_{VV} = \mu_{VH} = 0$. For different polarizations, α and γ may be different due to the different polarimetric characteristics of different polarization channels.

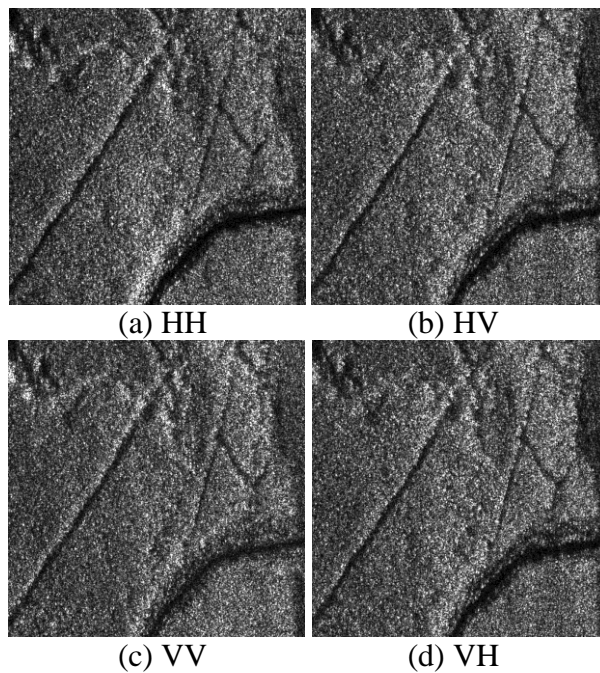


Figure 2.1. The amplitude images of polarimetric SAR data, Edson area. (a) HH, (b) HV, (c) VV, (d) VH.

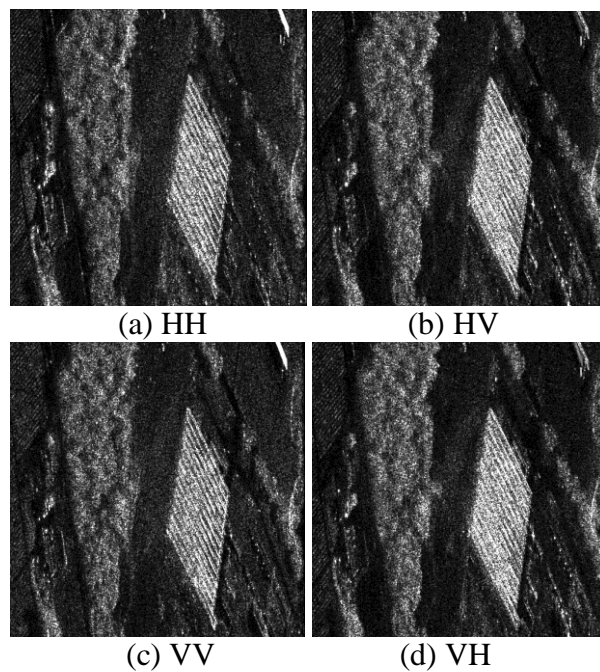


Figure 2.2. The amplitude images of polarimetric SAR data, Delta Fraser area. (a) HH, (b) HV, (c) VV, (d) VH.

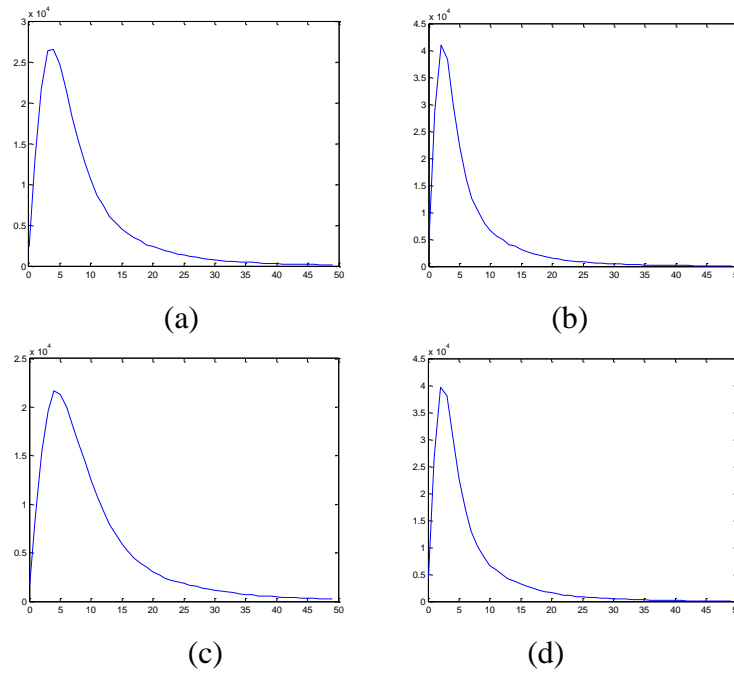


Figure 2.3. The histograms of the amplitudes of polarimetric SAR images, Delta area. (a) HH. (b) HV. (c) VV. (d) VH.

TABLE 2.1
ESTIMATED PARAMETERS OF POLARIMETRIC SAR DATA

Parameters		α	β	γ	μ
<i>Amplitude</i>	<i>HH</i>	1.9241	1.0	3.47740	7.17045
	<i>HV</i>	1.9428	1.0	1.59765	3.34600
	<i>VV</i>	1.9012	1.0	2.66505	5.80590
	<i>VH</i>	1.9239	1.0	1.58872	3.36080
<i>Symmetrize d Amplitude</i>	<i>HH</i>	1.6112	0.0241	3.34755	-0.0484316
	<i>HV</i>	1.6367	0.0101	1.56101	0.00418395
	<i>VV</i>	1.6553	0.0092	2.71891	-0.0190421
	<i>VH</i>	1.6463	0.0134	1.56919	0.00201623
<i>In-phase</i>	<i>HH</i>	1.6226	-0.0030	4.18928	0.0153376
	<i>HV</i>	1.6377	0.0048	1.95850	-0.00295551
	<i>VV</i>	1.6858	-0.0088	3.44901	0.0117014
	<i>VH</i>	1.6476	0.0111	1.97243	-0.0126495
<i>Quadrature</i>	<i>HH</i>	1.6212	0.0033	4.19741	-0.0116754
	<i>HV</i>	1.6493	0.0181	1.96868	-0.00912671
	<i>VV</i>	1.6819	-0.0029	3.43203	-0.00763687
	<i>VH</i>	1.6637	0.0237	1.98259	-0.0150660

These parameters are estimated using the STABLE software. The estimation is on the Edson area.

TABLE 2.2
ESTIMATED PARAMETERS OF POLARIMETRIC SAR DATA

Parameters		α	β	γ	μ
<i>Amplitude</i>	<i>HH</i>	1.4119	1.0	2.58667	4.42990
	<i>HV</i>	1.3453	1.0	1.41420	2.11980
	<i>VV</i>	1.4128	1.0	2.55052	4.43915
	<i>VH</i>	1.3474	1.0	1.40838	2.13140
<i>Symmetrized Amplitude</i>	<i>HH</i>	1.3642	-0.0104	2.10906	0.0248774
	<i>HV</i>	1.2715	0.0038	1.01396	-0.00377999
	<i>VV</i>	1.3775	-0.0151	2.11607	0.0159494
	<i>VH</i>	1.2817	0.0060	1.02376	-0.0105584
<i>In-phase</i>	<i>HH</i>	1.3805	0.0028	2.62231	0.00707275
	<i>HV</i>	1.2698	0.0091	1.25485	0.00365190
	<i>VV</i>	1.3981	-0.0026	2.61688	0.0150993
	<i>VH</i>	1.2785	0.0085	1.26699	-0.00118412
<i>Quadrature</i>	<i>HH</i>	1.3798	0.0015	2.61731	-0.0190060
	<i>HV</i>	1.2704	0.0085	1.25223	-0.0127902
	<i>VV</i>	1.3917	0.0012	2.61527	-0.00716129
	<i>VH</i>	1.2800	0.0087	1.26729	-0.00929617

These parameters are estimated using the STABLE software. The estimation is on the Delta Fraser area.

2.2.3 Model Analysis Using Real Polarimetric SAR Data

In order to test the statistical characteristics of the polarimetric SAR data, several experiments have been performed using the polarimetric SAR data acquired by the Intermap Technologies Corp. This data set was acquired using the airborne fully polarimetric TOPOSAR system. For the detailed information about this SAR sensor, please see [177]. The full polarization images of the Edson and Delta Fraser areas are illustrated in Figure 2.1 and Figure 2.2, respectively. Figure 2.1 is an area with very few manmade structures. Figure 2.2 is an area with some strong reflectors from manmade structures. Therefore, the image in Figure 2.1 is more homogenous than that in Figure 2.2. In the former research, Kuruoglu and Zerubia [160] modeled the SAR image amplitude as the heavy-tailed Rayleigh distribution and Nolan [171] discussed the density

function of the amplitude of sub-Gaussian distributions. Figure 2.3 illustrates the histograms of the amplitude image of the Delta Fraser area. From this, we found the image in this data set fits the heavy-tailed model; however, for different polarizations, the statistical characteristics are different.

In order to test the statistical characteristics of the polarimetric SAR data, we estimate the four parameters α , β , γ , and μ . In computing these parameters, we use the stable distribution analysis software STABLE which was developed by Nolan [168]. A detailed description of the STABLE software can be found in [169] and a description of the modifications in its new version is presented in [170]. In this software, the maximum likelihood estimation method proposed in [170] is used in the parameter estimation. Although the accuracy of this method depends on the number of samples used in the estimation, it is a relatively accurate method [170]. For the detailed analysis of the accuracy of this estimator, please see [170]. In this parameter estimation, the image data of size 512×512 is used. The estimated parameters of SAR data are illustrated in Table 2.1 ~ Table 2.2 for the Edson and Delta Fraser areas, respectively. Table 2.1 illustrates the estimated parameters from the Edson area, which is an area with few manmade structures. Table 2.2 shows the estimated parameters from the Delta Fraser area. In this paper, “in-phase” and “quadrature” denote the real and imaginary parts of the single-look complex image data, respectively; “amplitude data” means the amplitude of single-look complex image. From the estimated β , we observed that the amplitude of the SAR data is skewed, which verifies the analysis in [160]. From the in-phase and quadrature data, we found that the data can be approximated as the symmetric alpha-stable distribution, which validates the analysis in [183]. For different channels, the α may be similar

(Edson area) or slightly different (Delta Fraser area). For different polarization channels, the parameters of HH and VV are similar. Also, the parameters of HV and VH are very similar, enough that HV and VH can be considered as approximately equal [180][173]. From these parameters, we can also observe that the amplitude distribution of the single-look complex data of the test data is completely skewed to the right [176]. Therefore, the signal processing method which works on the amplitude data should use the skewed stable model. For the skewed stable distribution, we can use the symmetrized method proposed in [159] to change the data to a symmetric distribution; however, for the SAR image data, this operation produces data which is difficult to explain and hinders its applications. In Table 2.1 and Table 2.2, the parameters of symmetrized amplitude using the method in [159] are also illustrated.

From the data of different areas, we found that when there are more manmade structures in the data, there are more strong reflectors in the data, therefore the data has lower α . In the forest area, α is higher than that of the area with manmade structures. This means that when we process the polarimetric SAR data, it is better to use the spatial adaptive signal processing method (in this paper, it is spatially adaptive image despeckling method) according to the parameters estimated as this will be the most accurate way of handling the spatial statistical characteristics of the data. Therefore, it will be advantageous to use the spatial adaptive processing method which can change the parameters spatially in terms of the estimated statistical parameters of stable distributions.

For different channels of multi-polarization data (single-look complex data), β and μ are similar in different channels and can be approximated as zero, but α and γ are different for different polarizations, which means the model in (3) is appropriate for the

modeling of multi-polarization SAR data. From the estimated parameters, we found the parameters of the real and imaginary parts are similar. On the other hand, β and μ are close to zero, this verifies the assumption that the real and imaginary parts are identically distributed. Thus, the complex SAR data can be approximately modeled as an isotropic $S\alpha S$ distribution.

2.2.4 The Relationship Between the Characteristic Exponents of In-phase, Quadrature and Complex SAR Data

The estimation of the characteristic exponents of complex alpha-stable distribution is more complicated than its real counterparts. If we can find the relationship between the characteristic exponents of the real part, imaginary part, and the complex data, we can find a way to estimate the characteristic exponents of complex alpha-stable distribution by the estimation of real variables. In order to study the relationship between the characteristic exponents of in-phase, quadrature, and complex SAR data, we assume the SAR data conforms to the sub-Gaussian distribution [176]: $A \sim S(\alpha/2, 1, (\cos(\pi\alpha/4))^{2/\alpha}, 0)$, G_1 and G_2 are the variables with Gaussian distribution.

From pp. 21, pp. 77, and Corollary 2.6.4 of [176] and [182]: Assuming the single look complex SAR data is $X = X_1 + jX_2 = \sqrt{A}G_1 + j\sqrt{A}G_2$, the real part is $X_1 = \sqrt{A}G_1 \sim S(\alpha, 0, \gamma, 0)$, and the imaginary part is $X_2 = \sqrt{A}G_2 \sim S(\alpha, 0, \gamma, 0)$. Therefore, we have $X = X_1 + jX_2 \sim S(\alpha, 0, \gamma, 0)$. This means that if the symmetric complex distribution is sub-Gaussian, the α of the symmetric complex stable distribution is the same as the α of the real part and that of the imaginary part. Therefore, the characteristic exponents of the in-phase and quadrature equal that of the complex SAR data.

Based on this analysis, we can use the characteristic exponent of the stable distribution from in-phase or quadrature to represent that of the complex SAR data. From Table 2.1 and Table 2.2, we found the characteristic exponents of in-phase and quadrature are approximately the same. The slight difference is because the data used for estimation is not large enough for a more accurate estimation. Based on this knowledge, we can approximate the α of in-phase and quadrature data, and average the two approximations. The averaged α can then be used as the characteristic exponent of the complex SAR data and later used for the covariance matrix estimation. This means all the parameter estimation methods of real data can be used for the complex SAR data characteristic exponent estimation. Also, we can use the parameter estimation method in [164] which estimates the parameters of alpha-stable distribution using the complex SAR data.

2.2.5 Goodness-of-Fit Tests between the Proposed Model and Real Polarimetric SAR Data

It is important to test the goodness-of-fit of the proposed model, which will give us a hint on its merits and limitations. For polarimetric SAR data, since the scene characteristics (which reflects the target scattering characteristics) may vary from homogeneous (can be described by a Gaussian distribution) to heterogeneous (can be described by a heavy-tailed distribution), and even to extremely heterogeneous (can be described by a very heavy-tailed distribution). Therefore, the distribution model of polarimetric SAR data needs to cover a variety of situations, which ranges from Gaussian to very heavy-tailed distributions. The alpha-stable distribution may be a reasonable choice because the shape of its pdf varies from non-heavy-tailed (Gaussian, α is close to

2) to very heavy-tailed (α is close to 0) while we change its characteristic exponent.

A series of experiments has been conducted to examine the fitness of the proposed alpha-stable model with respect to the real polarimetric SAR data as a function of polarizations, target characteristics, number of samples, and wavelength of the SAR sensor. The accuracies of the estimated pdfs using alpha-stable model are evaluated by comparing them with the histograms of real SAR data. In order to test the validity of the proposed model, we need to conduct experiments which examine the statistics of the single-look complex polarimetric SAR data. Since our major concern here is the distribution of the single-look complex data, a direct way is to fit complex SAR data with a complex alpha-stable distribution. From the analysis in Section 2.4, we know that the distributions of complex data can be described by its real or imaginary parts when the underlying distribution is sub-Gaussian (i.e. the complex data is complex $S\alpha S$ means that both the real and imaginary parts are real $S\alpha S$). Therefore, in this paper, we use the real part of the focused single-look complex data to conduct the goodness-of-fit experiments.

These experiments are implemented as follows: first, the parameters of stable distribution are estimated using the STABLE software (i.e, using the maximum likelihood estimation method in [170]); second, the estimated parameters are used to calculate the pdf using the STABLE software; finally, the calculated pdf and the histogram of real polarimetric data are used to calculate the Hellinger distance [178] which is a measurement of the fitness of two distributions. The value of Hellinger distance is between 0 and 1, the smaller the Hellinger distance, the better is the fitness of two distributions [178].

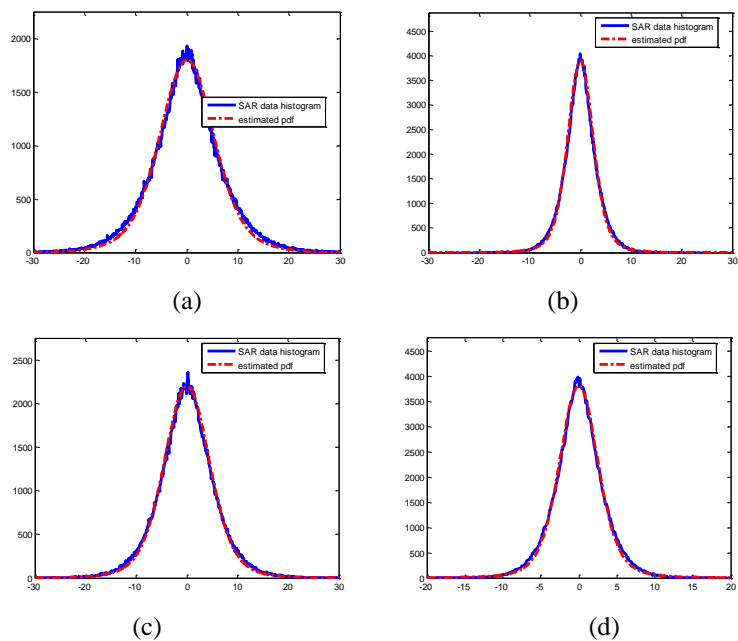


Figure 2.4. The goodness-of-fit experiment of L-band Edson area data. (a) HH. (b) HV. (c) VV. (d) VH.

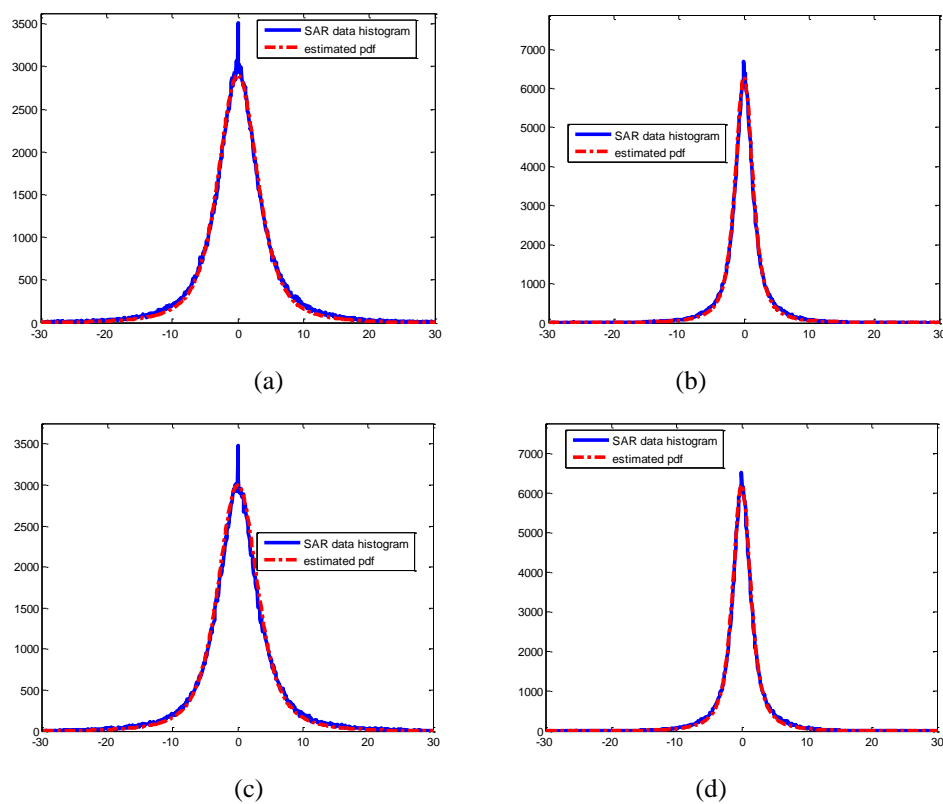


Figure 2.5. The goodness-of-fit experiment of L-band Delta area data. (a) HH. (b) HV. (c) VV. (d) VH.

2.2.5.1 Experiments of Different Polarizations

In this experiment, we examine the goodness-of-fit of different polarizations. The experiments of goodness-of-fit has been conducted on the two L-band fully polarimetric SAR data sets which have been used in the experiments of Section 2.3 and shown in Figure 2.1 (Edson area) and Figure 2.2 (Delta area). These two data sets have large number of samples. The estimated pdfs of Edson data and Delta data are calculated using the STABLE software using the estimated parameters in Table 2.1 and 2.2, respectively. The estimated pdfs and the histograms of the real part of Edson data in HH, HV, VV, and VH polarizations are plotted in Figure 2.4 (a), (b), (c), and (d), respectively. The estimated pdfs and the histograms of the real part of Delta data of HH, HV, VV, and VH polarizations are plotted in Figure 2.5 (a), (b), (c), and (d), respectively. From Figure 2.4 and Figure 2.5, we found that although the statistical characteristics are different for different polarizations (especially between the co-polarized and cross-polarized terms), the estimated pdfs and the histograms of real SAR data are matched very well for all the four polarizations. This means that the proposed alpha-stable model is suitable for the modeling of all the polarizations of the fully polarized SAR data. The Hellinger distances between the estimated pdf and the real SAR data are calculated and shown in Table 2.3. The Hellinger distances in Table 2.3 are close to zero for all the polarizations, which indicates the estimated pdfs fit the real polarimetric SAR data very well when the number of samples is large. Therefore, the alpha-stable model is suitable for the modeling of fully polarimetric SAR data. Comparing the results in Figure 2.4 and Figure 2.5, we found that although the data from Delta and Edson area have quite different scene statistical characteristics, in both areas, the estimated pdfs fits the real SAR data very well.

TABLE 2.3
HELLINGER DISTANCE OF POLARIMETRIC SAR DATA

	Polarizations	Hellinger Distance
<i>L-band Edson</i>	<i>HH</i>	0.0365
	<i>HV</i>	0.0510
	<i>VV</i>	0.0237
	<i>VH</i>	0.0500
<i>L-band Delta</i>	<i>HH</i>	0.0302
	<i>HV</i>	0.0330
	<i>VV</i>	0.0262
	<i>VH</i>	0.0328

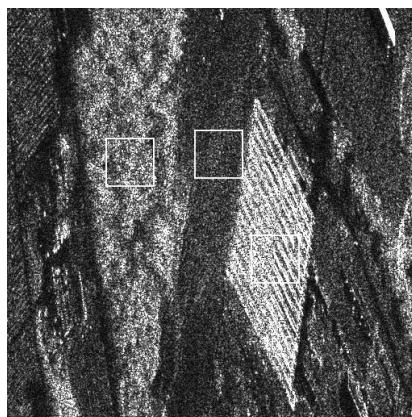


Figure 2.6. Three areas in the goodness-of-fit tests. The areas from left to right are (c), (b), and (a), respectively.

2.2.5.2 Experiments of Different Types of Targets:

In order to examine the modeling fitness with respect to target scattering characteristics (or scene characteristics), we perform the goodness-of-fit experiments on three selected areas of the Delta data. Three areas have been selected in terms of the follows: 1) Inside each area, the targets should have similar characteristics; 2) The type of dominant scatterers is different between any two of the three areas. Figure 6 shows the locations of the three testing areas, which are marked with squares, the squares from left to right in Figure 2.6 are area (c), (b), and (a), respectively.

TABLE 2.4
ESTIMATED PARAMETERS OF POLARIMETRIC SAR DATA

Parameters		α	β	γ	μ
<i>In-phase</i>	<i>HH</i>	1.6865	0.0258	8.69835	-0.121050
	<i>HV</i>	1.7600	0.1757	5.35792	-0.0683366
	<i>VV</i>	1.5991	0.0580	8.22691	-0.128653
	<i>VH</i>	1.7584	0.2775	5.28957	-0.122334
<i>Quadrature</i>	<i>HH</i>	1.7138	-0.0319	8.81907	-0.0345735
	<i>HV</i>	1.7654	-0.0146	5.37902	0.0116193
	<i>VV</i>	1.6394	0.1424	8.28765	-0.478279
	<i>VH</i>	1.7948	-0.0642	5.46454	0.180574

These parameters are estimated using the STABLE software. The estimation is on the Delta Fraser area, area A.

TABLE 2.5
ESTIMATED PARAMETERS OF POLARIMETRIC SAR DATA

Parameters		α	β	γ	μ
<i>In-phase</i>	<i>HH</i>	1.8172	0.1161	2.48804	-0.121979
	<i>HV</i>	1.8239	-0.0636	1.21146	0.0345459
	<i>VV</i>	1.9484	0.1158	2.58546	-0.0786491
	<i>VH</i>	1.7857	-0.0423	1.20595	0.0355041
<i>Quadrature</i>	<i>HH</i>	1.8976	0.1053	2.47720	0.0698504
	<i>HV</i>	1.8083	-0.0601	1.20480	0.0812927
	<i>VV</i>	1.9518	0.4851	2.50432	-0.0676317
	<i>VH</i>	1.8564	-0.1320	1.22155	0.0812304

These parameters are estimated using the STABLE software. The estimation is on the Delta Fraser area, area B.

TABLE 2.6
ESTIMATED PARAMETERS OF POLARIMETRIC SAR DATA

Parameters		α	β	γ	μ
<i>In-phase</i>	<i>HH</i>	1.7936	0.0241	4.46237	0.00963377
	<i>HV</i>	1.7505	0.0520	2.64887	0.0648852
	<i>VV</i>	1.8057	0.2431	4.69927	-0.131143
	<i>VH</i>	1.7521	0.0638	2.64328	0.0429481
<i>Quadrature</i>	<i>HH</i>	1.7566	-0.0497	4.48640	0.0497022
	<i>HV</i>	1.7523	-0.0361	2.59112	0.200631
	<i>VV</i>	1.7088	-0.0238	4.62435	0.124756
	<i>VH</i>	1.7513	-0.0581	2.59251	0.185676

These parameters are estimated using the STABLE software. The estimation is on the Delta Fraser area, area C.

Area (a) is the area of strong manmade objects which represents a heterogeneous area, area (b) is the bare earth with low vegetations which represents a relatively homogeneous area, area (c) is a forested area which has a heterogeneity measure [163] between those of area (a) and (b). In other words, area (a) is the area of the highest heterogeneity, area (b) is of the lowest heterogeneity. The estimated parameters of alpha-stable distribution of area (a), (b), and (c) are shown in Table 2.4, Table 2.5, and Table 2.6, respectively. Among these three areas, the estimated alpha values of area (a) is the smallest, area (b) is the biggest. Therefore, the distribution of area (a) is the most heavy-tailed, and the distribution of area (b) is the least heavy-tailed. This result indicates that the measured alpha value is a measurement similar to scene heterogeneity; the smaller the alpha value, the higher is the heterogeneity. Thus we can say that the estimated parameters of alpha-stable distribution (especially alpha) of the data can be used to classify the scenes of different statistical characteristics.

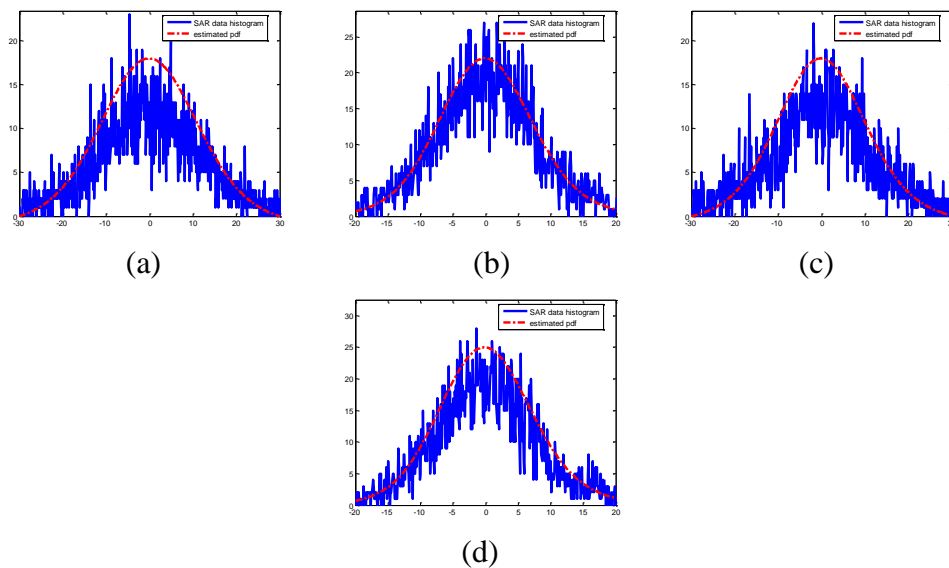


Figure 2.7. The goodness-of-fit experiment of L-band delta data, for area A,. (a) HH. (b) HV. (c) VV. (d) VH.

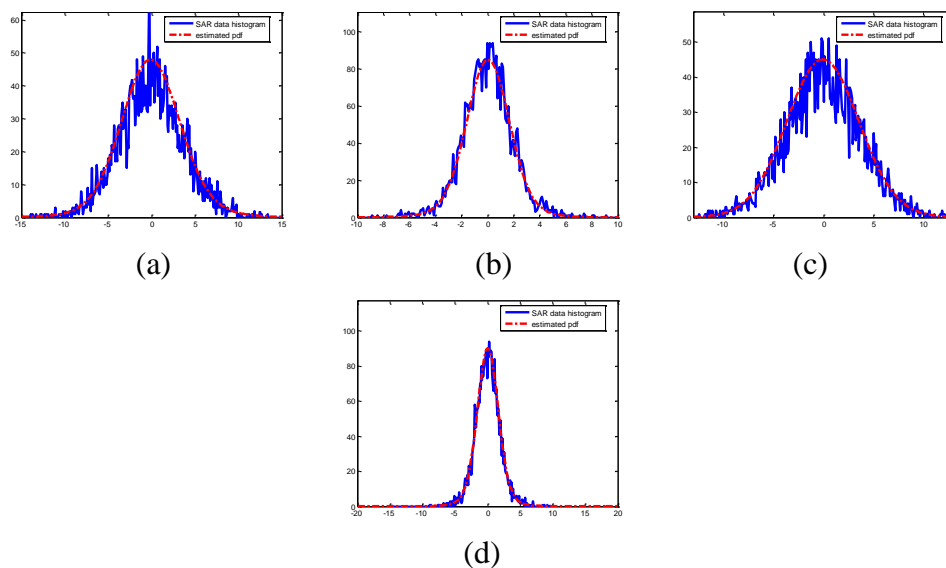


Figure 2.8. The goodness-of-fit experiment of L-band delta data, for area B. (a) HH. (b) HV. (c) VV. (d) VH.

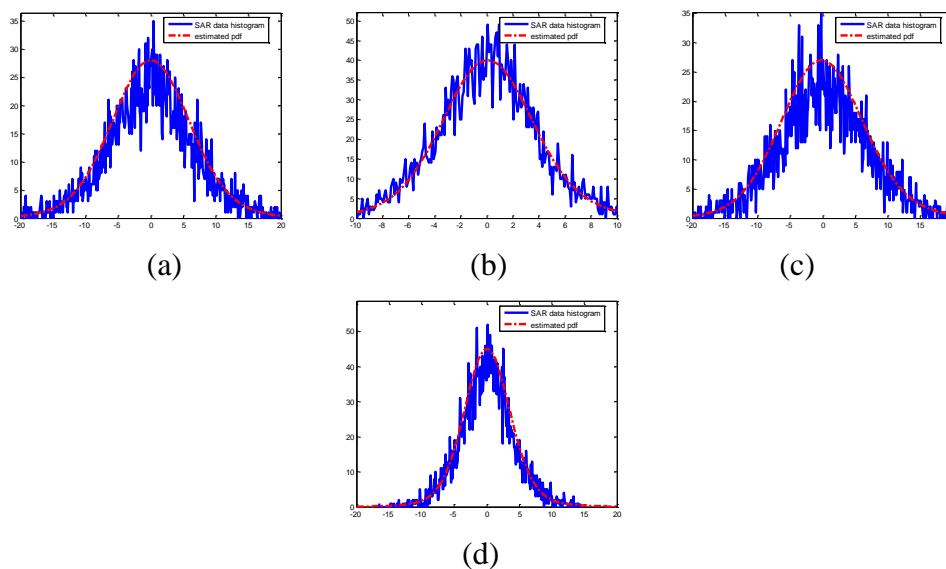


Figure 2.9. The goodness-of-fit experiment of L-band delta data, for area C. (a) HH. (b) HV. (c) VV. (d) VH.

TABLE 2.7
HELLINGER DISTANCE OF POLARIMETRIC SAR DATA

Parameters	Polarizations	Hellinger Distance
<i>Intermap L-band data, delta, area A</i>	<i>HH</i>	0.1655
	<i>HV</i>	0.1317
	<i>VV</i>	0.1741
	<i>VH</i>	0.1329
<i>Intermap L-band data, delta, area B</i>	<i>HH</i>	0.1181
	<i>HV</i>	0.0928
	<i>VV</i>	0.1009
	<i>VH</i>	0.0815
<i>Intermap L-band data, delta, area C</i>	<i>HH</i>	0.1255
	<i>HV</i>	0.0824
	<i>VV</i>	0.1367
	<i>VH</i>	0.1013

The goodness-of-fit experiments of these three areas have been conducted. The estimated pdfs and the histograms of polarimetric SAR data in area (a), area (b), and area (c) are plotted in Figure 2.7, Figure 2.8, and Figure 2.9, respectively. The Hellinger distances are calculated and shown in Table 2.7. Since the number of samples used in this experiment is much smaller than that of Section 2.5.1, we can get a coarse idea with regard to how much the sample size influences the accuracy of parameter estimation by comparing the Hellinger distances in Table 2.7 (the results in large areas) with those of Table 2.3 (the results in small areas). After this comparison, we found that when more samples are used in the parameter estimation, the goodness-of-fit of the resulting pdf is largely improved. This conforms to the results in [170]. Comparing the goodness-of-fit results for those three testing areas, we found that the Hellinger distance is the largest in area (a), smallest in area (b), this is probably because the estimator has a different accuracy for the different alpha values [170].

2.2.5.3 Experiments of Different Wavelengths:

The statistical characteristics of polarimetric SAR data vary for different wavelengths. In order to examine whether the alpha-stable model is suitable for the application in the polarimetric SAR data of various wavelengths, the experiments of a P-band data set is conducted in comparison with the aforementioned experiments of L-band Edson data. This P-band data set is acquired from Edson area, which is also acquired by Intermap Technologies Corp. (for the detailed description of this P-band SAR system, please see [155] and [153]).

TABLE 2.8
ESTIMATED PARAMETERS OF POLARIMETRIC SAR DATA

Parameters		α	β	γ	μ
<i>Amplitude</i>	<i>HH</i>	1.7901	1.0	533.044	1064.64
	<i>HV</i>	1.8716	1.0	236.889	504.251
	<i>VV</i>	1.9041	1.0	396.729	887.014
	<i>VH</i>	1.8759	1.0	253.827	535.110
<i>Symmetrized Amplitude</i>	<i>HH</i>	1.5609	0.0104	380.889	-3.21727
	<i>HV</i>	1.6387	-0.0075	200.797	0.976749
	<i>VV</i>	1.6814	0.0022	379.625	1.86820
	<i>VH</i>	1.6172	-0.0001	211.437	0.463859
<i>In-phase</i>	<i>HH</i>	1.5773	-0.0007	628.907	-1.23077
	<i>HV</i>	1.6547	0.0073	300.258	-1.90635
	<i>VV</i>	1.7132	0.0028	526.549	-2.94949
	<i>VH</i>	1.6403	0.0014	317.862	0.444630
<i>Quadrature</i>	<i>HH</i>	1.5694	0.0014	625.420	-3.59525
	<i>HV</i>	1.6479	0.0020	299.919	-0.924835
	<i>VV</i>	1.7084	-0.0035	526.676	0.896941
	<i>VH</i>	1.6393	-0.0048	317.566	1.39359

These parameters are estimated using the STABLE software. The estimation is on the Edson area (P-band Edson).

TABLE 2.9
HELLINGER DISTANCE OF POLARIMETRIC SAR DATA

Parameters	Polarizations	Hellinger Distance
<i>P-band Edson</i>	<i>HH</i>	0.0248
	<i>HV</i>	0.0326
	<i>VV</i>	0.0190
	<i>VH</i>	0.0306

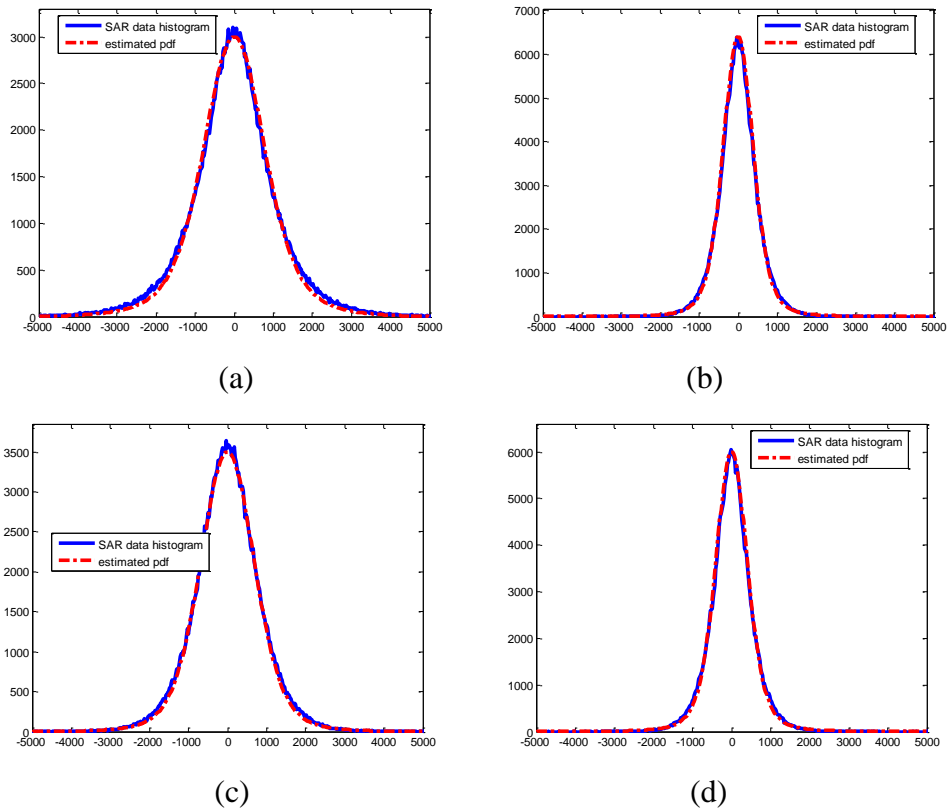


Figure 2.10. The goodness-of-fit experiment of Intermap P-band Edson data. (a) HH. (b) HV. (c) VV. (d) VH.

The estimated parameters of alpha-stable distributions of this P-band data are shown in Table 2.8. The estimated pdfs and the histograms of real polarimetric SAR data are plotted in Figure 2.10. The Hellinger distances between the estimated pdf and the

histogram of real SAR data are calculated and shown in Table 2.9. Comparing Table 2.3 and Table 2.9, we found a similar goodness-of-fit results for the P- and L-band data, this means that although the SAR data acquired using different wavelengths has the different statistical characteristics, the alpha-stable model fits both of them well. Although we cannot conclude that the model fits well for all the wavelengths since this experiment only include two wavelengths, the similarity of the results between P- and L-band data indicates that the alpha-stable distribution may be applicable to a broad range of wavelengths.

2.3 Covariance Matrix Based on FLOS

2.3.1 Review of Covariance Matrix

The statistical model of polarimetric SAR data was assumed as Gaussian in many applications. However, the SAR data can be more accurately modeled with complex alpha-stable distributions [160]. Therefore, the polarimetric SAR data should be modeled using the alpha-stable distribution as well.

The covariance matrix plays a significant role in the polarimetric SAR processing, which is important for the understanding of wave scattering such as measuring depolarization [145], and also in areas such as despeckling [144], target detection [172], and contrast enhancement [180]. The covariance matrix of polarimetric SAR is mostly based on the assumption that SAR data conforms to the Gaussian distribution. The polarimetric SAR image can be formulated using a vector representation as

$$\mathbf{k}_3 = \begin{bmatrix} HH \\ HV \\ VV \end{bmatrix}, \quad (2.4)$$

where HH , HV , and VV are the single look complex image data in HH, HV, and VV polarizations, respectively. Here only three polarizations are used because the HV and VH are correlated and are not used in the despeckling [173].

The traditional covariance matrix is [144][158]

$$\mathbf{C} = E(\mathbf{k}_3 \cdot \mathbf{k}_3^{*T}) = E \left(\begin{bmatrix} HH \\ HV \\ VV \end{bmatrix} \cdot \begin{bmatrix} HH^* & HV^* & VV^* \end{bmatrix} \right) = E \left(\begin{bmatrix} HH \cdot HH^* & HH \cdot HV^* & HH \cdot VV^* \\ HV \cdot HH^* & HV \cdot HV^* & HV \cdot VV^* \\ VV \cdot HH^* & VV \cdot HV^* & VV \cdot VV^* \end{bmatrix} \right), \quad (2.5)$$

where E denotes expectation, T means transpose, and “*” means conjugate.

2.3.2 Covariance Matrix Based on FLOS

In this section, we will develop the covariance matrix of polarimetric SAR using the fractional lower order statistics. When the noise model is non-Gaussian, the most popular noise model is the k-distribution, which was used in [146]. However, it is more flexible to use the stable distribution to model the non-Gaussian case [183]. As discussed before, the statistical distribution of three-channel polarimetric SAR single look complex data can be modeled with the three-channel isotropic $S\alpha S$ distribution:

$$\mathbf{k}_3 = \begin{bmatrix} HH \\ HV \\ VV \end{bmatrix} \sim \begin{bmatrix} S(\alpha_{HH}, 0, \gamma_{HH}, 0) \\ S(\alpha_{HV}, 0, \gamma_{HV}, 0) \\ S(\alpha_{VV}, 0, \gamma_{VV}, 0) \end{bmatrix}, \quad (2.6)$$

where HH , HV , and VV denote the single look complex images of HH, HV, and VV polarizations, respectively.

The covariation [176] in the alpha-stable distribution is by definition similar to the covariance in the Gaussian case; however, covariation is not symmetric [176]. Therefore, we use fractional lower order covariance instead of covariation to derive the covariance matrix based on FLOS. The covariance matrix will be developed based on the fractional

lower order covariance which was proposed in [165] and used in [183], which is

$$FLOC(X, Y) = [X, Y]_{a,b} = E\left(X^{(a)} \cdot Y^{(b)}\right). \quad (2.7)$$

We use the fractional lower order covariance (FLOC) proposed in [165][183] to derive the polarimetric SAR covariance matrix based on the alpha-stable distribution. The proposed covariance matrix is defined based on the operation

$$X^{(p)} = X \cdot |X|^{p-1}, \quad (2.8)$$

which is similar to the fractional lower order covariance in [165][183]. The only difference is that the conjugate is not used here. There are two reasons that we use this formation, which are as follows: First, this operation is similar to a conversion from the stable distribution to the Gaussian distribution, which will be analyzed in the following sections. Second, in order to maintain the basic structure of the covariance matrix which represents the wave scattering process of the polarimetric measurement [145], we discard the conjugate operation. The fractional lower order covariance [165] is symmetric when $a = b$, which is $[X, Y]_{a,a} = X|X|^{a-1} \cdot Y|Y|^{a-1} = [Y, X]_{a,a}$.

The traditional covariance matrix was derived according to the Gaussian noise assumption, whereas the covariance matrix based on fractional lower order statistics is a generalized version of the traditional covariance matrix in the alpha-stable distribution. Using the definition in (2.8), the proposed covariance matrix based on the FLOS is

$$\mathbf{C}_{FLOS} = E\left(\mathbf{k}_3^{(p)} \cdot \mathbf{k}_3^{(p)*T}\right), \quad (2.9)$$

where

$$\mathbf{K}_{FLOS} = \mathbf{k}_3^{(p)} = \begin{bmatrix} HH \cdot |HH|^{p_{HH}-1} & HV \cdot |HV|^{p_{HV}-1} & VV \cdot |VV|^{p_{VV}-1} \end{bmatrix}^T,$$

and where p_{HH} , p_{HV} , and p_{VV} are the p values for HH, HV, and VV channels,

respectively. Note, this \mathbf{K}_{FLOS} is only used in the estimation of the covariance matrix, the SAR image data is not changed. Therefore the covariance matrix based on FLOS is:

$$\begin{aligned}
\mathbf{C}_{FLOS} &= E \left\{ \begin{bmatrix} HH \cdot |HH|^{p_{HH}-1} \\ HV \cdot |HV|^{p_{HV}-1} \\ VV \cdot |VV|^{p_{VV}-1} \end{bmatrix} \cdot \begin{bmatrix} HH^* \cdot |HH|^{p_{HH}-1} & HV^* \cdot |HV|^{p_{HV}-1} & VV^* \cdot |VV|^{p_{VV}-1} \end{bmatrix} \right\} \\
&= E \left\{ \begin{bmatrix} A_{11} & A_{12} & A_{13} \\ A_{21} & A_{22} & A_{23} \\ A_{31} & A_{32} & A_{33} \end{bmatrix} \right\} \\
&= E \left\{ \begin{bmatrix} HH \cdot |HH|^{p_{HH}-1} \cdot HH^* \cdot |HH|^{p_{HH}-1} & HH \cdot |HH|^{p_{HH}-1} \cdot HV^* \cdot |HV|^{p_{HV}-1} & HH \cdot |HH|^{p_{HH}-1} \cdot VV^* \cdot |VV|^{p_{VV}-1} \\ HV \cdot |HV|^{p_{HV}-1} \cdot HH^* \cdot |HH|^{p_{HH}-1} & HV \cdot |HV|^{p_{HV}-1} \cdot HV^* \cdot |HV|^{p_{HV}-1} & HV \cdot |HV|^{p_{HV}-1} \cdot VV^* \cdot |VV|^{p_{VV}-1} \\ VV \cdot |VV|^{p_{VV}-1} \cdot HH^* \cdot |HH|^{p_{HH}-1} & VV \cdot |VV|^{p_{VV}-1} \cdot HV^* \cdot |HV|^{p_{HV}-1} & VV \cdot |VV|^{p_{VV}-1} \cdot VV^* \cdot |VV|^{p_{VV}-1} \end{bmatrix} \right\}.
\end{aligned} \tag{2.10}$$

When we know the parameter α in the data, the p value that satisfies the boundedness requirement can be derived using the following *Theorem 2.1*.

Theorem 2.1: When the HH, HV, and VV are statistically independent, the covariance matrix is bounded if $p_{HH} < \alpha_{HH}/2$, $p_{HV} < \alpha_{HV}/2$, and $p_{VV} < \alpha_{VV}/2$.

Proof: Specifically, for each term in the matrix, the boundedness should be satisfied when all the terms in (2.10) are bounded. Because the noise in different channels are statistically independent [180], we can assume that HH, HV, and VV are statistically independent.

(1) The A_{11} , A_{22} , and A_{33} term: From [167][166], it is easy to know that for A_{11} , A_{22} , and A_{33} , the boundedness is satisfied when $p_{HH} < \alpha_{HH}/2$, $p_{HV} < \alpha_{HV}/2$, $p_{VV} < \alpha_{VV}/2$, respectively.

(2) The A_{12} , A_{13} , A_{21} , A_{23} , A_{31} , and A_{32} term: Assume the HH, HV, and VH are

statistically independent, from [167][166], the requirements of boundedness are:

$$A_{12} : \quad p_{HH} < \alpha_{HH} / 2 \text{ and } p_{HV} < \alpha_{HV} / 2$$

$$A_{13} : \quad p_{HH} < \alpha_{HH} / 2 \text{ and } p_{VV} < \alpha_{VV} / 2$$

$$A_{21} : \quad p_{HV} < \alpha_{HV} / 2 \text{ and } p_{HH} < \alpha_{HH} / 2$$

$$A_{23} : \quad p_{HV} < \alpha_{HV} / 2 \text{ and } p_{VV} < \alpha_{VV} / 2$$

$$A_{31} : \quad p_{VV} < \alpha_{VV} / 2 \text{ and } p_{HH} < \alpha_{HH} / 2$$

$$A_{32} : \quad p_{VV} < \alpha_{VV} / 2 \text{ and } p_{HV} < \alpha_{HV} / 2$$

Therefore, all in all, the covariance matrix is bounded if $p_{HH} < \alpha_{HH} / 2$, $p_{HV} < \alpha_{HV} / 2$, and $p_{VV} < \alpha_{VV} / 2$. This concludes the proof.

Let

$$\sigma_{FLOS} = E\left(|HH|^{2p_{HH}}\right), \quad (2.11)$$

where the σ_{FLOS} term is actually the $2p_{HH}$ th order statistics of the HH data. In the $S\alpha S$ noise case, if $p_{HH} < \alpha_{HH} / 2$ and $\alpha_{HH} < 2$, we have $2p_{HH} < 2$, and the σ_{FLOS} term is the statistics with the order lower than the second order statistics.

By a similar arrangement as [144][180], by taking the σ_{FLOS} term out of the matrix in (2.10), the covariance matrix based on FLOS for polarimetric SAR data processing can be formulated as

$$\mathbf{C}_{FLOS} = \sigma_{FLOS} \begin{bmatrix} 1 & \omega_{FLOS} & \rho_{FLOS} \sqrt{\gamma_{FLOS}} \\ \omega_{FLOS}^* & f_{FLOS} & \kappa_{FLOS} \\ \rho_{FLOS}^* \sqrt{\gamma_{FLOS}} & \kappa_{FLOS}^* & \gamma_{FLOS} \end{bmatrix}, \quad (2.12)$$

where

$$\gamma_{FLOS} = \frac{E(|VV|^{2p_{VV}})}{E(|HH|^{2p_{HH}})}, \quad (2.13)$$

$$f_{FLOS} = \frac{E(|HV|^{2p_{HV}})}{E(|HH|^{2p_{HH}})}, \quad (2.14)$$

$$\rho_{FLOS} = \frac{E(|HH \cdot VV^*| |HH|^{p_{HH}-1} |VV|^{p_{VV}-1})}{\sqrt{E(|HH|^{2p_{HH}})E(|VV|^{2p_{VV}})}}. \quad (2.15)$$

γ_{FLOS} , f_{FLOS} , and ρ_{FLOS} are the most important terms and will be used later in the optimal despeckling. The other terms are

$$\omega_{FLOS} = \frac{E(|HH \cdot |HH|^{p_{HH}-1} \cdot HV^* \cdot |HV|^{p_{HV}-1})}{E(|HH|^{2p_{HH}})}, \quad (2.16a)$$

$$\kappa_{FLOS} = \frac{E(|HV \cdot |HV|^{p_{HV}-1} \cdot VV^* \cdot |VV|^{p_{VV}-1})}{E(|HH|^{2p_{HH}})}, \quad (2.16b)$$

which will not be used in the later optimal despeckling since they are close to 0 [146].

The values of p_{HH} , p_{HV} , and p_{VV} can be defined in terms of different applications and statistical environments. Therefore, the covariance matrix based on FLOS is very flexible. From the definition of covariance matrix based on FLOS, we know that the alpha-stable distribution is not polarization independent, which is different from the product model [146]. Therefore, for the application of the covariance matrix based on FLOS, we should estimate the characteristic exponent for each channel separately. Comparing the product model [181][162][144][149], the following are some advantages for the proposed covariance matrix based on FLOS:

- 1) This proposed covariance matrix performs well both in the urban and rural areas when we adaptively use the estimated α to calculate the covariance matrix.

2) Because the proposed method only uses the statistical information in the data, it can be applied to the data of any wavelength.

3) The proposed method can be applied in single-look or multi-look data.

4) The product model assumes the texture in each polarization is the same [146][162]; however, the proposed method does not have this assumption and is not polarization independent. This gives the advantage of the proposed method that when the polarization independent assumption of the product model fails, the proposed method still works.

2.3.3 Analysis of the Covariance Matrix Based on FLOS

It is well known that the closed form pdf of the alpha-stable distribution is not available when $1 < \alpha < 2$ and $0 < \alpha < 1$ [176][167]. Therefore, the SAR data cannot derive a closed form pdf under the stable noise distribution. However, from the following analysis, we find that when calculating the fractional lower order covariance, $X^{(\alpha/2)} = X \cdot |X|^{\alpha/2-1}$ is an operation which approximates the conversion of the stable distribution to the Gaussian distribution.

TABLE 2.10
ESTIMATED PARAMETERS OF POLARIMETRIC SAR DATA AFTER THE SCALED OPERATION

Parameters		α	β	γ	μ
<i>In-phase</i>	<i>HH</i>	2.0	0.0	1.52642	0.00710000
	<i>HV</i>	1.7190	0.0123	1.00940	0.00532212
	<i>VV</i>	1.9824	-0.0352	1.54276	0.0104154
	<i>VH</i>	1.9222	0.0402	0.993579	0.000499269
<i>Quadrature</i>	<i>HH</i>	2.0	0.0	1.52511	-0.0136500
	<i>HV</i>	1.7265	0.0232	1.01122	-0.0130095
	<i>VV</i>	1.9830	0.1295	1.54768	-0.0123935
	<i>VH</i>	1.9305	0.0677	0.993383	-0.00841240

These parameters are estimated using the STABLE software. The estimation is on the Delta Fraser area and the data are scaled use the equation: $X^{(\alpha/2)} = X \cdot |X|^{\alpha/2-1}$, where α is the estimated parameter using moving window with window size= 11×11 .

Although the covariance matrix is bounded when $p_{HH} < \alpha_{HH}/2$, $p_{HV} < \alpha_{HV}/2$, and $p_{VV} < \alpha_{VV}/2$, the method of selecting the value of p is important to have a meaningful result. From the definition of the fractional lower covariance, let $p = \alpha/2$, so we have $X^{(\alpha/2)} = X \cdot |X|^{\alpha/2-1}$, where X is the complex SAR data.

Theorem 2.2: When complex SAR data $X = X_1 + jX_2$ conforms to the isotropic complex $S\alpha S$ distribution $X \sim S(\alpha, 0, \gamma, 0)$, $X^{(\alpha/2)} = X \cdot |X|^{\alpha/2-1}$ tends to follow a Gaussian distribution.

Proof: Assuming the SAR data conforms to the sub-Gaussian distribution,

$$X = X_1 + jX_2 = \sqrt{A}G_1 + j\sqrt{A}G_2, \quad \text{where} \quad \text{we} \quad \text{have}$$

$$X^{(\frac{\alpha}{2})} = X \cdot |X|^{\frac{\alpha}{2}-1} = \frac{\sqrt{A}(G_1 + jG_2)}{(\sqrt{A})^{\frac{\alpha}{2}}(\sqrt{G_1^2 + G_2^2})^{1-\frac{\alpha}{2}}} = \frac{(\sqrt{A})^{\frac{\alpha}{2}}(G_1 + jG_2)}{(\sqrt{G_1^2 + G_2^2})^{1-\frac{\alpha}{2}}}.$$

(a) when $\alpha = 2$, the data is already Gaussian, there is no change for the data.

(b) when $0 < \alpha < 2$:

First, if α is low, the data is very impulsive. The $(\sqrt{A})^{\alpha/2}$ term tends to be much smaller than \sqrt{A} . Therefore, the impulsive term is reduced. Also, when α is low, $(\sqrt{G_1^2 + G_2^2})^{1-\alpha/2}$

is very high, and $\sqrt{G_1^2 + G_2^2} \geq G_1$, therefore $\frac{G_1}{(\sqrt{G_1^2 + G_2^2})^{1-\alpha/2}}$ is much smaller than G_1 . The

scaled in-phase is much smaller than the original in-phase. Also the quadrature is much smaller than the original quadrature. Therefore, the data $X^{(\alpha/2)}$ tends to be much smaller than X .

Second, when α is high, the data is slightly impulsive, and the $(\sqrt{A})^{\alpha/2}$ term tends to be

slightly smaller than \sqrt{A} , therefore the impulsive term is slightly reduced. Also when α is high, $\left(\sqrt{G_1^2 + G_2^2}\right)^{1-\alpha/2}$ tends to be 1 and $\sqrt{G_1^2 + G_2^2} \geq G_1$, therefore $\frac{G_1}{\left(\sqrt{G_1^2 + G_2^2}\right)^{1-\alpha/2}}$ is slightly smaller than G_1 and the data values tend to be slightly smaller after the processing. The scaled in-phase is slightly smaller than the original in-phase. Also the quadrature is slightly smaller than the original quadrature. Therefore, the data $X^{(\alpha/2)}$ tends to be slightly smaller than X .

Therefore, the data tends to be Gaussian after $X^{(\alpha/2)} = X \cdot |X|^{\alpha/2-1}$. This concludes the proof.

In order to test this assumption, several experiments were conducted. In these experiments, we used the data from the Delta Fraser area and calculated $X^{(\alpha/2)} = X \cdot |X|^{\alpha/2-1}$, where X is the complex SAR data of each polarization, α was estimated using the moving window of 11×11 and the parameter estimation method of complex data in [164] (For the accuracy of this estimator, please see Section 4.4 of this paper). Table 10 shows $X^{(\alpha/2)} = X \cdot |X|^{\alpha/2-1}$ for each polarization. From the parameters of in-phase and quadrature, we see that the data of $X^{(\alpha/2)}$ tends to be Gaussian. This means the operation in (8) is similar to the conversion from the non-Gaussian to the Gaussian.

Therefore, when we multiply the complex data with $|X|^{\alpha/2-1}$, the data tends to follow a Gaussian distribution. Therefore the covariance matrix based on FLOS can be calculated using $p_{HH} = \alpha_{HH}/2$, $p_{HV} = \alpha_{HV}/2$, and $p_{VV} = \alpha_{VV}/2$ as (2.17):

$$\begin{aligned}
& \mathbf{C}_{FLOS}^G \\
& = E \left\{ \begin{bmatrix} HH \cdot |HH|^{\alpha_{HH}/2-1} \cdot HH^* \cdot |HH|^{\alpha_{HH}/2-1} & HH \cdot |HH|^{\alpha_{HH}/2-1} \cdot HV^* \cdot |HV|^{\alpha_{HV}/2-1} & HH \cdot |HH|^{\alpha_{HH}/2-1} \cdot VV^* \cdot |VV|^{\alpha_{VV}/2-1} \\ HV \cdot |HV|^{\alpha_{HV}/2-1} \cdot HH^* \cdot |HH|^{\alpha_{HH}/2-1} & HV \cdot |HV|^{\alpha_{HV}/2-1} \cdot HV^* \cdot |HV|^{\alpha_{HV}/2-1} & HV \cdot |HV|^{\alpha_{HV}/2-1} \cdot VV^* \cdot |VV|^{\alpha_{VV}/2-1} \\ VV \cdot |VV|^{\alpha_{VV}/2-1} \cdot HH^* \cdot |HH|^{\alpha_{HH}/2-1} & VV \cdot |VV|^{\alpha_{VV}/2-1} \cdot HV^* \cdot |HV|^{\alpha_{HV}/2-1} & VV \cdot |VV|^{\alpha_{VV}/2-1} \cdot VV^* \cdot |VV|^{\alpha_{VV}/2-1} \end{bmatrix} \right\} \\
& \hspace{15em} (2.17)
\end{aligned}$$

Similar to the well known product model [146], this covariance matrix based on FLOS only changes the amplitude of the matrix but the phase information remains [146].

The depolarization measurement of polarimetric SAR is obtained by the estimation of covariance matrix or coherency matrix [145]. However, both these two matrices are estimated using the assumption that polarimetric SAR data are Gaussian distributed, which leads to estimation errors when the polarimetric SAR data includes heterogeneous scenes. Since the covariance matrix based on FLOS use a more accurate statistics which is alpha-stable, the depolarization measurement that estimated through the proposed covariance matrix based on FLOS may be improved. Moreover, the basic structure of the proposed covariance matrix based on FLOS remains the same with the original covariance matrix, the underlying wave scattering characteristics is maintained. Therefore, the proposed covariance matrix based on FLOS may obtain a better estimation of the target polarization characteristics.

2.3.4 pdf of the Covairance Matrix using FLOS

From the former analysis, the covariance matrix based on FLOS is similar to a preprocessing which changes the data from the $S\alpha S$ model to the Gaussian model [154], the statistics of the covariance matrix based on FLOS are now approximately Gaussian, therefore, the pdf can be developed similar to [162],

$$p(\mathbf{K}_{FLOS}) = \frac{1}{\pi^3 \det(\mathbf{C}_{FLOS})} \exp(-\mathbf{K}_{FLOS}^{*T} \mathbf{C}_{FLOS}^{-1} \mathbf{K}_{FLOS}). \quad (2.18)$$

where “det” means the determinant and \mathbf{K}_{FLOS}^{*T} means the conjugate transpose of \mathbf{K}_{FLOS} .

2.4 Polarimetric SAR Optimal Despeckling Using FLOS

2.4.1 Original Optimal Despeckling Method

The original optimal despeckling method was proposed by Novak and Burl [144] and was used in the target detection [27]; however, this method is only suitable for the single look image. Liu *et. al.* [161] extended the method in [144] to the multi-look case. Lopes and Sery [162] proposed some texture estimation methods for the product model which can be used in the multi-look case. However, as pointed out in [162], the despeckling method based on the product model does not perform well for areas with impulsive reflectors, such as urban areas. The despeckling method discussed in this paper is different to the problem of impulsive noise removal [152]. In this paper, we do not assume the noise is impulsive, the problem we discussed here is about the filtering when the signal distribution is heavy-tailed (strictly speaking, the noise contaminated signal is impulsive).

2.4.2 Despeckling Based on FLOS

In this chapter, we only discuss the despeckling on the single-look complex image. Following the method in [144], and applying the pdf in (2.18), we can derive the despeckling based on FLOS, which is

$$I = \frac{|HH|^{2p_{HH}}}{\sigma_{FLOS}(1-|\rho_{FLOS}|^2)} + \frac{|VV|^{2p_{VV}}}{\sigma_{FLOS}(1-|\rho_{FLOS}|^2)\gamma_{FLOS}} + \frac{|HV|^{2p_{HV}}}{\sigma_{FLOS}f_{FLOS}} - \frac{\rho_{FLOS}^* HH|HH|^{p_{HH}-1} VV^*|VV|^{p_{VV}-1} + \rho_{FLOS} HH^*|HH|^{p_{HH}-1} VV|VV|^{p_{VV}-1}}{\sigma_{FLOS}(1-|\rho_{FLOS}|^2)\sqrt{\gamma_{FLOS}}}. \quad (2.19)$$

This optimal despeckling is a generalized method in the stable distribution environment.

When $p_{HH} = p_{HV} = p_{VV} = 1.0$, this method is the same as the method in [144]. For different impulsive noise levels, we can select different p_{HH} , p_{HV} , and p_{VV} .

Because the modeling using the alpha-stable distribution only influences the covariance matrix estimation, i.e. the expectation of the data, in (2.19) we can use the original data instead of the scaled data in order to maintain the dynamic range of the image, which is

$$I = \frac{|HH|^2}{\sigma_{FLOS}(1-|\rho_{FLOS}|^2)} + \frac{|VV|^2}{\sigma_{FLOS}(1-|\rho_{FLOS}|^2)\gamma_{FLOS}} + \frac{|HV|^2}{\sigma_{FLOS}f_{FLOS}} - \frac{\rho_{FLOS}^* HH \cdot VV^* + \rho_{FLOS} HH^* \cdot VV}{\sigma_{FLOS}(1-|\rho_{FLOS}|^2)\sqrt{\gamma_{FLOS}}}.$$

This is the intensity of the image. If we want to obtain the amplitude image, the final despeckled image is \sqrt{I} . In this paper, the images and results are using the amplitude. Following the method in [144], the simplified version of the desepeckled image is

$$I = |HH|^2 + \frac{(1+|\rho_{FLOS}|^2)|HV|^2}{f_{FLOS}} + \frac{1}{\gamma_{FLOS}}|VV|^2. \quad (2.20)$$

2.4.3 Adaptive Despeckling Algorithm

Based on the former analysis, when calculating the γ_{FLOS} , f_{FLOS} , and ρ_{FLOS} using (2.13), (2.14), and (2.15), respectively, the values of p_{HH} , p_{HV} , and p_{VV} should be selected in terms of α_{HH} , α_{HV} , and α_{VV} , respectively. The best selection of p_{HH} , p_{HV} , and p_{VV} is in terms of the characteristic exponent as $p_{HH}(i, j) = \alpha_{HH}(i, j)/2$,

$$p_{HV}(i, j) = \alpha_{HV}(i, j)/2, \text{ and } p_{VV}(i, j) = \alpha_{HV}(i, j)/2.$$

The original despeckling method in [144] includes the non-adaptive method and adaptive method. In the adaptive method, we need to estimate the parameters in the covariance matrix. In the proposed method, when we estimate the covariance matrix based on FLOS, there are two classes of parameters that need to be estimated adaptively or non-adaptively. The first class of parameters are α_{HH} , α_{HV} , and α_{VV} for the calculation of p_{HH} , p_{HV} , and p_{VV} . The second class of parameters are γ_{FLOS} , f_{FLOS} , and ρ_{FLOS} , which need to be estimated. The adaptive ability is achieved by using a moving window of size $N \times N$. The size of the window needs to be selected carefully. If the window size is too large, the estimation resolution is too low. Inversely, if the window size is too small, the parameter estimation is not accurate due to the small number of samples used in the estimation. In estimating the covariance matrix based on FLOS, we can use the same parameters p_{HH} , p_{HV} , and p_{VV} for the whole image. This is the non-adaptive despeckling method (Note: In this non-adaptive method, the second class of parameters γ_{FLOS} , f_{FLOS} , and ρ_{FLOS} are still estimated adaptively, which means that we use the same parameters p_{HH} , p_{HV} , and p_{VV} for the whole image).

From the former analysis, we observed that for different areas of the image, the statistical parameters of the stable distribution vary. Therefore, when we apply the proposed despeckling method, the spatial adaptive ability is important. The proposed adaptive optimal despeckling method is as follows:

Parameter Estimation: Use a moving window with the window size $N \times N$ to calculate the mean and variance from the data inside the window, then apply the method

of [164] (Equation (21)) to calculate the $\hat{\alpha}$ from the samples inside each window. Then, for the pixel (i, j) of the center of the window, we obtain an $\hat{\alpha}(i, j)$.

p Value Calculation: The parameters estimated from the three channels are different. Therefore, we need to estimate the $\hat{\alpha}$ value for the three polarizations HH, HV, and VV. We calculate the p values of each polarization using the equations $p_{HH}(i, j) = \hat{\alpha}_{HH}(i, j)/2$, $p_{HV}(i, j) = \hat{\alpha}_{HV}(i, j)/2$, and $p_{VV}(i, j) = \hat{\alpha}_{VV}(i, j)/2$. For each pixel, we then obtain the values of $p_{HH}(i, j)$, $p_{HV}(i, j)$, and $p_{VV}(i, j)$. The reason that we choose $p(i, j) = \hat{\alpha}(i, j)/2$ is that when $\hat{\alpha}(i, j) = 2$ and $p(i, j) = 1$, the covariance estimation is equal to the Gaussian noise case.

Calculate γ_{FLOS} , f_{FLOS} , and ρ_{FLOS} : Use $p_{HH}(i, j)$, $p_{HV}(i, j)$, and $p_{VV}(i, j)$ estimated from step 2) to calculate γ_{FLOS} , f_{FLOS} , and ρ_{FLOS} using (2.13), (2.14), and (2.15), respectively. These parameters are also calculated adaptively using a moving window.

Optimal Despeckling: Perform the despeckling using equation (2.20).

2.4.4 Parameter Estimation

There are many parameter estimation methods for estimating α , β , γ , and μ . Fama and Roll [157] applied the sample fractiles to estimate the parameters. Press [174] proposed the moment estimation method which can be used in the parameter estimation of a wide range of parameter situations. However, the moment method is very slow [184]. Tsihrintzis and Nikias [184] proposed a fast estimation method using extreme value statistics. Also, most parameter estimation methods are only suitable for the real data so Ma and Nikias [164] estimated the parameters of real and complex data for the

$s\alpha S$ distribution. Since the method in [164] can only be used in the $s\alpha S$ distribution, Kuruoglu [159] extended the method in [164] to the skewed case.

For the proposed optimal despeckling method, we only need to estimate parameters $\hat{\alpha}_{HH}$, $\hat{\alpha}_{HV}$, and $\hat{\alpha}_{VV}$. Based on the analysis in part D of Section II, the characteristic exponents are the same for the in-phase, quadrature, and complex data. Therefore, there are two ways to estimate the characteristic exponent. First, we can estimate the characteristic exponent from the in-phase or quadrature using the real data estimation method [157][174]. Second, we can estimate the characteristic exponent of the complex data using the complex data estimation method in [164].

Now we will discuss the accuracy of these methods. For the parameter estimation method in [164], although the accuracy is high for large sample size, for real applications of the parameter estimation, when the window size is 11×11 , the estimation is not very accurate. The larger the window size, the more samples are used in the estimation and the more accurate the estimation. However, large window sizes lead to a coarser resolution. Therefore, we need to find an optimal window size for the parameter estimation.

When we use the parameter estimation method, we can use the real value parameter estimation method or the complex data estimation method. In the following experiment, we use the parameter estimation method of complex data in [164], which is

$$\hat{\alpha} = \frac{\pi}{\sqrt{6E\{(\log|X| - E(\log|X|))^2\}}}, \quad (2.21)$$

where X is the complex SAR image data. In real applications, characteristic exponent can be estimated using the sample data in the moving window $M \times N$.

Applying the results in [188], we can obtain the accuracy of the estimator in (2.21) as

$$E(\hat{\alpha} - \alpha)^2 = \frac{64(11N - 6)}{10\alpha^4(N^2 - N)}, \quad (2.22)$$

where N is the number of samples used in the estimation. This means that the accuracy of this estimator depends on the number of samples and the value of alpha: The more samples used in the parameter estimation, the higher is the accuracy; the smaller the alpha value, the higher is the error variance.

The accuracy of the parameter estimation is essential for the polarimetric SAR data modeling. From our experiments, we found that the estimator in [164] tends to obtain a less accurate estimation of alpha values when the number of input data samples are getting smaller, which conforms to equation (2.22). However, we found that the proposed despeckling method is not very sensitive to the estimation errors of alpha; therefore, we use the method in [164] in the proposed despeckling method because it is a relatively direct and fast method.

2.4.5 Computational Times

The proposed despeckling method needs extra CPU time for the characteristic exponent estimation. From the former analysis, we know that the only parameter that needs to be estimated is the characteristic exponent α . There are many parameter estimation methods in the literature. We use the characteristic exponent estimation method in [164] which is a relatively accurate method. The computational times for estimating $\hat{\alpha}$ in the proposed adaptive optimal despeckling method can be calculated. In this calculation, we assume that in the border area we also calculate the $\hat{\alpha}$ (for the experiments in this paper, we do not calculate the $\hat{\alpha}$ in the border area, the data in the border area are padded as zero).

Now we discuss the extra computational times that are required for estimating the covariance matrix based on FLOS using the method in [164] as an example. In the following discussion, we assume the data size is $P \times Q$ and window size is $M \times N$, where $M < P$ and $N < Q$. For each pixel, the calculation of the mean needs $M \times N - 1$ real value additions, the calculation of the variance needs $2M \times N - 2$ real value additions plus $M \times N - 1$ real value multiplications, and the calculation of $\hat{\alpha}$ needs 5 additional real value multiplications.

For the whole image, the calculation of the mean needs $P \times Q \times (M \times N - 1)$ real value additions, the calculation of the variance needs $P \times Q \times (2M \times N - 2)$ real value additions plus $P \times Q \times (M \times N - 1)$ real value multiplications, and the calculation of $\hat{\alpha}$ needs $5P \times Q$ additional multiplications.

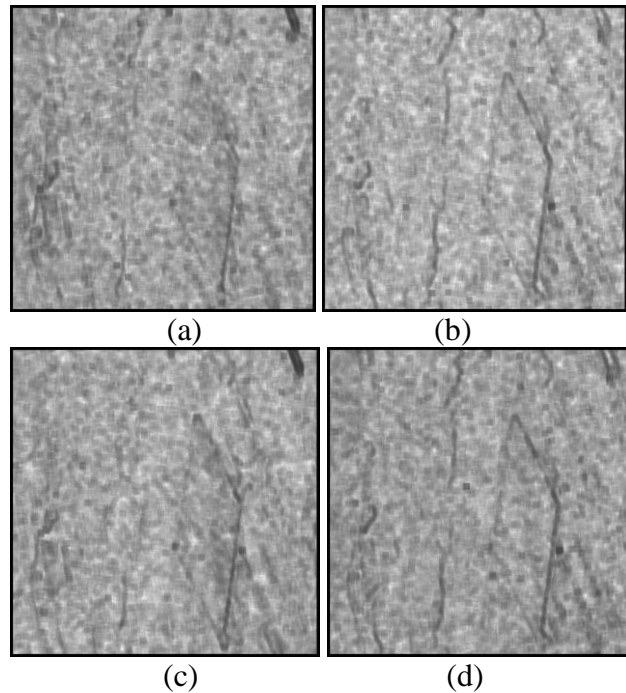


Figure 2.11. Estimated $\hat{\alpha}$ values from Delta data. Window size is 11×11 . (a) HH, (b) HV, (c) VV, (d) VH.

The total number of calculations for the $\hat{\alpha}$ of one channel are: $3P \times Q \times (M \times N - 1)$ real value additions and $P \times Q \times (M \times N - 1) + 5P \times Q$ real value multiplications.

When calculating the covariance matrix based on FLOS, we need to calculate the characteristic exponents in three polarizations, which are HH, HV, and VV. Therefore, the total number of additions is $9P \times Q \times (M \times N - 1)$ and the total number of multiplications is $3P \times Q \times (M \times N - 1) + 15P \times Q$.

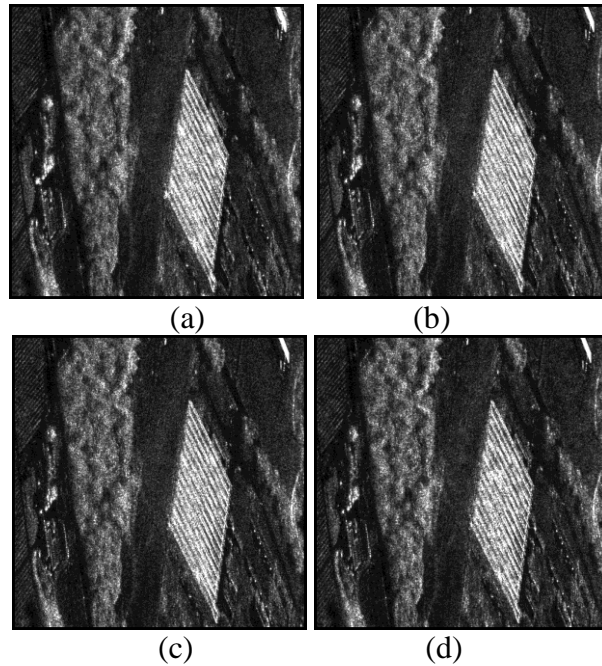


Figure 2.12. Despeckling results using the original despeckling method in [144] and the proposed non-adaptive and adaptive method. (a) Image after despeckling using the original despeckling method in [144], window size= 11×11 . (b) Image after despeckling using the proposed non-adaptive method (Equation (20), $p_{HH} = p_{HV} = p_{VV} = 0.5$, window size= 11×11). (c) Image after despeckling using the proposed non-adaptive method ($p_{HH} = p_{HV} = p_{VV} = 0.2$, window size= 11×11). (d) Image after despeckling using the proposed adaptive method (window size in alpha estimation and despeckling are 11×11).

2.4.6 Experiments of the Optimal Despeckling Method Using Alpha-Stable

Distribution

We use the despeckling method in (2.20) to examine the despeckling performance of the covariance matrix based on FLOS. The evaluation of the despeckling result includes the equivalent number of looks (ENL) [185][162] (when we compute the ENL, we use the amplitude of the image). The estimated $\hat{\alpha}_{HH}$, $\hat{\alpha}_{HV}(i, j)$, $\hat{\alpha}_{VV}(i, j)$, and $\hat{\alpha}_{VH}(i, j)$ are illustrated in Figure 2.11 (a), Figure 2.11 (b), Figure 2.11 (c), and Figure 2.11 (d), respectively (although $\hat{\alpha}_{VH}(i, j)$ is not used in the optimal despeckling, we show it here only for the comparison of the other polarizations). In Figure 2.11, the window size is 11×11 . Figure 2.11 shows the estimated $\hat{\alpha}$ of the Delta Fraser data from the HH, HV, VV, and VH polarizations, respectively (in the image, the $\hat{\alpha}$ value is scaled to obtain a better display result, white represents a higher $\hat{\alpha}$ value, black means a lower $\hat{\alpha}$ value). From the image, we observe that the $\hat{\alpha}$ value is the lowest in the area of strong reflectors, which mostly comes from manmade structures.

Figure 2.12 illustrates the despeckling result of the original despeckling method in [144] and the despeckling results using the proposed method. Figure 2.12 (a) is the result of the adaptive method in [144]. Figure 2.12 (b) and Figure 2.12 (c) are the results of the proposed method when the covariance matrix is estimated adaptively and p_{HH} , p_{HV} , and p_{VV} are using the fixed value for the whole image. In Figure 2.12 (b), $p_{HH} = p_{HV} = p_{VV} = 0.5$. In Figure 2.12 (c), $p_{HH} = p_{HV} = p_{VV} = 0.2$. Figure 2.12 (d) shows the despeckling result using the method which adaptively estimates both covariance matrix (γ_{FLOS} , f_{FLOS} , and ρ_{FLOS}) and characteristic exponents (α_{HH} , α_{HV} , and α_{VV}).

TABLE 2.11
ENL OF DESPECKLED AND ORIGINAL IMAGE (DELTA FRASER AREA)

	Original Image	Despeckled Using method in [144].	Despeckled Using proposed non-adaptive method $p_{HH} = p_{HV} = p_{VV} = 0.5$	Despeckled Using proposed non-adaptive method $p_{HH} = p_{HV} = p_{VV} = 0.2$	Despeckled Using proposed adaptive method
ENL	HH 1.878	2.905	2.830	2.774	2.875
ENL	HV 1.144				
ENL	VV 1.892				
ENL	VH 1.190				

From Figure 2.12 (a), we found that for the original despeckling method in [144], the despeckled image blurred the target in the top right part of the image, the edge of the square, and the other strong targets in the lower left part of the image. These blurs are because the statistical models around the strong target areas are very impulsive and deviate from the Gaussian assumption. Therefore, using the original method the estimation of γ_{FLOS} , f_{FLOS} , and ρ_{FLOS} is not accurate. When we use the non-adaptive method with $p_{HH} = p_{HV} = p_{VV} = 0.5$, these blurs are slightly reduced. When we use the non-adaptive method with $p_{HH} = p_{HV} = p_{VV} = 0.2$, these blurs are further reduced. However, when we compute the ENL (Table 2.11 illustrates the ENL of the original image and despeckled image), the non-adaptive method obtains a lower ENL than the original despeckling method in [144]. The lower the p_{HH} , p_{HV} , and p_{VV} , the lower the ENL.

When we use the adaptive despeckling method, we compute γ_{FLOS} , f_{FLOS} , and ρ_{FLOS} for each pixel of each channel. We use the alpha value of the respective pixel in the

respective channel, which is $p_{HH}(i, j) = \alpha_{HH}(i, j)/2$, $p_{HV}(i, j) = \alpha_{HV}(i, j)/2$, and $p_{VH}(i, j) = \alpha_{VH}(i, j)/2$. On the other hand, all the values of the characteristic exponents are scaled to $[0, 2]$. In this experiment, the window used for calculating $\hat{\alpha}$ is 11×11 , also the window for estimating γ_{FLOS} , f_{FLOS} , and ρ_{FLOS} is 11×11 . From the despeckled image (which is illustrated in Figure 2.5 (d)), we found the blurs are eliminated in all of the areas. In addition, the ENL is improved compared to the non-adaptive method and is only slightly lower than the original method. This means a similar amount of speckles are eliminated using the adaptive method as the original despeckling method in [144].

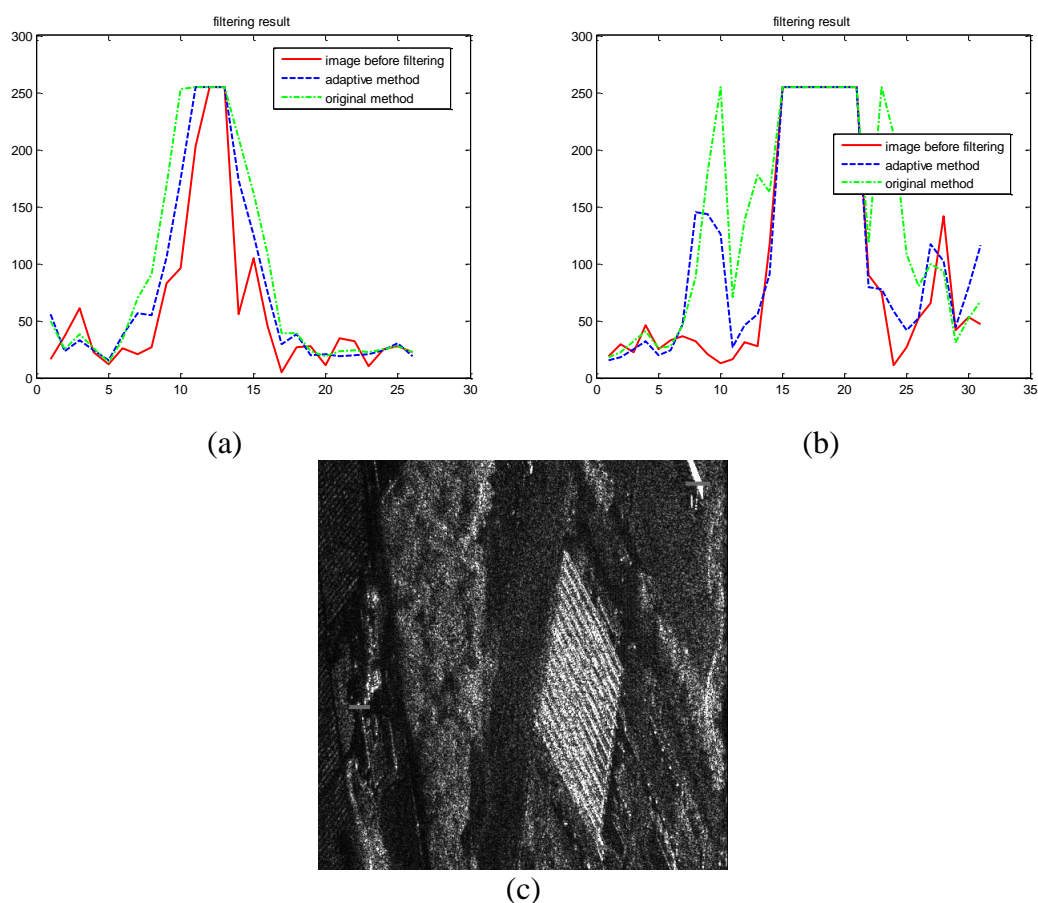


Figure 2.13. Profiles in some areas. Area A is left, Area B is the right. (a) Profile of area A. (b) Profile of area B. (c) The two areas.

In order to further examine the despeckling results, we plot the profiles of the image before despeckling, the despeckled result of the proposed adaptive method, and the despeckled result of the original method in [144] in Figure 2.13. Figure 2.13(a) and (b) show the profiles of a thin feature and an edge in the image, respectively. Figure 2.13 (c) shows the locations of these two profiles. In the lower left part of Figure 2.13(c), a grey line shows the location of the profile shown in Figure 2.13(a). In the higher right part of Figure 2.13(c), a grey line shows the location of the profile shown in Figure 13 (b). From these two profiles, we found that the proposed adaptive method has a much better performance in terms of keeping the edges of the image than the original despeckling method in [144].

All in all, the proposed adaptive method not only reduces the blurs in the areas of strong reflection, but also maintains the speckle reduction ability (ENL). This method keeps the sharpness around the strong reflectors and thus maintains the edges in the image. Thus, the despeckling result is more favorable in the application of classification, edge detection, etc than the original method in [144].

2.5 Conclusion

In this chapter, the polarimetric SAR data statistical model is established using the alpha-stable distribution and can be modeled as a multi-channel alpha-stable distribution.

The covariance matrix estimation method in the alpha-stable distribution environment is proposed based on the fractional lower order covariance. The covariance matrix is the generalization of the traditional covariance matrix. The proposed covariance matrix can be widely used in the image despeckling of polarimetric SAR data and can be

used in the polarimetric SAR processing under the non-Gaussian statistical assumption.

The polarimetric SAR optimal despeckling method based on the fractional lower order statistics was proposed. The proposed method reduces the blurs in strong reflection areas, which provides a better image for edge detection and classification applications. The proposed method obtains better performance than the original method at the cost of a heavier computational burden.

The future research will be using the mixture of alpha-stable model [175] to improve the proposed method.

CHAPTER 3: INTERFEROMETRIC SAR EXTENDED COHERENCE CALCULATION BASED ON FRACTIONAL LOWER ORDER STATISTICS²

A polarimetric synthetic aperture radar (SAR) coherence calculation method based on fractional lower order statistics (FLOS) was proposed in [199]. In this chapter, we apply this approach to the coherence calculation for interferometric SAR (InSAR) and provide a detailed analysis. An L-Band InSAR data set is used to provide comparative results between the coherence derived in the traditional manner and that based on FLOS. In the areas around strong scatterers, the coherence is found to be biased due to the deviation of the statistical model from Gaussian when using the traditional coherence calculation. However, the coherence based on FLOS largely reduces this bias. From the experimental results using the InSAR data, we found that this method reduces the artifacts in the traditional coherence calculation method. The removal of bias due to sample estimation is also discussed.

3.1 Introduction

Interferometric synthetic aperture radar (SAR) (InSAR) is widely used in the creation of digital elevation models. Coherence is an important concept in the application

² © 2010 IEEE. Reprinted, with permission, from [Yong Bian and Bryan Mercer, “Interferometric SAR extended coherence calculation based on fractional lower order statistics,” *IEEE Geoscience and Remote Sensing Letters*, vol. 7, no. 4, pp. 841-845, October 2010.].

of InSAR. It can be used in the phase unwrapping as a quality map [202], [127] or used in change-detection with repeat-pass InSAR data [196]. It is a fundamental parameter in polarimetric InSAR (PolInSAR) applications [189] and, recently, has been used for land cover classification [206]. There is much research related to InSAR coherence calculation, such as the early research in [191] and [200] and the recently developed methods in [195], [201], and [202].

In most of these coherence estimation methods, the complex InSAR images are assumed to be described by a Gaussian distribution [191]. However, some research has indicated that the InSAR image can more appropriately be represented using the alpha-stable distribution [183]. In particular, this may be the case when the underlying Gaussian assumptions break down. Therefore, if we can estimate the coherence of InSAR based on the alpha-stable distribution, the accuracy will likely be improved. There is some research concerning the correlation or coherence estimation of the alpha-stable distribution, such as the “association parameter” [194], [205], the correlation coefficient of the sub-Gaussian distribution [203], and the symmetric covariation [208]. However, these methods are not suitable for the estimation of the complex data and cannot be directly used in the InSAR coherence estimation. A polarimetric SAR coherence estimation method based on the alpha-stable distribution and fractional lower order statistics (FLOS) was proposed in [199], and some preliminary PolInSAR computations were introduced in [192]. In this chapter, we will apply this adaptive coherence estimation method in InSAR coherence estimation and give a detailed analysis.

3.2 Review of Alpha-Stable Distribution

Single look complex SAR image data $s = s_{re} + js_{im}$ can be modeled by an isotropic complex symmetric alpha-stable ($s_{\alpha S}$) distribution [183], [182]. Because its probability density function (pdf) does not generally exist in closed form, it is described by its characteristic function [156], [182], [176] Ψ , which is the Fourier transform of the pdf,

$$\Psi(\omega) = \exp\left\{-\int_{\chi_2} |\omega_{re}s_{re} + \omega_{im}s_{im}|^\alpha d\Gamma(s_{re}, s_{im})\right\} = \exp\left\{-\gamma|\omega|^\alpha\right\}, \quad (3.1)$$

where ω is the complex random variable, α is the characteristic exponent that determines the heavy-tailed characteristic of the distribution, and γ is the dispersion [179], which is similar to the variance in the Gaussian noise case.

3.3 Coherence Calculation Based on FLOS

In [199], a modified FLOS-based definition of coherence emerged relevant to polarimetric SAR images under the alpha-stable distribution following the derivation of the covariance matrix based on FLOS. Now, we apply this FLOS-based coherence to the calculation of InSAR coherence and give a detailed analysis.

3.3.1 Review of Standard Coherence Estimation

The standard definition of the complex coherence for InSAR is [191], [201], [130]

$$\delta = \frac{E(S_1 \cdot S_2^*)}{\sqrt{E(|S_1|^2)E(|S_2|^2)}} = A \exp(\phi) \quad (3.2)$$

where s_1 and s_2 are the master and slave complex InSAR scalar images, respectively;

“ E ” and “ $*$ ” are the expectation operator and complex conjugate, respectively. This definition is based on second-order moments (SOMs) and the assumption of the applicability of Gaussian statistics.

3.3.2 Coherence Based on FLOS

One of the properties of the alpha-stable distribution is that its SOMs generally do not exist [176], thus requiring a modification to the coherence definition of (2). The SOMs of alpha-stable distribution are not bounded when $\alpha < 2$ [179]; therefore, for the alpha-stable distribution, fractional lower order moments (FLOM) [167], [179] have been used to substitute for the SOM. Therefore, the definition in (2) cannot be used under the alpha-stable distribution environment, and we define a modified coherence in the $s_{\alpha S}$ environment using the fractional lower order covariance [183], [165]. We assume that complex InSAR master (s_1) and slave (s_2) images follow the complex isotropic $s_{\alpha_1 S}$ and $s_{\alpha_2 S}$ distribution, respectively. We proceed by analogy with [199] in which the coherence between HH and VV was obtained, based on FLOS. Letting $s^{(t)} = s \cdot |s|^{t-1}$, we can define the FLOS-based interferometric coherence as follows [199]:

$$\begin{aligned} \delta_{FLOS} &= \frac{E\left(s_1^{(t_1)} \cdot s_2^{*(t_2)}\right)}{\sqrt{E\left(\left|s_1^{(t_1)}\right|^2\right)E\left(\left|s_2^{(t_2)}\right|^2\right)}} = \frac{E\left(s_1 \cdot s_2^* |s_1|^{t_1-1} |s_2|^{t_2-1}\right)}{\sqrt{E\left(|s_1|^{2t_1}\right)E\left(|s_2|^{2t_2}\right)}} \quad (3.3) \\ &= A_{FLOS} \exp(j\phi_{FLOS}) \end{aligned}$$

This definition is similar to the FLOM in [197], and is similar to the generalization of the associated parameter [194], [205] in the complex $s_{\alpha S}$ case. When $t=1.0$, the coherence based on FLOS is the same as (3.2), the standard definition of coherence [189], [191], [130]. Therefore, the coherence based on FLOS can be called the generalized coherence

in the alpha-stable distribution environment, which is natural since it includes the Gaussian distribution as the special case when $\alpha = 2$ [176].

3.3.3 Discussion

In this section, we provide proof that δ_{FLOS} is bounded for $t_1 < \alpha_1/2$ and $t_2 < \alpha_2/2$, respectively, and that, moreover, $0 \leq |\delta_{FLOS}| \leq 1$.

Theorem 3.1: Assuming that s_1 and s_2 are complex $s_{\alpha_1}S$ and $s_{\alpha_2}S$, respectively,

$$\delta_{FLOS} = \frac{E\left(S_1 \cdot S_2^* |S_1|^{t_1-1} |S_2|^{t_2-1}\right)}{\sqrt{E\left(|S_1|^{2t_1}\right)E\left(|S_2|^{2t_2}\right)}} = \frac{\Theta}{N} \text{ are bounded when } t_1 < \alpha_1/2 \text{ and } t_2 < \alpha_2/2.$$

Proof: See the Appendix for the proof.

$$\textit{Theorem 3.2: } 0 \leq |\delta_{FLOS}| = \left| \frac{E\left(S_1 \cdot S_2^* |S_1|^{t_1-1} |S_2|^{t_2-1}\right)}{\sqrt{E\left(|S_1|^{2t_1}\right)E\left(|S_2|^{2t_2}\right)}} \right| = \left| \frac{\Theta}{N} \right| \leq 1 \text{ when } t_1 < \alpha_1/2 \text{ and } t_2 < \alpha_2/2.$$

Proof: Now we prove that $0 \leq |\delta_{FLOS}| \leq 1$. $|\Theta| = \left| E\left(S_1 \cdot S_2^* |S_1|^{t_1-1} |S_2|^{t_2-1}\right) \right| \leq E\left(|S_1| \cdot |S_2^*| |S_1|^{t_1-1} |S_2|^{t_2-1}\right)$
 $= E\left(|S_1|^{t_1} |S_2|^{t_2}\right) \leq E\left(|S_1|^{t_1}\right) E\left(|S_2|^{t_2}\right) \leq \sqrt{E\left(|S_1|^{2t_1}\right) E\left(|S_2|^{2t_2}\right)}$; therefore, $0 \leq |\delta_{FLOS}| \leq 1$.

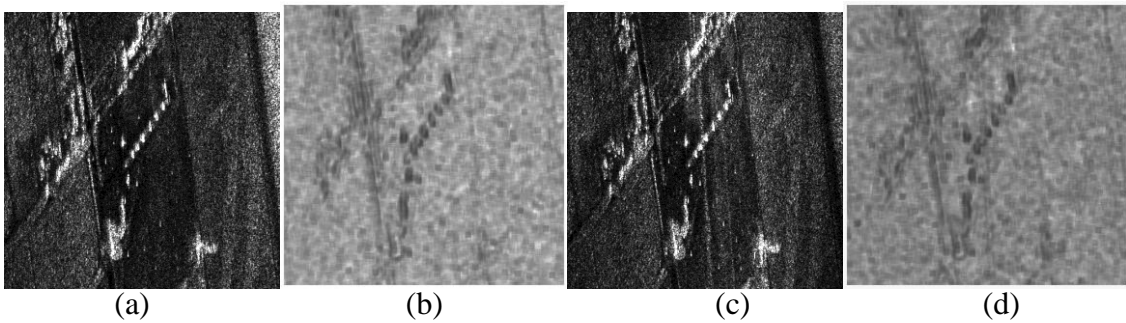


Figure 3.1. Single-look images and estimated alpha values (the value of α is from high to low is denoted from white to black; 11*11 window) from InSAR data. (a) Master image. (b) Estimated alpha values of master image. (c) Slave image. (d) Estimated alpha values of slave image.

For real-world applications, we generally use a moving window in computing the sample coherence based on FLOS. In the former analysis, we did not consider the phase fluctuation caused by surface topography [195] in the coherence estimation. Upon consideration of this, we may, following [190], [191], [195], and [130], write the definition of the FLOS-based sample coherence (with a $K \times L$ moving window) as (3.4),

$$\begin{aligned} \hat{\delta}_{FLOS} &= \hat{A}_{FLOS} \exp(j\hat{\phi}_{FLOS}) \\ &= \frac{\sum_{k=1}^K \sum_{l=1}^L \left(S_1(k,l) \cdot S_2^*(k,l) |S_1(k,l)|^{t_1-1} |S_2(k,l)|^{t_2-1} \exp(-j\phi_T(k,l)) \right)}{\sqrt{\sum_{k=1}^K \sum_{l=1}^L \left(|S_1(k,l)|^{2t_1} \right) \sum_{k=1}^K \sum_{l=1}^L \left(|S_2(k,l)|^{2t_2} \right)}}, \end{aligned} \quad (3.4)$$

where we have formally introduced ϕ_T to account for the effects of topography [195] on the total observed coherence. When the topography of the image is not changed very much (as is the case in this Chapter), the topographic phase term can be ignored.

3.3.4 Bias Removal

Although the boundedness has only been proved for $t_1 < \alpha_1/2$ and $t_2 < \alpha_2/2$, there are advantages in setting $t_1 = \alpha_1/2$ and $t_2 = \alpha_2/2$, which has been applied in [199] and [192], which, for modest sample sizes, is reasonable. Based on the analysis in [199], in this Chapter, we formally let $t_1 = (\alpha_1 - \varepsilon)/2$ and $t_2 = (\alpha_2 - \varepsilon)/2$, for which the coherence based on FLOS becomes

$$\begin{aligned} \delta_{FLOS}(\alpha_1, \alpha_2) &= \frac{E \left(|S_1 \cdot S_2^*| |S_1|^{\frac{\alpha_1 - \varepsilon}{2} - 1} |S_2|^{\frac{\alpha_2 - \varepsilon}{2} - 1} \right)}{\sqrt{E \left(|S_1|^{\alpha_1 - \varepsilon} \right) E \left(|S_2|^{\alpha_2 - \varepsilon} \right)}} \\ &= A_{FLOS}(\alpha_1, \alpha_2) \exp(j\phi(\alpha_1, \alpha_2)) \end{aligned} \quad (3.5)$$

where α_1 and α_2 are the characteristic exponents [165] of s_1 and s_2 , respectively, and ε

is an arbitrarily small constant value in order to retain the boundedness of the estimate.

FLOS-based coherence will be biased due to sample estimation factors, just as it is when based upon complex Gaussian statistics. This bias can be calculated as the difference between the estimated coherence magnitude and the true coherence magnitude [204]. Although the bias due to the statistical model deviation (statistical bias) can be compensated by using the FLOS-based sample coherence estimation, the bias due to sample estimation (sample bias) still exists. We assume here that the bias removal of the coherence estimate can be considered as a two-step process in which the first step eliminates the statistical bias by using the FLOS-based sample coherence estimator (as shown in (3.8)), while the second step removes the sample bias. We further assume by analogy that the sample bias can be removed by mimicking the relationship between the true coherence and the estimated coherence under the Gaussian statistics assumption using the method in [190] and [191], which leads to

$$\hat{A}_{FLOS} \cong E(\hat{A}_{FLOS}) = \frac{(1 - A_{FLOS}^2)^C {}_3F_2(1.5, C, C; C + 0.5, 1; A_{FLOS}^2) \Gamma(C) \Gamma(1.5)}{\Gamma(C + 0.5)} \quad (3.6)$$

where A_{FLOS} and \hat{A}_{FLOS} are the true and estimated coherence magnitudes, respectively, C is the sample number and ${}_3F_2$ is the generalized hypergeometric function (GHF) [207]. Following the method in [191], we can reduce the sample bias from the estimated result of FLOS-based sample coherence (using (3.4) or (3.8)) by inverting (3.6). While this assumed relationship for \hat{A}_{FLOS} is unproven at this point (to our knowledge), it appears plausible and is supported by the experimental results in the following sections. Therefore, the FLOS-based coherence estimation includes three steps: parameter estimation, sample coherence estimation (using (3.8)); and, sample-bias removal (by

inverting (3.6) or other methods).

In [191], the average of the estimated complex sample coherence is used to reduce the sample bias, and this method can be also used for the FLOS-based method, i.e.,

$$\bar{\delta}_{FLOS} = \sum_{i=1}^I \sum_{j=1}^J \hat{\delta}_{FLOS}(i, j). \quad (3.7).$$

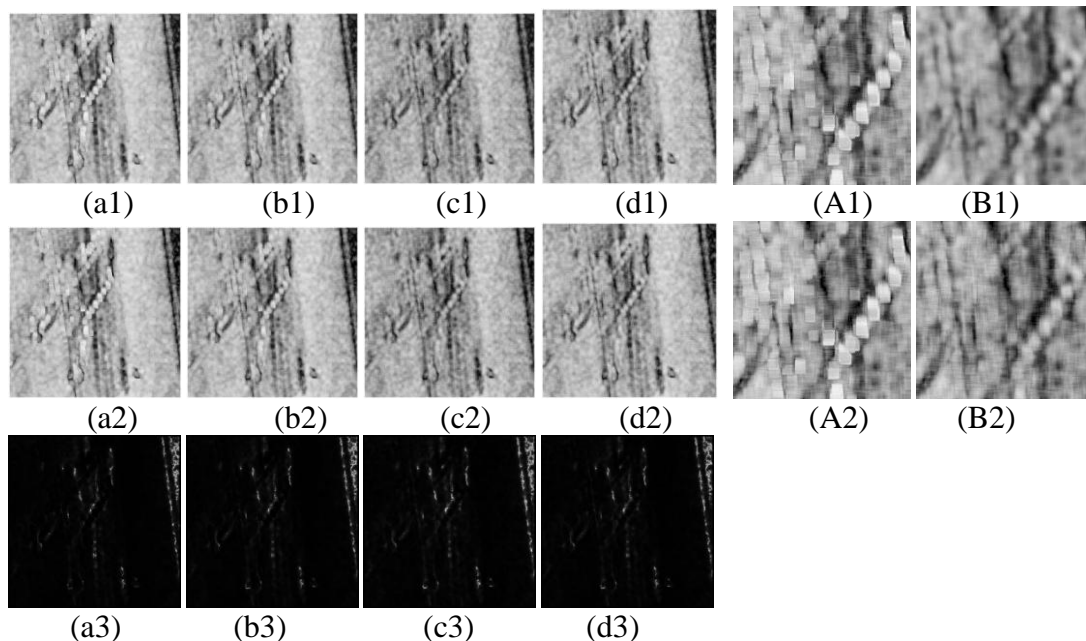


Figure 3.2. Experimental results of InSAR data. (a1)-(d1) Coherence maps before sample-bias removal. (a2)-(d2) Coherence maps after sample-bias removal. (a1) and (a2) Coherence maps using the standard coherence estimation method. (a3)-(d3) Difference maps between the coherence before and after sample-bias removal. (b1) and (b2) ((c1) and (c2)) Coherence maps using the non-adaptive FLOS-based coherence estimation method when $t=0.6$ (when $t=0.25$). (d1) and (d2) Coherence maps using the adaptive FLOS-based coherence estimation method. (A1), (B1), (A2), and (B2) are zoomed-in looks of (a1), (d1), (a2), and (d2), respectively.

3.4 Implementations and Experiments

3.4.1 Adaptive Sample Coherence Estimation

Because the alpha varies spatially [199], an adaptive method is expected to have better performance in calculating the FLOS-based coherence. Similarly, we can represent the definition of adaptive coherence estimation using alpha-stable distributions when a moving window ($K \times L$) is used in computing the sample coherence as in (3.8) [199],

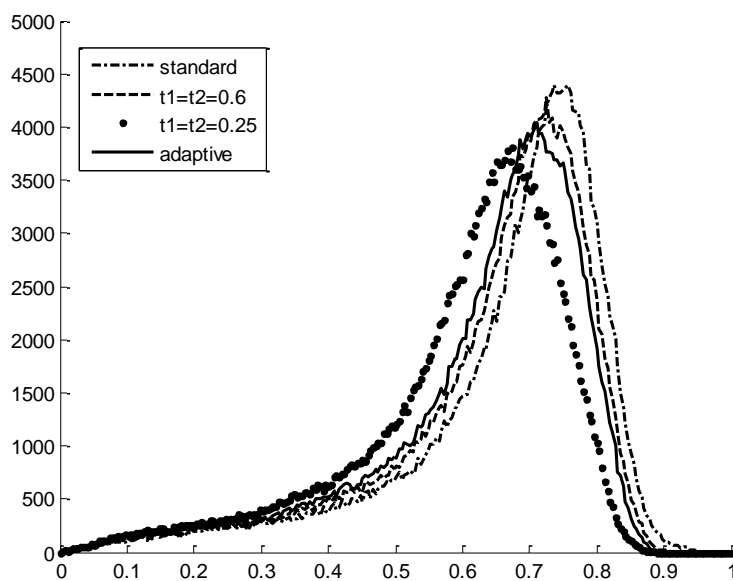
$$\begin{aligned} \hat{\delta}_{FLOS}(\hat{\alpha}_1, \hat{\alpha}_2) &= \hat{A}_{FLOS}(\hat{\alpha}_1, \hat{\alpha}_2) \exp(j\hat{\phi}_{FLOS}(\hat{\alpha}_1, \hat{\alpha}_2)) \\ &= \frac{\sum_{k=1}^K \sum_{l=1}^L \left(|S_1(k, l) \cdot S_2^*(k, l)| |S_1(k, l)|^{\frac{\hat{\alpha}_1(k, l) - \varepsilon}{2}} |S_2(k, l)|^{\frac{\hat{\alpha}_2(k, l) - \varepsilon}{2}} \exp(-j\varphi_T(k, l)) \right)}{\sqrt{\sum_{k=1}^K \sum_{l=1}^L \left(|S_1(k, l)|^{\hat{\alpha}_1(k, l) - \varepsilon} \right) \sum_{k=1}^K \sum_{l=1}^L \left(|S_2(k, l)|^{\hat{\alpha}_2(k, l) - \varepsilon} \right)}} \end{aligned} \quad (3.8)$$

where $\hat{\alpha}_1$ and $\hat{\alpha}_2$ are estimated from the data on a pixel-to-pixel basis.

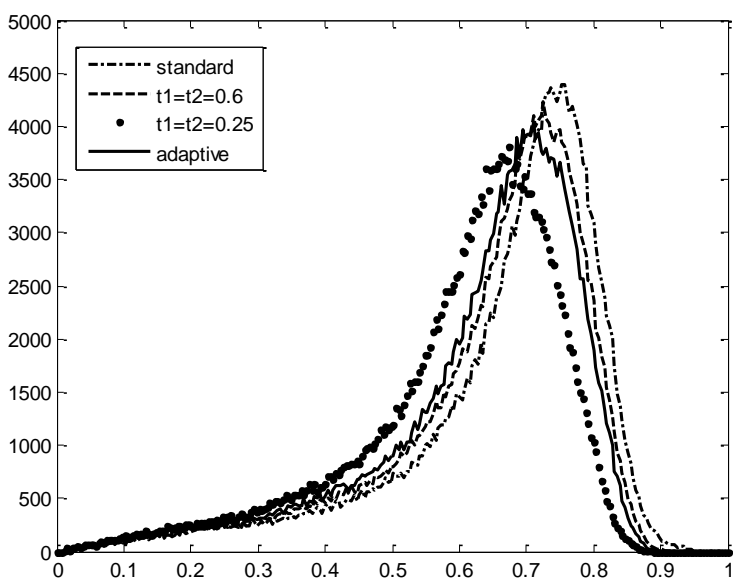
3.4.2 Sampled Estimate of the FLOS-Based Coherence

The implementation of a sampled estimate of the FLOS-based coherence is similar to [199], which is to use a moving window to estimate $\hat{\alpha}$ first, then select the value of t for a moving window using the value $t = (\hat{\alpha} - \varepsilon)/2$ (in the following experiments, $\varepsilon = 0.002$), and finally, estimate the coherence using the definition of (3.8). Although this estimator is not the maximum likelihood estimation of the coherence [193], it reduces the statistical bias that exists in the standard sample coherence estimation as can be seen from the following experiments. We use the alpha parameter estimator of complex data as proposed in [164] (see Eqn. (23) of [164] for details), and which has been successfully used in [199] and [192]. Similar to that of the optimal despeckling method in [199], some extra computational time (relative to the nonadaptive case) comes from the estimation of alpha. The main difference is due to the need only to compute alpha for a single polarization

channel (but two interferometric channels) in this case, rather than the four polarimetric channels in the referenced case in [199].



(a)



(b)

Figure 3.3. Coherence histograms of the results in Figure 3.2. (a) Before sample-bias removal. (b) After sample-bias removal.

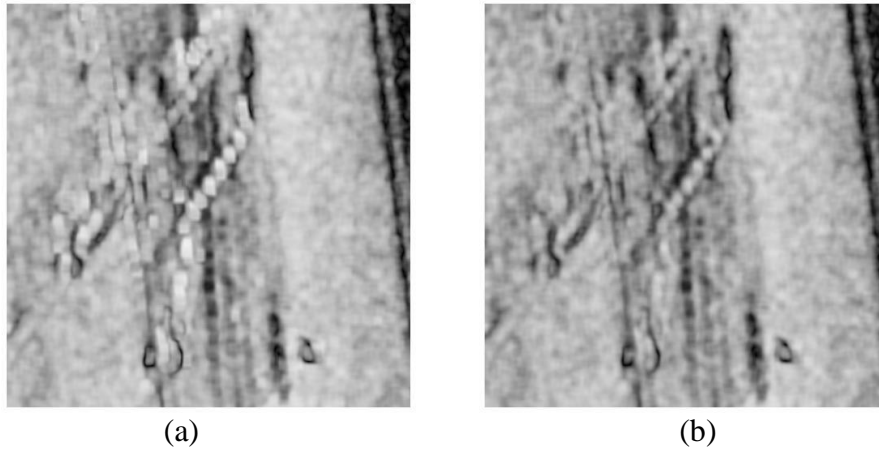


Figure 3.4. Coherence maps of the average of complex sample estimation (5*5 window).
 (a) Standard method. (b) FLOS-based adaptive method.

The sample-bias removal (the inverse of (6)) involves the calculation of GHF, which needs a lot of CPU time. Therefore, we use a lookup table as suggested in [191] for different window sizes. The GHF calculation is implemented using the code provided in [207] and [209].

3.4.3 Experimental Results

In this experiment, an L-Band single-look complex InSAR image set is used. Figure 3.1 shows the master and slave images and the estimated characteristic exponents (α) for each. The experiments with and without sample-bias removal have been conducted. Figure 3.2 shows the experimental results of the traditional coherence calculation method and the FLOS-based coherence calculation. Figure 3.2(a1)-(d1) and (a2)-(d2) show the experimental results before and after sample-bias removal, respectively. Figure 3.2(a1) and (a2) show the estimated coherence maps using the definition in (2). There appear to be some artifacts around the strong scatterers particularly in Figure 3.2(a1) and (a2). This is assumed to be due to the departure from Gaussian in the areas around the strong

scatterers. Figure 3.2 (b1) and (b2) (Figure 3.2(c1) and (c2)) show the calculated coherence using the non-adaptive FLOS-based method when $t_1 = t_2 = 0.6$ ($t_1 = t_2 = 0.25$) before and after bias removal, respectively. For $t_1 = t_2 = 0.25$, the artifacts are mostly eliminated. Figure 3.2 (d1) and (d2) show the coherence using the adaptive FLOS-based method before and after bias removal, respectively. These artifacts appear to be further reduced in Figure 3.2(d1) and (d2). In the larger homogeneous areas, there appears to be little difference between the standard and the adaptive FLOS-based methods, i.e., the adaptive FLOS-based method is equal to the standard method when the alpha parameter approaches 2.0. In summary, the coherence anomalies appear to be visibly reduced near the strong scatterers, while in other areas, the adaptive method results in similar coherences as found in the standard Gaussian-based approach.

Figure 3.3 (a) and (b) show the histograms of the calculated coherences shown in Figure 3.2 before and after sample-bias removal, respectively. For both the histograms before and after bias removal, the standard coherences are larger than those computed using FLOS. This appears to be due to the areas near the strong scatterers which could be assumed to be a combination of the strong scatterers themselves and multiple weak scatterers included within the 11×11 coherence windows. This interpretation therefore suggests that the standard method overestimates the coherence in these local areas (this reaches a similar conclusion as [192] in the PolInSAR case). The adaptive method itself provides coherences intermediate between the two “fixed t ” coherence computations. The histogram for the adaptive case appears to be quite close to that for $t_1 = t_2 = 0.6$, corresponding to $\alpha = 1.2$, which itself implies a distribution different from Gaussian

($\alpha = 2$).

Comparison of the results Before and After Sample-Bias Removal: The difference between the results with or without bias removal is shown in Figure 3.2(a3)-(d3). Figure 3.2(a3)~(d3) shows that the bias removal is mostly effective in the low-coherence area for both the standard and FLOS-based methods. Comparing the histograms before and after bias removal (Figure 3.3), it is apparent that the histograms are very similar. This is explainable given that the coherence values of most of the map are relatively high so that the sample-bias removal only affects a small part of the coherence map. During the sample-bias removal, the high coherence values are almost unchanged, but the low coherence values are corrected (which has been observed in [191]). On the contrary, during statistical-bias removal, the low coherence values are almost unchanged, but the high coherence values are corrected. Therefore, the FLOS-based method requires both the statistical bias (FLOS-based sample coherence estimation itself) and sample-bias removal. The results appear to support the two-stage sample-bias removal as invoked earlier.

3.4.4 Experiments Using Averaged Complex Sample Coherence

The experiments using the averaged complex sample-coherence method in [191] were also performed and the results are shown in Figure 3.4. Contrasting the coherence maps between the standard and similarly averaged adaptive FLOS-based methods, we found comparable, but less conspicuous differences, between the two methods. For the standard method, the averaging process smoothes but cannot remove the artifacts around the strong scatterers. The FLOS-based method, on the other hand, has fewer observable artifacts around these strong scatterers.

3.5 Conclusion

In this chapter, the coherence calculation method based on FLOS and the isotropic complex $S\alpha S$ distribution is applied in the InSAR coherence estimation. The statistical and sample-bias removal techniques are discussed and experimental results compared with those from the standard Gaussian-based approach. The standard coherence calculation method appears to overestimate the coherence around strong scatterers relative to that based on FLOS. This method reduces the artifacts seen in the standard method at the cost of a slight increase of computational burden.

3.6 Appendix

Here, we provide a proof of Theorem 3.1. Now, we need to prove that the expectations in (3) are bounded [156], [167], [179]. This includes the boundedness of Θ and N . Assume that $S = S_{re} + jS_{im}$.

(a) Now, we prove that Θ is bounded: In order to prove that Θ is bounded, we use the method similar to the proof of Theorem 1 of [198], which is to prove that both the real and imaginary parts of Θ are bounded. Similar to the proof of Theorem 1 in [198], we have

$$\begin{aligned} \Re\{\Theta\} &= \Re\left\{E\left(S_1 \cdot S_2^* |S_1|^{t_1-1} |S_2|^{t_2-1}\right)\right\} = E\left\{\Re\left(S_1 \cdot S_2^* |S_1|^{t_1-1} |S_2|^{t_2-1}\right)\right\} \\ &\leq E\left\{\Re\left(|S_1| \cdot |S_2| |S_1|^{t_1-1} |S_2|^{t_2-1}\right)\right\} = E\left\{\Re\left(|S_1|^{t_1} |S_2|^{t_2}\right)\right\} = E\left\{|S_1|^{t_1} |S_2|^{t_2}\right\} \end{aligned}$$

From the analysis in [156] and [167], it is easy to know that, when $t_1 < \alpha_1$ and $t_2 < \alpha_2$, no matter whether s_1 and s_2 are complex [156] or real, $E\left(|S_1|^{t_1} |S_2|^{t_2}\right) < \infty$ [167]. Therefore,

when $t_1 < \alpha_1/2$ and $t_2 < \alpha_2/2$, $\Re\{\Theta\}$ is bounded. Similarly, the imagery part of Θ is also bounded. Therefore, Θ is bounded.

(b) Now, we prove that N is bounded: $N = E(|S_1|^{2t_1})E(|S_2|^{2t_2})$ is bounded only if both $E(|S_1|^{2t_1})$ and $E(|S_2|^{2t_2})$ are bounded; when $t_1 < \alpha_1/2$ and $t_2 < \alpha_2/2$, then both $E(|S_1|^{2t_1})$ and $E(|S_2|^{2t_2})$ are bounded. Therefore, when $t_1 < \alpha_1/2$ and $t_2 < \alpha_2/2$, $N = E(|S_1|^{2t_1})E(|S_2|^{2t_2})$ is bounded.

CHAPTER 4: INTERFEROMETRIC SAR PHASE FILTERING IN THE WAVELET DOMAIN USING SIMULTANEOUS DETECTION AND ESTIMATION³

In this chapter, two interferometric SAR (InSAR) phase-filtering methods are proposed. These methods are performed in the wavelet domain and employ the simultaneous detection and estimation technique. In the wavelet domain, closed-form estimator and detector equations are derived, based upon a quadratic cost function, to minimize the combined risk of detection and estimation and, thus, the least square errors. Both methods occur within the wavelet domain; however, the first method employs the wavelet packet, while the second method is performed in the undecimated wavelet domain. A major characteristic of InSAR phase data is that the noise level is spatially variable, and the proposed methods have a particularly good comparative performance in these situations. Tests are performed using simulated phase data and show that the proposed methods have lower root-mean-square error and less noisy fringes in the filtering results than those of three existing “state-of-the-art” wavelet-domain phase-filtering methods. Tests using real InSAR data also demonstrate the superiority of the proposed methods in terms of visual and quantitative evaluation.

³ © 2011 IEEE. Reprinted, with permission, from [Yong Bian and Bryan Mercer, “Interferometric SAR phase filtering in the wavelet domain using simultaneous detection and estimation,” *IEEE Transactions on Geoscience and Remote Sensing*, vol. 49, no. 4, pp. 1396-1416, April 2011.].

4.1 Introduction

Synthetic aperture radar (SAR) is an active remote sensing technology which has been and is still widely studied due to its successful applications in many areas. One of these important applications is interferometry. In interferometric SAR (InSAR), the quality of the interferogram determines the accuracy of many final products. However, due to many decorrelation factors [130], the interferogram (and the associated interferometric phase) is usually corrupted by noise. This leads to errors in the extracted digital elevation model, which is one of the most important products of InSAR. Usually, phase filtering is performed prior to unwrapping, although sometimes, the filtering may not be required provided the phase-unwrapping methods have the capability to process noisy phase [210][211][212]. Therefore, many research efforts have been engaged with the filtering of the interferometric phase.

The interferometric-phase-filtering approaches in the literature can be generally classified into two groups. The first approach uses direct filtering without transformation and includes the methods in [213][141][214][150][215][216]. The second approach is transformation-domain filtering [217] [218] [219] [220]. Direct filtering has the advantage of using the phase quality directly to guide the filtering, such as the method in [141], which uses residues to direct the filtering, or the methods in [150] and [216], which employ coherence to achieve spatially adaptive filtering. Transformation-domain methods [217][218][219][220] mostly proceed through filtering in the wavelet domain. The advantage of wavelet-domain phase-filtering approaches is that the time-frequency analysis capability [221] of wavelet decomposition allows retention of some of the

specified frequency bands while filtering unfavorable frequency bands. This property has been widely used in image filtering.

For the InSAR phase denoising problem, the wavelet-domain method is promising because the phase information and noise can be more easily separated in the wavelet domain. The InSAR phase-filtering method in the wavelet domain was first proposed in [218]. Phase-noise modeling in the wavelet domain and a phase-filtering method using wavelet or wavelet packets were proposed in [217], which has been of great importance to subsequent work. Recently, wavelet-domain phase filtering employing Wiener filtering has been studied in [219]. These research efforts provide some very useful wavelet-domain phase-filtering methods; however, there are still many issues that need to be tackled. For example, the existing wavelet-domain phase-filtering methods need improvement when dealing with phase data from low-coherence interferometric sources.

In this chapter, we approach the InSAR phase-filtering problem in the wavelet domain and employ a more advanced method which incorporates simultaneous detection and estimation. A simultaneous detection and estimation technique was first applied in statistical communication [222] and later used in speech processing [223][224]. Since simultaneous detection and estimation considers the estimation problem under the uncertainty of signal appearance [222], this method may improve the accuracy of filtering in the wavelet domain. This is similar to the idea of simultaneous filtering and unwrapping [210][211][212] which performs the two tasks at the same time and may obtain improved or alternative performance. More importantly, it is suitable for estimation in the nonstationary noise environment, which has been proven to be a success in the speech enhancement [223]. Since the noise level of the interferometric phase is

spatially nonstationary and is determined by coherence [150], this method may have a robust phase-filtering performance. In the formulation developed here, an estimator and detector are derived under the assumption that the noisy wavelet coefficients are Gaussian distributed, and the clean coefficients are Laplacian distributed. Using this estimator and detector, two wavelet-domain phase-filtering methods are developed. The first method uses the wavelet packet, while the second method performs the filtering in the undecimated wavelet domain.

The major contributions of this chapter then are as follows:

- 1) We discuss the potential of using the method of simultaneous detection and estimation in the wavelet domain and apply it to InSAR phase filtering. The simultaneous detection and estimation technique is applied in the wavelet domain, and the estimator and detector are derived using a quadratic cost function under the assumption that the noisy wavelet coefficients are Gaussian distributed, and the clean coefficients are Laplacian distributed.

- 2) We investigate InSAR phase filtering in the undecimated wavelet domain, which has not been widely discussed before. In this paper, we propose two phase-filtering methods in the wavelet domain using the full scheme of strongly coupled simultaneous detection and estimation. The first method uses wavelet packets, while the second uses undecimated wavelets. The detailed implementations of these two methods are presented, and their performances are compared with each other and with other wavelet-based methods. The performances of the filtering in the wavelet-packet domain and in the undecimated wavelet domain are compared and discussed.

The organization of this chapter is as follows. In section 4.2, the InSAR phase-noise model and the concept of simultaneous detection and estimation in the wavelet domain are introduced. The InSAR phase-filtering method using the wavelet packet is discussed in Section 4.3. The InSAR phase-filtering method in the undecimated wavelet domain is presented in Section 4.4. In Section 4.5, the implementation issues of the two proposed methods are discussed. The experimental results of the simulated and real InSAR data are presented in Sections 4.6 and 4.7, respectively. The final section concludes this chapter.

4.2 Simultaneous Detection and Estimation for Phase Filtering in the Wavelet Domain

4.2.1 Model

The noise of the extracted interferometric phase angle is assumed to be additive [150]. From the modeling analysis of [217], we can say that the noise in the real and imaginary parts are additive and slightly signal dependent (can be approximately considered as signal independent as the arrangement in [217]). Since the filtering should be performed on the real and imaginary parts of the phase separately in order to maintain the phase jumps in the filtering result [127], the noise model should be developed for the real and imaginary parts instead of the phase angle or complex phase. The noise model of the real and imaginary parts of interferometric phase in the two-dimensional (2-D) wavelet domain can be formulated as [217]

$$DWT_{2D}\{\cos(\theta)\} = 2^j N_c \cos(\varphi) + U_c, \quad (4.1a)$$

$$DWT_{2D}\{\sin(\theta)\} = 2^j N_c \sin(\varphi) + U_s, \quad (4.1b)$$

where θ and φ represent the observed noisy phase in the spatial domain and the clean phase in the wavelet domain, respectively, U_c and U_s denote the signal-dependent noise in the wavelet domain of the real and imaginary parts, respectively, 2^j is the scale of wavelet, N_c is a parameter similar to coherence [202], and $DWT_{2D}\{x\}$ denotes the 2-D discrete wavelet transform of x . This formulation was derived based on the assumption that the wavelet is orthogonal and has ideal filtering response [217], although, for wavelet which does not satisfy this requirement, this model may be modified according to the specified filter banks used. For analysis purpose, this model is simple and meaningful.

It is well known that the noise standard deviation of the interferometric phase is different for different areas, and the local noise level is determined by the local coherence values [150] [7]. In the wavelet domain, the noise level of real and imaginary parts of the interferometric phase is spatially variable as well [217]. Since the simultaneous detection and estimation approach has been proven to be suitable for nonstationary noise filtering [223], in the following, we will examine whether this method can tackle the problem of spatially variant noise filtering, which is exactly the case of wavelet-domain phase filtering.

It is also well known that the signal energy in the wavelet domain is mostly carried by the largest few coefficients, and most of the small coefficients carry little or no signal energy [225]. However, this assumption does not hold when the noise level is large and spatially variable. In this situation, the small wavelet coefficients may carry signal energy, and some of the large coefficients may be contaminated by noise. If we include this as a special case, we can classify the wavelet coefficients into clean signal, noise-

contaminated signal, and noise only. In order to simplify the wavelet-domain phase filtering as a two-state signal detection and estimation problem, the clean signal and noisy signal can be combined as signal plus noise. Under this assumption, the phase-filtering problem can be formulated as a signal detection and estimation problem, which is to classify the wavelet coefficients into signal-plus-noise and noise-only components. This is similar to the technique proposed in [217]. The simultaneous detection and estimation problem of the real and imaginary parts can be formulated as follows:

$$\begin{aligned}
 H_1: \quad W_j^c(m, n) &= 2^j N_c(m, n) \cos(\varphi(m, n)) + U_c(m, n) \\
 &= S_c(m, n) + U_c(m, n) \\
 H_0: \quad W_j^c(m, n) &= U_c(m, n)
 \end{aligned} \tag{4.2a}$$

and

$$\begin{aligned}
 H_1: \quad W_j^s(m, n) &= 2^j N_c(m, n) \sin(\varphi(m, n)) + U_s(m, n) \\
 &= S_s(m, n) + U_s(m, n) \\
 H_0: \quad W_j^s(m, n) &= U_s(m, n)
 \end{aligned} \tag{4.2b}$$

where $W_j^c(m, n)$ and $W_j^s(m, n)$ denote the wavelet coefficients of the real and imaginary parts, respectively, H_1 and H_0 represent the signal-plus-noise and noise-only situations, respectively, and (m, n) are the spatial indices.

Therefore, the filtering process is to obtain the estimations of $S_c(m, n)$ and $S_s(m, n)$ from the observations of $W_j^c(m, n)$ and $W_j^s(m, n)$, respectively. The major difficulty of InSAR phase filtering is that, when the coherence level is very low (which means that the noise standard deviation is very high), some weak signals may be submerged in the noise

and are not easily detected. In this situation, a complex signal-estimation method is required. Since the filtering using simultaneous detection and estimation considers the uncertainty of signal appearance [222] during the estimation, it may have a good performance for the InSAR phase filtering when the coherence is low.

In order to simplify the symbols, the 2-D index, wavelet decomposition level, and symbols that represent real and imaginary parts are omitted in the following representations. In the remaining part of this chapter, the wavelet coefficients and other parameters are in 2-D, in different scale levels, and both for real and imaginary parts unless otherwise mentioned.

4.2.2 Simultaneous Detection and Estimation in the Wavelet Domain

The simultaneous detection and estimation technique was discussed in [226] under the assumption that the noise is Gaussian distributed, while the closed-form estimator and detector were discussed in [227] for the purpose of amplitude estimation. In [223], the closed-form estimator and detector were derived for the purpose of amplitude estimation and in the short-time Fourier transform domain. Research of simultaneous detection and estimation was mostly related to statistical communication and speech processing. Recently, one of the most important concepts of simultaneous detection and estimation (generalized likelihood ratio) has been applied in wavelet-domain filtering [228], [229]. However, to the best of our knowledge, there is no research that uses the full scheme of simultaneous detection and estimation in wavelet-domain filtering. In this section, we follow the scheme in [222] and [223] and derive a closed-form estimator and detector of simultaneous detection and estimation for the purpose of filtering in the 2-D wavelet domain.

Simultaneous detection and estimation method considers both the risk of detection and estimation [222], [226] and is designed to improve the estimation and detection performance by minimizing the combined risk of detection and estimation [222], [226], [230]. We define $C_{i,j}(S, \hat{S})$ as the cost function, where $i=0,1$ represent H_0 and H_1 , respectively, and where $j=0,1$ represent η_0 (the detection of noise) or η_1 (the detection of signal), respectively. Accordingly, $C_{1,0}$, $C_{1,1}$, $C_{0,1}$, and $C_{0,0}$ represent the cost of the detection under the following four situations: 1) false detection of noise while the truth is that it is signal; 2) the correct detection of signal; 3) the false detection of a signal while the truth is that it is a noise; 4) the correct detection of noise [223], [230]. The space of a specified variable is a range that includes all the possible values [231]. Because the noisy and clean wavelet coefficients may take the values from negative infinity to positive infinity, this means that the spaces of these coefficients also range from negative infinity to positive infinity; under this assumption, the combined average risk can be defined as [222], [223]

$$\begin{aligned}
 R_{SDE} = & \sum_{i=0}^1 \int_{-\infty}^{\infty} \int_{-\infty}^{\infty} C_{i,0}(S, \hat{S}) p(S) p(W|S) P(\eta_0|W) dS dW \\
 & + \sum_{i=0}^1 \int_{-\infty}^{\infty} \int_{-\infty}^{\infty} C_{i,1}(S, \hat{S}) p(S) p(W|S) P(\eta_1|W) dS dW
 \end{aligned} \tag{4.3}$$

where $p(S)$ is the probability density function (pdf) of the signal, which can be formulated as $p(S) = \delta(S)P(H_0) + p(S|H_1)P(H_1)$ [230] ($P(H_1)$ and $P(H_0)$ are the *a priori* probabilities of the signal and noise in each wavelet subband, respectively) under the assumption that $p(S|H_0) = \delta(S)$ ($\delta(S)$ is the Dirac delta function), $p(W|S)$ is the conditional pdf of the wavelet coefficients under the condition that a signal is given, and

$P(\eta_j | W)$ is the conditional probability of the detection of signal [230] ($P(\eta_1 | W)=1$) or noise ($P(\eta_0 | W)=1$) when the wavelet coefficients are known.

4.2.3 Estimator in the Wavelet Domain

From [222] and [223], in order to obtain an estimator which minimizes the Bayes risk R_{SDE} during the simultaneous detection and estimation process, we need to solve the minimization problem $\arg \min_{\hat{S}_j} \{\chi_{0j}(W) + \chi_{1j}(W)\}$, where [223]

$$\chi_{0j}(W) = P(H_0) \int_{-\infty}^{\infty} C_{0,j}(S, \hat{S}) p(S | H_0) p(W | S) dS \quad (4.4a)$$

$$\chi_{1j}(W) = P(H_1) \int_{-\infty}^{\infty} C_{1,j}(S, \hat{S}) p(S | H_1) p(W | S) dS \quad (4.4b)$$

and where $\chi_{0j}(W)$ and $\chi_{1j}(W)$ represent the risk of the signal being absent or present, respectively (see section 4.2.4 below).

For the filtering problem using strongly coupled simultaneous detection and estimation [222], the estimation is first performed; then, the detection is performed using the output of the estimation. After detection, the input data are classified into signal and noise. Finally, the filtering result is obtained using both the results of estimation and classification. Therefore, the final filtering result depends both on the output of the estimator and the decision of the detector [223]. In the following, we will derive the estimator and detector based upon the same statistical model.

In order to obtain the closed form-estimator and detector, an appropriate cost function must be defined, which is one of the most important issues in the simultaneous detection and estimation. There are many cost functions which can be found in [222] and [231]. In this chapter, we use a quadratic cost function [222], [223] similar to [223]

$$\begin{cases} C_{0,j}(S, \hat{S}) = \kappa_{0j} (\hat{S}_j - W\rho)^2 \\ C_{1,j}(S, \hat{S}) = \kappa_{1j} (\hat{S}_j - S)^2 \end{cases} \quad (4.5)$$

where ρ is a small-value parameter; κ_{10} , κ_{11} , κ_{01} , and κ_{00} are the weight parameters for the cost $C_{1,0}$, $C_{1,1}$, $C_{0,1}$, and $C_{0,0}$, respectively, (see Section 4.6.2 hereafter). Using the quadratic cost function in (4.5) and simplifying the results using the assumption that $p(S | H_0) = \delta(S)$, the estimation of clean wavelet coefficients can be further formulated as

$$\begin{aligned} \hat{W}_j &= \arg \min_S (\chi_{0j}(W) + \chi_{1j}(W)) \\ &= \arg \min_S \left\{ \kappa_{0j} (\hat{S}_j - W\rho)^2 P(H_0) p(W | H_0) \right. \\ &\quad \left. + \kappa_{1j} P(H_1) \int_{-\infty}^{\infty} (\hat{S}_j - S)^2 p(S | H_1) p(W | S) dS \right\} \end{aligned} \quad (4.6)$$

In order to obtain a closed-form estimator and detector, the following conditional pdfs must be defined in terms of the statistical characteristics [231] of the wavelet coefficients. In [232], the wavelet coefficients of clean and noisy phase are modeled, respectively, as a generalized gamma model and as a Gaussian model. In this paper, we assume the clean wavelet coefficients to follow a Laplacian distribution because 1) this is a heavy-tailed distribution and 2) it is easy to obtain a closed-form solution. Therefore, in order to simplify the analysis, we assume that the noisy wavelet coefficients are Gaussian distributed and that the clean wavelet coefficients are Laplacian distributed. Following [259], we then define the following conditional pdfs:

$$p(W | S) = \frac{1}{\sqrt{2\pi}\sigma_U} \exp\left(-\frac{(W-S)^2}{2\sigma_U^2}\right) \quad (4.7a)$$

$$p(S | H_1) = \frac{1}{\sqrt{2}\sigma_S} \exp\left(-\frac{\sqrt{2}|S|}{\sigma_S}\right) \quad (4.7b)$$

$$p(W | H_1) = \frac{1}{\sqrt{2}\sigma_W} \exp\left(-\frac{\sqrt{2}|W|}{\sigma_W}\right) \quad (4.7c)$$

$$p(W | H_0) = \frac{1}{\sqrt{2\pi}\sigma_U} \exp\left(-\frac{W^2}{2\sigma_U^2}\right) \quad (4.7d)$$

where σ_U , σ_S , and σ_W are the standard deviations of the noise, clean coefficients, and noisy coefficients, respectively, and $\sigma_W^2 = \sigma_S^2 + \sigma_U^2$ since we assume that the signal and noise are independent. For the image-filtering method in the wavelet domain, σ_U can be estimated using the widely used method of [225] and [233], which is

$$\hat{\sigma}_U = \text{Med}(|W_{HH1}| - \text{Med}(W_{HH1})) / 0.6745 \quad (4.8)$$

where W_{HH1} represents the wavelet coefficients in the first level HH wavelet subband; “ $\text{Med}(x)$ ” means to obtain the median value of x . This estimator is based on the median absolute deviation [234], [235] and is developed under the assumption that the noise standard deviation is spatially invariant, which is not the case for InSAR phase noise. In the proposed phase-filtering methods, this parameter should be adjusted to obtain a better filtering performance. This modification should be applied according to some factors, such as the level of spatial coherence variability and fringe densities of the phase data, which will be discussed in the following part of this chapter.

Substituting (4.7) into (4.6) and solving this minimization problem by letting

$\frac{\partial}{\partial \hat{S}} \{\chi_{0j}(W) + \chi_{1j}(W)\} = 0$ [223], we have the estimator as follows:

$$\hat{S}_j = \frac{\kappa_{1j}\Lambda(W)B + \kappa_{0j}W\rho}{\kappa_{1j}\Lambda(W)A + \kappa_{0j}} \quad (4.9)$$

where

$$A = \frac{1}{p(W | H_1)} \int_{-\infty}^{\infty} p(S | H_1) p(W | S) dS \quad (4.10a)$$

$$B = \frac{1}{p(W | H_1)} \int_{-\infty}^{\infty} S p(S | H_1) p(W | S) dS \quad (4.10b)$$

and $\Lambda(W)$ is the generalized likelihood ratio [222]. Using (4.7c) and (4.7d), $\Lambda(W)$ can be represented as

$$\Lambda(W) = \frac{p(W | H_1) P(H_1)}{p(W | H_0) P(H_0)} = \frac{\sqrt{\pi} \sigma_U P(H_1)}{\sigma_W P(H_0)} \exp\left(\frac{W^2}{2\sigma_U^2} - \frac{\sqrt{2}|W|}{\sigma_W}\right) \quad (4.11)$$

where $P(H_1)$ and $P(H_0)$ can be defined by the user according to the probability of signal appearance of each subband which is determined by the fringe densities of the input phase data. In the proposed phase-filtering methods, we use the same $P(H_1)$ and $P(H_0)$ values for all the subbands.

In order to obtain the closed-form estimator of the signal, the integration of (4.10a) and (4.10b) needs to be solved. Following [259], after solving the integration of (4.10a) and (4.10b) (for the detailed derivation of (4.12a) and (4.12b), see Appendix A), we have

$$A = \frac{\sigma_W}{2\sigma_S} \exp\left(\frac{\sqrt{2}|W|}{\sigma_W} - \frac{W^2}{2\sigma_U^2}\right) \left[\exp(\psi^2) \operatorname{erfc}(\psi) + \exp(\xi^2) \operatorname{erfc}(\xi) \right] \quad (4.12a)$$

$$B = \frac{\sigma_U \sigma_W}{\sqrt{2}\sigma_S} \exp\left(\frac{\sqrt{2}|W|}{\sigma_W} - \frac{W^2}{2\sigma_U^2}\right) \left[\exp(\psi^2) \operatorname{erfc}(\psi) - \exp(\xi^2) \xi \operatorname{erfc}(\xi) \right]. \quad (4.12b)$$

where $\psi = \frac{\sigma_U}{\sigma_S} + \frac{W}{\sqrt{2}\sigma_U}$, $\xi = \frac{\sigma_U}{\sigma_S} - \frac{W}{\sqrt{2}\sigma_U}$, and $\operatorname{erfc}(x) = \frac{2}{\sqrt{\pi}} \int_x^{\infty} \exp(-t^2) dt$ [237] is the

complementary error function which will be also used in the following equations.

Substituting (4.12a) and (4.12b) into (4.9), we obtain the closed-form estimator as (4.13):

$$\hat{S}_j = \frac{\frac{\kappa_{1j}\sigma_U\sigma_W\Lambda(W)}{\sqrt{2}\sigma_S} \exp\left(\frac{\sqrt{2}|W|}{\sigma_W} - \frac{W^2}{2\sigma_U^2}\right) \left[\exp(\psi^2) \operatorname{erfc}(\psi) - \exp(\xi^2) \xi \operatorname{erfc}(\xi) \right] + \kappa_{0j}W\rho}{\frac{\kappa_{1j}\sigma_W\Lambda(W)}{2\sigma_S} \exp\left(\frac{\sqrt{2}|W|}{\sigma_W} - \frac{W^2}{2\sigma_U^2}\right) \left[\exp(\psi^2) \operatorname{erfc}(\psi) + \exp(\xi^2) \operatorname{erfc}(\xi) \right] + \kappa_{0j}} \quad (4.13)$$

where $j=0,1$. This is the estimator using the quadratic cost function under the assumption that the noisy wavelet coefficients are Gaussian distributed, and the clean wavelet coefficients are Laplacian distributed in each wavelet subband. Similar to the analysis in [223], the major difference between \hat{S}_0 and \hat{S}_1 is in the parameters κ_{1j} and κ_{0j} . \hat{S}_0 and \hat{S}_1 are determined by σ_U , σ_S , σ_W , $\Lambda(W)$, κ_{1j} , κ_{0j} , and ρ . σ_U , σ_S , σ_W , and $\Lambda(W)$ can be estimated using the observed wavelet coefficients. κ_{1j} , κ_{0j} , and ρ are the user-defined parameters. Since this estimator incorporates both the knowledge of the likelihood of signal appearance ($\Lambda(W)$) and the local statistics of wavelet coefficients (σ_U , σ_S , σ_W), we refer to it as an advanced estimator.

The filtering performance can be adjusted by selecting the user-defined parameters κ_{1j} , κ_{0j} , and ρ . By selecting appropriate parameters, we can obtain a filter with desired performance. In wavelet-domain InSAR phase filtering, it is preferable to obtain a soft method in order to reduce the artifacts in the filtering result [217], [218], [225], [233], [236], which means that the wavelet coefficients are only shrunk but not totally eliminated when they are detected as noise. In order to obtain a soft method, when a wavelet coefficient is detected as $\eta_0=1$, it should not be killed but rather suppressed. Based on the analysis in [223], in order to obtain a soft method, κ_{01} should not be too large.

4.2.4 Detection in the Wavelet Domain

In the proposed phase-filtering method, we use strongly coupled simultaneous detection and estimation [222] in which the detection depends upon the result of estimation [223].

Introducing (4.7a) and (4.7b) into (4.4a) and solving its integral, the risk when the signal is not present can be formulated as

$$\begin{aligned}\chi_{0j}(W) &= P(H_0) \int_{-\infty}^{\infty} \kappa_{0j} (\hat{S}_j - W\rho)^2 p(S|H_0) p(W|S) dS \\ &= \frac{\kappa_{0j} P(H_0) (\hat{S}_j - W\rho)^2}{\sqrt{2\pi}\sigma_U} \exp\left(-\frac{W^2}{2\sigma_U^2}\right)\end{aligned}\quad (4.14a)$$

Following [259], substituting (4.7a) and (4.7b) into (4.4b), the risk when the signal is present can be written as (see Appendix B for the detailed derivation of (4.14b))

$$\begin{aligned}\chi_{1j}(W) &= P(H_1) \int_{-\infty}^{\infty} \kappa_{1j} (\hat{S}_j - S)^2 p(S|H_1) p(W|S) dS \\ &= \frac{\kappa_{1j} P(H_1)}{\sigma_S} \exp\left(-\frac{W^2}{2\sigma_U^2}\right) \left\{ \sigma_U^2 \Gamma(3) 2^{-\frac{5}{2}} \left[\frac{1}{\Gamma(2)} \Phi\left(\frac{3}{2}, \frac{1}{2}; \psi^2\right) - \frac{2\psi}{\Gamma(1.5)} \Phi\left(2, \frac{3}{2}; \psi^2\right) + \frac{1}{\Gamma(2)} \Phi\left(\frac{3}{2}, \frac{1}{2}; \xi^2\right) - \frac{2\xi}{\Gamma(1.5)} \Phi\left(2, \frac{3}{2}; \xi^2\right) \right] \right. \\ &\quad \left. + \hat{S}_j \sigma_U \left[\exp(\xi^2) \xi \operatorname{erfc}(\xi) - \exp(\psi^2) \psi \operatorname{erfc}(\psi) \right] + \frac{\hat{S}_j^2}{2\sqrt{2}} \exp(\psi^2) \operatorname{erfc}(\psi) + \frac{\hat{S}_j^2}{2\sqrt{2}} \exp(\xi^2) \operatorname{erfc}(\xi) \right\}\end{aligned}\quad (4.14b)$$

where $\Gamma(x)$ is the gamma function defined as $\Gamma(x) = \int_0^{\infty} \exp(-t) t^{x-1} dt$ [237]. In (4.14b) (and in the remaining part of this chapter), $\Phi(\alpha, \gamma; z)$ is the confluent hypergeometric function, which is a very complex function to calculate. A detailed discussion on calculating $\Phi(\alpha, \gamma; z)$ will be given in Section 4.5.

The optimum detection rule can be derived, according to [223], [230], and [231], by minimizing the combined risk in (4.3). This detection rule, in the two circumstances of $\eta_0 = 1$ (the detection of noise only) or $\eta_1 = 1$ (the detection of signal plus noise), is shown

in (4.15) [223], [230], [231]

$$\chi_{00}(W) + \chi_{10}(W) \underset{\eta_0=1}{\overset{\eta_1=1}{\geq}} \chi_{01}(W) + \chi_{11}(W). \quad (4.15)$$

Following [259], substituting (4.14a) and (4.14b) into (4.15) and after some simplification arrangements, we arrive at the closed-form decision rule as follows:

a) The detector decides $\eta_1 = 1$ when

$$M_l \geq M_r. \quad (4.16a)$$

b) The detector decides $\eta_0 = 1$ when

$$M_l < M_r. \quad (4.16b)$$

In (4.16a) and (4.16b), we have

$$M_l = \frac{P(H_1)\sigma_U^2\Gamma(3)(\kappa_{10} - \kappa_{11})}{\sigma_S} 2^{-\frac{5}{2}} \left[\frac{1}{\Gamma(2)} \Phi\left(\frac{3}{2}, \frac{1}{2}; \psi^2\right) - \frac{2\psi}{\Gamma(1.5)} \Phi\left(2, \frac{3}{2}; \psi^2\right) + \frac{1}{\Gamma(2)} \Phi\left(\frac{3}{2}, \frac{1}{2}; \xi^2\right) - \frac{2\xi}{\Gamma(1.5)} \Phi\left(2, \frac{3}{2}; \xi^2\right) \right] \\ + \frac{P(H_1)}{\sigma_S} \left\{ (\kappa_{10}\hat{S}_0 - \kappa_{11}\hat{S}_1)\sigma_U \left[\exp(\xi^2) \xi \operatorname{erfc}(\xi) - \exp(\psi^2) \psi \operatorname{erfc}(\psi) \right] + \frac{\kappa_{10}\hat{S}_0^2 - \kappa_{11}\hat{S}_1^2}{2\sqrt{2}} \exp(\psi^2) \operatorname{erfc}(\psi) + \frac{\kappa_{10}\hat{S}_0^2 - \kappa_{11}\hat{S}_1^2}{2\sqrt{2}} \exp(\xi^2) \operatorname{erfc}(\xi) \right\} \quad (4.17a)$$

$$M_r = \frac{P(H_0)}{\sqrt{2\pi}\sigma_U} \left[\kappa_{01}(\hat{S}_1 - W\rho)^2 - \kappa_{00}(\hat{S}_0 - W\rho)^2 \right]. \quad (4.17b)$$

This detection rule uses standard deviations (σ_W , σ_U , and σ_S) as the local statistical parameters similar to [226]. However, since different statistical models are used, the detector is different from that in [226].

Similar to the method in [223], for the proposed InSAR phase-filtering methods, when a wavelet coefficient is detected as noise, it is shrunk instead of killed. This is because the signal coefficients may be detected as noise, and if we eliminate these coefficients, large amount of errors will result. Therefore, we expect both the proposed

methods to act as soft wavelet-domain filtering methods.

4.2.5 Summary of the Proposed Simultaneous Detection and Estimation Algorithm

As mentioned before, for the wavelet-domain phase-filtering methods using strongly coupled simultaneous detection and estimation, the estimation is first computed; then, the detection is performed using the estimated result. The final filtering result is based on both the results of estimation and detection. No matter which of the wavelet packet or wavelet decomposition is used, the proposed algorithms are performed following similar steps as follows.

- 1) The data are transformed into the wavelet domain.
- 2) In the wavelet domain, the estimator is computed for each coefficient using (4.13).
- 3) The detector is implemented from (4.17a) and (4.17b) using the estimator output.
- 4) The detector result is then used to classify the wavelet coefficients as signal or noise (using (4.16a) and (4.16b)).

5) If a coefficient is classified as signal, the value of \hat{S}_1 is used as the filtering result. Otherwise, \hat{S}_0 is used as the filtering result. Therefore, the two proposed methods are a soft wavelet-domain filtering method.

- 6) The filtered data are transformed back to the spatial domain.

In the following, we present the two methods to implement the InSAR phase filtering.

4.3 Phase Filtering Using Wavelet Packet and Simultaneous Detection and Estimation

4.3.1 Simultaneous Detection and Estimation Using Wavelet Packet

The first method is phase filtering using wavelet packet and simultaneous detection and estimation (PFWPSDE), which performs the phase filtering in the full tree of wavelet-packet decomposition, and the filtering in each node uses the full scheme of simultaneous detection and estimation filtering introduced in Section 4.2.

Wavelet packets, since their introduction in [238], have been widely used in image compression and filtering. Wavelet packets, unlike wavelet transforms, not only decompose the approximation coefficients but also the detail coefficients when further level of decomposition is performed [239][240][241]. This gives the wavelet-packet method an advantage in suppressing the noise in high-frequency signals [242]. Since wavelet-packet methodology has stronger frequency-selection capability than wavelet transforms [243], [244], it has the ability to perform the filtering for the frequency bands of any interesting frequency ranges. This is a benefit for InSAR phase filtering since the phase information of different fringe densities is described in different frequency bands.

Since phase information (after flat-Earth removal [7]) of InSAR data is mostly of lower spatial frequencies and the noise is in higher frequencies, most of the phase information is concentrated in the low-frequency nodes of the wavelet-packet decomposition [217]. Moreover, how much phase information the other nodes contain depends on the densities of the phase fringes. If the phase shows very sparse fringes, then the phase information is mostly in the low-frequency nodes. As the fringe density

increases, phase information will also be found in the higher frequency nodes: If the phase contains the low and moderate density fringes, then the phase information is mostly in the low- and middle-frequency nodes. If the phase contains the low, moderate, and high density fringes, then the low-, middle-, and even high-frequency nodes may contain phase information.

In the PFWPSDE method, based on the analysis in [127], the real and imaginary parts need to be filtered separately but to the same degree. However, in order to preserve the low-frequency phase information, the node of the lowest frequency is not filtered since it contains most of the phase information [217], [218]. For the same decomposition level, more nodes may be decomposed using the full tree of the wavelet packet than the subbands of the wavelet method. Therefore, a wider range of frequency information can be separated from the noise using the wavelet packet than using the wavelet transform. This is a major advantage of the phase-filtering method using wavelet-packet methods.

For example, when the interferometric phase contains densely populated fringes, the high-frequency nodes (or subbands) contain part of the signal energy. The wavelet-transform method may eliminate part of the high-frequency phase fringes (high-frequency signal) because the signal has similar characteristic as noise in the high-frequency subband. The wavelet packet can partly solve this problem because the high resolution in the high-frequency nodes provides strong signal and noise separation ability.

4.3.2 Processing Steps

The flowchart of the PFWPSDE algorithm is shown in Figure 4.1. In Figure 4.1, the square box plotted using the dashed lines denotes the module of the full scheme of simultaneous detection and estimation, which is the key procedure in the proposed

method. In Figure 4.1, the dotted and solid lines denote the parameter flow and data flow, respectively. The proposed PFWPSDE method is performed using the following steps:

1) Estimate the Noise Standard Deviation: Since the estimator and detector both require the parameters of local statistics and the calculation of σ_S needs the value of σ_U , the noise standard deviation σ_U needs to be estimated first. In the PFWPSDE method, the noise standard deviation is calculated in the wavelet domain (using the discrete wavelet transform (DWT) [244]). Therefore, we first transform the original data into the wavelet domain using the specified type of wavelet. The type of wavelet used in estimating the noise standard deviation should be the same as that used in the later wavelet-packet decomposition. Since we use all the nodes of the full tree [241], [243] except the node of the lowest frequency to do the filtering, it means that the algorithm conducts the filtering at the nodes of the same decomposition level. Since, in the PFWPSDE method, the noise standard deviations are the same for all the nodes in the same decomposition level [217], the same σ_U is used for all the nodes to be filtered. In the following part of this paper, we refer to the nodes to be filtered in the algorithm as the “filtering nodes”.

As noted earlier, when σ_U is estimated, the method of [225] needs to be modified since the noise standard deviation in interferometric phase is spatially variable. In the PFWPSDE method, we modify the method in [225] by considering the special requirements of InSAR phase filtering, which is implemented by introducing a scaling parameter, as shown in the following:

$$\sigma_U = \lambda \hat{\sigma}_{U,ave}, \quad (4.18)$$

where λ is an operator-set scaling parameter that reflects the scene-wide magnitude of

the noise, $\hat{\sigma}_{U.ave}$ is the average of the noise standard deviations of the real ($\hat{\sigma}_{U.real}$) and imaginary ($\hat{\sigma}_{U.imag}$) parts, which, since they are approximately equal, reduces to

$$\hat{\sigma}_{U.ave} = (\hat{\sigma}_{U.real} + \hat{\sigma}_{U.imag})/2. \quad (4.19)$$

In order to maintain the phase jumps in the filtered phase, the real and imaginary parts must perform the same degree of filtering; therefore, we use the same noise standard deviation for the filtering of the real and imaginary parts.

The estimation of the noise standard deviation in the PFWPSDE method is implemented employing the following substeps: First, the real and imaginary parts are decomposed using the wavelet transform. Second, the noise standard deviation of real ($\hat{\sigma}_{U.real}$) and imaginary ($\hat{\sigma}_{U.imag}$) parts are estimated using (4.8). Third, $\hat{\sigma}_{U.ave}$ is calculated using (4.19). Finally, σ_U is calculated using (4.18).

In the PFWPSDE method, the same σ_U is used for all the filtering nodes. This is unlike σ_W and σ_S , which are estimated in every filtering node using a moving square window.

2) *Wavelet-Packet Transform*: The real and imaginary parts of the original phase data are transformed into the wavelet packet-domain (using the discrete wavelet-packet transform (DWPT) [260]). After the wavelet-packet decomposition, many nodes are generated. In the subsequent filtering, all the nodes in the full tree except the node of the lowest frequency are filtered.

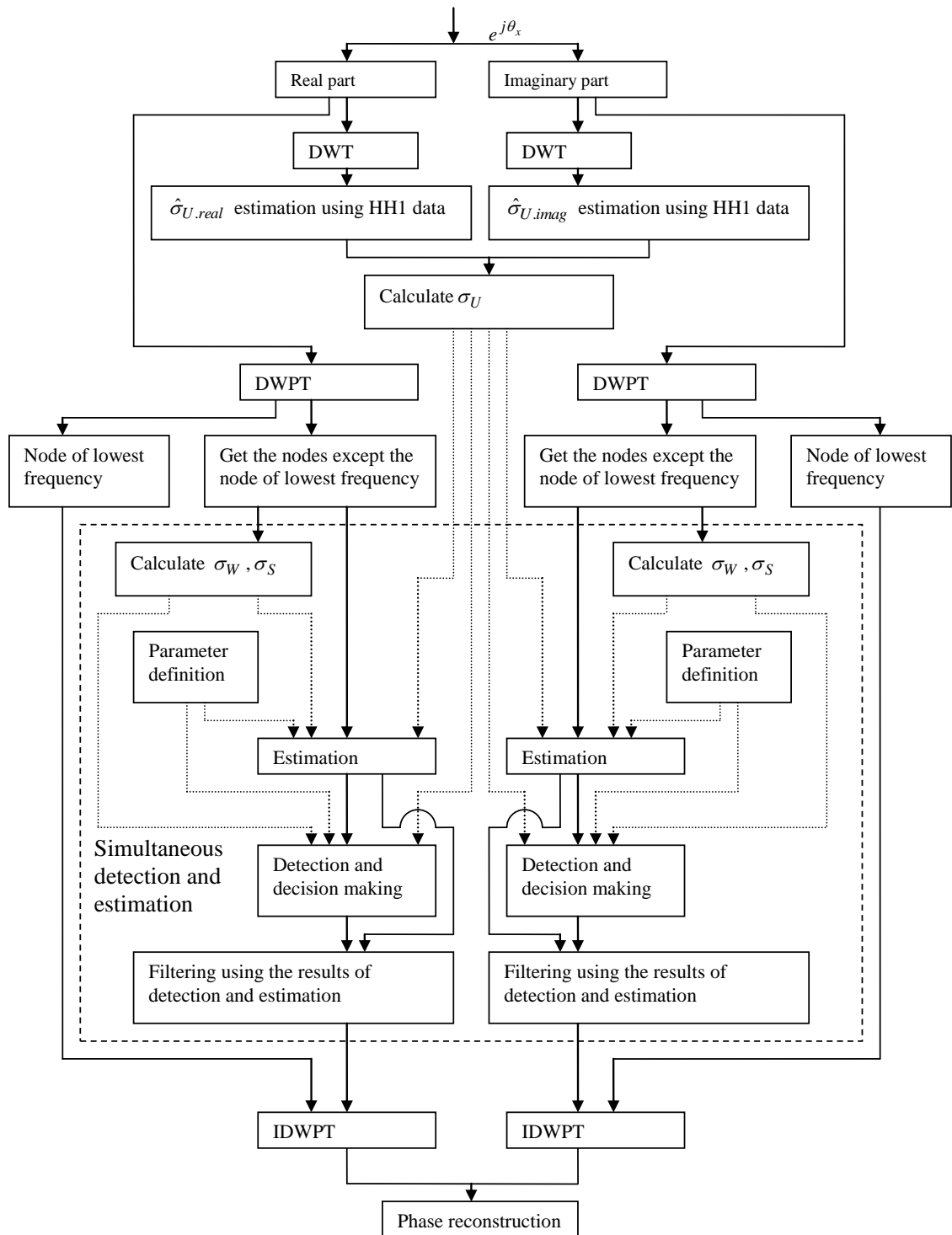


Figure 4.1. Flowchart of the proposed PFWPSDE method. The dotted lines denote the parameter flow, while the solid lines describe the data flow.

Note: The following step 3) to step 6) are the steps that conduct the full scheme of simultaneous detection and estimation, which are performed in the real and imaginary parts and in all the nodes of the full tree except the node of lowest frequency. In PFWPSDE method, the estimation and detection are performed in every wavelet coefficient of the filtering node.

3) *Parameter Estimation or Calculation in Each Node:* In this step, we estimate the parameters for all the nodes except the node of the lowest frequency. In the wavelet-packet decomposition, for every coefficient of the filtering nodes, σ_W and σ_S are estimated using the input wavelet coefficients. First, the standard deviation of noisy coefficients σ_W is estimated using a moving window as the method in [219], which is

$$\sigma_W = \sqrt{\frac{1}{MN} \sum_{m=0}^{M-1} \sum_{n=0}^{N-1} (W^2(m,n) - \bar{W}^2)} \quad (4.20)$$

where \bar{W} is the mean value in a $M \times N$ moving window.

After obtaining the values of σ_U and σ_W , the signal standard deviation σ_S is calculated using the relation

$$\sigma_S = \sqrt{\max(\sigma_W^2 - \sigma_U^2, 0)} \quad (4.21)$$

where the “max” operation is to make sure that the value of σ_S is not less than zero.

The parameter $\Lambda(W)$ also needs to be calculated using (4.11). In (4.11), $P(H_1)$ and $P(H_0)$ can be defined by the user. The same $P(H_1)$ and $P(H_0)$ values are used for all the filtering nodes.

4) *Estimation:* In each filtering node, we use the estimated parameters (σ_U , σ_W , σ_S) and the user-defined parameters κ_{1j} , κ_{0j} , and ρ to estimate the coefficients (\hat{S}_0 and \hat{S}_1)

using equation (4.13). The estimated results of \hat{S}_0 and \hat{S}_1 will be used for the following detection step (step 5) and the filtering step (step 6).

5) *Detection and Decision Making*: The purpose of detection and decision making is to classify the coefficients in each filtering node into signal or noise. In this step, first, M_l and M_r are calculated using (4.17a) and (4.17b), respectively (the implementation of calculating M_l and M_r will be discussed in Section 4.5.1). The estimated parameters (σ_U , σ_W , σ_S) and the user-defined parameters κ_{1j} , κ_{0j} , and ρ are used in this calculation. More importantly, the estimation results of step 4) are used in calculating (4.17a) and (4.17b). After M_l and M_r are calculated, we use the decision rule in (4.16a) and (4.16b) to classify all wavelet coefficients of each filtering node into signal or noise.

6) *Filtering Using the Results of Detection and Estimation*: After decision making, the wavelet coefficients of each filtering node are classified as signal or noise. If a coefficient is classified as signal, the value of \hat{S}_1 is assigned as the filtering result; otherwise, \hat{S}_0 is assigned as the filtering result.

7) *Inverse Discrete Wavelet-Packet Transform*: In this step, the filtered nodes and the unfiltered node of the lowest frequency are used as the input to the inverse wavelet-packet transform (IDWPT) [260] to reconstruct the phase of real and imaginary parts.

8) *Phase Reconstruction*: In this step, the filtered phase is retrieved using the filtered real and imaginary parts, given by

$$\hat{\theta} = \arctan(\hat{\theta}_{imag} / \hat{\theta}_{real}) \quad (4.22)$$

where $\hat{\theta}_{imag}$ and $\hat{\theta}_{real}$ are the filtered real and imaginary parts, respectively.

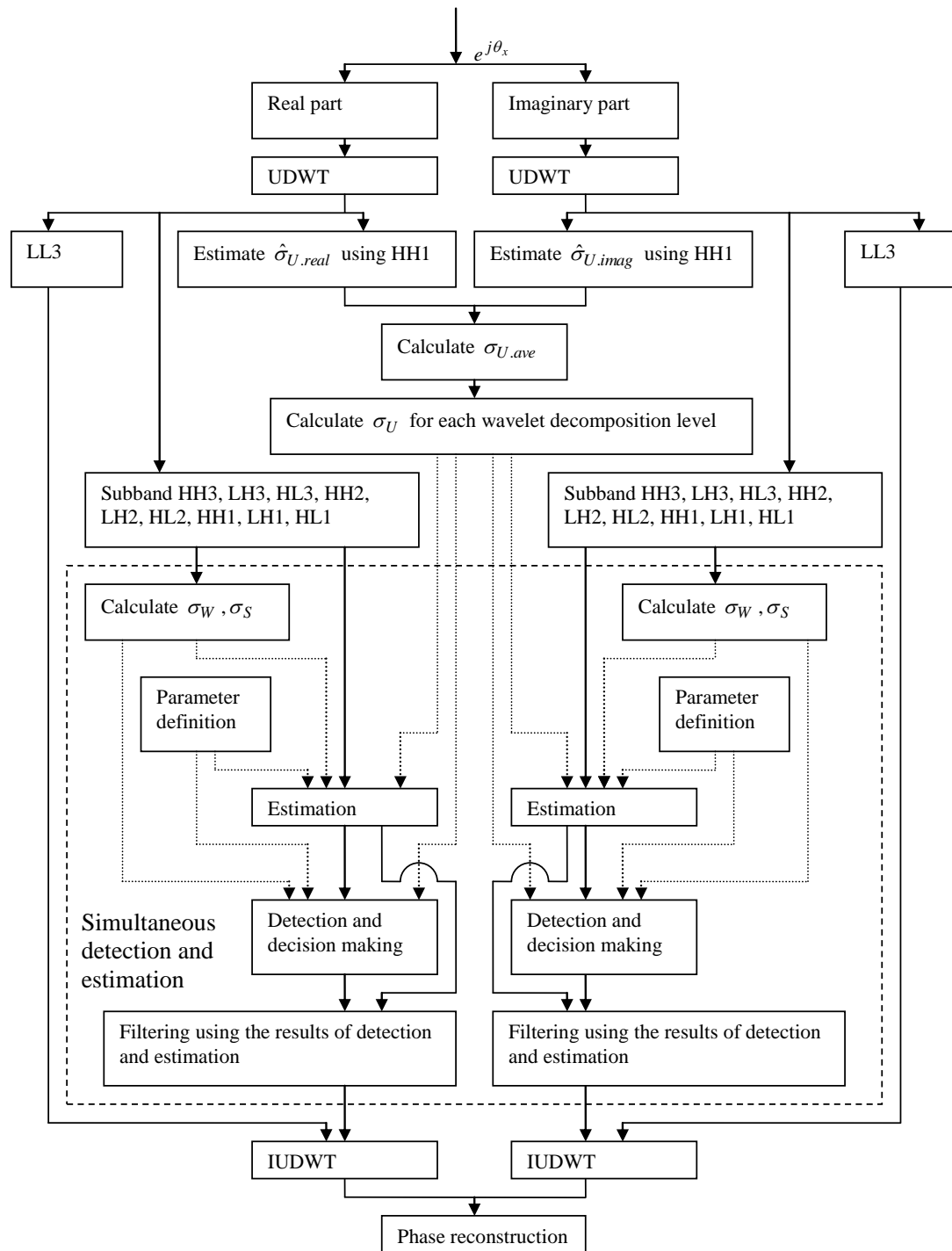


Figure 4.2. Flowchart of the proposed PFUWSDE method. The dotted lines denote the parameter flow, while the solid lines describe the data flow.

4.4 Phase Filtering in the Undecimated Wavelet Domain Using Simultaneous Detection and Estimation

4.4.1 Detection and Estimation in the Undecimated Wavelet Domain

It is well known that filtering in the undecimated wavelet domain reduces artifacts in the results due to redundancy [245], [246], [247]. However, to the best of our knowledge, none of the state-of-the-art InSAR phase-filtering methods is conducted in the undecimated wavelet domain. In this chapter, we propose a phase-filtering method which performs filtering in this domain while employing the full scheme of simultaneous detection and estimation introduced in Section 4.2. We refer to this as phase filtering in the undecimated wavelet domain using simultaneous detection and estimation (PFUWSDE). In the PFUWSDE method, the undecimated wavelet transform is achieved through use of the “a trous” method [248]. The flowchart of the proposed PFUWSDE method is shown in Figure 4.2. In Figure 4.2, the square box plotted using the dashed lines denotes the module of the full scheme of simultaneous detection and estimation. In Figure 4.2, the dotted and solid lines denote the parameter flow and data flow, respectively. In this algorithm, the real and imaginary parts are filtered separately as well.

4.4.2 Processing Steps

The processing steps of the PFUWSDE method are as follows:

1) *Wavelet Transform*: In this step, the real and imaginary parts of the InSAR phase data are transformed into the undecimated wavelet domain (using the undecimated discrete wavelet transform (UDWT) [248]). Using the three-level (three-scale)

decomposition as an example, after wavelet decomposition, the detail coefficients of first (HH1, HL1, LH1), second (HH2, HL2, LH2), and third level (HH3, HL3, LH3) are obtained, and the approximation coefficients of the third level (LL3) are computed. All the detail coefficients will be filtered (the “filtering subband”), while the approximation coefficients will not be filtered but will be saved in memory and used in the reconstruction.

2) *Parameter Estimation*: For the PFUWSDE method, the filtering happens at different decomposition levels. For the subbands of different decomposition levels, the noise standard deviation may be different depending on the type of filter banks used [249]. For most types of wavelets, the greater the decomposition level is, the lower is the noise standard deviation. Therefore, the noise standard deviation for different levels of decomposition should be calculated separately. Although there are methods in estimating the noise variances for different levels in the undecimated wavelet domain, such as the method in [229] and [249], these methods are designed for the filtering of images and are for the estimation of spatially invariant noise. Since the noise level of the interferometric phase is spatially variable, in order to filter the phase noise thoroughly, in the PFUWSDE method, we use a modified noise standard-deviation estimation method based on the method in [229] and [249] as

$$\sigma_{U_j}^{LH} = \sigma_{U_j}^{HL} = \lambda_j \hat{\sigma}_{U.ave} \sqrt{\left(\sum_{k_1} g_{k_1}^2 \right) \left(\sum_{k_2} h_{k_2}^2 \right)^{2j-1}} \quad (4.23a)$$

$$\sigma_{U_j}^{HH} = \lambda_j \hat{\sigma}_{U.ave} \sqrt{\left(\sum_{k_1} g_{k_1}^2 \right)^2 \left(\sum_{k_2} h_{k_2}^2 \right)^{2(j-1)}} \quad (4.23b)$$

where j is the level of decomposition, σ_{Uj}^{LH} , σ_{Uj}^{HL} , and σ_{Uj}^{HH} are the noise standard deviation in LH, HL, and HH subbands, respectively, λ_j is a scaling parameter similar to that of (4.18), g and h are the high-pass and low-pass filter coefficients of wavelet decomposition, respectively, and $\hat{\sigma}_{U.ave}$ is the average noise standard deviation of the real ($\hat{\sigma}_{U.real}$) and imaginary ($\hat{\sigma}_{U.imag}$) parts, which is calculated using (4.19). The scaling parameter (mostly taking values between 1.0 and 2.0) can be selected in terms of the level of phase-noise variation and the fringe density. Also, we can improve the value of σ_U if we want to suppress more noise in the phase.

There are three substeps when σ_{Uj}^{LH} , σ_{Uj}^{HL} , and σ_{Uj}^{HH} are calculated: First, the noise standard deviations of the real ($\hat{\sigma}_{U.real}$) and imaginary ($\hat{\sigma}_{U.imag}$) parts are calculated using the HH1 subbands of the real and imaginary parts (i.e. using (4.8)), respectively. Second, $\hat{\sigma}_{U.ave}$ is calculated using (4.19). Third, σ_{Uj}^{LH} , σ_{Uj}^{HL} , and σ_{Uj}^{HH} are calculated using (4.23a) and (4.23b).

In the PFUWSDE method, for each filtering subband, σ_W , σ_S , and $\Lambda(W)$ are estimated or calculated using the same method as that in PFWPSDE (i.e. by using (4.20), (4.21), and (4.11)). The same $P(H_1)$ and $P(H_0)$ values are used for all the filtering subbands.

3) *Simultaneous Detection and Estimation*: This step is performed for all the filtering subbands and for the real and imaginary parts. We use a three-level decomposition as an example. In this step, the algorithm conducts the filtering in the third-level detail coefficients (HH3, HL3, LH3), second-level detail coefficients (HH2, HL2, LH2), and

first level-detail coefficients (HH1, HL1, LH1). For each decomposition level, the different $\sigma_{U_j}^{LH}$, $\sigma_{U_j}^{HL}$, and $\sigma_{U_j}^{HH}$ (which are calculated using (4.23a) and (4.23b)) are used. The detailed processing steps of simultaneous detection and estimation are similar to the step 3) to step 6) of section 4.3.3 (the only difference is that the filtering nodes should be substituted by the filtering subbands).

4) *Wavelet Reconstruction*: In this step, performed for real and imaginary parts, the filtered subbands and the unfiltered LL subband are used as the input of the inverse undecimated discrete wavelet transform (IUDWT) [248] to reconstruct the filtered real and imaginary parts.

5) *Interferometric-Phase Retrieval*: In this step, the filtered phase is retrieved from (4.22) using the filtered real and imagery parts.

4.5 Implementation Issues

4.5.1 Function Calculation

For the PFUWSDE method, for every level of wavelet decomposition, each subband has the same size as the original data. For both the PFWPSDE and PFUWSDE methods, the computational cost largely depends on the simultaneous detection and estimation step (in the simultaneous detection and estimation, most of the CPU time is spent during the calculation of the detector), and the processing time is proportional to the total number of coefficients in all the filtering subbands. For the same level of decomposition, the total number of coefficients in all the filtering subbands of the undecimated wavelet domain is much greater than that of the full tree of wavelet-packet decomposition. Therefore, the

computational cost and memory requirement of the PFUWSDE method is much higher than that of the PFWPSDE method. This is a major drawback of the PFUWSDE method.

For both the PFWPSDE and PFUWSDE methods, several mathematical functions need to be calculated during filtering. When the estimator is calculated (equation (4.13)), several complementary error functions are calculated. When the detector is calculated (equation (4.17a) and (4.17b)), the complementary error function, gamma function, and confluent hypergeometric function need to be calculated. These three functions are calculated for every coefficient of all the filtering subbands (or filtering nodes), therefore requiring a large amount of CPU time.

The gamma function and the complementary error function are easily calculated using the MATLAB function. The computation of the confluent hypergeometric function, however, is complex and time consuming. Most of the CPU time is used in calculating the confluent hypergeometric function if we perform the calculation every time we use this function. In order to speed up the algorithm, in the proposed PFWPSDE and PFUWSDE methods, we precalculated all the values of $\Phi(1.5, 0.5; x)$ and $\Phi(2, 1.5; x)$ for different possible values of x using the method in [250]. These values are saved in two lookup tables. The filtering algorithm each time searches the respective values from the respective lookup table according to the values of ξ^2 or ψ^2 . By introducing these two lookup tables, much CPU time is saved. This is particularly important for the PFUWSDE method because more coefficients need to be filtered than for the PFWPSDE at the same decomposition level.

4.5.2 Wavelet Decomposition Level

For filtering of different types of InSAR phase data, different levels of decomposition may be used. When the noise level is low and the phase fringes are sparse, the phase information is mostly concentrated in the lowest frequency subband (or node). In this case, we can only filter the middle- and high-frequency subbands (or nodes), while the subband (or node) of the lowest frequency should not be filtered. When the phase is very noisy and the decomposition level is low, even the subband (or node) of the lowest frequency may be noisy. In this case, we still do not want to filter the lowest frequency subband (or node) in order to maintain the phase information as much as possible. Instead, we should apply additional levels of decomposition. When additional levels of decomposition are applied, the two proposed methods are implemented in different ways. For the PFWPSDE method, all the nodes are further decomposed. For the PFUWSDE method, only the subband of the lowest frequency is further decomposed; all the other frequency subbands are not changed. For the PFWPSDE method, all the nodes in the new decomposition level except the node of the lowest frequency are filtered. For the PFUWSDE method, the newly generated lowest frequency subband (approximation coefficients) is not filtered; the other three relatively high-frequency subbands (detail coefficients) are added to the other subbands of the filtering queue. Based on this analysis, the level of decomposition of the two proposed methods cannot be too low.

On the other hand, the decomposition level cannot be too high for both the PFWPSDE and PFUWSDE methods. In the PFWPSDE method, the filtering accuracy depends on the accuracy of local statistics estimation, and when the decomposition level is too high, the number of coefficients available for parameter estimation of simultaneous

detection and estimation may be too small. If this is the case, the estimated parameters will be insufficiently accurate for the filtering. In PFUWSDE method, the higher the decomposition level, the more coefficients need to be filtered and the higher is the computational cost.

Therefore, for both the PFWPSDE and PFUWSDE methods, the decomposition level cannot be too high or too low. For most cases of InSAR phase filtering, three-level decomposition is a reasonable compromise.

4.6 Experimental Results Using Simulated Data

4.6.1 Methods Used in the Experiments

In this section, we introduce the experimental results using simulated InSAR phase data. In all the experiments in this section, for the two proposed methods, a 7×7 window was used in the estimation of parameters.

1) *PFWPSDE Method*: In this experiment, three-level wavelet-packet decomposition is used, and the same scaling parameter $\lambda = 1.0$ is used. The node of the lowest frequency contains most of the phase information [217], [218] and is not filtered. All the other 63 nodes in the full tree are filtered. All the filtering operations are performed in the third decomposition level.

2) *PFUWSDE Method*: This method also uses three-level decomposition, so the approximation coefficients of the third level are not filtered. The first filtering is in the third level of detail coefficients, the second filtering is in the second level, and the last filtering step is in the first level. All the three detail coefficients for horizontal, vertical, and diagonal directions are filtered. The simulated phase data are very noisy at high-

frequency subbands; therefore, in order to reduce the noise sufficiently, we set the scaling parameters as $\lambda_1 = 2.0, \lambda_2 = \lambda_3 = 1.0$.

4.6.2 Parameter Selection in Simultaneous Detection and Estimation

From the analysis in Section 4.2, we know that there are several parameters that need to be defined by the user both for the PFWPSDE and PFUWSDE methods. The parameter selection supports the flexibility of the algorithm but must be considered carefully in order to obtain a qualitatively strong filtering performance.

The parameter selection of the estimator and detector is based on the basic idea that wrong classification should have a higher cost than correct classification [231]. As long as this is satisfied, small changes of the parameters does not influence the filtering performance significantly. On the other hand, it is not necessary to change the parameters for most applications. In this experiment, we use the same parameters for both the proposed PFWPSDE and PFUWSDE methods. Following [223], we set the parameters $\kappa_{00} = \kappa_{11} = 1$. The other parameters are defined as $\kappa_{01} = 30$, $\kappa_{10} = 4.5$, and $\rho = 0.02$. In this set of parameters, κ_{01} is larger than that in [223] in order to reduce the detection errors when the detection result is a signal when, in reality, it is a noise.

For the selection of $P(H_1)$ and $P(H_0)$, although these probabilities are different for different subbands (or nodes), we can use the same value for all the subbands in the two proposed methods. For the wavelet image denoising, $P(H_1) = P(H_0) = 0.5$ is used [251]. Since most of the signal energy of InSAR phase data is concentrated in a small number of wavelet coefficients, we reduce the possibility of signal appearance to $P(H_1) = 0.4$. Since $P(H_1) + P(H_0) = 1$, we have $P(H_0) = 0.6$.

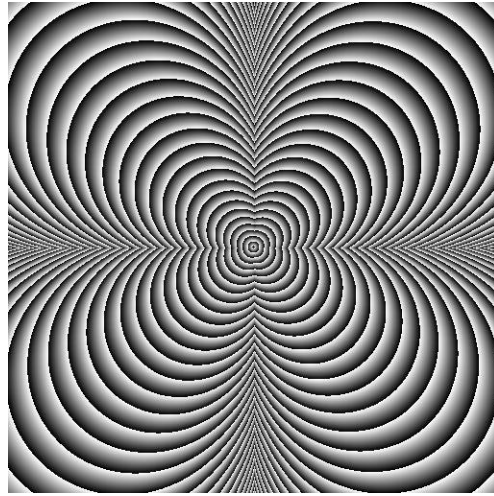


Figure 4.3. “Clean” (noise-free) simulated phase.

4.6.3 Experimental Results of Simulated Data I

In order to examine the filtering performance of the two proposed methods, three simulated data sets are used (Data I, Data II, and Data III). All these 512×512 data sets are generated using the same clean phase, which is shown in Figure 4.3. The fringe density ranges from very dense to very sparse and therefore can be used to examine the filtering performance for various types of phase data. Although the very high density fringes of the simulated data do not occur often in the interferometric phase of real InSAR data, for a theoretical study, this gives us some insight on how the proposed algorithms behave for a wide range of fringe densities.

Data I is designed for examining the filtering performance of spatially invariant noise, while Data II and Data III are designed for examining the filtering performance of spatially varying noise. In this section, we will introduce Data I and the experimental results using Data I. In the following tests, for comparative purposes, we present results from the earlier wavelet-based algorithms reported in [217], [218], and [219] as well as from the two methods developed here.

TABLE 4.1
RESIDUAL ERRORS (RMSEs) OF THE FILTERED RESULTS OF DATA I

	Method in [218]	Method in [217]	Method in [219]	Proposed PFWPSDE method	Proposed PFUWSDE method
Data I-1	1.7352	0.8868	0.9649	0.5495	0.3850
Data I-2	2.6390	1.0837	1.1470	0.7326	0.5521
Data I-3	3.3344	1.3628	1.3005	0.8962	0.7114

TABLE 4.2
RESIDUAL ERRORS (RMSEs) OF THE FILTERED RESULTS OF DATA II

	Method in [218]	Method in [217]	Method in [219]	Proposed PFWPSDE method	Proposed PFUWSDE method
Data II-1	4.2368	2.1286	3.9053	1.9947	1.6729
Data II-2	4.4956	2.3337	4.3621	1.7678	1.6694
Data II-3	4.1107	2.1613	3.3319	1.3312	1.1993

TABLE 4.3
RESIDUAL ERRORS (RMSEs) OF THE FILTERED RESULTS OF DATA III

	Method in [218]	Method in [217]	Method in [219]	Proposed PFWPSDE method	Proposed PFUWSDE method
Data III-1	2.6909	1.6863	1.5421	1.2054	0.8714
Data III-2	3.5968	2.2084	1.9698	1.4998	1.2880
Data III-3	3.6813	2.3782	2.2787	1.6043	1.4463

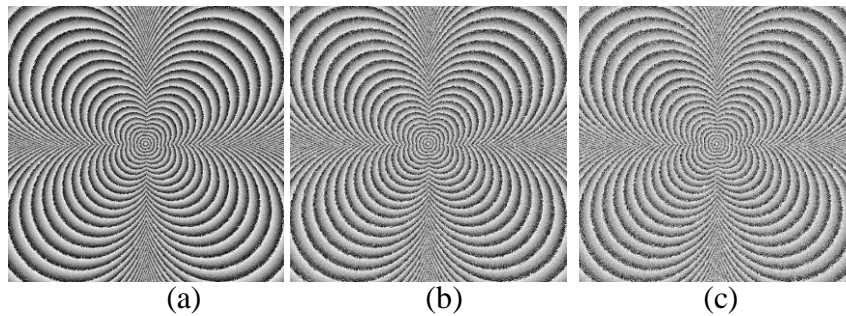


Figure 4.4. Simulated input data contaminated by noise: Data I. (a), (b), and (c) are Data I-1, Data I-2, and Data I-3, respectively.

The distribution of phase noise can be modeled as Wishart [252], but in order to simplify the analysis, it is also modeled as Gaussian [220], [253]. Data I adds additive phase noise of constant variance for the whole phase data set. The simulated data contaminated by noise of increasing variance are shown in Figure 4.4(a) (Data I-1, noise variance is 0.45), Figure 4.4(b) (Data I-2, noise variance is 0.65), and Figure 4.4(c) (Data I-3, noise variance is 0.85), respectively. Columns A, B, C, D and E of Figure 4.5 show the filtering results of the method of [218], [217], [219], PFWPSDE, and PFUWSDE, respectively. In Figure 4.5, the first, second, and third rows show the filtering results of Data I-1, Data I-2, and Data I-3, respectively. In Figure 4.5, the fourth row shows the difference maps between the filtered results and the original clean phase of Data I-3. In this experiment, for both the PFWPSDE and PFUWSDE methods, the Daubechies wavelet with four vanishing moments [254] is used.

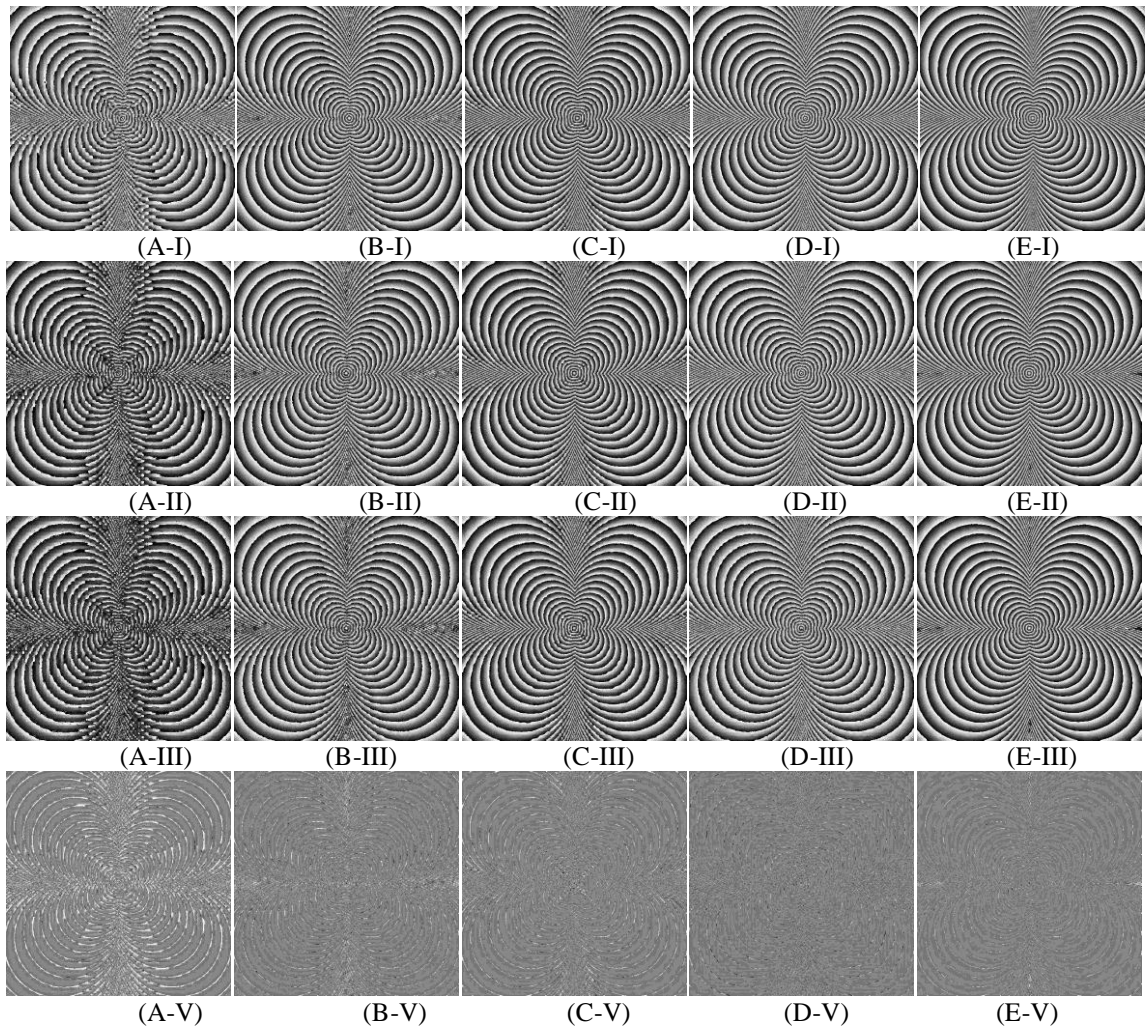


Figure 4.5. Phase-filtering results using simulated Data I. First row: (A-I)-(E-I) includes the filtered results of Data I-1; second row: (A-II)-(E-II) includes the filtered results of Data I-2; third row: (A-III)-(E-III) includes the filtered results of Data I-3. Fourth row: (A-V)-(E-V) includes difference maps between the filtering results of Data I-3 and the original clean phase. Column (A): Filtering results of the method in [218]. Column (B): Filtering results of the method in [217]. Column (C): Filtering results of the method in [219]. Column (D): Filtering results of the proposed PFWPSDE method. Column (E): Filtering results of the proposed PFUWSDE method.

In order to evaluate the filtering performance quantitatively, the root-mean-square errors (RMSEs) of the experimental results are calculated and presented in Table 4.1. We observe that, for each input noise level, both the proposed PFWPSDE and PFUWSDE methods have slightly lower RMSEs than those of the methods in [217], and [219] and considerably lower RMSEs than those of method in [218]. The PFUWSDE method has lower RMSEs than those of PFWPSDE method.

A qualitative comparative evaluation is performed by visual inspection of Figure 4.5, which can be conducted by comparing the filtering results in the areas of different fringe densities. We arrive at the following conclusions:

- 1) The filtering results of the method from [218] show large numbers of errors in almost all the areas of the phase image. These increase with increasing input noise level.
- 2) The filtering results of the methods in [217] and [219] show far fewer errors than those of the method in [218]. The filtering results of the method in [217] appear to have more large-scale errors than the method of [219] and the two proposed methods in the filtered phase. Qualitatively, the filtering results of the PFWPSDE method appear similar to the method in [219] upon first examination. Upon closer scrutiny, the errors of the PFWPSDE method are smaller in almost all the areas of the image than those of the method in [219].
- 3) Among these five methods, the PFUWSDE method has the least residual noise and artifacts remaining in the areas of low and moderate fringe density (which is true in most cases in real InSAR phase data), particularly for the data set with high input-noise level. This supports the suggestion that the redundancy of wavelet coefficients provides a stronger filtering performance than can be obtained in the wavelet-packet domain.

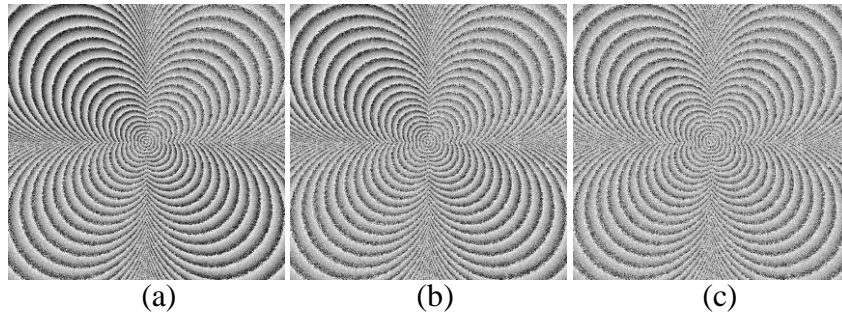


Figure 4.6. Simulated input data contaminated by noise: Data II. (a), (b), and (c) are Data II-1, Data II-2, and Data II-3, respectively.

4) When the noise level is high (Data I-2, Data I-3), some very high density phase fringes are eliminated in the PFUWSDE method. For the PFWPSDE method, this does not occur. This shows that the PFUWSDE method has weaker performance than the PFWPSDE method when the phase fringes are of very high density. This is because in the wavelet-packet decomposition, the high-frequency phase information is more easily separated from the noise because its frequency resolution is high in the high-frequency filtering node. On the contrary, in the undecimated wavelet domain, the high-frequency information is harder to be separated from the noise because of the low resolution in the high-frequency subbands.

4.6.4 Experimental Results of Simulated Data II

In this section, we will introduce the simulated data set “Data II” and the corresponding experimental results. Data II is the simulated phase data with different noise levels for the four quadrants of the synthetic phase image.

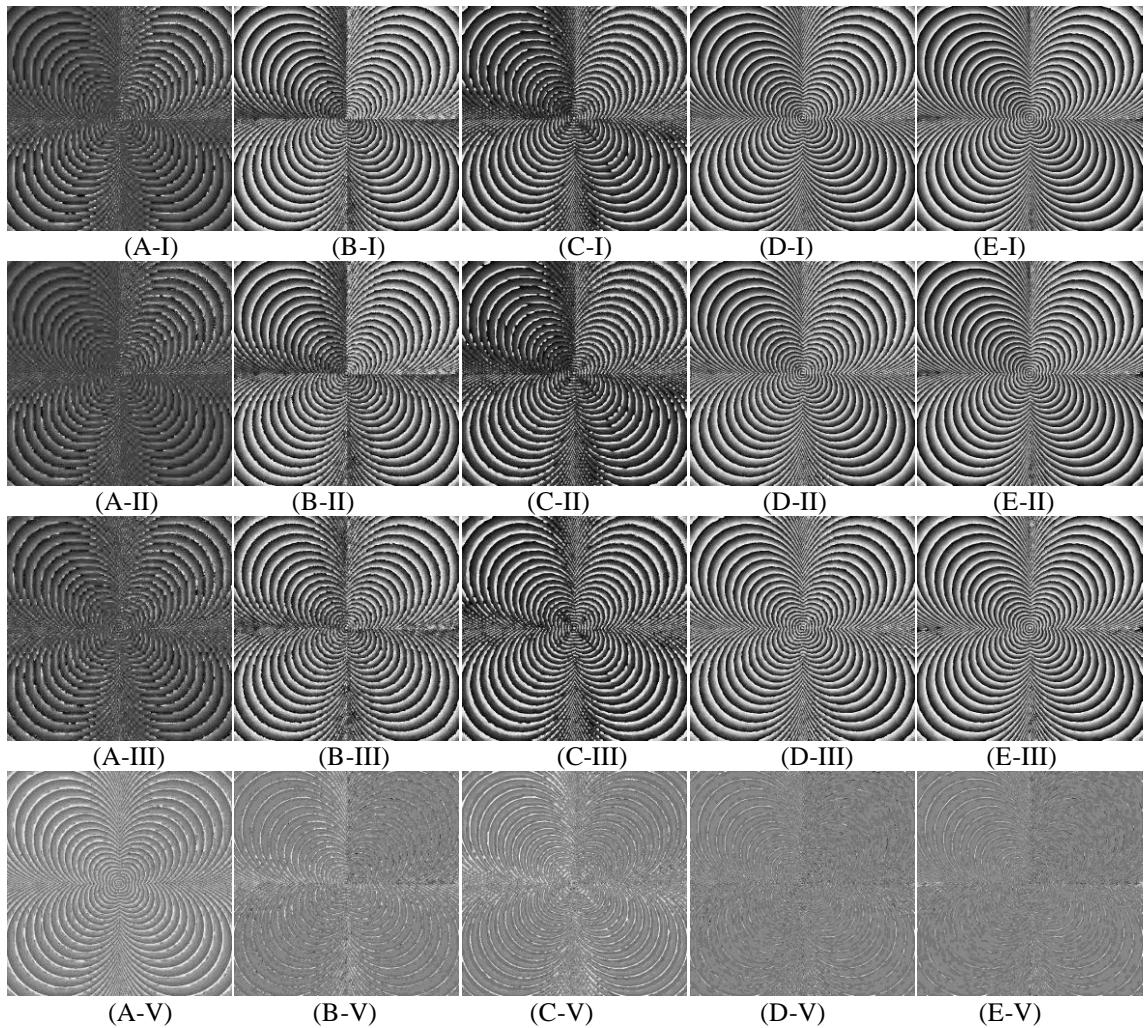


Figure 4.7. Phase-filtering results using simulated Data II. First row: (A-I)-(E-I) are the experimental results of Data II-1; Second row: (A-II)-(E-II) are the experimental results of Data II-2; Third row: (A-III)-(E-III) are the experimental results of Data II-3; Fourth row: (A-V)-(E-V) are difference maps between the filtered results of Data II-3 and the clean phase. Column (A): Filtering results of the method in [218]. Column (B): Filtering results of the method in [217]. Column (C): Filtering results of the method in [219]. Column (D): Filtering results of the proposed PFWPSDE method. Column (E): Filtering results of the proposed PFUWSDE method.

There are two layers of noise added in Data II. The first layer has constant variance for the whole phase data set. The noise variances of the first layer of noise added to Data II-1, Data II-2, and Data II-3 are 0.25, 0.35, and 0.55, respectively. In order to examine the filtering performance under a spatially variable noise environment, the second layer of noise is added in the simulated Data II. The second layer of noise is generated using a method similar to [214], which generates different noise levels for four quadrants. During the generation of the second layer of noise, different levels of noise are added to the four quadrants of the simulated data, but the noise level inside each quadrant is constant. Figure 4.6(a)-(c) shows the noisy input phase data of Data II-1, II-2, and II-3, respectively. The first, second, and third rows of Figure 4.7 show the filtering results of Data II-1, II-2, and II-3, respectively. In the second layer of noise, the noise levels (variances) of Data I-1 are 0.85, 0.25, 0.65, and 0.45 for the first, second, third, and fourth quadrants, respectively. In the second layer of noise, the noise levels of Data I-2 are 0.95, 0.35, 0.75, and 0.55 for the first, second, third, and fourth quadrants, respectively. In the second layer of noise, the noise levels of Data I-3 are 0.85, 0.55, 0.75, and 0.65 for the first, second, third, and fourth quadrants, respectively. Thus the noise level in each quadrants changes as we go down from row to row. Columns A, B, C, D, and E of Figure 4.7 show the filtering results using the methods of [218], [217], [219], PFWPSDE, and PFUWSDE, respectively. In this experiment, Daubechies wavelet with 20 and 10 vanishing moments [254] are used in the PFWPSDE and PFUWSDE methods, respectively.

From the noise-level scheme of the second layer of noise in data II, it can be seen that in Data II-1, the noise level has large differences among the four quadrants, but the

overall noise level is relatively low. In Data II-2, the noise level also has large differences for four quadrants, and the noise level is higher than that of Data II-1. In Data II-3, the noise level has only small differences among the four quadrants, but the noise level is higher than that of Data II-1.

The RMSEs (filtered minus clean-phase data) of the experimental results using simulated Data II are calculated and illustrated in Table II. By comparing the RMSEs of the filtering results of simulated Data II, we have the following conclusions:

- 1) For all the methods except the method in [217], the experimental results of Data II-3 have lower RMSEs than those of Data II-1 and Data II-2. This is because the noise-level change (variability) is smaller in Data II-3 than that of the others; therefore, filtering is relatively easier.
- 2) For all three data sets, the results from both the PFWPSDE and PFUWSDE methods show lower RMSEs than those of methods [217] and [219] and much lower RMSEs than those of the method of [218]. This demonstrates that both the proposed methods exhibit improved comparative performance relative to the method in [217], [218], and [219] when the noise level is spatially variable. The reason behind this is that the simultaneous detection and estimation scheme has better estimation ability in the case of nonstationary noise.
- 3) The RMSEs of the PFUWSDE and PFWPSDE methods are similar.

Qualitatively, the results of the four methods can be intercompared by inspection of the images of Figure 4.7, which is conducted by comparing the filtering results for the areas of different fringe densities. We arrive at the following conclusions.

- 1) There are large numbers of errors in the filtering results from the application of the

method of [218]. Most of the phase fringes are modified in the filtering results of the method of [218].

2) The results from the method of [219] are considerably improved relative to [218]. However, several artifacts, such as scalloping, are observed at all noise levels. The results from the method of [217] have fewer artifacts than those of [219].

3) Both PFWPSDE and PFUWSDE results appear to have fewer artifacts than those of [217], [218], and [219].

4) Similarly to the simulated Data I, for the area of sparse fringes and the area of phase fringes with moderate densities, the filtering results of the PFUWSDE method have fewer artifacts and less noise remained than those of the PFWPSDE method. Visually PFUWSDE appears very close to the input clean phase image of Figure 4.3. This shows that the PFUWSDE method outperforms the PFWPSDE method when the phase fringes are sparse or with moderate density.

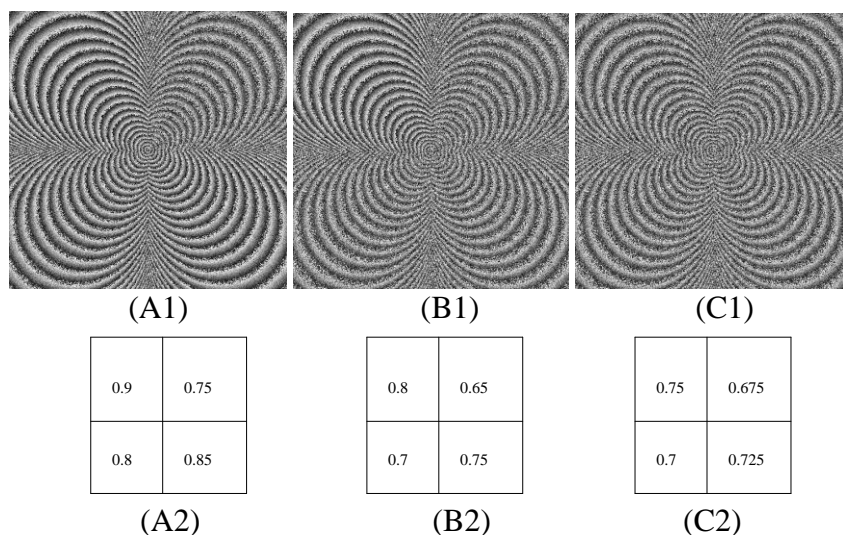


Figure 4.8. Simulated input data contaminated by noise: Data III. (A1), (B1), and (C1) are Data III-1, Data III-2, and Data III-3, respectively. (A2), (B2), and (C2) are the coherence levels of Data III-1, Data III-2, and Data III-3, respectively.

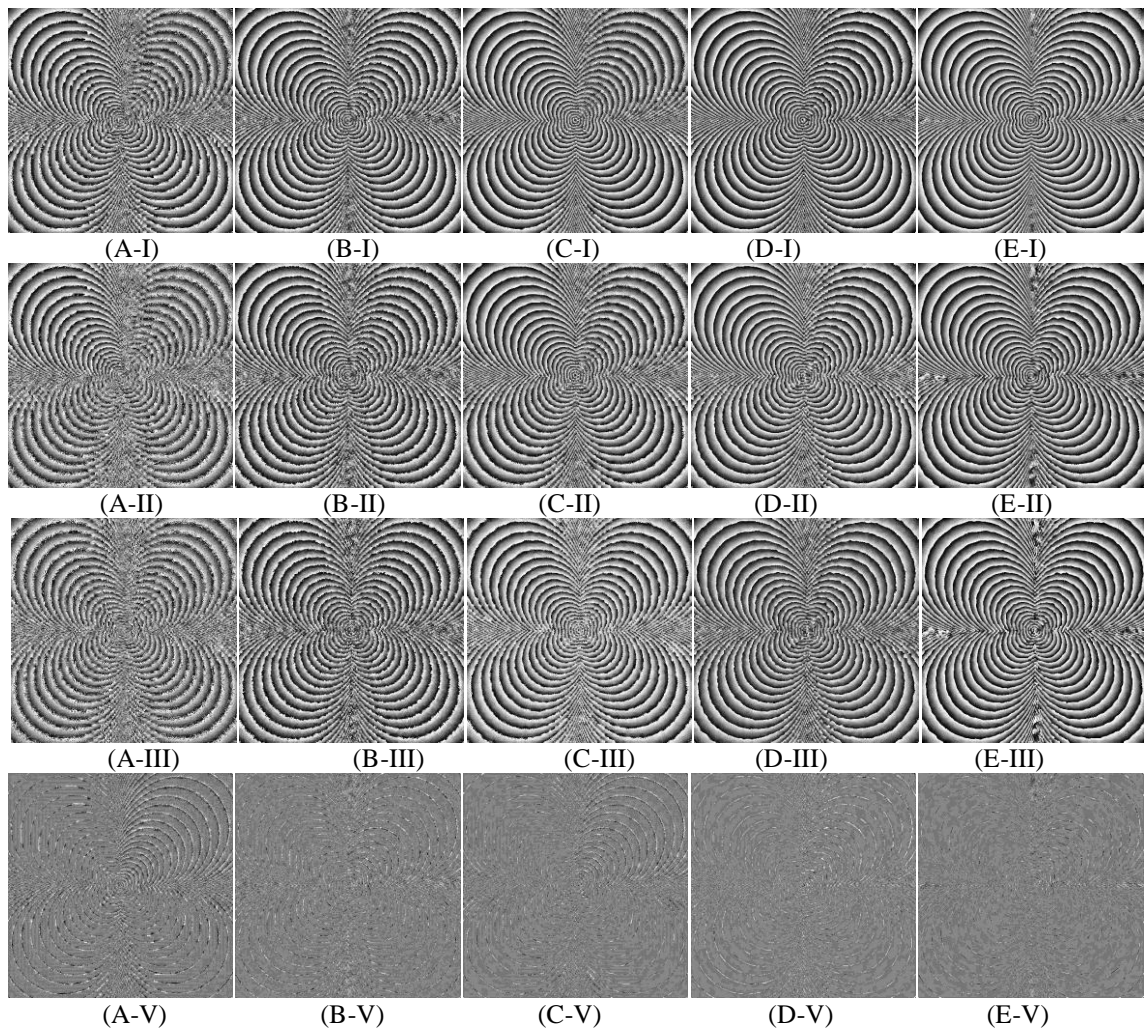


Figure 4.9. Phase-filtering results using simulated Data III. First row: (A-I)-(E-I) are the experimental results of Data III-1; Second row: (A-II)-(E-II) are the experimental results of Data III-2; Third row: (A-III)-(E-III) are the experimental results of Data III-3; Fourth row: (A-V)-(E-V) are difference maps between the filtering results of Data III-1 and the clean phase. Column (A): Filtering results of the method in [218]. Column (B): Filtering results of the method in [217]. Column (C): Filtering results of the method in [219]. Column (D): Filtering results of the proposed PFWPSDE method. Column (E): Filtering results of the proposed PFUWSDE method.

5) Some phase fringes around the area of very high fringe densities are eliminated in the PFUWSDE method, which is more conspicuous than the experiments of simulated Data I. This shows that the PFWPSDE method outperforms the PFUWSDE method when the phase fringes are very dense. The explanation is similar to that discussed for simulated Data I in Section 4.6.4.

Based on these analyses, we can say that the two proposed methods outperform the methods of [217], [218], and [219] when the noise standard deviation in the phase is spatially variable.

4.6.5 Experimental Results of Simulated Data III

Data III also applies different noise levels for different quadrants of the simulated data, and the noise is additive and generated using the method in [215]. Figure 4.8(A1), (B1), and (C1) shows the noisy input phase data of Data III-1, III-2, and III-3, respectively. The coherence levels inside each quadrant are calculated using the method in [150] and [7] and are shown in the second row of Figure 4.8. In this experiment, Daubechies wavelet with 20 and 10 vanishing moments [254] are used in the PFWPSDE and PFUWSDE methods, respectively. Figure 4.8(A2), (B2), and (C2) shows the input quadrant coherence levels for Data III-1, III-2, and III-3, respectively. The RMSEs of the experimental results of Data III are illustrated in Table 4.3. From Table 4.3, we observe that the two proposed methods have lower RMSEs than the other considered methods. The filtering results of Data III are shown in Figure 4.9. From Figure 4.9, we can see the following:

- 1) The filtering results of the method in [218] are still very noisy, which reflects that large amount of noise still remain in the filtering results.

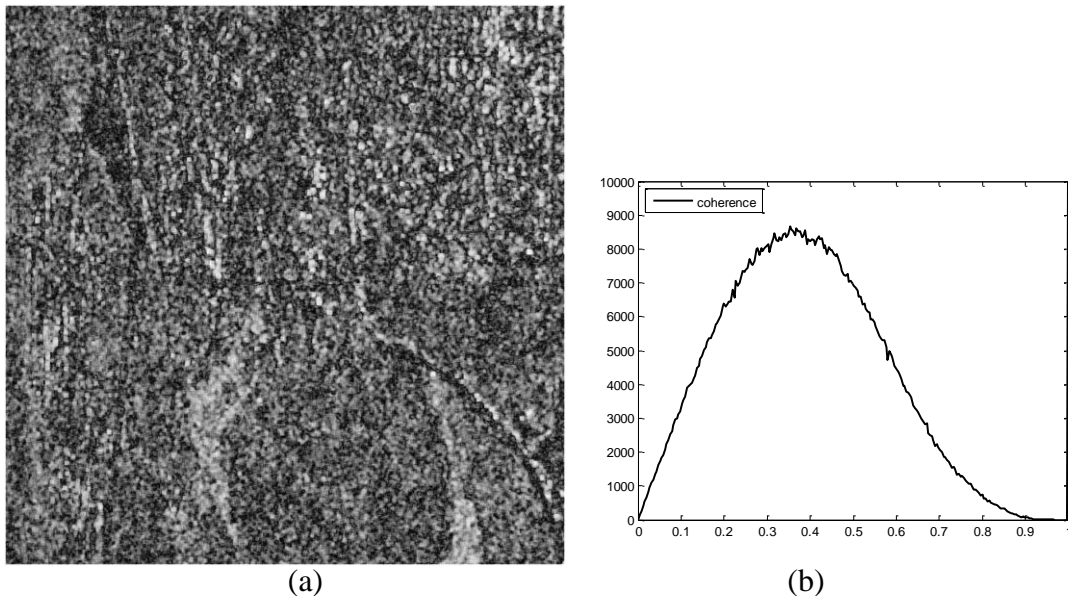


Figure 4.10. (a) Coherence of the Intermap InSAR data. (b) Histogram of the coherence.

2) The filtering results of the method in [217] and [219] are much less noisy than those of [218]; however, there are still some noise remaining in the filtered results.

3) The least amount of noise remains in the filtering results of the proposed PFWPSDE and PFUWSDE methods. This suggests that the two proposed methods have stronger noise-removal ability than the other considered methods.

4.6.6 Processing Speeds of the Algorithms

The average processing times of the methods of [218], [217], [219], PFWPSDE, and PFUWSDE method are 4.5, 15.5, 1.0×10^2 , 7.3×10^2 , and 3.9×10^3 s, respectively. Because these were executed in MATLAB (with some C routines), they are useful only in showing relative computation times. We note that the method in [217], [218], and [219] are faster than the two proposed methods, and the proposed PFUWSDE method is the slowest method. This is because large amounts of CPU time are consumed in the

calculation of the simultaneous detection and estimation step (which is mostly in the calculation of the detector) in the two proposed methods. The more pixels that need to be classified, the higher is the processing time. The PFUWSDE method requires more CPU time than the PFWPSDE method because more coefficients are used in the PFUWSDE method for the same decomposition level.

4.7 Experimental Results Using Real InSAR Data

Further tests were conducted with real InSAR data sets to examine the performance of the two proposed methods. The particular examples shown here are two real InSAR data sets. The first real InSAR data set uses repeat-pass InSAR data acquired by Intermap Technologies Corporation. The data were selected because of the conveniently varying fringe density (after flat-Earth removal [7]) over a small sloping area, along with a wide range of coherence values reflecting, in part, the spatially varying signal-to-noise ratio (SNR). The data are from a heterogeneous area of forest and suburban features. Figure 4.10(a) and (b) shows the coherence map of this data set and its histogram, respectively. From the coherence histogram of these data, we observe that the coherence level ranges from very low to very high (which means that the noise standard deviation changes drastically for different areas), part of which is due to decorrelation effects other than noise and part due to the variability of the SNR within the area. Figure 4.11(a) shows the interferometric phase (image size is 1024×1024) of these real InSAR data. These InSAR phase data are directly extracted from the single-look complex images, unlike the data used in [253] and [255], which are the output of the coherence optimization. Therefore,

the data used in this experiment are much noisier than those used in [253] and [255]. This data set is relatively noisy and has a very low average coherence (0.39). The second real InSAR data set is the ALOS PALSAR data acquired by the Japan Aerospace Exploration Agency (JAXA). Figure 4.12(a) shows the interferometric phase (image size is 512×512) of these data.

In this experiment, the same parameters as defined in Section 4.6.2 are used, and a 7×7 moving window was used in the estimation of parameters.

Figure 4.11(b), (c), (d), (e) and (f) shows the filtered phase maps resulting from application of the methods of [218], [217], [219], PFWPSDE, and PFUWSDE on the Intermap data, respectively. Figure 4.12(b), (c), (d), (e) and (f) shows the filtered phase maps resulting from application of the methods of [218], [217], [219], PFWPSDE, and PFUWSDE on the ALOS data, respectively. From visual inspection of these results in Figure 4.11 and Figure 4.12, it appears that the phase filtered result according to the method in [218] is still relatively noisy; not much of the noise is eliminated. The phase map resulting from the method in [219] is less noisy than that of [218]; however, some phase fringes are not clearly visible. The filtering result of the method in [217] is less noisy than that of [219], but significant noise remains. Both of the methods proposed in this chapter appear to demonstrate lower noise content and better definition in these results than those using the earlier wavelet approaches of [217], [218], and [219].

We now examine the results of the two proposed methods in more detail. In this experiment, both the PFWPSDE and PFUWSDE methods use the three-level decomposition.

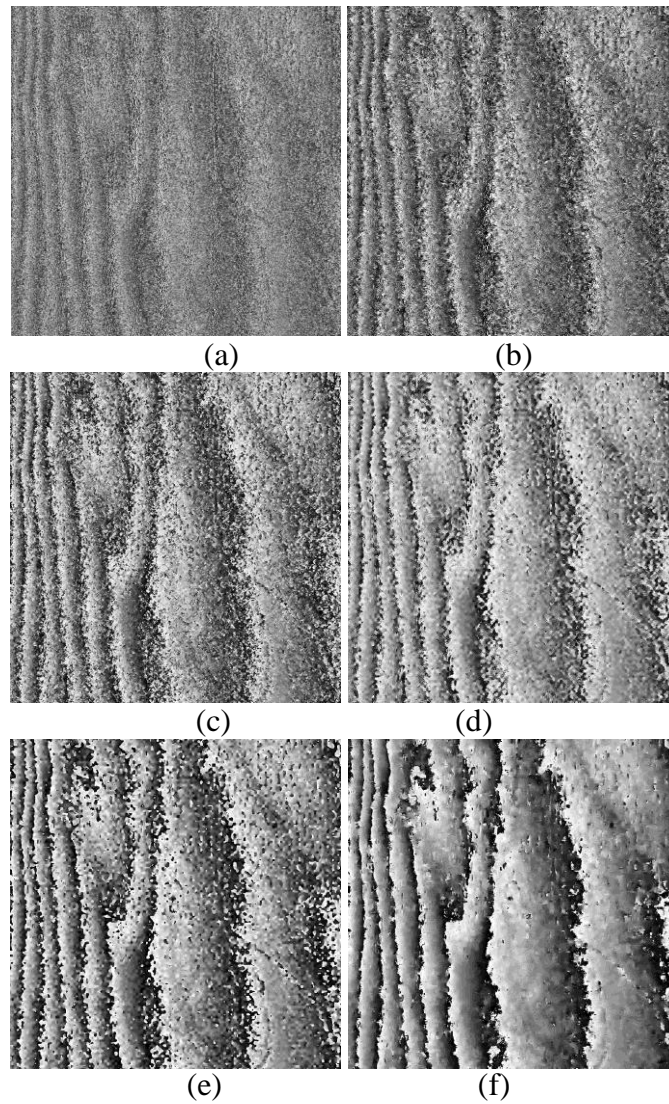


Figure 4.11. Original interferometric phase and the filtering results of Intermap InSAR data (1024*1024). (a) Interferometric phase of real InSAR data. (b) Filtering result of the method in [218]. (c) Filtering result of the method in [217]. (d) Filtering result of the method in [219]. (e) Filtering result of the proposed PFUWSDE method. (f) Filtering result of the proposed PFWPSDE method.

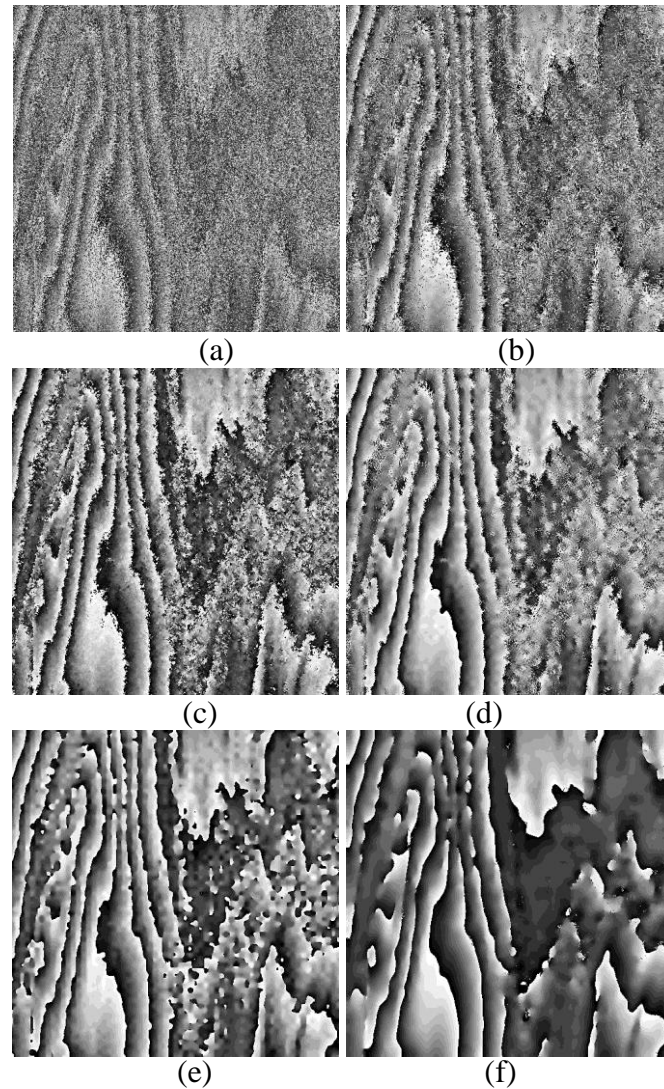


Figure 4.12. Original interferometric phase and the filtering results of ALOS PALSAR data (512*512). (a) Interferometric phase of real InSAR data. (b) Filtering result of the method in [218]. (c) Filtering result of the method in [217]. (d) Filtering result of the method in [219]. (e) Filtering result of the proposed PFWPSDE method. (f) Filtering result of the proposed PFUWSDE method.

PFWPSDE Method: Because the input phase data are very noisy and coherence changes drastically for different areas, the scaling parameter $\lambda = 2.0$ is used to improve the filtering ability. In this experiment, Daubechies wavelet with four vanishing moments was used.

Comparing the filtering results, we observe the following.

- 1) For both the results of Intermap and ALOS data, the PFWPSDE method eliminates more noise than the methods in [217], [218], and [219]. The phase fringes are easier to be observed from the filtering result of the PFWPSDE method than those of the methods in [217], [218], and [219].
- 2) Inspecting the results of Intermap InSAR data, all the four methods, the PFWPSDE method and the methods in [217], [218], and [219] show numerous anomalous phase jumps, and the filtered results are not as smooth as expected in these areas of sparse fringes. This may be explainable in a manner similar to [256], which is the case of orthogonal wavelet filtering: The PFWPSDE method performs the filtering using the orthogonal wavelet packet, which may cause the artifacts in the filtering result.
- 3) For the ALOS data, since the coherence is higher than the Intermap data, the anomalous phase jumps are much less than the Intermap data. However, there is much less noise remaining in the result of the PFWPSDE method than the methods in [217], [218], and [219].

PFUWSDE Method: The two real InSAR phase data sets are very noisy, and the noise standard deviation varies spatially. Since the noise dominates part of the low-frequency and high-frequency wavelet subbands, therefore, when calculating the noise standard deviation using (4.23a) and (4.23b), scaling parameters $\lambda_1 = \lambda_2 = \lambda_3 = 1.5$ are used

in the PFUWSDE method. Since the fringes in the InSAR phase data sets are not densely populated, greater smoothness in the wavelet is preferable, such as the quadratic spline wavelet proposed in [257], which has been used in [258]. In this experiment, the quadratic spline wavelet in [257] is employed in the PFUWSDE method.

Comparing the filtering results of the PFWPSDE method and PFUWSDE method, it is easy to observe that the PFUWSDE method has stronger noise-removal ability than the PFWPSDE method. For the Intermap data, in the filtering result of the PFUWSDE method, there are much fewer anomalous jumps than that of the PFWPSDE method, and the phase fringes of the filtered phase are more distinct than that of the PFWPSDE method. Therefore, it appears that the PFUWSDE method is more suitable for the phase filtering of the InSAR phase data of low coherence than the PFWPSDE method. For the ALOS data, the PFUWSDE method obtains a smoother result than the PFWPSDE method.

Residues have been used in the evaluation of InSAR phase-filtering performance in [214] and [215]. In this chapter, we also evaluate the proposed methods quantitatively by comparing the residues before and after filtering. The percentage of remaining residues of the filtered phase for the methods of [218], [217], [219], PFWPSDE, and PFUWSDE are calculated and illustrated in Table 6.4. From Table 6.4, it is easy to draw the following conclusions: 1) For percentage of residues removed from the original data as a figure of merit, the proposed PFWPSDE and PFUWSDE methods considerably outperform the benchmark methods of [217], [218], and [219] and 2) the PFUWSDE method has the fewest residues left in the filtering result, which means that the PFUWSDE method has the highest noise-removal ability than all the other tested methods.

In summary, the proposed PFWPSDE and PFUWSDE methods outperform the methods in [217], [218], and [219] in terms of the visual inspection and quantitative evaluation (residuals) for both the two real InSAR phase data sets tested. The proposed PFUWSDE method outperforms the PFWPSDE method in terms of the quality of the filtered phase when using real InSAR phase data.

TABLE 4.4
PERCENTAGE OF RESIDUES LEFT IN THE FILTERING RESULTS

	Residues in Original Data	Method in [218]	Method in [217]	Method in [219]	Proposed PFWPSDE method	Proposed PFUWSDE method
Percentage left (Intermap data)	100	30.20	11.82	7.94	1.32	1.05
Percentage left (ALOS data)	100	57.70	16.69	19.86	1.02	0.47

4.8 Conclusion

In this chapter, the simultaneous detection and estimation have been applied to interferometric SAR phase filtering in the wavelet domain. Using this strongly coupled simultaneous detection and estimation scheme, two wavelet-domain InSAR phase-filtering methods were proposed. The first, referred to as the PFWPSDE method, uses the wavelet packet; the second, referred to as the PFUWSDE method, performs filtering in the undecimated wavelet domain. The detailed implementations of these two methods were presented.

Three sets of simulated phase data were used to test the performance of the two

proposed methods. The first data set was designed for the testing of spatially invariant noise. For relative comparison to the proposed methods, three other wavelet-based methods for phase filtering presented in literature were implemented and tested against the same data sets. The experimental results demonstrate that the two proposed methods have slightly better performance quantitatively (RMSE-based) and qualitatively (inspection-based) than the other considered methods. The second data set was designed to examine the filtering performance when the phase noise level is spatially variable, which is particularly useful to examine because the noise level of real interferometric phase data is often spatially variable. The experimental results demonstrate that the two proposed methods have the stronger filtering ability when they are applied in the filtering of spatially variable noise compared with the other considered methods. This suggests that the two proposed methods appear promising for filtering of real InSAR phase data. The third data set further verifies that the two proposed methods outperform the other considered methods according to their experimental results.

The two proposed methods can be selected according to the specified situations of the InSAR phase data. Since the proposed PFWPSDE method has a stronger ability for the filtering of high-frequency information but weaker ability for noise removal, therefore it is suitable for phase filtering when phase fringes are of high density and phase quality is good. The proposed PFUWSDE method has the stronger ability to filter very noisy phase data and can reduce the artifacts in the filtering result but with phase fringes of relatively low to moderate density. In addition, because the PFUWSDE method is slower and needs more memory than the PFWPSDE method, the PFWPSDE method is preferred when large-area filtering is required. For real-world InSAR data, because most phase

fringes are of moderate to low density, the PFUWSDE method is promising because it can obtain a filtering result with fewer residues and clearer fringes than that of the PFWPSDE method.

4.9 Appendix A

In this Appendix, we give the detailed derivations of (4.12a) and (4.12b), which are obtained by solving the integrations of (4.10a) and (4.10b), respectively.

Substituting (4.7a), (4.7b), and (4.7c) into (4.10a), and using the 3.322.2 of [237] to solve the integral of (4.10a), we derive (4.12a). Substituting (4.7a), (4.7b), and (4.7c) into (4.10b), and using the 3.462.1 and 9.254.2 of [237] to solve the integral of (4.10b), we derive (4.12b).

4.10 Appendix B

In this Appendix, we give a detailed derivation of (4.14b). Substituting (4.7a) and (4.7b) into (4.4b), we have

$$\begin{aligned}
 \chi_{1j}(W) &= P(H_1) \int_{-\infty}^{\infty} \kappa_{1j} (\hat{S}_j - S)^2 p(S | H_1) p(W | S) dS \\
 &= \frac{P(H_1)}{2\sqrt{\pi}\sigma_S\sigma_U} \int_{-\infty}^0 \kappa_{1j} (\hat{S}_j - S)^2 \exp\left(-\frac{\sqrt{2}|S|}{\sigma_S}\right) \exp\left(-\frac{(W-S)^2}{2\sigma_U^2}\right) dS \\
 &\quad + \frac{P(H_1)}{2\sqrt{\pi}\sigma_S\sigma_U} \int_0^{\infty} \kappa_{1j} (\hat{S}_j - S)^2 \exp\left(-\frac{\sqrt{2}|S|}{\sigma_S}\right) \exp\left(-\frac{(W-S)^2}{2\sigma_U^2}\right) dS \\
 &= A_r + B_r
 \end{aligned} \tag{4.24}$$

where

$$\begin{aligned}
A_r &= \frac{P(H_1)\kappa_{1j}}{2\sqrt{\pi}\sigma_S\sigma_U} \int_{-\infty}^0 S^2 \exp\left(-\frac{\sqrt{2}|S|}{\sigma_S}\right) \exp\left(-\frac{(W-S)^2}{2\sigma_U^2}\right) dS \\
&+ \frac{P(H_1)\kappa_{1j}}{2\sqrt{\pi}\sigma_S\sigma_U} \int_{-\infty}^0 (-2\hat{S}_j S) \exp\left(-\frac{\sqrt{2}|S|}{\sigma_S}\right) \exp\left(-\frac{(W-S)^2}{2\sigma_U^2}\right) dS \\
&+ \frac{P(H_1)\kappa_{1j}}{2\sqrt{\pi}\sigma_S\sigma_U} \int_{-\infty}^0 \hat{S}_j^2 \exp\left(-\frac{\sqrt{2}|S|}{\sigma_S}\right) \exp\left(-\frac{(W-S)^2}{2\sigma_U^2}\right) dS \\
&= D_1 + E_1 + F_1
\end{aligned} \tag{4.25a}$$

$$\begin{aligned}
B_r &= \frac{P(H_1)\kappa_{1j}}{2\sqrt{\pi}\sigma_S\sigma_U} \int_0^{\infty} S^2 \exp\left(-\frac{\sqrt{2}|S|}{\sigma_S}\right) \exp\left(-\frac{(W-S)^2}{2\sigma_U^2}\right) dS \\
&+ \frac{P(H_1)\kappa_{1j}}{2\sqrt{\pi}\sigma_S\sigma_U} \int_0^{\infty} (-2\hat{S}_j S) \exp\left(-\frac{\sqrt{2}|S|}{\sigma_S}\right) \exp\left(-\frac{(W-S)^2}{2\sigma_U^2}\right) dS \\
&+ \frac{P(H_1)\kappa_{1j}}{2\sqrt{\pi}\sigma_S\sigma_U} \int_0^{\infty} \hat{S}_j^2 \exp\left(-\frac{\sqrt{2}|S|}{\sigma_S}\right) \exp\left(-\frac{(W-S)^2}{2\sigma_U^2}\right) dS \\
&= D_2 + E_2 + F_2
\end{aligned} \tag{4.25b}$$

Using the 3.462.1 and 9.240 of [237], we can solve the integrals in D_1 and D_2 . Using the 3.462.1 and 9.254.2 of [237], we can solve the integrals and obtain E_1 and E_2 . Using the 3.322.2 of [237], we can solve the integrals in F_1 and F_2 . Finally, after some arrangements, we obtain (4.14b).

CHAPTER 5: WEIGHTED REGULARIZED PRECONDITIONED CONJUGATE GRADIENT (PCG) PHASE UNWRAPPING METHOD⁴

In this chapter, a weighted regularized preconditioned conjugate gradient (PCG) phase unwrapping method based on the fast cosine transform is proposed. The boundary conditions of this method are researched. By adding weights to the regularized PCG method, the unwrapping accuracy of a noisy phase map is improved. The method is tested with both simulated phase data and real interferometric synthetic aperture radar (InSAR) data. In particular, the simulated data show both visual and quantitative improvements while in the case of the real InSAR data set that was used, it is demonstrated that certain large scale unwrapping errors can be reduced.

5.1 Introduction

Phase unwrapping is an important processing step for many imaging systems, and especially for interferometric synthetic aperture radar (InSAR). There are many phase unwrapping algorithms in the literature, including the widely used global and local methods [127]. The basic global method is a least squares algorithm which was proposed

⁴ © 2009 IOP Publishing Ltd. Reprinted, with permission, from [Yong Bian and Bryan Mercer, “Weighted regularized preconditioned conjugate gradient (PCG) phase unwrapping method,” *Journal of Optics A: Pure and Applied Optics*, vol. 11, issue 1, Article number: 015504, 11pp, 2009. doi:10.1088/1464-4258/11/1/015504.].

in [266] [267]. Many research activities have been focused on the improvement of the least squares method. By applying weights in the least squares method, the ‘weighted least squares’ method [264] shows improvements in the unwrapping accuracy when the phase map is contaminated by noise. The PCG method [264] is one of the efficient implementations of the weighted least squares approach.

In order to improve the processing efficiency, a wavelet based unweighted least squares method was proposed in [284] and later this was expanded to the weighted case [285] which uses the wavelet to solve the partial differential equation and thus improve the processing speed. However, the processing accuracy is not improved in these methods [285]. In order to improve the unwrapping accuracy of the weighted least squares method, more accurate weights to improve the processing accuracy were proposed recently in [286]. However, the objective function in this method is the same as the traditional weighted least squares method, which limits its applications.

In the traditional least squares method, the *a priori* information of the wrapped phase is not used. When the error sources of phase unwrapping are known, we can use the *a priori* information of the error sources to define the objective function [261] [262]. After the appropriate consideration of the error sources in the objective function, the unwrapping errors can be reduced [261] [262]. In order to take advantage of the *a priori* information, a regularization based method was proposed in [261] which aimed to interpolate areas of invalid data. After that, the constrained method based on the Fourier transform was proposed in [262]. In the InSAR phase unwrapping, when the phase quality is very low, these methods which can combine *a priori* information can be used to improve the unwrapping accuracy.

However in these investigations of the regularized methods, weights were not considered. When the phase map is noisy, it may be beneficial to take advantage of weights in the unwrapping process. For example, with InSAR, a noisy phase map leads to large scale unwrapping errors when the traditional PCG method is used. In this chapter, we further investigate the regularized unwrapping method, and propose a weighted regularized PCG (WRPCG) unwrapping method based on the traditional PCG [264] [127] approach. Since the WRPCG method is based on the fast cosine transform, the boundary conditions are also investigated in this chapter.

The organization of this chapter is as follows. Section 5.2 is the introduction of the WRPCG method. Some issues, relating to the boundary conditions, implementations of the PCG method, and weight definition, will be introduced in Section 5.3. Several unwrapping experiments using simulated data and the evaluation of the WRPCG method are introduced in Section 5.4. The unwrapping method and unwrapping experiments using real InSAR data are introduced in Section 5.5. Discussion and conclusion occur in Section 5.6.

5.2 Weighted Regularized PCG Method

5.2.1 Review of Least Squares Method

The PCG method was proposed in [264]; it is in essence a least squares method. Assuming that the wrapped phase is $M \times N$, the unweighted least squares method is based on minimizing the following objective function [264] [127],

$$\begin{aligned}
F = & \sum_{i=0}^{M-2N-1} \sum_{j=0}^{N-1} [\phi(i+1, j) - \phi(i, j) - h_x(i, j)]^2 \\
& + \sum_{i=0}^{M-1} \sum_{j=0}^{N-2} [\phi(i, j+1) - \phi(i, j) - h_y(i, j)]^2, \tag{5.1}
\end{aligned}$$

where

$$\begin{aligned}
h_x(i, j) &= W[\varphi(i+1, j) - \phi(i, j)], \\
h_y(i, j) &= W[\varphi(i, j+1) - \phi(i, j)], \tag{5.2}
\end{aligned}$$

where $\phi(i, j)$, $\varphi(i, j)$ denotes the unwrapped and wrapped phase, respectively; $W(a)$ is a wrapping process to limit the value of a to the range of $[-\pi, \pi)$.

5.2.2 Weighted Regularized PCG Method

The regularization process uses some *a priori* information from the phase map and provides some constraints on the minimization problem [261] [262]. The original PCG method does not use any regularization processes for the unwrapping.

There are many regularization functions for the phase unwrapping [261] [262] [263] [265] [277]. For different applications, different *a priori* information can be provided; therefore, different regularizations should be used. For InSAR, there are many error sources for the phase unwrapping [255] [136] [274] [275]. Most error sources of the phase data can be evaluated according to the amount and distribution of the residues in the phase map [142] [276]. The essence of residue is that it reflects the discontinuity in the wrapped phase [142] [276] [278]. In this Chapter, we combine the weighted PCG method [264] with the regularized terms in [262] to improve the robustness for the phase unwrapping and reduce the influence of discontinuities in the wrapped phase. The reason that we choose the regularization terms in [262] is that these regularization terms reduce

the influence of phase discontinuity (or residue) in the unwrapping [262] [265], thus making it potentially attractive for unwrapping of InSAR phase data. In the proposed WRPCG method, the weights and regularization are simultaneously used in the phase unwrapping; therefore this method can be used on the InSAR phase unwrapping especially when the phase quality is low.

Assuming that the wrapped phase map can be divided into the valid area V and invalid area I (the valid and invalid areas can be classified according to different criteria for different data sets which will be discussed in the following section), the proposed method is based on the following objective function:

$$\begin{aligned}
F = & \sum_{[i,j] \in V} \chi(i, j) [\phi(i+1, j) - \phi(i, j) - h_x(i, j)]^2 \\
& + \sum_{[i,j] \in V} \zeta(i, j) [\phi(i, j+1) - \phi(i, j) - h_y(i, j)]^2 + \delta R(i, j) \\
& + \varepsilon \sum_{[i,j] \in I} [\phi(i, j) - \phi(i-1, j)]^2 + \varepsilon \sum_{[i,j] \in I} [\phi(i, j) - \phi(i, j-1)]^2, \quad (5.3)
\end{aligned}$$

where

$$\begin{aligned}
R(i, j) = & \sum_{[i,j] \in V \cup I} \{ \phi(i, j) - \phi(i-1, j) + [\phi(i-1, j-1) - \phi(i, j-1)] \\
& + [\phi(i, j-1) - \phi(i, j)] + [\phi(i-1, j) - \phi(i-1, j-1)] \}^2. \quad (5.4)
\end{aligned}$$

In this objective function, the first and second terms are the same as in the weighted least squares method. $\delta R(i, j)$ is a regularization term which penalizes the data with discontinuities [262] [265]; it was used in [262] to constrain the phase consistency, and was also used in [265]. Compared to the definition of residue, this regularization is very similar to the computation of residue; the main difference is that, in the computation of residue, the phase difference is wrapped to $[-\pi, \pi)$ while this regularization is without this

processing. Due to this similarity, the penalization of the data with discontinuities also means the data around the residues are penalized. The fourth and fifth terms were also used in [262], which are the regularization terms aim to processing the invalid data [262]. On the other hand, these terms only exist in the specified areas of the data [262]: The first and second terms exist in the valid area, the third term exists in both valid and invalid areas, while the fourth and fifth terms exist only in the invalid areas. $\chi(i, j)$ and $\zeta(i, j)$ are the user-defined weights in the row and column directions, respectively. In the valid areas, the data are weighted by the user-defined weights, unlike [262], where no weight is applied. δ and ε are the parameters of the regularized term: δ should be big enough and ε should be small enough for the regularization [262].

This minimization problem can be solved by solving the following partial differential equation [270]:

$$\frac{\partial}{\partial i} \left(\frac{\partial F}{\partial \phi} \right) + \frac{\partial}{\partial j} \left(\frac{\partial F}{\partial \phi} \right) = 0. \quad (5.5)$$

Using a method similar to that in [261], the derivatives of ϕ and h are computed with respect to i and j , respectively, and the terms are rearranged to give an equation of the form

$$Q\phi = \mu, \quad (5.6)$$

where

$$Q\phi = E_{\chi\zeta} + E_{\delta} + E_{\varepsilon}, \quad (5.7)$$

and

$$\begin{aligned} \mu(i, j) = & \chi(i, j)h_x(i, j) - \chi(i-1, j)h_x(i-1, j) \\ & + \zeta(i, j)h_y(i, j) - \zeta(i, j-1)h_y(i, j-1). \end{aligned} \quad (5.8)$$

In (5.7), the definitions of E_{χ_ζ} , E_δ , and E_ε are as (5.9a), (5.9b), and (5.9c), respectively, which are as follows:

$$E_{\chi_\zeta} = \chi(i-1, j)[\phi(i, j) - \phi(i-1, j)] - \chi(i, j)[\phi(i+1, j) - \phi(i, j)] \\ + \zeta(i, j-1)[\phi(i, j) - \phi(i, j-1)] - \zeta(i, j)[\phi(i, j+1) - \phi(i, j)], \quad (5.9a)$$

$$E_\delta = \delta\{[\phi(i, j) - \phi(i-1, j)] - [\phi(i+1, j) - \phi(i, j)] \\ + [[\phi(i-1, j-1) - \phi(i, j-1)] - [\phi(i, j-1) - \phi(i+1, j-1)]] \\ + [[\phi(i, j-1) - \phi(i, j)] - [\phi(i, j) - \phi(i, j+1)]] \\ + [[\phi(i-1, j) - \phi(i-1, j-1)] - [\phi(i-1, j+1) - \phi(i-1, j)]]\}, \quad (5.9b)$$

$$E_\varepsilon = \varepsilon\{[\phi(i, j) - \phi(i-1, j)] - [\phi(i+1, j) - \phi(i, j)] \\ + [\phi(i, j) - \phi(i, j-1)] - [\phi(i, j+1) - \phi(i, j)]\}. \quad (5.9c)$$

In Equations (5.9a)-(5.9c), all the terms for both valid and invalid areas are included, and they need to be separated as further discussed in Section 5.3. As expressed in (5.8), μ is defined as the weighted Laplacian in [264] [127].

5.2.3 Valid and Invalid Data Areas

The regularization method in [262] differentiates the data into different areas of valid and invalid phase data. In the real applications of InSAR phase unwrapping, we do not know which area is valid or invalid before we do the unwrapping; therefore we should first classify the data into valid and invalid according to some criteria before the unwrapping step, as the discussion in the following section. In the method in [261] [262], the phase data are simply differentiated as valid and invalid, but when there are noisy regions of the wrapped phase in the valid areas, we need to use the weights to improve

the unwrapping accuracy. In the proposed method, the wrapped phases are separated into valid and invalid, and the valid data components are weighted according to the phase quality.

1) For the areas with valid data, the $Q\phi = \mu$ is formulated as

$$Q\phi = E_{\chi\zeta} + E_{\delta}, \quad (5.10)$$

and the definition of $\mu(i, j)$ is the same as (5.8).

2) For the areas with invalid data, the $Q\phi = \mu$ is formulated as

$$Q\phi = E_{\delta} + E_{\varepsilon}, \quad (5.11)$$

and the definition of $\mu(i, j)$ is the same as (5.8).

In the method of [262], $\mu(x, y) = 0$ in the invalid areas. In the proposed method, in the area of invalid data, we replace this with (5.8). This is because we found that setting $\mu(x, y) = 0$ reduced the robustness of the method when used in the computation of the Laplacian in the invalid data area.

5.3 Implementation of the WRPCG Method

5.3.1 Border Manipulation

In the solution of (5.6), we use the fast cosine transform method of [264]. This requires an appropriate arrangement of border conditions. As noted in [261] [262] [264] [127], the border term should be carefully defined to get a workable boundary condition. We will test two different boundary conditions in the WRPCG method. Assuming the data size is $M \times N$, the two boundary conditions are defined as follows:

5.3.1.1 Boundary Condition One: Boundary condition one is a simplified boundary

condition. The process here is to define the phase values outside the boundary as the data inside the boundary according to a partly symmetric assumption. The complete symmetric assumption is that the data outside the boundary should be symmetric with the data inside the boundary, using the data on the boundary as the symmetric axis [127]. Some conditions of boundary condition one conform to the symmetric assumption, while others do not. We therefore refer to it as a partly symmetric boundary condition. Boundary condition one is defined by the following conditional expressions (5.12a)-(5.12g):

$$\phi(i, j) - \phi(i-1, j) = \begin{cases} \phi(i, j) - \phi(i-1, j), 1 \leq i \leq M-1 \\ \phi(i, j) - \phi(i+1, j), i = 0 \end{cases} \quad (5.12a)$$

$$\phi(i, j) - \phi(i, j-1) = \begin{cases} \phi(i, j) - \phi(i, j-1), 0 \leq j \leq N-2 \\ \phi(i, j) - \phi(i, j+1), j = N-1 \end{cases} \quad (5.12b)$$

$$\phi(i+1, j) - \phi(i, j) = \begin{cases} \phi(i+1, j) - \phi(i, j), 0 \leq i \leq M-2 \\ \phi(i-1, j) - \phi(i, j), i = M-1 \end{cases} \quad (5.12c)$$

$$\phi(i, j+1) - \phi(i, j) = \begin{cases} \phi(i, j+1) - \phi(i, j), 0 \leq j \leq N-2 \\ \phi(i, j-1) - \phi(i, j), j = N-1 \end{cases} \quad (5.12d)$$

$$\phi(i-1, j-1) = \begin{cases} \phi(i-1, j-1), 1 \leq i \leq M-1, 1 \leq j \leq N-1 \\ \phi(i+1, j+1), i = 0, j \leq N-2 \\ \text{or } 0 \leq i \leq M-2, j = 0 \\ \phi(i, j), \text{ otherwise} \end{cases} \quad (5.12e)$$

$$\phi(i-1, j+1) = \begin{cases} \phi(i-1, j+1), 1 \leq i \leq M-1, 0 \leq j \leq N-2 \\ \phi(i+1, j-1), i = 0, 1 \leq j \leq N-1 \\ \text{or } 0 \leq i \leq M-2, j = N-1 \\ \phi(i, j), \text{ otherwise} \end{cases} \quad (5.12f)$$

$$\phi(i+1, j-1) = \begin{cases} \phi(i+1, j-1), 0 \leq i \leq M-2, 1 \leq j \leq N-1 \\ \phi(i-1, j+1), i = M-1, 0 \leq j \leq N-2 \\ \text{or } 1 \leq i \leq M-1, j = 0 \\ \phi(i, j), \text{ otherwise} \end{cases} \quad (5.12g)$$

The first four of these conditions ((5.12a)-(5.12d)) are the same as those of [127], while the remainder ((5.12e)-(5.12g)) are new.

Boundary condition one is not a condition completely based on the assumption that the data are symmetric with the border as the symmetric axis [127]. In the expressions (5.12a)-(5.12d) and the first three cases of (5.12e)-(5.12g), the boundary condition follows the symmetric assumption. In the “otherwise” of (5.12e), $\phi(i-1, j-1) = \phi(i, j)$; this is similar to the boundary condition in [264] which does not conform with the symmetric assumption. Similarly, in the “otherwise” of expressions (5.12f) and (5.12g), the boundary conditions are similar to those in [264] and are not conformed with the symmetric assumption. Therefore, the boundary condition one is not completely symmetric with the border as the symmetric axis. Because this is a partly symmetric boundary condition, for different parts of the boundary, the data may define their values in different ways because of the symmetric and non-symmetric boundary arrangements existing in the same method. This may cause an inconsistency in the boundary area and thus cause unstable unwrapping results. Since, in boundary condition one, instabilities may result from these deviations from the symmetric assumption, this motivates us to introduce boundary condition two.

5.3.1.2 Boundary Condition Two: This boundary condition differs from the first, in that it is the phase difference at the boundary rather than the phase itself that is arranged to obtain a symmetric boundary. The first four conditions in boundary condition two are the same as in boundary condition one, namely (5.12a)-(5.12d); the remaining four conditions are defined in (5.13a)-(5.13d):

$$\begin{aligned}
& \phi(i-1, j-1) - \phi(i, j-1) \\
& = \begin{cases} \phi(i-1, j-1) - \phi(i, j-1), 1 \leq i \leq M-1, 1 \leq j \leq N-1 \\ \phi(i+1, j-1) - \phi(i, j-1), i=0, 1 \leq j \leq N-1 \\ \phi(i+1, j+1) - \phi(i, j+1), i=0, j=0 \\ \phi(i-1, j+1) - \phi(i, j+1), 1 \leq i \leq M-1, j=0 \end{cases} \quad (5.13a)
\end{aligned}$$

$$\begin{aligned}
& \phi(i, j-1) - \phi(i+1, j-1) \\
& = \begin{cases} \phi(i, j-1) - \phi(i+1, j-1), 0 \leq i \leq M-2, 1 \leq j \leq N-1 \\ \phi(i, j-1) - \phi(i-1, j-1), i=M-1, 1 \leq j \leq N-1 \\ \phi(i, j+1) - \phi(i-1, j+1), i=M-1, j=0 \\ \phi(i, j+1) - \phi(i+1, j+1), 0 \leq i \leq M-2, j=0 \end{cases} \quad (5.13b)
\end{aligned}$$

$$\begin{aligned}
& \phi(i-1, j) - \phi(i-1, j-1) \\
& = \begin{cases} \phi(i-1, j) - \phi(i-1, j-1), 1 \leq i \leq M-1, 1 \leq j \leq N-1 \\ \phi(i+1, j) - \phi(i+1, j-1), i=0, 1 \leq j \leq N-1 \\ \phi(i+1, j) - \phi(i+1, j+1), i=0, j=0 \\ \phi(i-1, j) - \phi(i-1, j+1), 1 \leq i \leq M-1, j=0 \end{cases} \quad (5.13c)
\end{aligned}$$

$$\begin{aligned}
& \phi(i-1, j+1) - \phi(i-1, j) \\
& = \begin{cases} \phi(i-1, j+1) - \phi(i-1, j), 1 \leq i \leq M-1, 0 \leq j \leq N-2 \\ \phi(i+1, j+1) - \phi(i+1, j), i=0, 0 \leq j \leq N-2 \\ \phi(i+1, j-1) - \phi(i+1, j), i=0, j=N-1 \\ \phi(i-1, j-1) - \phi(i-1, j), 1 \leq i \leq M-1, j=N-1 \end{cases} \quad (5.13d)
\end{aligned}$$

Condition two is different from condition one because condition two considers the phase difference instead of phase value in the boundary area. All the conditions in boundary condition two conform to the assumption that the data are symmetric, using the border as the symmetric axis [127]. Therefore, boundary condition two is a complete symmetric boundary condition and the unwrapping method using boundary condition two is more stable than that using boundary condition one.

5.3.2 PCG Method

In [262], a fast unwrapping method based on a fast Fourier transform (FFT) and the PCG method was proposed; however, the user-defined weights were not considered. In

this paper, we used a method similar to that in [264] to solve the weighted regularized unwrapping problem using a fast cosine transform and the PCG method.

The processing steps of the proposed method are as follows.

- 1) Let $\mathbf{d}_0 = \boldsymbol{\mu}$.
- 2) Solve the equation $\mathbf{Q}\mathbf{e} = \boldsymbol{\mu}$ using the fast cosine transform method described in [264].
- 3) When $m = 0$, set $\mathbf{p}_1 = \mathbf{e}_0$. Otherwise, set $\gamma_{m+1} = \mathbf{d}_m^T \mathbf{e}_m / \mathbf{d}_{m-1}^T \mathbf{e}_{m-1}$, $\mathbf{p}_{m+1} = \mathbf{e}_m + \gamma_{m+1} \mathbf{p}_m$.
- 4) In computing the $\boldsymbol{\Theta} = \mathbf{Q}\mathbf{p} = \mathbf{Q}\boldsymbol{\phi}$, the data should be classified into valid and invalid areas. Compute $\boldsymbol{\Theta} = \mathbf{Q}\mathbf{p} = \mathbf{Q}\boldsymbol{\phi}$ using $\mathbf{Q}\boldsymbol{\phi}$ from (5.10) for the valid data area, and $\boldsymbol{\Theta} = \mathbf{Q}\mathbf{p} = \mathbf{Q}\boldsymbol{\phi}$ using $\mathbf{Q}\boldsymbol{\phi}$ from (5.11) for the invalid data area. Note: when we compute $\boldsymbol{\Theta}$, the border conditions are used.
- 5) Set $\lambda_{m+1} = \mathbf{d}_m^T \mathbf{e}_m / \boldsymbol{\Theta} \mathbf{p}_{m+1}$, $\phi_{m+1} = \phi_m + \lambda_{m+1} \mathbf{p}_{m+1}$, $\mathbf{d}_{m+1} = \mathbf{d}_m - \lambda_{m+1} \boldsymbol{\Theta}$.
- 6) When the iteration times are reached, end the processing; otherwise go to step 2). In the literature, there are several criteria which are designed to determine when to terminate the iteration, such as the methods described in [283] and [261]. In the WRPCG method, we use the method of [283], which is to compare the difference of the unwrapped phases between the neighboring iterations, and end the iteration when the difference between the neighboring iterations is lower than a preset value.

In these steps, step 4) is the key step in the WRPCG method: by using the (5.10) and (5.11) for the valid and invalid areas, respectively, the regularization terms are combined in the PCG method. In (5.10) as well as the computation of the Laplacian, the weights are used. For the real applications, there should be a step to differentiate the valid and invalid area. This implementation is based on the traditional PCG method in [264] [127], but by

using the fast cosine transform it is different from the method in [262], which uses the FFT.

5.3.3 Weight Selection

We use the same weight definition as in [264] [127], which is

$$\chi(i, j) = \min(\kappa_{i+1, j}^2, \kappa_{i, j}^2), \quad (5.14a)$$

$$\zeta(i, j) = \min(\kappa_{i, j+1}^2, \kappa_{i, j}^2), \quad (5.14b)$$

where $\kappa_{i, j}$ is the weight in the (i, j) pixel of the quality map. There are many kinds of quality maps [127] [268] [281] [282], appropriate to different applications. For the unwrapping of InSAR data, we mostly use the phase derivative variance (PDV) [268] [127] and maximum phase gradient (MPG) [127]. (For the definitions of PDV and MPG, please refer to [127]).

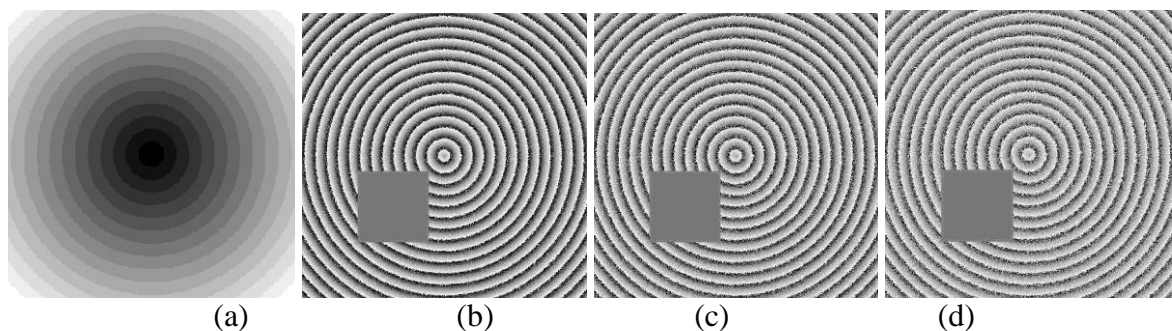


Figure 5.1. The original phase before wrapping and the wrapped phase. (a) Correct unwrapped phase. (b)-(d) are the wrapped phases contaminated by Gaussian noise when the noise variance is 0.5, 0.7, and 0.9, respectively.

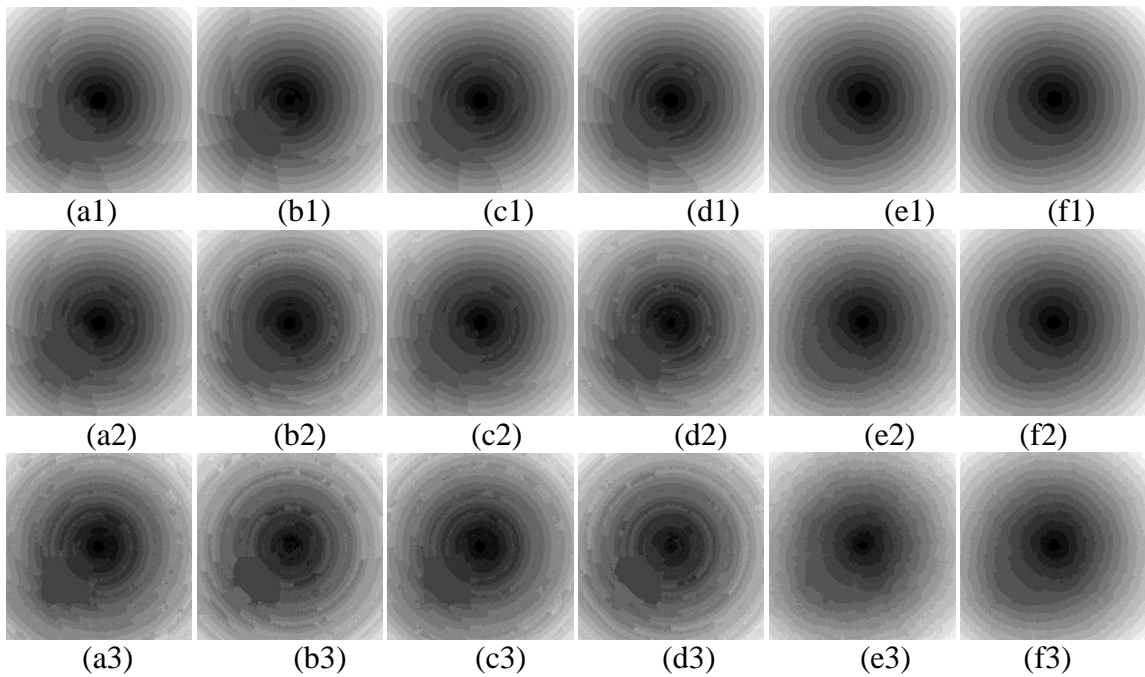


Figure 5.2. The unwrapped phase results for the simulated data in Figure 5.1. In these experiments, we use the PDV as a quality map. The first, second, and third rows are the unwrapping results using different methods when the noise variance of the input data is 0.5 (Figure 5.1 (b)), 0.7 (Figure 5.1 (c)), and 0.9 (Figure 5.1 (d)), respectively. (a1)-(a3) are the unwrapping results using the multigrid method in [268] [127], with weights; the quality map is thresholded. (b1)-(b3) are the unwrapping results using the multigrid method in [268] [127], with weights, but the quality map is not thresholded. (c1)-(c3) are the unwrapping results using the original PCG method in [264] [127], with weights; the quality map is thresholded. (d1)-(d3) are the unwrapping results using the original PCG method in [264] [127], with weights, but the quality map is not thresholded. (e1)-(e3) are the unwrapping results using the WRPCG method, $\delta = 1200$, $\varepsilon = 0.015$, no weights, and boundary condition one. (f1)-(f3) are the unwrapping results using the WRPCG method, $\delta = 1200$, $\varepsilon = 0.015$, with weights, and boundary condition one; the quality map is not thresholded.

5.4 Unwrapping Experiments on Simulated Data

5.4.1 Simulated Data

In order to give a quantitative evaluation of the WRPCG method, we have performed several experiments on the simulated wrapped phase. This simulated data are similar to the data used in [280]: the main difference is that an area with missing phase data is added in the simulated data. In this simulated data set (as shown in Figure 5.1), the total data size is 512×512 , and it includes a 128×128 square subset containing no phase data. We denote this subset as an invalid area, while the remaining data are described as a valid area. These wrapped phase data are contaminated by Gaussian noise, with increasingly large noise variances 0.5, 0.7, and 0.9, respectively. For the simulated data, we know where the data are missing; therefore there is no need to find the area with missing data.

The phase before wrapping is shown in Figure 5.1 (a); this is also what the correct unwrapped phase should be. The wrapped phases of the simulated noisy data with increasing noise variance (0.5, 0.7, and 0.9) are illustrated in Figure 5.1 (b), Figure 5.1 (c), and Figure 5.1 (d), respectively; the square in the middle of the wrapped phase is the area with no phase data.

5.4.2 Unwrapping Experiment on Simulated Data

In order to test the unwrapping result of the WRPCG method, the unwrapping experiments of the original PCG method [264] [127] and the multigrid method [268] [127] are also conducted for performance comparison. In all the experiments described in this chapter, the quality map is averaged in a 3×3 window as suggested in [127] and the unwrapping results are obtained after 30 iterations for the WRPCG and PCG methods,

and after 4 iterations for the multigrid method.

After 30 iterations, WRPCG and PCG algorithms are considered to be converged since further iterations do not improve the results significantly. Similarly, 4 iterations are adequate to achieve convergence of the multigrid algorithm. Therefore, the results are suitable for the comparison study.

Figure 5.2 shows the unwrapping results for the simulated data in Figure 5.1. In Figure 5.2, the first, second, and third rows show the unwrapping results of different methods when the noise variance of the input data is 0.5 (Figure 5.1 (b)), 0.7 (Figure 5.1 (c)), and 0.9 (Figure 5.1 (d)), respectively. (a1)-(a3) are the unwrapping results using the multigrid method in [268] [127] while the PDV is used as a quality map and the quality map is thresholded; (b1)-(b3) are the unwrapping results using the multigrid method in [268] [127] while the PDV is used as a quality map and the quality map is not thresholded; (c1)-(c3) are the unwrapping results using the weighted PCG method in [264] [127] while the PDV is used as a quality map and the quality map is thresholded; (d1)-(d3) are the unwrapping results using the weighted PCG method in [264] [127] while the PDV is used as a quality map and the quality map is not thresholded; (e1)-(e3) are the unwrapping results using the WRPCG method with no weight: the regularization parameters are $\delta = 1200$, $\varepsilon = 0.015$; (f1)-(f3) are the unwrapping results using the WRPCG method with weight, the PDV is used as a quality map, and not thresholded, and the parameters are $\delta = 1200$, $\varepsilon = 0.015$. In this experiment, in the WRPCG method, boundary condition one is used; the unwrapping result when using boundary condition two is similar to condition one; therefore in order to save space, the unwrapping result of boundary condition two is omitted here.

TABLE 5.1
MEAN RELATIVE ERROR, STANDARD DEVIATION OF UNWRAPPING ERROR, AND RMSE OF THE UNWRAPPING RESULT

Data and Parameter				Error Metrics (noise variance= 0.5) $\delta = 1200$, $\varepsilon = 0.015$	Error Metrics (noise variance= 0.5) $\delta = 9000$, $\varepsilon = 0.0025$	Error Metrics (noise variance= 0.7) $\delta = 1200$, $\varepsilon = 0.015$	Error Metrics (noise variance= 0.7) $\delta = 9000$, $\varepsilon = 0.0025$	Error Metrics (noise variance= 0.9) $\delta = 1200$, $\varepsilon = 0.015$	Error Metrics (noise variance= 0.9) $\delta = 9000$, $\varepsilon = 0.0025$
Multigrid [268] [127] with weight, threshold quality map.	PDV	ζ		0.0723486		0.106984		0.131636	
		ν		13.7430		14.5757		16.9482	
		τ		17.1540		20.9195		24.6555	
	MPG	ζ		0.0720922		0.307578		0.480783	
		ν		13.8618		35.5659		46.5899	
		τ		17.0974		45.0704		81.3470	
Multigrid [268] [127] with weight, not threshold quality map.	PDV	ζ		0.0931849		0.0955678		0.115453	
		ν		12.7954		13.5381		15.8681	
		τ		17.6380		18.4993		20.3108	
	MPG	ζ		0.0715647		0.0939449		0.129498	
		ν		13.6347		14.7578		17.2748	
		τ		16.8769		18.0749		23.7293	
PCG [264] [127] with weight, threshold quality map.	PDV	ζ		0.0923011		0.0979659		0.122683	
		ν		11.5350		13.7322		15.1089	
		τ		17.3620		19.2705		22.5253	
	MPG	ζ		0.0830878		0.321930		0.354781	
		ν		13.4914		26.4145		31.9377	
		τ		18.2129		48.0339		50.8089	
PCG [264] [127] with weight, not threshold quality map.	PDV	ζ		0.0783783		0.0906183		0.113122	
		ν		10.9839		13.4420		15.5101	
		τ		15.1362		17.1359		19.5049	
	MPG	ζ		0.0934688		0.157692		0.156875	
		ν		14.6788		17.6336		18.4822	
		τ		19.1668		27.7298		27.2029	
Boundary Condition One	WRPCG Method with weight	PDV	ζ	0.0668806	0.0667911	0.0732251	0.0698172	0.0665961	0.0652012
			ν	10.1517	10.1479	10.5090	10.4700	10.5311	10.5457
			τ	13.8263	13.8117	14.7046	14.2312	13.4927	13.1620
		MPG	ζ	0.0617150	0.0601976	0.0713062	0.0715910	0.0644896	0.0672019
			ν	10.1749	10.1666	10.5445	10.4782	10.3949	10.5556
			τ	13.3075	13.1295	14.2969	14.3714	12.6022	13.0105 (invert)
	WRPCG Method with no weight	PDV	ζ	0.0702864	0.0695064	0.0764416	0.0783375	0.0780758	0.0774673
			ν	10.1972	10.1972	10.6116	10.7000	11.5147	11.4872
			τ	14.1487	14.0787	15.0611	15.3165	13.9483	13.8182
		MPG	ζ						
			ν						
			τ						
Boundary Condition Two	WRPCG Method with weight	PDV	ζ	0.0668578	0.0664736	0.0732189	0.0734679	0.0663076	0.0671603
			ν	10.1564	10.1434	10.4534	10.4673	10.5487	10.5505
			τ	13.8305	13.7805	14.6933	14.7275	13.3984	13.5680
		MPG	ζ	0.0618698	0.0618610	0.0702133	0.0710902	0.0646967	0.0654481
			ν	10.1740	10.1926	10.5013	10.5811	10.4109	10.4885
			τ	13.3279	13.3354	14.1625	14.2434	12.6374	12.5644
	WRPCG Method with no weight	PDV	ζ	0.0708909	0.0703797	0.0770030	0.0751377	0.0771094	0.0785673
			ν	10.2066	10.1850	10.5963	10.5860	11.4669	11.5738
			τ	14.2136	14.1302	15.1332	14.8822	13.7609	13.8421
		MPG	ζ						
			ν						
			τ						

From Figure 5.2, we observe that the multigrid method and weighted PCG method have large global errors in the unwrapping result due to the invalid data in the wrapped phase. The WRPCG method without weights can eliminate the large scale unwrapping errors in the unwrapping result, but in the valid area, some unwrapping errors still exist. When weights are used in the proposed WRPCG method, the large scale unwrapping errors are eliminated and the errors in the valid area are further reduced due to the weights used in the unwrapping. For different noise levels, the different methods have similar results: the lower the noise level, the better the unwrapping result.

5.4.3 Evaluation and Discussion of the Unwrapping Results

In order to fully evaluate the unwrapping result, three evaluation methods are used. First, the mean relative error [273] is computed. (For the definition of mean relative error, please refer to [273].) Second, the standard deviation [271] [272] of the phase error is computed. (For the definition of standard deviation, please refer to [271] [272].) Finally, the root mean square error (RMSE) [244] is computed; the definition of RMSE is [244]

$$RMSE = \sqrt{\frac{1}{MN} \sum_{i=0}^{M-1} \sum_{j=0}^{N-1} [\phi_{correct}(i, j) - \phi_{unwrap}(i, j)]^2}, \quad (5.15)$$

where $\phi_{correct}(i, j)$ and $\phi_{unwrap}(i, j)$ are the correct unwrapped and real unwrapped phase, respectively. In addition, the invalid area is excluded in the computations of mean relative error, standard deviation, and RMSE computations.

It should be noted that, in the unwrapping result of the WRPCG method, the dynamic range is changed; therefore, we rescale the unwrapping result before computing the mean relative error, standard deviation of the phase error, and RMSE. This scaling is different from the scaling in [261] which rescales the shape of the unwrapped phase. In the

proposed method, the scaling is just to rescale the dynamic range of the unwrapped phase; the shape is not changed during the scaling.

Table 5.1 shows the mean relative error (ζ), standard deviation of the phase error (ν), and RMSE (τ) for different unwrapping methods using the PDV and MPG as quality maps, respectively.

From the unwrapping result, we found that the unwrapping result of the WRPCG method sometimes may get a unwrapping result which is totally the inverted version of the correct unwrapping result; therefore, we need to invert the unwrapping result when this happens (when the inversion operation is performed, we indicate by ‘invert’ in table 5.1). The inversion operation is $S(i, j) = \max(S) - S(i, j)$, where $S(i, j)$ is the unwrapped phase. The reason for this inversion is still not clear, but we found in our experiment that this inversion mostly occurs when the parameter δ is too large and with the boundary condition one. This first of these indicates that the parameter δ can not be too large, while the second suggests the instability associated with boundary condition one.

The major results to note from Table 5.1 are that the mean relative error, standard deviation of the phase error, and RMSE from all the experiments. These experiments include the various combinations of unwrapping algorithms, parameters, boundary conditions, noise level, etc.

Comparing the mean relative error, standard deviation, and RMSE of the unwrapping results of Table 5.1, we can get the following results.

5.4.3.1 Different Unwrapping Methods. For the weighted multigrid and PCG method, the mean relative error, standard deviation, and RMSE are all high compared to the WRPCG method. This is due to the large scale errors propagated from the invalid area.

When using the WRPCG method with no weights applied, the mean relative error, standard deviation, and RMSE are all reduced. When using the WRPCG method with weights, the mean relative error, standard deviation, and RMSE are further reduced.

5.4.3.2 Low and Moderate Noise Level. Now we compare the unwrapping results of Table 5.1 when the noise level is low or moderate (i.e. noise variance is 0.5 or 0.7). The mean relative error, standard deviation, and RMSE of the multigrid and weighted PCG method are all slightly higher than those of the WRPCG method with or without weight. The WRPCG method with weight mostly has lower mean relative error, standard deviation, and RMSE than the WRPCG method without weight. (Only one case is an exception: when noise variance is 0.5, $\delta = 9000$, $\varepsilon = 0.0025$, the weighted WRPCG method using MPG as weight obtains slightly higher standard deviation than the WRPCG method without weight. This means that, at a low noise level, the δ value should not be too high while the ε value should not be too low.) This indicates that the WRPCG method is slightly better than the multigrid and PCG method when the noise level is low or moderate. Since the WRPCG method is designed for the unwrapping of noisy data, it is not unexpected that only minor improvements are seen in low or moderate noise situations. On the other hand, the WRPCG method with weight is slightly better than the WRPCG without weight when the noise level is low or moderate.

5.4.3.3 High Noise Level. When the noise level is high (i.e. noise variance is 0.9), the WRPCG method with or without weight shows conspicuously lower mean relative error, standard deviation, and RMSE than the multigrid and PCG methods. This means the WRPCG method outperforms the multigrid and PCG method for the unwrapping of noisy phase data. When the noise level is high, for the WRPCG method with weight, the mean

relative error, standard deviation, and RMSE are all conspicuously lower than those of the WRPCG method without weight. This means that the WRPCG method with weight outperforms the WRPCG method without weight when the noise level is high. Comparing the mean relative error, standard deviation, and RMSE of the weighted and unweighted WRPCG methods, we found that the weighted method further reduces the unwrapping errors.

5.4.3.4 Impact of Boundary Conditions and Quality Maps. Now we compare the different boundary conditions and quality maps in the WRPCG method. For different boundary conditions in the proposed method, the mean relative error, standard deviation, and RMSE are similar; this means that both boundary condition one and two perform well in the unwrapping. (But, as previously noted, the inversion of the unwrapping result mostly happens when using boundary condition one, suggesting a stability problem owing to the lack of full symmetry. This shows the boundary condition two is more stable than condition one.) For the different quality maps, the unwrapping results vary. When the MPG is used as a quality map, the mean relative errors and RMSEs are mostly lower than those when the PDV is used as a quality map. When the MPG is used as a quality map, the standard deviations are sometimes lower than these when the PDV is used as a quality map, but sometimes higher than these when the PDV is used as a quality map.

5.4.3.5 Parameter Sensitivity of the WRPCG Method. For different parameters, the performance of the proposed method varies. For different parameters in the regularization term, δ should be big enough to penalize the discontinuous data, and ε should be small enough [262]. We conducted experiments using two sets of parameters: first, $\delta = 1200$, $\varepsilon = 0.015$; second $\delta = 9000$, $\varepsilon = 0.0025$. From Table 5.1, we found that the relative error,

standard deviation, and RMSE of the second case are sometimes lower than those of the first case, but sometimes are higher than those of the first case. Although from these evaluations we cannot say which parameter is better, because the inversions mostly occurred in the second case, this means that the second case is less stable than the first case.

5.4.3.6 Error Metrics. Comparing the different evaluation methods (mean relative error, standard deviation, and RMSE), we found that although each method has different characteristics, the same conclusion is achieved irrespective of the error metric.

In summary, the error performance shown in Table 5.1 indicates that the WRPCG method with weight outperforms the WRPCG method without weight, the weighted multigrid method in [268] [127], and the PCG method in [264] in terms of mean relative error, standard deviation, RMSE. This supports the conclusion of the visual comparison.

5.4.4 Memory Requirement and CPU Time

The memory requirement and processing time are important in phase unwrapping, as discussed in [127] for the PCG case. For the proposed WRPCG method for the unwrapping of real InSAR data, the memory requirement is slightly increased, relative to PCG, because two phase quality maps are needed (see Section 5.5 for the details): one is for the computation of weights, and the other is for the classification of valid and invalid areas. Compared to the PCG method, in which only one quality map is used [127], the WRPCG method needs slightly more memory than the PCG method.

As regards the CPU time, the WRPCG method only adds some steps for the classification of valid and invalid areas, and thus adds little computational time relative to the PCG method. Therefore, the WRPCG method has a slightly higher computational

time than the PCG method. For the unwrapping experiments in Table 5.1, the processing time varies slightly for different situations, but the average processing time for the PCG method is 12.5 s, while the average processing time for the WRPCG method is 13.6 s.

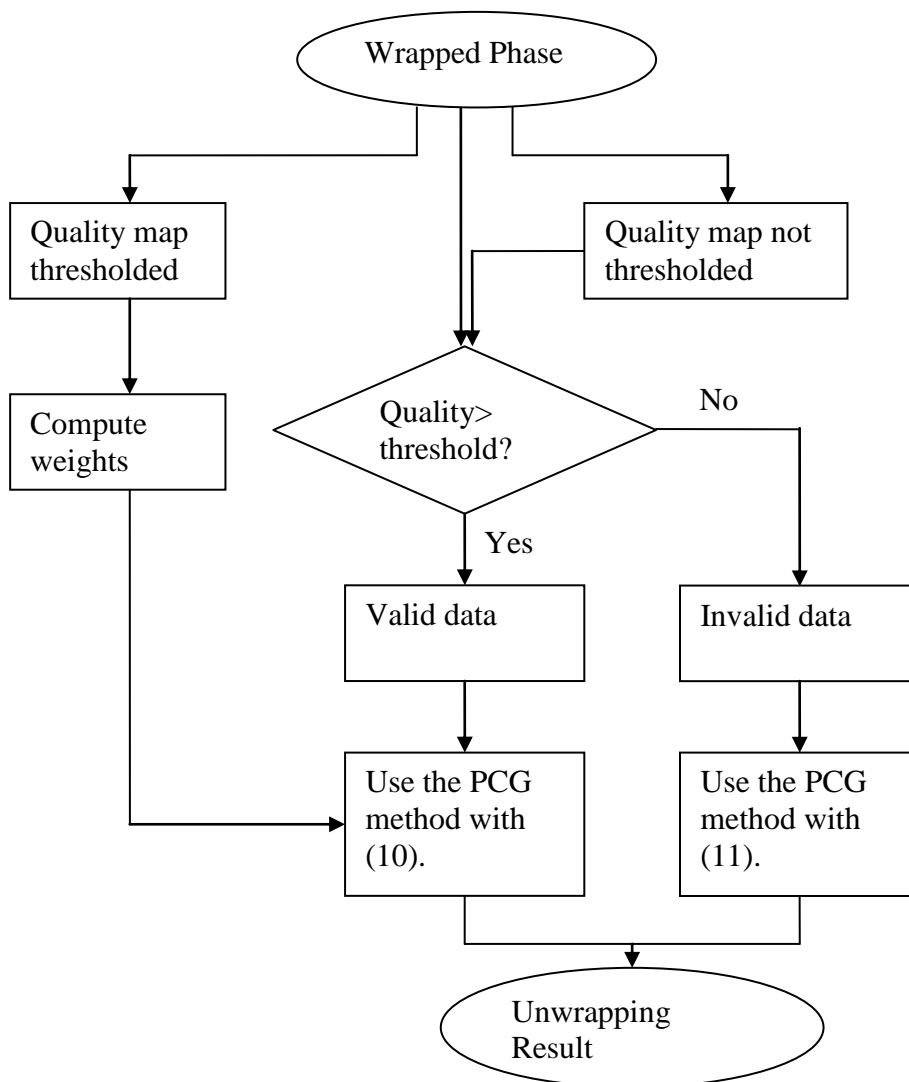


Figure 5.3. The flowchart of the WRPCG method when unwrapping the real SAR data.

5.5 Unwrapping Method and Experiments on Real SAR Data

5.5.1 Unwrapping Method for Real SAR Data

In this section, we apply the WRPCG method to real InSAR data. In the case of InSAR phase unwrapping, if the noise level is high, or the shadow or layover occurs in the wrapped phase [127] [134] [136] [274] [279], the phase data may be of very low quality. Therefore, when the phase quality is very low, we can classify these data as invalid data, otherwise, the data can be classified as valid data.

For the real InSAR data, the valid and invalid data should be differentiated according to the quality map. When the quality value is lower than a threshold, it is assumed that this area has invalid data; otherwise the data are considered valid. Because the quality map of the PCG method is generally thresholded before the computing of weights [127], we should use two quality maps in this processing: one is thresholded and is for the computing of weights, and the other is not thresholded and is used to differentiate the valid data from the invalid data; this means that the memory requirement for the WRPCG method is higher than that for the PCG method. The different processing methods of the data in valid and invalid areas are shown in the flowchart in Figure 5.3. First, the quality map is computed. Second, the quality map is used to compare a user-defined threshold for assignment of a valid/invalid label. If the quality value is lower than the threshold, we assign the data as invalid data; otherwise, we assign the data as valid data. Third, the quality map is thresholded to compute the weights for later processing. Fourth, for the valid data, we use the PCG method with (5.10); for the invalid data, we use the PCG method with (5.11).

For the real InSAR data, we should also rescale the unwrapping result; in order to do

this, we can use the ground truth or the crude digital elevation model (DEM) or light detection and ranging (LiDAR) [269] DEM.

5.5.2 Unwrapping Experiment on Real SAR Data

In this experiment, we use the polarimetric InSAR (PolInSAR) data which is after coherence optimization [16]. Similar to [255], the phase data with the lowest coherence are used to examine the unwrapping ability of the proposed method. In this experiment, the threshold is 0.3, and the quality map is in the range $[0,1]$; this means that data with quality lower than 0.3 are classified as an invalid area; otherwise they are classified as valid data.

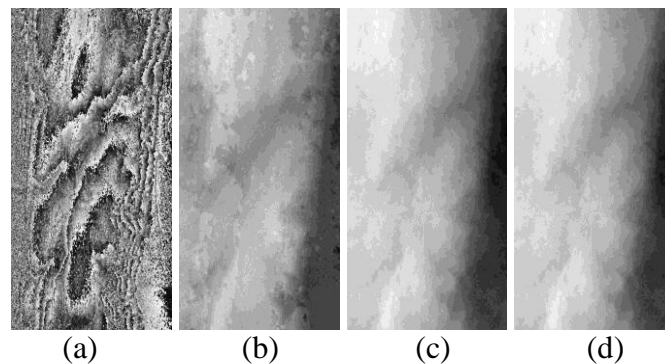


Figure 5.4. The wrapped phase and unwrapping result of the PolInSAR data. In this experiment, PDV is used as a quality map; the quality map is thresholded and fattened by two pixels using the method in [127]. (a) Wrapped phase (we use the same phase data as [255]). (b) Unwrapping result using the original PCG method in [264], with weight. (c) Unwrapping result using the WRPCG method, $\delta = 9000$, $\varepsilon = 0.0002$, with weight, and boundary condition one; the unwrapping result is inverted. (d) Unwrapping result using the WRPCG Method, $\delta = 9000$, $\varepsilon = 0.0002$, with weight, and boundary condition two.

In this experiment, we use the same phase data as [255]; the wrapped phase of the phase data set with the lowest coherence is shown in Figure 5.4(a). The unwrapping result of the weighted PCG method [264] [127] is illustrated in Figure 5.4(b): the PDV quality map is thresholded and fattened by two pixels using the method in [127]. In the unwrapping result of the weighted PCG method, several large scale unwrapping errors (the discontinuities in the unwrapped result [127]) occur. The unwrapping result of the WRPCG method with weight and using boundary condition one is shown in Figure 5.4 (c). In Figure 5.4 (c), the unwrapping result is inverted in this figure because the unwrapping result is the inverted version of the correct unwrapping result. This inversion is believed due to the instability of boundary condition one. In Figure 5.4 (c), the large scale unwrapping errors are mostly eliminated. In this experiment, the boundary condition one is used, $\delta = 9000$, $\varepsilon = 0.0002$, and the PDV quality map is fattened by two pixels using the method in [127]. Figure 5.4 (d) shows the unwrapping result of the WRPCG method with weight and using boundary condition two while the other parameters are the same as Figure 5.4 (c). Compare the unwrapping result of condition one and two, we found that boundary condition one and two have a similar unwrapping result apart from the inversion. In the unwrapping result of the WRPCG method with weight, the large scale unwrapping errors are mostly eliminated; this provides a better unwrapped phase than the weighted PCG method in [264].

5.6 Discussion and Conclusion

In this chapter, the WRPCG phase unwrapping method is proposed. The WRPCG method combines weights in the regularized PCG method as well the use of the fast

cosine transform to compute the preconditioner of the PCG method. By applying regularization and weights in the same unwrapping method, the WRPCG method not only reduces the large scale unwrapping errors that occur in the traditional weighted PCG method when some of the phase data are missing, but also improves the unwrapping accuracy in the valid area. Two boundary conditions are introduced in solving the boundary problem. Boundary condition one is a simplified boundary condition, and sometimes may cause unstable unwrapping results. Boundary condition two is completely symmetric and is more stable than condition one.

The unwrapping result of simulated data shows that the WRPCG method reduces the large scale unwrapping errors in the PCG method. Several quantitative evaluation methods are used to evaluate the proposed method. The WRPCG method further reduced the unwrapping errors in terms of relative error, standard deviation, RMSE, and visual evaluation.

The implementation of the WRPCG method for real InSAR data was also introduced. The WRPCG method is applied on the real PolInSAR phase unwrapping. The unwrapping results showed that the WRPCG method reduced the large scale phase unwrapping errors which exist in that of the traditional PCG method.

In summary, the WRPCG method achieves better unwrapping results than the traditional PCG method by combining the weights and regularization, at a cost of algorithm complexity and slightly more processing time.

CHAPTER 6: USING SECOND ORDER RESIDUE IN POLINSAR PHASE UNWRAPPING⁵

In this chapter, the residue is extended to the second order, which is called second order residue. Second order residue is researched and applied in the interferometric synthetic aperture radar (SAR) phase unwrapping. Similar to the residue, the second order residue reflects the discontinuity in the wrapped phase. In phase unwrapping, the traditional residue is normally used to form the branch cut according to some criterions. The second order residue can be directly or indirectly used as quality map. The second order residue is used as quality map in the polarimetric interferometric SAR (PolInSAR) phase unwrapping. The experiments using real PolInSAR data show that the second order residue is a promising quality map in SAR phase unwrapping.

6.1 Introduction

Phase unwrapping is a very important technique in the interferometric SAR (InSAR) processing. Although there are many phase unwrapping algorithms in the literature [276] [287] [288] [268] [289] [136] [290] [127] [278] [291] [142], the unwrapping problem is still not fully solved due to its complexity. For different applications, the phase unwrapping has different difficulties. The special characteristics of InSAR imaging

⁵ © 2008 IEEE. Reprinted, with permission, from [Yong Bian and Bryan Mercer, “Using second order residue in PolInSAR phase unwrapping,” *Proceedings of the 2008 IEEE Radar Conference*, Rome, Italy, May 26-30, 2008, pp. 1-5.].

determine its phase unwrapping to be a very tough problem. Due to the layover [134], shadow [138], noise [150], etc, many phase unwrapping algorithms failed in the unwrapping of InSAR data [127] [136]. In order to improve the robustness against these low quality data, many phase unwrapping algorithms use quality map to guide the phase unwrapping [268] [136] [127] [276]. Therefore, phase quality map plays a key role in many phase unwrapping methods. The correct usage of phase quality map determines the unwrapping accuracy of many phase unwrapping algorithms. There are many types of quality maps for many applications. In this research, the second order residue is introduced and applied as quality map on the InSAR phase unwrapping.

The residue [142] indicates the phase quality but can not be directly used as quality map. The branch cut method [142] connects the residue to avoid the integration path across the branch cuts which connects the residues [142]. Recently, more and more researches are focusing on the relationship between phase gradient and residue in order to get a better quality map [276] [291]. Also, second difference [289] [287] [288] was used to measure the phase quality in optical phase unwrapping but not used in the SAR phase unwrapping. In this paper, we propose the second order residue based on the second difference and use the second order residue as the quality map in the polarimetric InSAR (PolInSAR) [16] phase unwrapping. In PolInSAR, there are three wrapped phase in the output of coherence optimization [16]. Because these three wrapped phases have different levels of coherence and noise, we use these wrapped phases to test the noise immune ability of phase unwrapping.

This chapter is organized as following. Section 6.2 is the introduction of second order residue. Section 6.3 is the application of second order residue in the PolInSAR phase unwrapping. The final section is the conclusion.

6.2 Second Order Residue

6.2.1 Review of First Order Residue

The residue theory [142] is based on the assumption that the closed loop summation of the gradient should equal zero when the phase quality is high [276]. We call the residue as the first order residue here in order to differentiate the second order residue. The residue is computed by the neighboring four pixels (see Figure 6.1 (a)) [276], the computation of residue is as the following equation [290]:

$$\begin{aligned}
 R_f(i, j) = & [\Phi(i+1, j) - \Phi(i, j)] + [\Phi(i+1, j+1) - \Phi(i+1, j)] \\
 & + [\Phi(i, j+1) - \Phi(i+1, j+1)] + [\Phi(i, j) - \Phi(i, j+1)], \quad (6.1)
 \end{aligned}$$

where $R_f(i, j)$ means the first order residue, $\Phi(i, j)$ denotes the wrapped phase at the pixel (i, j) , $[\]$ means the wrapping processing to confine the phase difference to $[-\pi, \pi)$ [278]. The residue value only equals 0, 1 or -1 [276]. The residue of spiral data which was distributed with book [127] was illustrated in the Fig. 3 (b) of [276].

6.2.2 Second Order Residue

The second difference [289] [287] [288] was originally used as the quality map in

optical phase unwrapping but not applied on the InSAR data phase unwrapping. Here, we define the second order residue based on the second difference. The second order residue is based on a similar assumption as residue: the summation of the closed loop in the phase map of the second difference should be zero when the phase quality is high, which is the following equation:

$$\oint D_s = 0, \quad (6.2)$$

where D_s means the second difference in the wrapped phase map.

The first order residue is the smallest circle in the phase map. The second order residue is the second smallest circle in the phase map, which is computed using the eight pixels surrounding the center pixel. The definition of the second order residue is the summation of the second differences in a closed circle formed by eight pixels surrounding the center pixel (see Figure 6.1 (b)), this can be formulated as the equation:

$$\begin{aligned} R_s(i, j) = & \left[\left[\Phi(i+1, j+1) - \Phi(i+1, j) \right] - \left[\Phi(i+1, j) - \Phi(i+1, j-1) \right] \right] \\ & + \left[\left[\Phi(i+1, j-1) - \Phi(i, j-1) \right] - \left[\Phi(i, j-1) - \Phi(i-1, j-1) \right] \right] \\ & + \left[\left[\Phi(i-1, j-1) - \Phi(i-1, j) \right] - \left[\Phi(i-1, j) - \Phi(i-1, j+1) \right] \right] \\ & + \left[\left[\Phi(i-1, j+1) - \Phi(i, j+1) \right] - \left[\Phi(i, j+1) - \Phi(i+1, j+1) \right] \right], \end{aligned} \quad (6.3)$$

where $R_s(i, j)$ denotes the second order residue in pixel (i, j) , $[]$ means the wrapping processing to confine the phase difference to $[-\pi, \pi)$.

Similar to the first order residue, the second order residue have positive or negative values. Different to the first order residue, the second order residue can have the values

within $[-1,1]$. More important, the second order residue forms a structure similar to the residue vector which was proposed in [276] (See Figure 6.1 (c). Figure 6.1 (c) is the second order residue of the spiral data [127].), this is a very helpful characteristic in phase unwrapping. Similar to the residue vector, the second order residue shows the direction information of phase discontinuities. The residue vector needs the vertical and horizontal gradient maps to describe the residue vector in each direction respectively [276]. Differently, the second order residue uses one map to describe both the information of horizontal and vertical directions.

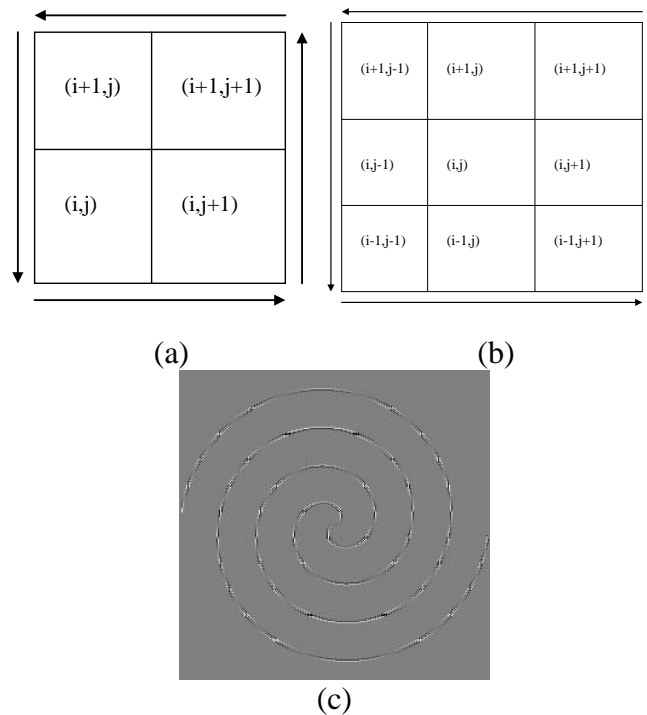


Figure 6.1. The first and second order residue. (a) The computation of first order residue [276]. (b) The definition of second order residue. (c) The second order residue of the spiral data, this data is distributed with [127].

Although the residue reflects the phase quality, the residue map can only be used in the branch cut setting and can not be directly used as the quality map. Recently, a residue vector method [276] was proposed which can be directly used as quality map. Similar to the residue vector, the second order residue can be used directly or indirectly as quality map. The second order residue of the spiral data (this spiral data is distributed with [127]) as is shown in Figure 6.1 (c) can be directly used as the quality map in phase unwrapping after some slightly arrangement which will be discussed in the next section. Fig. 3 (b) of [276] shows the first order residue in the spiral data (this data is distributed with the book [127] and also was used to show the residue vector in [276]). From Figure 6.1 (c) and compare the so called residue vector in [276], we found the second order residue shows the low quality area directly.

6.3 Phase Unwrapping Using Second Order Residue

6.3.1 Unwrapping Method Using Second Order Residue

We use the quality guided path following method (QGPF) [127] to examine the performance of the second order residue as quality map. The QGPF method begins unwrapping at the highest quality area, and then unwrap the area with the modest quality, finally unwrap the area with the lowest quality [127] [289], this unwrapping sequence prevents the error propagation in the unwrapping result. The unwrapping path is very important in the QGPF method, and the generation of unwrapping path depends on the correctness of quality map, therefore the quality map is the key problem in this method. In terms of these analyses, QGPF method is an ideal method to test the

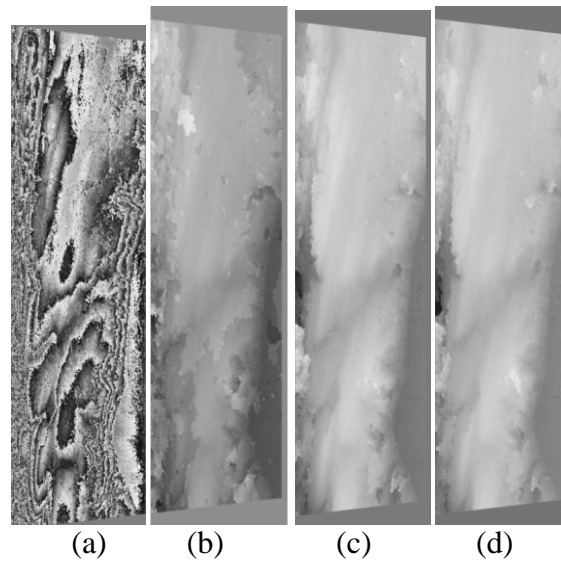


Figure 6.2. Unwrapping result of the QGPF method using the coherence and second order residue as quality map, the data is the third optimization data. (a) Wrapped phase of the third optimization. (b) Unwrapping result of QGPF method using coherence as quality map. (c) Unwrapping result of QGPF method using second order residue as quality map (*Method One*). (d) Unwrapping result of QGPF method using second order residue as quality map (*Method Two*).

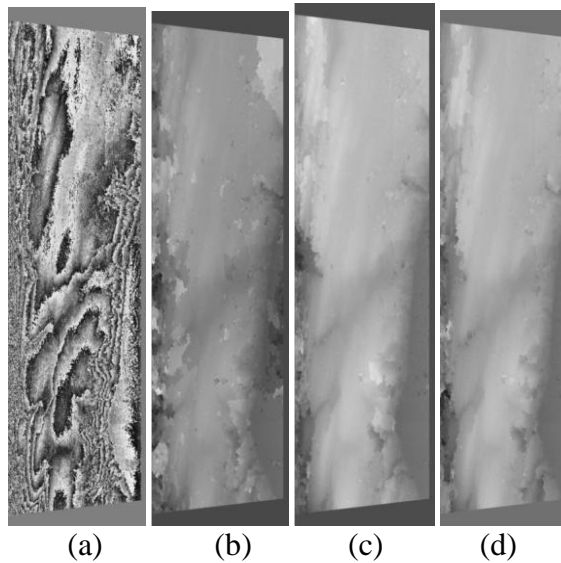


Figure 6.3. Unwrapping result of the QGPF method using the coherence and second order residue as quality map, the data is the second optimization data. (a) Wrapped phase of the second optimization. (b) Unwrapping result of QGPF method using coherence as quality map. (c) Unwrapping result of QGPF method using second order residue as quality map (*Method One*). (d) Unwrapping result of QGPF method using second order residue as quality map (*Method Two*).

performance of the phase quality map.

The second order residue can be easily used as quality map. In order to reduce the influence of noise in the wrapped phase, the second order residue should be averaged when it is used directly as quality map. The second way is to use the variance of second order residue to reduce the influence of noise.

Method One: The first way is to average the second order residue in a window, which is:

$$R_s^{average}(i, j) = \frac{1}{W} \sum_{i=m-W/2}^{m+W/2} \sum_{j=n-W/2}^{n+W/2} |R_s(i, j)|, \quad (6.4)$$

where $R_s^{average}(i, j)$ is the averaged second order difference in a $W \times W$ window. The average is used to reduce the influence of noise in the wrapped phase.

Method Two: The second method is to compute the variance of the second order residue. The variance of second order residue can be computed using a method similar to the computation of phase derivative variance [127] [268], which is computed using the equation:

$$R_s^{variance}(i, j) = \frac{1}{W^2} \sqrt{\sum_{i=m-W/2}^{m+W/2} \sum_{j=n-W/2}^{n+W/2} \left(R_s(m, n) - \bar{R}_s(i, j) \right)^2}, \quad (6.5)$$

where $\bar{R}_s(i, j)$ is the averaged second order residue in the $W \times W$ window, $R_s^{variance}(i, j)$ is the variance of second order residue centered at pixel (i, j) .

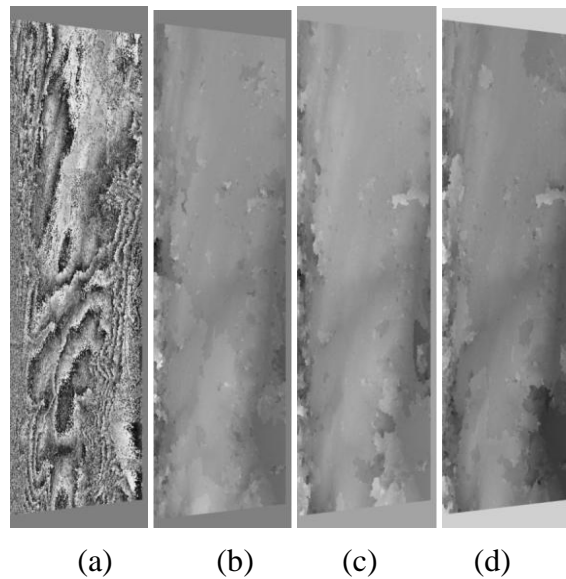


Figure 6.4. Unwrapping result of the QGPF method using the coherence and second order residue as quality map, the data is the first optimization data. (a) Wrapped phase of the first optimization. (b) Unwrapping result of QGPF method using coherence as quality map. (c) Unwrapping result of QGPF method using second order residue as quality map (Method One). (d) Unwrapping result of QGPF method using second order residue as quality map (Method Two).

6.3.2 Unwrapping Experiment and Result

In this experiment, we use the PolInSAR data to examine the performance of second order residue when it is used as quality map. The PolInSAR is using the coherence optimization [16] technique to improve the coherence and reduce the noise in the wrapped phase. In this experiment, we use the PolInSAR data acquired by the TOPOSAR system developed by Intermap Technologies Corp. as the test data. We use the wrapped phase after coherence optimization [16] to examine the performance of phase unwrapping. After coherence optimization, there are three new wrapped phases with

different coherence values which are illustrated in Figure 6.2 (a), Figure 6.3 (a), and Figure 6.4 (a) respectively. The first optimization (see Figure 6.4 (a)) has the lowest coherence and highest noise level, the second optimization (see Figure 6.3 (a)) has the moderate coherence and modest noise level, the third optimization (see Figure 6.2 (a)) has the highest coherence and lowest noise level. In the real application of PolInSAR system, only the wrapped phase with the highest coherence (here is the third optimization) is used to acquire the digital elevation model. Because the three optimization data have different levels of noises, these three optimization data can be used as a dataset to examine the unwrapping ability of phase unwrapping methods in different noise levels. Here we use these three wrapped phases to test the noise immune ability of the phase unwrapping algorithm using different phase quality maps.

The wrapped phase for the three optimizations are illustrated in Figure 6.2 (a), Figure 6.3 (a), and Figure 6.4 (a) respectively. The third, second, and first optimization data have 59374, 112495, and 239058 residues, respectively. The differences in the number of residues are due to the different levels of noises in the wrapped phases after coherence optimization [292]. In *Method One*, we use a 3×3 window in averaging. In *Method Two*, we use a 3×3 window in computing the variance of the second order residue. Several experiments are conducted to examine the unwrapping performance of the second order residue based QGPF method. We conduct experiments on *Method One* and *Method Two* respectively in order to compare their performances. Firstly, *Method One* is used to average the second order residue. The averaged second order residue is used as quality map in the QGPF method. This second order residue based QGPF method is used in the phase unwrapping of the three optimization dataset. The unwrapping result

of third, second, and first optimization data are illustrated in Figure 6.2 (c), Figure 6.3 (c), and Figure 6.4 (c) respectively. Secondly, we use the *Method Two* to compute the variance of second order residue and used it as quality map in the QGPF method. The unwrapping results of third, second, and first optimization data are showed in Figure 6.2 (d), Figure 6.3 (d), and Figure 6.4 (d) respectively.

Coherence is widely used as quality map in InSAR phase unwrapping [136], therefore we use the coherence as quality map to compare the performance with the second order residue. In order to examine the performance of second order residue, we conduct several experiments using the coherence as quality map on the same dataset. Figure 6.2 (b), Figure 6.3 (b), and Figure 6.4 (b) show the unwrapping result of QGPF method using coherence as quality map for the third, second, and first optimization data respectively. In computing the coherence, the data should be smoothed in the range and azimuth direction in order to reduce the influence of noise [127]. In these experiments, we smooth the data 13 pixels in range direction and 19 pixels in azimuth direction.

From these unwrapping results, we found:

- 1) For the third and second optimization data, both the *Method One* and *Method Two* outperforms the coherence quality map. In the unwrapping result of coherence, many large scale areas are wrongly unwrapping, which are the abrupt transition areas in the unwrapping result. Both unwrapping results of *Method One* and *Method Two* only have slightly errors. This means the second order residue is good in the unwrapping of low and moderate noise level data.
- 2) In the first optimization data, both the second order residue method and coherence have few large scale unwrapping errors. *Method One* has less unwrapping errors than

Method Two. This means in high noise level, the *Method One* is better than *Method Two*. In high noise level, second order residue has the similar performance with the coherence.

- 3) Compare the unwrapping errors in the three optimization data when using the coherence as quality map, we found the noise level do not influence very much the performance of phase unwrapping when coherence is used as quality map.

All in all, the second order residue outperforms the coherence as quality map when the noise level is low or moderate. The second order residue has the similar performance with coherence when the noise level is high.

6.4 Conclusion

In this chapter, the first order residue is extended to the second order residue. The second order residue can be directly used as the quality map in phase unwrapping because the more information is provided than the first order residue. The second order residue is a method to describe discontinuities in the wrapped phase. When the second order residue is directly used as quality map to guide the unwrapping, some preprocessing should be conducted such as compute the averaged values or the variance of the second order residue.

The unwrapping experiments on the PolInSAR data are conducted using the second order residue as quality map and QGPF method. The unwrapping experiments show that the second order residue as quality map outperforms the coherence as quality map in low and moderate noise level. When the noise level is high, large scale errors occurred in both the unwrapping results of second order residue and coherence.

CHAPTER 7: POLINSAR STATISTICAL ANALYSIS AND COHERENCE OPTIMIZATION USING FRACTIONAL LOWER ORDER STATISTICS⁶

In this chapter, the polarimetric synthetic aperture radar (SAR) interferometry (PolInSAR) statistical model is studied using the alpha-stable distribution. Based on this model, a vector coherence formulation using fractional lower order statistics (FLOS) is proposed. This vector coherence is the generalization of the vector coherence in [16] when the PolInSAR data are non-Gaussian and conform to the symmetrical form of the alpha-stable distribution. The standard coherence optimization method in [16] is modified based on this generalized vector coherence. Results were demonstrated using a small L-band PolInSAR data set and suggest that this proposed coherence optimization method reduces artifacts in the optimized phases in certain areas.

7.1 Introduction

Polarimetric synthetic aperture radar (SAR) interferometry (PolInSAR) is being studied in a number of application areas, including tree-height estimation [23], agricultural parameter estimation [296], urban area mapping [31], and digital-elevation-model extraction [297]. In the PolInSAR context, the coherence is a complex vector

⁶ © 2010 IEEE. Reprinted, with permission, from [Yong Bian and Bryan Mercer, “PolInSAR statistical analysis and coherence optimization using fractional lower order statistics,” *IEEE Geoscience and Remote Sensing Letters*, vol. 7, no. 2, pp. 314-318, April 2010.].

quantity, as described, for example, in [16] and [23]. The biophysical or geophysical parameters of interest are usually recovered by inversion from the phase and magnitude elements of this vector through the intermediary of an appropriate model [23], [91]. For a distributed target, the elements of the scattering matrix are stochastic variables. The extraction of information from this matrix requires that statistical parameters need to be estimated. However, estimation uncertainty introduces bias into the derived parameters [7], [300] due to the limited number of samples that can be used in the estimation. It is often assumed that the stochastic properties of the complex SAR images can be described by independent bivariate Gaussian distribution [143], and this assumption has been generalized to polarimetric channels and to each of the interferometric channels [298]. While this is supported by observation in many cases, there are circumstances in which the underlying assumptions of Gaussian statistics are not supported [298].

In this chapter, we introduce into the PolInSAR context the simplified form of the alpha-stable distribution, which allows for “heavy-tailed” distributions. It has been suggested by some authors [299], [160] that this type of distribution may be appropriate for areas consisting of nonhomogeneous scatterers, perhaps urban mixtures. Such an example was demonstrated for polarimetric L-band data in [199], and in this chapter, we extend the analysis to the PolInSAR case. Coherence optimization is fundamental to the application of PolInSAR technology, particularly in the context of separation of the underlying scattering mechanism, as first proposed in [16]. Several alternative approaches also appear in the literature including [293] [294] [295]. For purposes of this chapter, we will follow the approach of [16] in the context of the alpha-stable distribution.

This chapter is organized in the following manner. In Section 7.2 of this chapter, the statistical characteristics of PolInSAR data will be discussed using the alpha-stable distribution. Then, in Section 7.3, we apply fractional lower order statistics (FLOS) to the computation of the standard coherency matrices ($\mathbf{\Omega}_{12}$, \mathbf{T}_{11} , \mathbf{T}_{22}), based upon the alpha-stable distribution. Based on these new coherency matrices, the vector coherence in [16] is generalized to a formulation which can be used when the PolInSAR data conform to the alpha-stable distribution. We then formulate, in Section 7.4, a coherence optimization process based upon this generalized vector coherence and FLOS, by analogy with [16]. Experimental results for a particular data set are presented in Section 7.5 and conclusions are given in Section 7.6.

7.2 PolInSAR Statistical Analysis Using Alpha-stable Distribution

7.2.1 Review of Alpha-Stable Distribution

Since the probability density function (pdf) of the alpha-stable distribution does not generally exist in closed form [179], [176], it is approached through its characteristic function Φ , which represents the Fourier transform of its pdf. The full expression of $\Phi(\mathbf{t})$ is characterized by four parameters related to the mean location (μ), the skewness (β), a scale parameter (g), and its characteristic exponent (α). For analytical simplicity, we limit ourselves to the “isotropic symmetric” case [179], [176], equivalent to a zero-mean symmetric distribution. The characteristic function of isotropic symmetric alpha-stable distribution of complex data is then reduced to [182]

$$\Phi(\mathbf{t}) = \exp\left\{-g|\mathbf{t}|^\alpha\right\}. \quad (7.1)$$

In the special case $\alpha = 2$, the distribution becomes Gaussian, but as α gets smaller, the distribution function becomes “heavier tailed” and more strongly peaked. For the isotropic symmetric alpha-stable distribution, $\beta = 0$ and $\mu = 0$. Moreover, because of these characteristics, the second and higher order moments do not exist [179], [176] when $\alpha < 2$. Therefore, a different, but analogous approach, based upon FLOS is introduced in Section 7.3 to obtain the equivalent vector coherence.

7.2.2 PolInSAR Statistical Analysis Using Isotropic Symmetric Alpha-Stable

Distribution

The observed PolInSAR data set includes eight single-look complex images or channels, denoted as Z_{HHi} , Z_{HV_i} , Z_{VHi} , and Z_{VVi} , where $i = 1, 2$ refers to antennas 1 and 2, respectively. Assuming reciprocity [295], $HV = VH$, and the eight channels are reduced to six. The modeling of polarimetric SAR data as four-channel isotropic symmetric-distributed random complex variables was introduced in [199], and based on this scheme, we generalize the analysis of [199] to the PolInSAR case. We assume the PolInSAR data to be six-channel isotropic symmetric alpha-stable-distributed complex random variables Z , with \mathbf{k}_i vectors for antennas $i = 1$ and 2 written as

$$\mathbf{k}_i = \begin{pmatrix} Z_{HHi} \\ Z_{HV_i} \\ Z_{VVi} \end{pmatrix} \sim \begin{pmatrix} S(\alpha_{HHi}, 0, g_{HHi}, 0) \\ S(\alpha_{HV_i}, 0, g_{HV_i}, 0) \\ S(\alpha_{VVi}, 0, g_{VVi}, 0) \end{pmatrix} \quad (7.2)$$

where Z_{HH1} , Z_{HV1} , and Z_{VV1} are the master images in the HH, HV, and VV polarizations, respectively; Z_{HH2} , Z_{HV2} , and Z_{VV2} are the slave images in the HH, HV, and VV polarizations, respectively; and the symbol $S(\alpha, 0, g, 0)$ defines the parameters of the alpha-stable distribution.

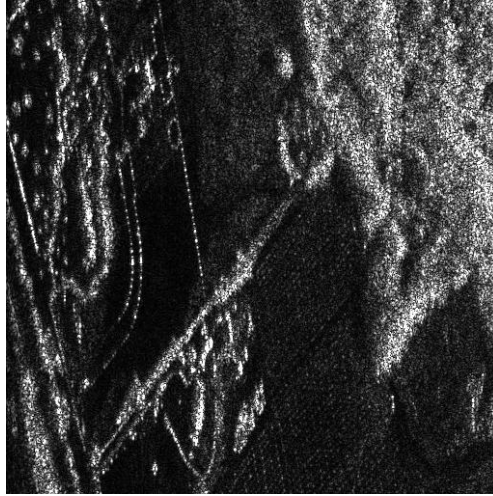


Figure 7.1. L-band PolInSAR image. Master image of HH.

In this model, there are 12 parameters that define the stochastic properties. We assume that the distributions associated with the two antennas are similar so that we can simplify to six parameters as follows: $\alpha_{HH1} \approx \alpha_{HH2}$, $\alpha_{HV1} \approx \alpha_{HV2}$, $\alpha_{VV1} \approx \alpha_{VV2}$, $g_{HH1} \approx g_{HH2}$, $g_{HV1} \approx g_{HV2}$, and $g_{VV1} \approx g_{VV2}$. In the following, only the characteristic exponents α are relevant to the proposed coherence optimization method based on FLOS and are estimated using the six input data channels.

7.3 Vector Coherence Based on FLOS

7.3.1 Review of Vector Coherence

In this chapter, “*”, “ T ”, and “ \dagger ” denote complex conjugate, transposition, and complex conjugate transposition, respectively. With $\mathbf{k} = [Z_{HH} \ \sqrt{2}Z_{HV} \ Z_{VV}]^T$ in lexicographic basis (for the Pauli basis, we can obtain a similar result), the standard vector coherence is given by [16], [295]:

$$\gamma = \frac{\omega_1^\dagger \mathbf{\Omega}_{12} \omega_2}{\sqrt{(\omega_1^\dagger \mathbf{T}_{11} \omega_1)(\omega_2^\dagger \mathbf{T}_{22} \omega_2)}} = |\gamma| \exp(j\theta) \quad (7.3)$$

where ω_i is the polarization choice for antennas 1 and 2, and the cross- and copolar matrices are given by

$$\mathbf{\Omega}_{12} = E(\mathbf{k}_1 \mathbf{k}_2^\dagger), \mathbf{T}_{11} = E(\mathbf{k}_1 \mathbf{k}_1^\dagger), \mathbf{T}_{22} = E(\mathbf{k}_2 \mathbf{k}_2^\dagger), \quad (7.4)$$

where E denotes the expectation operator.

As noted earlier, this representation is defined based on the second-order statistics [294] and is not applicable to isotropic symmetric alpha-distributions, where $\alpha < 2$, because the second-order moment becomes infinite [176].

7.3.2 Vector Coherence Based on FLOS

For alpha-stable distributions, the second-order moments do not exist when $\alpha < 2$ [179], and therefore, the matrix elements in (7.4) cannot be computed. If we assume that the PolInSAR data follow the alpha-stable distribution, then our approach is to use fractional lower order moments. In this chapter, we use the fractional lower order covariance as expressed in [165] to calculate the fractional lower moments, which are here defined as $\mathbf{\Omega}_{12}^{FLOS}$, \mathbf{T}_{11}^{FLOS} , and \mathbf{T}_{22}^{FLOS} by analogy with (7.4). (These converge to standard Gaussian-based covariance elements when $\alpha = 2$). We then define new \mathbf{k} vectors based upon the transformed Z variables:

$$\mathbf{k}^{(u)} = \begin{bmatrix} Z_{HH}^{(u)} & \sqrt{2} Z_{HV}^{(u)} & Z_{VV}^{(u)} \end{bmatrix}^T$$

where $Z^{(u)} = Z \cdot |Z|^{u-1}$, and subsequently compute revised matrices $\mathbf{\Omega}_{12}^{FLOS}$, \mathbf{T}_{11}^{FLOS} , and \mathbf{T}_{22}^{FLOS}

which are defined in (7.5a)-(7.5c), respectively.

$$\begin{aligned}
\mathbf{\Omega}_{12}^{FLOS} &= E\left(\mathbf{k}_1^{(u_1)} \mathbf{k}_2^{(u_2)\dagger}\right) \\
&= E \begin{bmatrix} Z_{HH1}|Z_{HH1}|^{\mu_{HH1}-1} Z_{HH2}^*|Z_{HH2}|^{\mu_{HH2}-1} & \sqrt{2}Z_{HH1}|Z_{HH1}|^{\mu_{HH1}-1} Z_{HV2}^*|Z_{HV2}|^{\mu_{HV2}-1} & Z_{HH1}|Z_{HH1}|^{\mu_{HH1}-1} Z_{VV2}^*|Z_{VV2}|^{\mu_{VV2}-1} \\ \sqrt{2}Z_{HV1}|Z_{HV1}|^{\mu_{HV1}-1} Z_{HH2}^*|Z_{HH2}|^{\mu_{HH2}-1} & 2Z_{HV1}|Z_{HV1}|^{\mu_{HV1}-1} Z_{HV2}^*|Z_{HV2}|^{\mu_{HV2}-1} & \sqrt{2}Z_{HV1}|Z_{HV1}|^{\mu_{HV1}-1} Z_{VV2}^*|Z_{VV2}|^{\mu_{VV2}-1} \\ Z_{VV1}|Z_{VV1}|^{\mu_{VV1}-1} Z_{HH2}^*|Z_{HH2}|^{\mu_{HH2}-1} & \sqrt{2}Z_{VV1}|Z_{VV1}|^{\mu_{VV1}-1} Z_{HV2}^*|Z_{HV2}|^{\mu_{HV2}-1} & Z_{VV1}|Z_{VV1}|^{\mu_{VV1}-1} Z_{VV2}^*|Z_{VV2}|^{\mu_{VV2}-1} \end{bmatrix}
\end{aligned} \tag{7.5a}$$

$$\begin{aligned}
\mathbf{T}_{11}^{FLOS} &= E\left(\mathbf{k}_1^{(u_1)} \mathbf{k}_1^{(u_2)\dagger}\right) \\
&= E \begin{bmatrix} Z_{HH1}|Z_{HH1}|^{\mu_{HH1}-1} Z_{HH1}^*|Z_{HH1}|^{\mu_{HH1}-1} & \sqrt{2}Z_{HH1}|Z_{HH1}|^{\mu_{HH1}-1} Z_{HV1}^*|Z_{HV1}|^{\mu_{HV1}-1} & Z_{HH1}|Z_{HH1}|^{\mu_{HH1}-1} Z_{VV1}^*|Z_{VV1}|^{\mu_{VV1}-1} \\ \sqrt{2}Z_{HV1}|Z_{HV1}|^{\mu_{HV1}-1} Z_{HH1}^*|Z_{HH1}|^{\mu_{HH1}-1} & 2Z_{HV1}|Z_{HV1}|^{\mu_{HV1}-1} Z_{HV1}^*|Z_{HV1}|^{\mu_{HV1}-1} & \sqrt{2}Z_{HV1}|Z_{HV1}|^{\mu_{HV1}-1} Z_{VV1}^*|Z_{VV1}|^{\mu_{VV1}-1} \\ Z_{VV1}|Z_{VV1}|^{\mu_{VV1}-1} Z_{HH1}^*|Z_{HH1}|^{\mu_{HH1}-1} & \sqrt{2}Z_{VV1}|Z_{VV1}|^{\mu_{VV1}-1} Z_{HV1}^*|Z_{HV1}|^{\mu_{HV1}-1} & Z_{VV1}|Z_{VV1}|^{\mu_{VV1}-1} Z_{VV1}^*|Z_{VV1}|^{\mu_{VV1}-1} \end{bmatrix}
\end{aligned} \tag{7.5b}$$

$$\begin{aligned}
\mathbf{T}_{22}^{FLOS} &= E\left(\mathbf{k}_2^{(u)} \mathbf{k}_2^{(u)\dagger}\right) \\
&= E \begin{bmatrix} Z_{HH2}|Z_{HH2}|^{\mu_{HH2}-1} Z_{HH2}^*|Z_{HH2}|^{\mu_{HH2}-1} & \sqrt{2}Z_{HH2}|Z_{HH2}|^{\mu_{HH2}-1} Z_{HV2}^*|Z_{HV2}|^{\mu_{HV2}-1} & Z_{HH2}|Z_{HH2}|^{\mu_{HH2}-1} Z_{VV2}^*|Z_{VV2}|^{\mu_{VV2}-1} \\ \sqrt{2}Z_{HV2}|Z_{HV2}|^{\mu_{HV2}-1} Z_{HH2}^*|Z_{HH2}|^{\mu_{HH2}-1} & 2Z_{HV2}|Z_{HV2}|^{\mu_{HV2}-1} Z_{HV2}^*|Z_{HV2}|^{\mu_{HV2}-1} & \sqrt{2}Z_{HV2}|Z_{HV2}|^{\mu_{HV2}-1} Z_{VV2}^*|Z_{VV2}|^{\mu_{VV2}-1} \\ Z_{VV2}|Z_{VV2}|^{\mu_{VV2}-1} Z_{HH2}^*|Z_{HH2}|^{\mu_{HH2}-1} & \sqrt{2}Z_{VV2}|Z_{VV2}|^{\mu_{VV2}-1} Z_{HV2}^*|Z_{HV2}|^{\mu_{HV2}-1} & Z_{VV2}|Z_{VV2}|^{\mu_{VV2}-1} Z_{VV2}^*|Z_{VV2}|^{\mu_{VV2}-1} \end{bmatrix}
\end{aligned} \tag{7.5c}$$

The limiting choices of u are described in [183]. In [199], it is further argued that $u = \alpha/2$ for each of the channels. Therefore, in (7.5), we have

$$u_l = \alpha_l / 2 \tag{7.6}$$

where $l \in \{HH1, HV1, VV1, HH2, HV2, VV2\}$. The estimator of alpha will be discussed in Section 7.4.2.

Finally, the vector coherence based upon the isotropic symmetric alpha-stable distribution and FLOS is represented as

$$\gamma_{FLOS} = \frac{\omega_1^\dagger \mathbf{\Omega}_{12}^{FLOS} \omega_2}{\sqrt{(\omega_1^\dagger \mathbf{T}_{11}^{FLOS} \omega_1)(\omega_2^\dagger \mathbf{T}_{22}^{FLOS} \omega_2)}} = |\gamma_{FLOS}| \exp(j\theta_{FLOS}). \tag{7.7}$$

This vector coherence is the generalized version of the vector coherence described in [16] and shown in (7.3) and is valid for the case of an isotropic symmetric alpha-stable distribution.

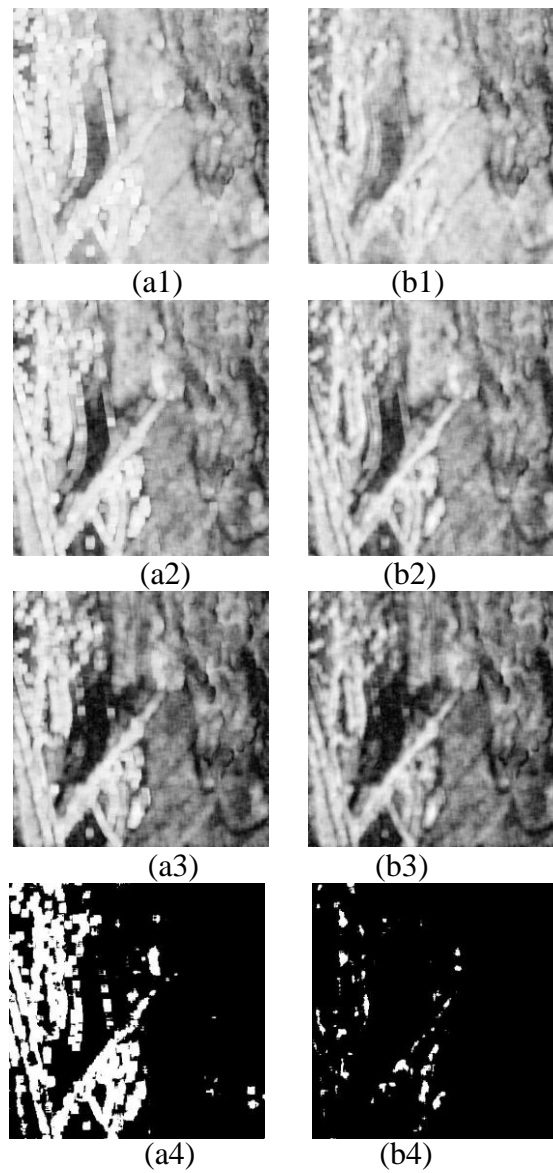


Figure 7.2. (a1)-(a3) are the optimized coherences of the first, second, and third optimizations of the standard method in [16], respectively. (b1)-(b3) are the optimized coherences of the first, second, and third optimizations of the proposed method, respectively. (a4) is the mask of (a1) shown in white when the optimized coherence is higher than 0.9. (b4) is the mask of (b1) shown in white when the optimized coherence is higher than 0.9.

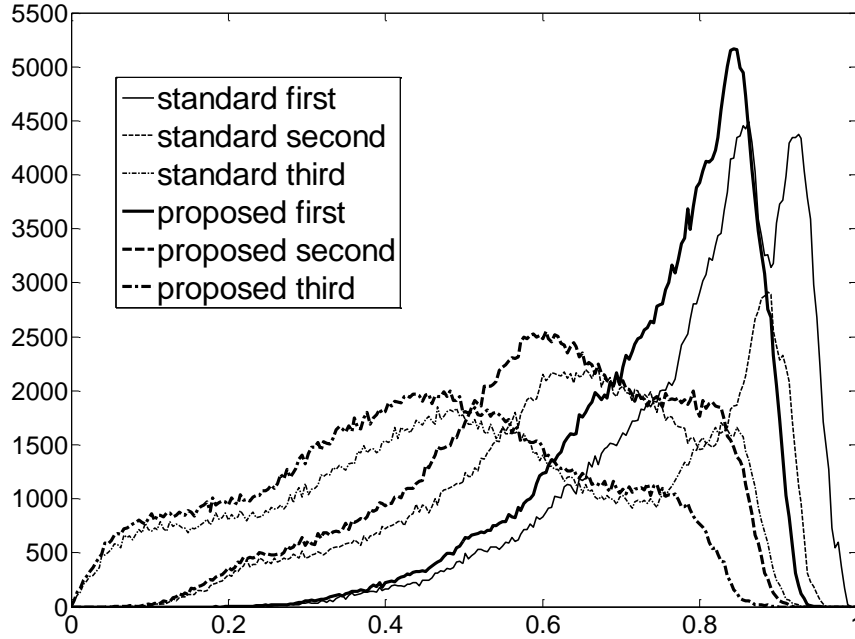


Figure 7.3. Coherence magnitude histograms of the results in Figure 7.2. Histograms represent the first, second, and third optimized coherences using (thick lines) the standard method in [16] and (thin lines) the proposed method.

7.4 Coherence Optimization Based on FLOS

7.4.1 Definition

Much effort has been addressed to the problem of coherence optimization [16] [293] [294] [295], based upon underlying Gaussian statistics. In this chapter, we generalize the methods in [16] using the FLOS-based vector coherence. Using the proposed vector coherence definition in (7.7), the coherence optimization based on FLOS can be formulated as

$$\mathbf{M} = \omega_1^\dagger \mathbf{\Omega}_{12}^{FLOS} \omega_2 + \rho_1 (\omega_1^\dagger \mathbf{T}_{11}^{FLOS} \omega_1 - A) + \rho_2 (\omega_2^\dagger \mathbf{T}_{22}^{FLOS} \omega_2 - B). \quad (7.8)$$

The other parts of the FLOS coherence optimization are the same as the standard method described in [16], which leads to the final result as

$$\left(\mathbf{T}_{22}^{FLOS}\right)^{-1}\left(\mathbf{\Omega}_{12}^{FLOS}\right)^\dagger\left(\mathbf{T}_{11}^{FLOS}\right)^{-1}\mathbf{\Omega}_{12}^{FLOS}\omega_2 = \rho_1\rho_2^*\omega_2 \quad (7.9a)$$

$$\left(\mathbf{T}_{11}^{FLOS}\right)^{-1}\mathbf{\Omega}_{12}^{FLOS}\left(\mathbf{T}_{22}^{FLOS}\right)^{-1}\left(\mathbf{\Omega}_{12}^{FLOS}\right)^\dagger\omega_1 = \rho_1\rho_2^*\omega_1. \quad (7.9b)$$

7.4.2 Implementation

Both for the calculation of the generalized vector coherence and the coherence optimization based on FLOS, (7.5a)-(7.5c) need to be calculated first. In order to calculate $\mathbf{\Omega}_{12}$, \mathbf{T}_{11} , and \mathbf{T}_{22} , the parameter u needs to be calculated using (7.6). The task then is to estimate the alpha parameters from the observational data. In this method, we use the alpha estimator of complex data which was proposed in [164] and used in [199]. This alpha estimator is related to the observed mean and variance of the logarithm of the absolute value of the complex SAR data Z_l and is expressed as [164]

$$\hat{\alpha} = \pi / \sqrt{6E\left(\left(\log|Z_l| - E(\log|Z_l|)\right)^2\right)} \quad (7.10)$$

where $l \in \{HH1, HV1, VV1, HH2, HV2, VV2\}$ refers to the six channels of PolInSAR data. It should be noted that g , which is the scale parameter, drops out of the calculations of the \mathbf{k} vectors and subsequent computations.

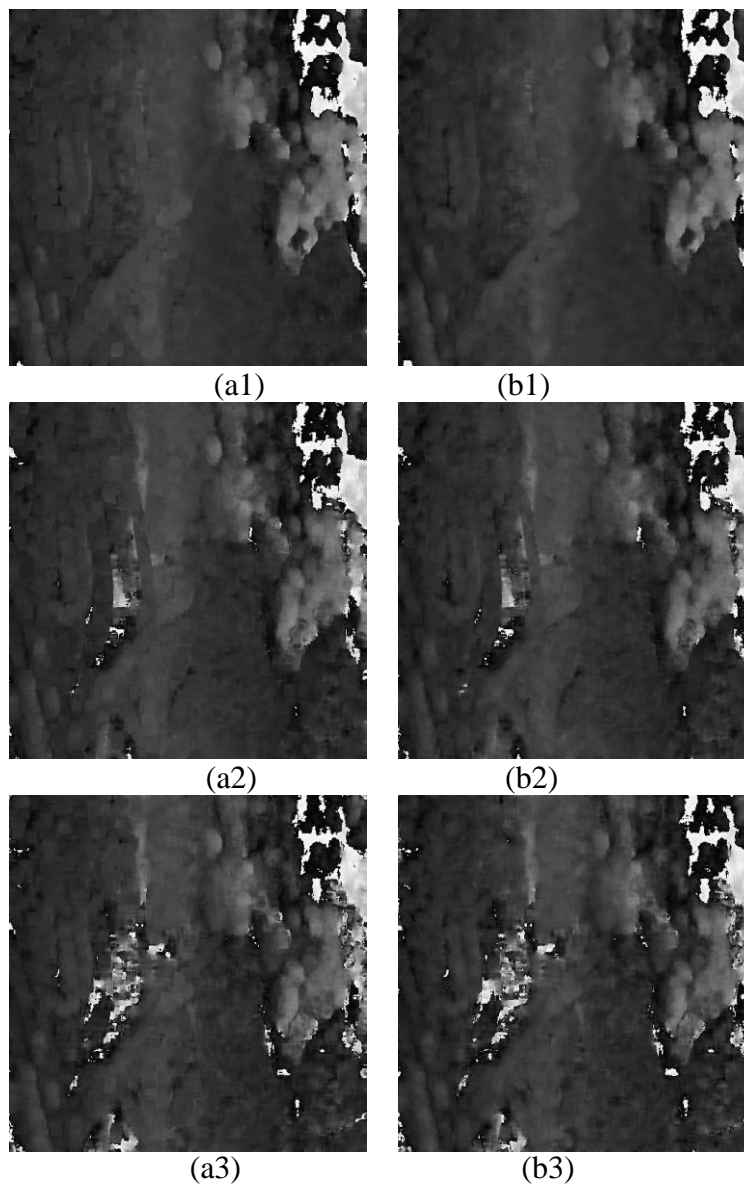


Figure 7.4. (a1)-(a3) are the optimized phases of the first, second, and third optimizations of the standard method in [16], respectively. (b1)-(b3) are the optimized phases of the first, second, and third optimizations of the proposed method, respectively.

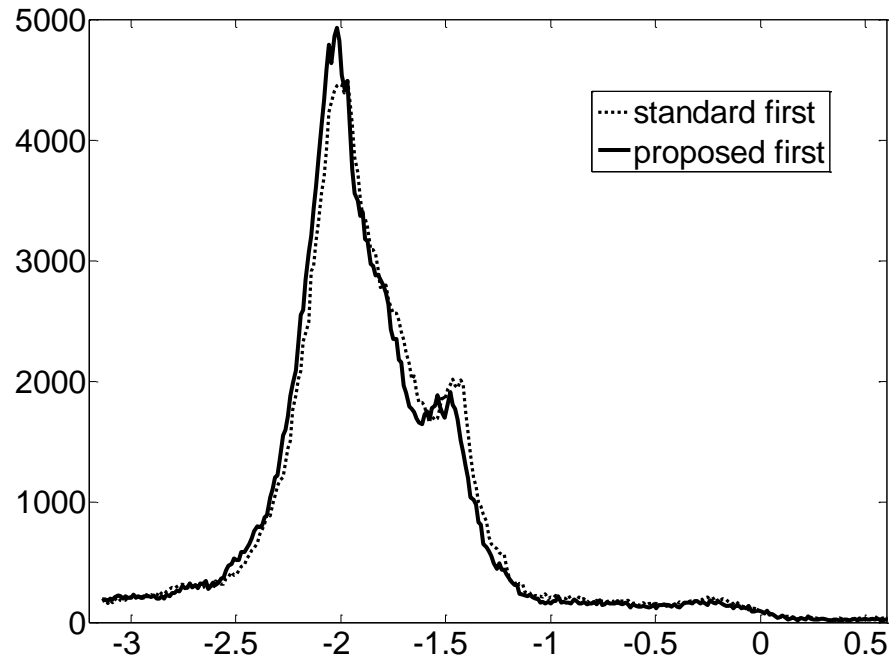


Figure 7.5. Phase histogram of the result in Figure 7.4. Phase histogram of the first optimized coherence using the method in [16] and the proposed method. The histogram of solid line is from the standard method, and the dotted line is from the proposed method. The horizontal axis is the phase in radians.

7.5 Experimental Results

In order to examine the performance of the proposed coherence optimization method based on FLOS, several experiments are conducted using real PolInSAR data. The single-look complex data set used in this experiment was obtained by Intermap Technologies Corporation, using its PolInSAR system described in [297]. An HH amplitude image is shown in Figure 7.1. The area includes forest (upper right), pasture (dark areas), and a mixture of low buildings, single trees, clusters of trees, and roads (left side). Thus, they are basically a mixture of strong and weak scatterers.

In Figure 7.2 and Figure 7.4, we show the amplitude and phase of the optimized coherence derived from the two methods, respectively. From top to bottom, they represent the first, second, and third optimizations: On the left side, the standard optimization method of [16] was applied, while on the right side, the FLOS-based method is applied. A 15×15 moving window was used in each implementation. In this chapter, we use the first, second, and third optimizations as the output from the highest, second highest, and third highest eigenvalues, respectively. Upon comparative inspection of these results, there appear to be artifacts (which are the squares around the strong scatterers, particularly of the first optimization) in the optimized coherence and optimized phase of the method in [16], probably introduced by the moving window. In the proposed method, these artifacts are largely reduced from all the three optimization results, particularly for the first optimization. Figure 7.2 (a4) and (b4) show the masked area where the coherence amplitudes greater than 0.9 are shown as white. From these two figures, we observe that the proposed method reduces the blockiness of the coherence images and that the coherence has a more natural shape than the standard method. The coherences greater than 0.9 occur mostly around strong scatterers.

Histograms of these coherences are shown in Figure 7.3 for comparative inspection. In general, the histograms exhibit better separation of the first and second optimizations using the proposed approach than the standard method. This reflects a better separation of the scattering mechanisms in the relevant areas. The biggest difference between the methods is revealed in the peak region of the coherence associated with the first optimization. Whereas the standard method reveals a double peak, the proposed method, based upon the alpha-stable distribution, shows a single peak. A similar double peak

occurs for the second optimization derived by the standard process. One interpretation is that some portions of the targets, particularly near strong scatters, are alpha-stable distributed, causing the double peak in the standard optimization but resulting in a single peak for the proposed method. This may be due to a sharp transition from Gaussian-dominated to alpha-stable statistics near these strong scatterers. This would result in corresponding changes of the optimized coherence values (standard method) in the local area and the appearance of artifacts. However, we suggest that the transformed data are effectively corrected under the alpha-stable distribution model, and therefore, the artifacts are reduced if not removed. More work is needed to clarify this interpretation.

In Figure 7.4, we show the phases associated with the three optimized coherences. While much of the test area shows similar phase characteristics, inspection of the subareas where differences in the optimized coherence magnitudes were observed also reveals differences in the phase determined by the two methods. A histogram of the phases associated with the first optimization, as derived by the two methods, is shown in Figure 7.5. While superficially similar, these distributions show that the peak of the histogram is shifted by about 0.05 rad. These show up in the phases from standard optimization as probable artifacts in the vicinity of strong scatters. The phase histograms of the second and third optimizations show less dissimilarity between the methods and are not reproduced here.

7.6 Conclusion

In this chapter, we have proposed a formalism that allows the generalization to PolInSAR methodology of the isotropic symmetric version of the alpha-stable

distribution, of which the Gaussian distribution is a special case. A method for obtaining the vector coherence was presented based upon FLOS. An approach for the optimization of the coherence magnitude, based upon this approach, was then developed by analogy with a well-known standard method in [16]. An experimental data set of L-band PolInSAR was analyzed comparatively with respect to the merits of this standard method and the proposed FLOS-based method. The two methods show overall similarity but with important differences. The FLOS-based method shows better separation of the optimized coherence and appears to remove phase artifacts near strongly scattering targets, although this is to be further clarified. A range of scattering situations and other optimization approaches will be addressed in future work.

CHAPTER 8: SUMMERY AND OUTLOOK OF FUTURE RESEARCH

In this Chapter, the research contributions and results of this thesis will be summarized, and the topics of future research will be provided.

8.1 Summary

A PolInSAR system includes polarimetric SAR and interferometric SAR as its subsystems. This thesis addresses the statistical analysis and some important signal processing issues that are included in this system. In this thesis, we started with the statistical analysis and signal processing of the polarimetric SAR subsystem. Then, we studied the signal processing methods of the interferometric SAR subsystem, such as coherence estimation, phase filtering, phase unwrapping, and phase quality representation. Finally, we addressed the PolInSAR statistical analysis and signal processing. Some signal processing methods, such as coherence estimation, phase filtering, phase unwrapping, are discussed using the InSAR subsystem as examples. However, since the PolInSAR system is the combination of PolSAR and InSAR subsystems, these methods are also applicable to the whole PolInSAR system. In this research, we mostly addressed these issues in the following manner: First, we started with the theoretical analysis or model establishment. Then, we proposed the related methods based on the results of theoretical analysis. Finally, the proposed methods were validated by the experiments conducted on simulated data and/or real SAR data.

In this thesis, the following issues have been addressed:

1) In Chapter 2, three major issues have been addressed. First, the statistical analysis of polarimetric SAR data has been studied. In this study, the multichannel isotropic complex symmetric alpha-stable ($S\alpha S$) distribution has been used to model the multichannel complex polarimetric SAR data. Polarimetric SAR data need to be described by a distribution which can cover the different statistical characteristics of various types of scenes. From the experiments of Chapter 2, we found that alpha-stable distribution is not only suitable for modeling the polarimetric SAR data of all the four polarizations and different type of targets, but also suitable for modeling the data obtained from SAR systems that work at different wavelengths. This is because the pdf of alpha-stable distribution ranges from non-heavy-tailed to very heavy-tailed when different input parameters are used. Therefore, it can obtain a more accurate statistical description of the polarimetric SAR data than the Gaussian distribution.

Second, using the proposed statistical model and based on the result of theoretical analysis, the covariance matrix based on fractional lower order statistics (FLOS) has been proposed in Chapter 2. Several related theoretical issues of this new covariance matrix definition have been discussed. The traditional covariance matrix estimation is inaccurate when the SAR data is non-Gaussian distributed due to the model deviation. This proposed covariance matrix definition incorporates the statistical information estimated from the observed data, and thus may solve this aforementioned problem.

Finally, using this FLOS-based covariance matrix, the revised adaptive optimal despeckling method based on the original method in [144] has been proposed in Chapter

2. The experimental results demonstrated that the proposed despeckling method obtains a better edge preservation ability than the original method in [144].

However, it is well known that the alpha-stable distribution does not have the closed-form probability density functions for most of the alpha values [176]. Therefore, it is difficult to apply this model to the applications that require the closed-form pdf.

2) Chapter 3 discusses the issues related to coherence estimation, which is a very important measurement in the InSAR subsystem, PolSAR subsystem, and whole PolInSAR system. However, the sample coherence estimation based on Gaussian distribution suffers from two sources of bias. First, it is statistically biased when the input data is non-Gaussian distributed. This statistical bias under alpha-stable model assumption has not been widely discussed before. Second, it is biased because only limited samples can be used in the estimation. In order to reduce both the statistical and sample biases, the coherence calculation based on fractional lower order statistics has been proposed in Chapter 3. This definition has been validated by mathematical proofs. The experimental results of real InSAR data show that the proposed coherence calculation method can reduce both the statistical bias and the sample bias.

3) In Chapter 4, wavelet-domain phase-filtering method has been studied. The wavelet domain phase filtering has been formulated as a simultaneous signal detection and estimation problem. The closed-form detector and estimator of this formulation have been derived based on the statistical modeling of the wavelet coefficients. Applying this derived detector and estimator, two new wavelet-domain phase-filtering methods using simultaneous detection and estimation technique have been proposed. Simultaneous detection and estimation technique considers the detection and estimation at the same

time; therefore, it can obtain accurate signal estimation and thus achieve robust filtering. First, the phase filtering method using simultaneous detection and estimation and wavelet packet has been proposed. Second, the phase filtering method using undecimated wavelet and simultaneous detection and estimation has been proposed. Some related implementation issues such as function calculation and the selection of wavelet decomposition levels have been discussed.

The experiments of simulated and real InSAR data have been conducted. First, the experiments with simulated phase data have been conducted. The experimental results show that the two proposed methods obtain better filtering results than the other tested methods in terms of RMSE and visual evaluation. Second, experiments with real InSAR data have been conducted. The experimental results indicate that the two proposed methods remove more residues than several other tested methods when applied to a noisy phase map. The proposed wavelet-packet method is not only a relatively fast method, but also outperforms the proposed undecimated wavelet method when filtering the phase data of high fringe densities. The proposed undecimated wavelet method outperforms the proposed wavelet-packet method when the phase fringes are not very dense at the cost of higher computational and memory requirements.

However, the proposed filtering method that uses the undecimated wavelet requires a large amount of CPU time and memory. How to improve the computational efficiency is a topic of future research.

4) In Chapter 5, a phase unwrapping method using the weighted regularized PCG technique has been proposed. When valid phase data are missing in some areas, there may be holes in the phase map. The regularization operation can interpolate through these

holes and obtain a smooth phase map. A weighting operation can suppress the phase noise during unwrapping. This method incorporates the regularization and weights in one phase unwrapping method. Therefore, the proposed method can not only smooth out the holes in the phase map, but also reduce the unwrapping errors due to noise. First, the experiments on the simulated phase data have been conducted. The experimental results show that the proposed WRPCG method obtains a better unwrapping result than the other tested methods in terms of several error metrics. Second, the experiments of real InSAR data have been conducted. The experimental results show that the proposed method reduces the large scale errors that often occur in the other tested methods.

All in all, the proposed phase unwrapping method not only benefits from the regularization operation which can smooth through the holes where the valid data are missing due to shadow or other reasons, but also benefits from the weighting operation which can obtain a robust result in the areas of noisy data.

However, the proposed WRPCG method is still a global method. The performance of this method is not as stable as the local method, and the global errors in the results of this method are only reduced but not completely eliminated. This is an inevitable drawback of the global phase unwrapping methods. How to further reduce these errors will be the topic of future study.

5) In Chapter 6, the concept of second order residue has been proposed. The second order residue is an extension of the first order residue concept. First order residue cannot be directly used as a quality map. However, second order residue can be directly used as quality map after simple arrangements. Therefore, the second order residue is suitable as the input for many quality-guided or weighted phase unwrapping methods. From the

experimental results using real PolInSAR data, we found that the proposed method is promising in the description of phase quality.

6) In Chapter 7, three issues associated with the PolInSAR system have been studied. First, the multichannel complex PolInSAR data have been modeled as following a multichannel isotropic complex symmetric alpha-stable distribution. Then, the PolInSAR coherence formulation has been studied using this statistical model, and the PolInSAR vector coherence based on fractional lower order statistics has been proposed. Finally, using this FLOS-based vector coherence, the FLOS-based coherence optimization method has been proposed. Coherence optimization experiments using L-band PolInSAR data have been conducted. In the optimized coherence amplitude and phase of the proposed method, the artifacts around the strong scatterers are significantly reduced. The experimental results also demonstrate that the proposed method can obtain a better separation of the optimized results due to the better modeling of the PolInSAR data.

8.2 Outlook of Future Studies

PolInSAR technology involves the application and combination of many successful SAR techniques. Therefore, it is a very complex system involving a variety of signal processing techniques. These signal processing techniques can be developed under the assumption of various statistical models due to the development of modern statistical theory. This thesis tried to shed some light on the statistical models and signal processing methods of PolInSAR and obtained some promising results. However, this thesis can

only be considered as the tip of the iceberg comparing to the huge amount of research work that needed to be done in the related areas. Therefore, many topics and much more work need to be done in the future.

The polarimetric and interferometric SAR is a very important research topic, which has various research areas. Some of the future PolInSAR research topics that relate to statistical analysis and signal processing are as follows:

- 1) With the development of new statistical models in the statistical theory, the application of these models to the modeling of PolInSAR data will be the topic of future research.
- 2) Sometimes, if we consider the specific applications during the development of the signal processing methods, it would be easier to obtain a successful method. Therefore, the PolInSAR signal processing methods which tailor to the specific applications will be the topic of future research.
- 3) With the growing demand of accurate geographical information, the accuracy and processing ability of the signal processing methods of PolInSAR need to be significantly improved. The research that improves the accuracy of the signal processing methods will be the topic of future research.
- 4) With the advancement of modern statistical theory, the development of successful signal processing methods will become more and more depending on the research of statistical model selection and simplification.
- 5) With the advancement of PolInSAR techniques, the new data obtained from these new PolInSAR systems require the development of new signal processing methods.

- 6) In statistical signal processing, the more complex the statistical model, the more difficult is to obtain a closed-form method. The signal processing without closed-form expression will generally be carried out through the implementation of numerical methods, which increases its computational complexity. How to simplify these models to obtain a closed-form expression is the topic of future study.

All in all, the statistical analysis and signal processing of PolInSAR is an important research area. With the emerging new applications of PolInSAR, the new signal processing methods need to be developed to solve the increasingly complex problems.

BIBLIOGRAPHY

- [1] H. A. Zebker and J. J. van Zyl, "Imaging radar polarimetry: a review," *Proceedings of the IEEE*, vol. 79, no. 11, pp. 1583-1606, November 1991.
- [2] H. A. Zebker, J. J. van Zyl, and D. N. Held, "Imaging radar polarimetry from wave synthesis," *Journal of Geophysical Research*, vol. 92, no. B1, pp. 683-701, January 10, 1987.
- [3] R. Touzi, W. M. Boerner, J. S. Lee, and E. Lueneburg, "A review of polarimetry in the context of synthetic aperture radar: concepts and information extraction," *Can. J. Remote Sensing*, vol. 30, no. 3, pp. 380-407, 2004.
- [4] J. J. van Zyl and H. A. Zebker, "Imaging radar polarimetry," *PIER3: Progress in Electromagnetics Research*, Edited by J. A. Kong, Elsevier Science Publishing Co., Inc., New York, 1990.
- [5] A. Freeman and S. L. Durden, "A three-component scattering model for polarimetric SAR data," *IEEE Transactions on Geoscience and Remote Sensing*, vol. 36, no. 3, pp. 963-973, May 1998.
- [6] P. A. Rosen, S. Hensley, I. R. Joughin, F. K. Li, S. N. Madsen, E. Rodriguez, and R. M. Goldstein, "Synthetic aperture radar interferometry," *Proceedings of the IEEE*, vol. 88, no. 3, pp. 333-382, March 2000.
- [7] R. Bamler and P. Hartl, "Synthetic aperture radar interferometry," *Inverse Problems*, vol. 14, pp. R1-R54, 1998.
- [8] R. M. Goldstein and H. A. Zebker, "Interferometric radar measurement of ocean surface currents," *Nature*, vol. 328, pp. 707-709, August 1987.

- [9] H. A. Zebker and R. M. Goldstein, "Topographic mapping from interferometric synthetic aperture radar observations," *Journal of Geophysical Research*, vol. 91, no. B5, pp. 4993-4999, April 10, 1986.
- [10] E. Rodriguez and J. M. Martin, "Theory and design of interferometric synthetic aperture radars," *IEE Proceedings-F*, vol. 139, no. 2, pp. 147-159, April 1992.
- [11] R. Gens and J. L. van Genderen, "SAR interferometry-issues, techniques, applications," *International Journal of Remote Sensing*, vol. 17, no. 10, pp. 1803-1835, 1996.
- [12] G. Krieger, I. Hajnsek, K. P. Papathanassiou, M. Younis, and A. Moreira, "Interferometric synthetic aperture radar (SAR) missions employing formation flying," *Proceedings of the IEEE*, vol. 98, no. 5, pp. 816-843, May 2010.
- [13] R. Scheiber and A. Moreira, "Coregistration of interferometric SAR images using spectral diversity," *IEEE Transactions on Geoscience and Remote Sensing*, vol. 38, no. 5, pp. 2179-2191, September 2000.
- [14] R. Romeiser, S. Suchandt, H. Runge, U. Steinbrecher, and S. Grunler, "First analysis of TerraSAR-X along-track InSAR-derived current fields," *IEEE Transactions on Geoscience and Remote Sensing*, vol. 48, no. 2, pp. 820-829, February 2010.
- [15] Z. Xiang, K. Wang, and X. Liu, "A model-spectrum-based flattening algorithm for airborne single-pass SAR interferometry," *IEEE Geoscience and Remote Sensing Letters*, vol. 6, no. 2, pp. 307-311, April 2009.

- [16] S. R. Cloude and K. P. Papathanassiou, "Polarimetric SAR interferometry," *IEEE Transactions on Geoscience and Remote Sensing*, vol. 36, no. 5, pp. 1551-1565, September 1998.
- [17] R. N. Treuhaft and P. R. Siqueira, "Vertical structure of vegetated land surfaces from interferometric and polarimetric radar," *Radio Science*, vol. 35, no. 1, pp. 141-177, January-February 2000.
- [18] R. N. Treuhaft and S. R. Cloude, "The structure of oriented vegetation from polarimetric interferometry," *IEEE Transactions on Geoscience and Remote Sensing*, vol. 37, no. 5, pp. 2620-2624, September 1999.
- [19] K. P. Papathanassiou and S. R. Cloude, "Single-baseline polarimetric SAR interferometry," *IEEE Transactions on Geoscience and Remote Sensing*, vol. 39, no. 11, pp. 2352-2363, November 2001.
- [20] F. Garestier, P. C. Dubois-Fernandez, and I. Champion, "Forest height inversion using high-resolution P-band Pol-InSAR data," *IEEE Transactions on Geoscience and Remote Sensing*, vol. 46, no. 11, pp. 3544-3559, November 2008.
- [21] J. D. Ballester-Berman and J. M. Lopez-Sanchez, "Applying the Freeman-Durden decomposition concept to polarimetric SAR interferometry," *IEEE Transactions on Geoscience and Remote Sensing*, vol. 48, no. 1, pp. 466-479, January 2010.
- [22] J. M. Lopez-Sanchez and J. D. Ballester-Berman, "Potentials of polarimetric SAR interferometry for agriculture monitoring," *Radio Science*, vol. 44, RS2010, 2009.
- [23] S. R. Cloude and K. P. Papathanassiou, "Three-stage inversion process for polarimetric SAR interferometry," *IEE Proc.-Radar Sonar Navig.*, vol. 150, no. 3, pp. 125-134, June 2003.

- [24] W. An, Y. Cui, and J. Yang, "Three-Component model-based decomposition for polarimetric SAR data," *IEEE Transactions on Geoscience and Remote Sensing*, vol. 48, no. 6, pp. 2732-2739, June 2010.
- [25] I. Hajnsek, E. Pottier, and S. R. Cloude, "Inversion of surface parameters from polarimetric SAR," *IEEE Transactions on Geoscience and Remote Sensing*, vol. 41, no. 4, pp. 727-744, April 2003.
- [26] S. R. Cloude and E. Pottier, "A review of target decomposition theorems in radar polarimetry," *IEEE Transactions on Geoscience and Remote Sensing*, vol. 34, no. 2, pp. 498-518, March 1996.
- [27] L. M. Novak, M. C. Burl, and W. W. Irving, "Optimal polarimetric processing for enhanced target detection," *IEEE Transactions on Aerospace and Electronic Systems*, vol. 29, no. 1, pp. 234-244, January 1993.
- [28] A. Marino, S. R. Cloude, and I. H. Woodhouse, "A polarimetric target detector using the Huynen fork," *IEEE Transactions on Geoscience and Remote Sensing*, vol. 48, no. 5, pp. 2357-2366, May 2010.
- [29] W. An, Y. Cui, J. Yang, and H. Zhang, "Fast alternatives to H/α for polarimetric SAR," *IEEE Geoscience and Remote Sensing Letters*, vol. 7, no. 2, pp. 343-347, April 2010.
- [30] Y. Wang, C. Han, and F. Tupin, "PolSAR data segmentation by combining tensor space cluster analysis and Markovian framework," *IEEE Geoscience and Remote Sensing Letters*, vol. 7, no. 1, pp. 210-214, January 2010.

- [31] S. Guillaso, L. Ferro-Famil, A. Reigber, and E. Pottier, "Building characterization using L-band polarimetric interferometric SAR data," *IEEE Geoscience and Remote Sensing Letters*, vol. 2, no. 3, pp. 347-351, July 2005.
- [32] R. Z. Schneider, K. P. Papathanassiou, I. Hajnsek, and A. Moreira, "Polarimetric and interferometric characterization of coherent scatterers in urban areas," *IEEE Transactions on Geoscience and Remote Sensing*, vol. 44, no. 4, pp. 971-984, April 2006.
- [33] M. Jager, M. Neumann, S. Guillaso, and A. Reigber, "A self-initializing PolInSAR classifier using interferometric phase differences," *IEEE Transactions on Geoscience and Remote Sensing*, vol. 45, no. 11, pp. 3503-3518, November 2007.
- [34] S. R. Cloude, J. Fortuny, J. M. Lopez-Sanchez, and A. J. Sieber, "Wide-band polarimetric radar inversion studies for vegetation layers," *IEEE Transactions on Geoscience and Remote Sensing*, vol. 37, no. 5, pp. 2430-2441, September 1999.
- [35] A. Freeman, "Fitting a two-component scattering model to polarimetric SAR data from forests," *IEEE Transactions on Geoscience and Remote Sensing*, vol. 45, no. 8, pp. 2583-2592, August 2007.
- [36] Y. Yamaguchi, T. Moriyama, M. Ishido, and H. Yamada, "Four-component scattering model for polarimetric SAR image decomposition," *IEEE Transactions on Geoscience and Remote Sensing*, vol. 43, no. 8, pp. 1699-1706, August 2005.
- [37] H. Yamada, Y. Yamaguchi, Y. Kim, E. Rodriguez, and W.-M. Boerner, "Polarimetric SAR interferometry for forest analysis based on the ESPRIT algorithm," *IEICE Trans. Electron.*, vol. E84 C, no. 12, pp. 1917-1924, December 2001.

- [38] M. Neumann, "Remote sensing of vegetation using multi-baseline polarimetric SAR interferometry: theoretical modeling and physical parameter retrieval," Ph.D. dissertation, University of Rennes 1, Rennes, France, January 2009. [online, available at: http://www.openthesis.org/document/view/600827_0.pdf]
- [39] M. Neumann, L. Ferro-Famil, and A. Reigber, "Estimation of forest structure, ground, and canopy layer characteristics from multibaseline polarimetric interferometric SAR data," *IEEE Transactions on Geoscience and Remote Sensing*, vol. 48, no. 3, pp. 1086-1104, March 2010.
- [40] A. Reigber and A. Moreira, "First demonstration of airborne SAR tomography using multibaseline L-band data," *IEEE Transactions on Geoscience and Remote Sensing*, vol. 38, no. 5, pp. 2142-2152, September 2000.
- [41] S. R. Cloude, "Polarization coherence tomography," *Radio Science*, vol. 41, RS4017, doi: 10.1029/2005RS003436, 2006.
- [42] S. R. Cloude, "Dual-baseline coherence tomography," *IEEE Geoscience and Remote Sensing Letters*, vol. 4, no. 1, pp. 127-131, January 2007.
- [43] J. M. Lopez-Sanchez, J. D. Ballester-Berman, and Y. Marquez-Moreno, "Model limitations and parameter-estimation methods for agricultural applications of polarimetric SAR interferometry," *IEEE Transactions on Geoscience and Remote Sensing*, vol. 45, no. 11, pp. 3481-3493, November 2007.
- [44] S. Tebaldini, "Algebraic synthesis of forest scenarios from multibaseline PolInSAR data," *IEEE Transactions on Geoscience and Remote Sensing*, vol. 47, no. 12, pp. 4132-4142, December 2009.

- [45] L. Zhang, B. Zou, J. Zhang, and Y. Zhang, "An extended multiple-component scattering model for PolSAR images," *International Journal of Remote Sensing*, vol. 30, no. 21, pp. 5515-5525, 10 November 2009.
- [46] J. Chen, Y. Chen, and J. Yang, "Ship detection using polarization cross-entropy," *IEEE Geoscience and Remote Sensing Letters*, vol. 6, no. 4, pp. 723-727, October 2009.
- [47] F. Garestier, P. C. Dubois-Fernandez, D. Guyon, and T. Le Toan, "Forest biophysical parameter estimation using L- and P-band polarimetric SAR data," *IEEE Transactions on Geoscience and Remote Sensing*, vol. 47, no. 10, pp. 3379-3388, October 2009.
- [48] R. Touzi, A. Deschamps, and G. Rother, "Phase of target scattering for wetland characterization using polarimetric C-band SAR," *IEEE Transactions on Geoscience and Remote Sensing*, vol. 47, no. 9, pp. 3241-3261, September 2009.
- [49] R. Touzi, "Target scattering decomposition in terms of roll-invariant target parameters," *IEEE Transactions on Geoscience and Remote Sensing*, vol. 45, no. 1, pp. 73-84, January 2007.
- [50] S. Sauer, L. Ferro-Famil, A. Reigber, and E. Pottier, "Polarimetric dual-baseline InSAR building height estimation at L-band," *IEEE Geoscience and Remote Sensing Letters*, vol. 6, no. 3, pp. 408-412, July 2009.
- [51] J. Praks, E. C. Koeniguer, and M. T. Hallikainen, "Alternatives to target entropy and alpha angle in SAR polarimetry," *IEEE Transactions on Geoscience and Remote Sensing*, vol. 47, no. 7, pp. 2262-2274, July 2009.

- [52] S.-E. Park, W. M. Moon, and D.-J. Kim, "Estimation of surface roughness parameter in intertidal mudflat using airborne polarimetric SAR data," *IEEE Transactions on Geoscience and Remote Sensing*, vol. 47, no. 4, pp. 1022-1031, April 2009.
- [53] D. L. Schuler, J.-S. Lee, D. Kasilingam, and G. Nesti, "Surface roughness and slope measurements using polarimetric SAR data," *IEEE Transactions on Geoscience and Remote Sensing*, vol. 40, no. 3, pp. 687-698, March 2002.
- [54] F. Mattia, T. L. Toan, J.-C. Souyris, G. De Carolis, N. Floury, F. Posa, and G. Pasquariello, "The effect of surface roughness on multifrequency polarimetric SAR data," *IEEE Transactions on Geoscience and Remote Sensing*, vol. 35, no. 4, pp. 954-966, July 1997.
- [55] G. Margarit, J. J. Mallorqui, and X. Fabregas, "Single-pass polarimetric SAR interferometry for vessel classification," *IEEE Transactions on Geoscience and Remote Sensing*, vol. 45, no. 11, pp. 3494-3502, November 2007.
- [56] G. Margarit, J. J. Mallorqui, J. Fortuny-Gusach, and C. Lopez-Martinez, "Exploitation of ship scattering in polarimetric SAR for an improved classification under high clutter conditions," *IEEE Transactions on Geoscience and Remote Sensing*, vol. 47, no. 4, pp. 1224-1235, April 2009.
- [57] I. Hajnsek, T. Jagdhuber, H. Schon, and K. P. Papathanassiou, "Potential of estimating soil moisture under vegetation cover by means of PolSAR," *IEEE Transactions on Geoscience and Remote Sensing*, vol. 47, no. 2, pp. 442-454, February 2009.

- [58] D. L. Schuler, T. L. Ainsworth, and J. S. Lee, "Topographic mapping using polarimetric SAR data," *International Journal of Remote Sensing*, vol. 19, no. 1, pp. 141-160, 1998.
- [59] D. L. Schuler, J.-S. Lee, T. L. Ainsworth, and M. R. Grunes, "Terrain topography measurement using multipass polarimetric synthetic aperture radar data," *Radio Science*, vol. 35, no. 3, pp. 813-832, May-June 2000.
- [60] X. Chen, C. Wang, and H. Zhang, "DEM generation combining SAR polarimetry and shape-from-shading techniques," *IEEE Geoscience and Remote Sensing Letters*, vol. 6, no. 1, pp. 28-32, January 2009.
- [61] S. R. Cloude, D. G. Corr, and M. L. Williams, "Target detection beneath foliage using polarimetric synthetic radar interferometry," *Waves Random Media*, vol. 14, pp. S393-S414, 2004.
- [62] J.-C. Souyris, P. Imbo, R. Fjortoft, S. Mingot, and J.-S. Lee, "Compact polarimetry based on symmetry properties of geophysical media: the $\pi/4$ mode," *IEEE Transactions on Geoscience and Remote Sensing*, vol. 43, no. 3, pp. 634-646, March 2005.
- [63] M. E. Nord, T. L. Ainsworth, J.-S. Lee, and N. J. S. Stacy, "Comparison of compact polarimetric synthetic aperture radar modes," *IEEE Transactions on Geoscience and Remote Sensing*, vol. 47, no. 1, pp. 174-188, January 2009.
- [64] L. Zhang, B. Zou, H. Cai, and Y. Zhang, "Multiple-component scattering model for polarimetric SAR image decomposition," *IEEE Geoscience and Remote Sensing Letters*, vol. 5, no. 4, pp. 603-607, October 2008.

- [65] D. L. Schuler and J.-S. Lee, "Mapping ocean surface features using biogenic slick-fields and SAR polarimetric decomposition techniques," *IEE Proc.-Radar Sonar Navig.*, vol. 153, no. 3, pp. 260-270, June 2006.
- [66] M. Migliaccio, A. Gambardella, and M. Tranfaglia, "SAR polarimetry to observe oil spills," *IEEE Transactions on Geoscience and Remote Sensing*, vol. 45, no. 2, pp. 506-511, February 2007.
- [67] L. Ferro-Famil, E. Pottier, and J.S. Lee, "Classification and interpretation of polarimetric interferometric SAR data," *IGARSS'02*, vol. 1, pp. 635-637, 2002.
- [68] P. C. Dubois-Fernandez, J.-C. Souyris, S. Angelliaume, and F. Garestier, "The compact polarimetry alternative for spaceborne SAR at low frequency," *IEEE Transactions on Geoscience and Remote Sensing*, vol. 46, no. 10, pp. 3208-3222, October 2008.
- [69] H. Kimura, "Radar polarization orientation shifts in built-up areas," *IEEE Geoscience and Remote Sensing Letters*, vol. 5, no. 2, pp. 217-221, April 2008.
- [70] X. Li and J. Chong, "Processing of Envisat alternating polarization data for vessel detection," *IEEE Geoscience and Remote Sensing Letters*, vol. 5, no. 2, pp. 271-275, April 2008.
- [71] M. L. Williams, "Potential for surface parameter estimation using compact polarimetric SAR," *IEEE Geoscience and Remote Sensing Letters*, vol. 5, no. 3, pp. 471-473, July 2008.
- [72] T. L. Ainsworth, D. L. Schuler, and J.-S. Lee, "Polarimetric SAR characterization of man-made structures in urban areas using normalized circular-pol correlation coefficients," *Remote Sensing of Environment*, vol. 112, pp. 2876-2885, 2008.

- [73] F. Garestier, P. C. Dubois-Fernandez, and K. P. Papathanassiou, "Pine forest height inversion using single-pass X-band PolInSAR data," *IEEE Transactions on Geoscience and Remote Sensing*, vol. 46, no. 1, pp. 59-68, January 2008.
- [74] E. Krogager, "New decomposition of the radar target scattering matrix," *Electronics Letters*, vol. 26, no. 18, pp. 1525-1527, 30th August 1990.
- [75] J.-C. Souyris and C. Tison, "Polarimetric analysis of bistatic SAR images from polar decomposition: a quaternion approach," *IEEE Transactions on Geoscience and Remote Sensing*, vol. 45, no. 9, pp. 2701-2714, September 2007.
- [76] J. Praks, F. Kugler, K. P. Papathanassiou, I. Hajnsek, and M. Hallikainen, "Height estimation of boreal forest: interferometric model-based inversion at L- and X-band versus HUTSCAT profiling scatterometer," *IEEE Geoscience and Remote Sensing Letters*, vol. 4, no. 3, pp. 466-470, July 2007.
- [77] F. Garestier, P. Dubois-Fernandez, X. Dupuis, P. Paillou, and I. Hajnsek, "PolInSAR analysis of X-band data over vegetated and urban areas," *IEEE Transactions on Geoscience and Remote Sensing*, vol. 44, no. 2, pp. 356-364, February 2006.
- [78] C. S. Rowland and H. Balzter, "Data fusion for reconstruction of a DTM, under a woodland canopy, from airborne L-band InSAR," *IEEE Transactions on Geoscience and Remote Sensing*, vol. 45, no. 5, pp. 1154-1163, May 2007.
- [79] Y. Zhang, C. Vincent Tao, and J. B. Mercer, "An initial study on automatic reconstruction of ground DEMs from airborne IfSAR DSMs," *Photogrammetric Engineering & Remote Sensing*, vol. 70, no. 4, pp. 427-438, April 2004. [available online: <http://www.asprs.org/publications/pers/2004journal/april/abstracts.html#p427>]

- [80] W. L. Cameron, N. N. Youssef, and L. K. Leung, "Simulated polarimetric signatures of primitive geometrical shapes," *IEEE Transactions on Geoscience and Remote Sensing*, vol. 34, no. 3, pp. 793-803, May 1996.
- [81] J.-S. Lee, E. Krogager, T. L. Ainsworth, and W.-M. Boerner, "Polarimetric analysis of radar signature of a manmade structure," *IEEE Geoscience and Remote Sensing Letters*, vol. 3, no. 4, pp. 555-559, October 2006.
- [82] J.-S. Lee, T. L. Ainsworth, J. P. Kelly, and C. Lopez-Martinez, "Evaluation and bias removal of multilook effect on entropy/alpha/anisotropy in polarimetric SAR decomposition," *IEEE Transactions on Geoscience and Remote Sensing*, vol. 46, no. 10, pp. 3039-3052, October 2008.
- [83] A. Ferretti, C. Prati, and F. Rocca, "Permanent scatterers in SAR interferometry," *IEEE Transactions on Geoscience and Remote Sensing*, vol. 39, no. 1, pp.8-20, January 2001.
- [84] A. Freeman, "SAR calibration: an overview," *IEEE Transactions on Geoscience and Remote Sensing*, vol. 30, no. 6, pp. 1107-1121, November 1992.
- [85] J. J. van Zyl, "Calibration of polarimetric radar images using only image parameters and trihedral corner reflector responses," *IEEE Transactions on Geoscience and Remote Sensing*, vol. 28, no. 3, pp. 337-348, May 1990.
- [86] M. W. Whitt, F. T. Ulaby, P. Polatin, and V. V. Liepa, "A general polarimetric radar calibration technique," *IEEE Transactions on Antennas and Propagation*, vol. 39, no. 1, pp. 62-67, January 1991.

- [87] T. L. Ainsworth, L. Ferro-Famil, and J.-S. Lee, "Orientation angle preserving a posteriori polarimetric SAR calibration," *IEEE Transactions on Geoscience and Remote Sensing*, vol. 44, no. 4, pp. 994-1003, April 2006.
- [88] F. Xu and Y.-Q. Jin, "Deorientation theory of polarimetric scattering targets and application to terrain surface classification," *IEEE Transactions on Geoscience and Remote Sensing*, vol. 43, no. 10, pp. 2351-2364, October 2005.
- [89] S. R. Cloude and E. Pottier, "An entropy based classification scheme for land applications of polarimetric SAR," *IEEE Transactions on Geoscience and Remote Sensing*, vol. 35, no. 1, pp. 68-78, January 1997.
- [90] O. Stebler, A. Schwerzmann, M. Luthi, E. Meier, and D. Nuesch, "Pol-InSAR observations from an Alpine glacier in the cold infiltration zone at L- and P-band," *IEEE Geoscience and Remote Sensing Letters*, vol. 2, no. 3, pp. 357-361, July 2005.
- [91] J. D. Ballester-Berman, J. M. Lopez-Sanchez, and J. Fortuny-Guasch, "Retrieval of biophysical parameters of agricultural crops using polarimetric SAR interferometry," *IEEE Transactions on Geoscience and Remote Sensing*, vol. 43, no. 4, pp. 683-694, April 2005.
- [92] H. Wakabayashi, T. Matsuoka, K. Nakamura, and F. Nishio, "Polarimetric characteristics of sea ice in the sea of Okhotsk observed by airborne L-band SAR," *IEEE Transactions on Geoscience and Remote Sensing*, vol. 42, no. 11, pp. 2412-2425, November 2004.
- [93] F. Gatelli, A. Monti Guarnieri, F. Parizzi, P. Pasquali, C. Prati, and F. Rocca, "The wavenumber shift in SAR interferometry," *IEEE Transactions on Geoscience and Remote Sensing*, vol. 32, no. 4, pp. 855-865, July 1994.

- [94] V. Alberga, "Volume decorrelation effects in polarimetric SAR interferometry," *IEEE Transactions on Geoscience and Remote Sensing*, vol. 42, no. 11, pp. 2467-2478, November 2004.
- [95] V. Alberga, *Comparison of polarimetric methods in image classification and SAR interferometry applications*, Ph.D. thesis, Technical University of Chemnitz, Chemnitz, Germany, 2004, [online available: [http://www.qucosa.de/recherche/frontdoor/?tx_slubopus4frontend\[id\]=4873](http://www.qucosa.de/recherche/frontdoor/?tx_slubopus4frontend[id]=4873)]
- [96] A. Freeman, "Calibration of linearly polarized polarimetric SAR data subject to Faraday rotation," *IEEE Transactions on Geoscience and Remote Sensing*, vol. 42, no. 8, pp. 1617-1624, August 2004.
- [97] W. B. Gail, "A simplified calibration technique for polarimetric radars," *IGARSS'93*, vol. 2, pp. 377-379, 1993.
- [98] Y. Yu and S. T. Acton, "Automated delineation of coastline from polarimetric SAR imagery," *International Journal of Remote Sensing*, vol. 25, no. 17, pp. 3423-3438, 10 September 2004.
- [99] D. L. Schuler, J. S. Lee, D. Kasilingam, and E. Pottier, "Measurement of ocean surface slopes and wave spectra using polarimetric SAR image data," *Remote Sensing of Environment*, vol. 91, pp. 198-211, 2004.
- [100] P. Lombardo, M. Sciotti, T. Macri Pellizzeri, and M. Meloni, "Optimum model-based segmentation techniques for multifrequency polarimetric SAR images of urban areas," *IEEE Transactions on Geoscience and Remote Sensing*, vol. 41, no. 9, pp. 1959-1975, September 2003.

- [101] F. Cao, W. Hong, Y. Wu, and E. Pottier, "An unsupervised segmentation with an adaptive number of clusters using the SPAN/H/ α /A space and the complex Wishart clustering for fully polarimetric SAR data analysis," *IEEE Transactions on Geoscience and Remote Sensing*, vol. 45, no. 11, pp. 3454-3467, November 2007.
- [102] C.-T. Chen, K.-S. Chen, and J.-S. Lee, "The use of fully polarimetric information for the fuzzy neural classification of SAR images," *IEEE Transactions on Geoscience and Remote Sensing*, vol. 41, no. 9, pp. 2089-2100, September 2003.
- [103] A. Ferretti, C. Prati, and F. Rocca, "Nonlinear subsidence rate estimation using permanent scatterers in differential SAR interferometry," *IEEE Transactions on Geoscience and Remote Sensing*, vol. 38, no. 5, pp. 2202-2212, September 2000.
- [104] G. Fornaro, G. Franceschetti, "Image registration in interferometric SAR processing," *IEE Proc.-Radar, Sonar Navig.*, vol. 142, no. 6, pp. 313-320, December 1995.
- [105] R. Hanssen and R. Bamler, "Evaluation of interpolation kernels for SAR interferometry," *IEEE Transactions on Geoscience and Remote Sensing*, vol. 37, no. 1, pp. 318-321, January 1999.
- [106] E. Sansosti, P. Berardino, M. Manunta, F. Serafino, and G. Fornaro, "Geometrical SAR image registration," *IEEE Transactions on Geoscience and Remote Sensing*, vol. 44, no. 10, pp. 2861-2870, October 2006.
- [107] B.-Q. Liu, D.-Z. Feng, P.-L. Shui, and N. Wu, "Analytic search method for interferometric SAR image registration," *IEEE Geoscience and Remote Sensing Letters*, vol. 5, no. 2, pp. 294-298, April 2008.

- [108] D. E. Alsdorf, J. M. Melack, T. Dunne, L. A. K. Mertes, L. L. Hess, and L. C. Smith, "Interferometric radar measurements of water level changes on the Amazon flood plain," *Nature*, vol. 404, pp. 174-177, 9 March 2000.
- [109] Z. Lu and Oh-ig Kwoun, "Radarsat-1 and ERS InSAR analysis over southeastern coastal Louisiana: Implications for mapping water-level changes beneath swamp forests," *IEEE Transactions on Geoscience and Remote Sensing*, vol. 46, no. 8, pp. 2167-2184, August 2008.
- [110] C. H. Gierull, "Statistical analysis of multilook SAR interferograms for CFAR detection of ground moving targets," *IEEE Transactions on Geoscience and Remote Sensing*, vol. 42, no. 4, pp. 691-701, April 2004.
- [111] A. Budillon, V. Pascazio, and G. Schirinzi, "Estimation of radial velocity of moving targets by along-track interferometric SAR systems," *IEEE Geoscience and Remote Sensing Letters*, vol. 5, no. 3, pp. 349-353, July 2008.
- [112] L. Yang, T. Wang, and Z. Bao, "Ground moving target indication using an InSAR system with a hybrid baseline," *IEEE Geoscience and Remote Sensing Letters*, vol. 5, no. 3, pp. 373-377, July 2008.
- [113] J. J. Mohr, and J. P. M. Boncori, "An error prediction framework for interferometric SAR data," *IEEE Transactions on Geoscience and Remote Sensing*, vol. 46, no. 6, pp. 1600-1613, June 2008.
- [114] D. Perissin and F. Rocca, "High-accuracy urban DEM using permanent scatterers," *IEEE Transactions on Geoscience and Remote Sensing*, vol. 44, no. 11, pp. 3338-3347, November 2006.

- [115] C. Colesanti, A. Ferretti, F. Novali, C. Prati, and F. Rocca, "SAR monitoring of progressive and seasonal ground deformation using the permanent scatterers technique," *IEEE Transactions on Geoscience and Remote Sensing*, vol. 41, no. 7, pp. 1685-1701, July 2003.
- [116] J. Dall, "InSAR elevation bias caused by penetration into uniform volumes," *IEEE Transactions on Geoscience and Remote Sensing*, vol. 45, no. 7, pp. 2319-2324, July 2007.
- [117] J. Selva, and J. M. Lopez-Sanchez, "Efficient interpolation of SAR images for coregistration in SAR interferometry," *IEEE Geoscience and Remote Sensing Letters*, vol. 4, no. 3, pp. 411-415, July 2007.
- [118] M. Migliaccio and F. Bruno, "A new interpolation kernel for SAR interferometric registration," *IEEE Transactions on Geoscience and Remote Sensing*, vol. 41, no. 5, pp. 1105-1110, May 2003.
- [119] H. Balzter, A. Luckman, L. Skinner, C. Rowland, and T. Dawson, "Observations of forest stand top height and mean height from interferometric SAR and LiDAR over a conifer plantation at Thetford forest, UK," *International Journal of Remote Sensing*, vol. 28, no. 6, pp. 1173-1197, 20 March 2007.
- [120] M.-H. Ka and A. A. Kononov, "Effect of look angle on the accuracy performance of fixed-baseline interferometric SAR," *IEEE Geoscience and Remote Sensing Letters*, vol. 4, no. 1, pp. 65-69, January 2007.
- [121] C. Tison, F. Tupin, and H. Maitre, "A fusion scheme for joint retrieval of urban height map and classification from high-resolution interferometric SAR images,"

- IEEE Transactions on Geoscience and Remote Sensing*, vol. 45, no. 2, pp. 496-505, February 2007.
- [122] P. Gamba, B. Houshmand, and M. Saccani, "Detection and extraction of buildings from interferometric SAR data," *IEEE Transactions on Geoscience and Remote Sensing*, vol. 38, no. 1, pp. 611-618, January 2000.
- [123] R. Romeiser, "Current measurements by airborne along-track InSAR: measuring technique and experimental results," *IEEE Journal of Oceanic Engineering*, vol. 30, no. 3, pp. 552-569, July 2005.
- [124] H. C. Graber, D. R. Thompson, and R. E. Carande, "Ocean surface features and currents measured with synthetic aperture radar interferometry and HF radar," *Journal of Geophysical Research*, vol. 101, no. C11, pp. 25813-25832, November 15, 1996.
- [125] M. Preiss, D. A. Gray, and N. J. S. Stacy, "Detecting scene changes using synthetic aperture radar interferometry," *IEEE Transactions on Geoscience and Remote Sensing*, vol. 44, no. 8, pp. 2041-2054, August 2006.
- [126] L. Cascini, S. Ferlisi, G. Fornaro, R. Lanari, D. Peduto, and G. Zeni, "Subsidence monitoring in Sarno urban area via multi-temporal DInSAR technique," *International Journal of Remote Sensing*, vol. 27, no. 8, pp. 1709-1716, 20 April 2006.
- [127] D. C. Ghiglia and M. D. Pritt, *Two-Dimensional Phase Unwrapping: Theory, Algorithms, and Software*, John Wiley & Sons, Inc., 1998.
- [128] Z. Li, Z. Bao, H. Li, and G. Liao, "Image autocoregistration and InSAR interferogram estimation using joint subspace projection," *IEEE Transactions on Geoscience and Remote Sensing*, vol. 44, no. 2, pp. 288-297, February 2006.

- [129] J. Schulz-Stellenfleth and S. Lehner, "Ocean wave imaging using an airborne single pass across-track interferometric SAR," *IEEE Transactions on Geoscience and Remote Sensing*, vol. 39, no. 1, pp. 38-45, January 2001.
- [130] H. A. Zebker and J. Villasenor, "Decorrelation in interferometric radar echoes," *IEEE Transactions on Geoscience and Remote Sensing*, vol. 30, no. 5, pp. 950-959, September 1992.
- [131] H. Lee and Jian Guo Liu, "Analysis of topographic decorrelation in SAR interferometry using ratio coherence imagery," *IEEE Transactions on Geoscience and Remote Sensing*, vol. 39, no. 2, pp. 223-232, February 2001.
- [132] F. K. Li, and R. M. Goldstein, "Studies of multibaseline spaceborne interferometric synthetic aperture radars," *IEEE Transactions on Geoscience and Remote Sensing*, vol. 28, no. 1, pp. 88-97, January 1990.
- [133] G. Fornaro and A. M. Guarnieri, "Minimum mean square error space-varying filtering of interferometric SAR data," *IEEE Transactions on Geoscience and Remote Sensing*, vol. 40, no. 1, pp. 11-21, January 2002.
- [134] C. W. Chen and H. A. Zebker, "Two-dimensional phase unwrapping with use of statistical models for cost functions in nonlinear optimization," *J. Opt. Soc. Am. A*, vol. 18, no. 2, pp. 338-351, February 2001.
- [135] R. Gens, "Two-dimensional phase unwrapping for radar interferometry: developments and new challenges," *International Journal of Remote Sensing*, vol. 24, no. 4, pp. 703-710, 2003.

- [136] W. Xu and I. Cumming, "A region-growing algorithm for InSAR phase unwrapping," *IEEE Transactions on Geoscience and Remote Sensing*, vol. 37, no. 1, pp. 124-134, January 1999.
- [137] R. Abdelfattah and J. M. Nicolas, "Topographic SAR interferometry formulation for high-precision DEM generation," *IEEE Transactions on Geoscience and Remote Sensing*, vol. 40, no. 11, pp. 2415-2426, November 2002.
- [138] M. Eineder and S. Suchandt, "Recovering radar shadow to improve interferometric phase unwrapping and DEM reconstruction," *IEEE Transactions on Geoscience and Remote Sensing*, vol. 41, no. 12, pp. 2959-2962, December 2003.
- [139] M. Eineder, "Efficient simulation of SAR interferograms of large areas and of rugged terrain," *IEEE Transactions on Geoscience and Remote Sensing*, vol. 41, no. 6, pp. 1415-1427, June 2003.
- [140] J.-S. Lee, M. R. Grunes, E. Pottier, and L. Ferro-Famil, "Unsupervised terrain classification preserving polarimetric scattering characteristics," *IEEE Transactions on Geoscience and Remote Sensing*, vol. 42, no. 4, pp. 722-731, April 2004.
- [141] G. Ferraiuolo and G. Poggi, "A Bayesian filtering technique for SAR interferometric phase fields," *IEEE Transactions on Image Processing*, vol. 13, no. 10, pp. 1368-1378, October 2004.
- [142] R. M. Goldstein, H. A. Zebker, and C. L. Werner, "Satellite radar interferometry: Two-dimensional phase unwrapping," *Radio Science*, vol. 23, no. 4, pp. 713-720, July-August 1988.

- [143] N. R. Goodman, "Statistical analysis based on a certain multivariate complex Gaussian distribution (An introduction)," *The Annals of Mathematical Statistics*, vol. 34, no. 1, pp. 152-177, March 1963.
- [144] L. M. Novak and M. C. Burl, "Optimal speckle reduction in polarimetric SAR imagery," *IEEE Transactions on Aerospace and Electronic Systems*, vol. 26, no. 2, pp. 293-305, March 1990.
- [145] S. R. Cloude, *Polarisation: Applications in Remote Sensing*, Oxford University Press, New York: 2010.
- [146] S. Quegan and I. Rhodes, "Statistical models for polarimetric data: consequences, testing and validity," *International Journal of Remote Sensing*, vol. 16, no. 7, pp. 1183-1210, 1995.
- [147] R. Touzi and A. Lopes, "The principle of speckle filtering in polarimetric SAR imagery," *IEEE Transactions on Geoscience and Remote Sensing*, vol. 32, no. 5, pp. 1110-1114, September 1994.
- [148] J.-S. Lee, M. R. Grunes, and G. de Grandi, "Polarimetric SAR speckle filtering and its implication for classification," *IEEE Transactions on Geoscience and Remote Sensing*, vol. 37, no. 5, pp. 2363-2373, September 1999.
- [149] D. R. Sheen and L. P. Johnston, "Statistical and spatial properties of forest clutter measured with polarimetric synthetic aperture radar (SAR)," *IEEE Transactions on Geoscience and Remote Sensing*, vol. 30, no. 3, pp. 578-588, May 1992.
- [150] J.-S. Lee, K. P. Papathanassiou, T. L. Ainsworth, M. R. Grunes, and A. Reigber, "A new technique for noise filtering of SAR interferometric phase images," *IEEE*

- Transactions on Geoscience and Remote Sensing*, vol. 36, no. 5, pp. 1456-1465, September 1998.
- [151] Y. Kobayashi, K. Sarabandi, L. Pierce, and M. C. Dobson, "An evaluation of the JPL TOPSAR for extracting tree heights," *IEEE Transactions on Geoscience and Remote Sensing*, vol. 38, no. 6, pp. 2446-2454, November 2000.
- [152] L. Alparone, S. Baronti, and R. Carla, "An adaptive rank-conditioned median filter for edge-preserving image smoothing," *Image and Signal Processing For Remote Sensing III: 23-25 September 1996*, Taormina, Italy, edited by Jacky Desachy, 1996.
- [153] H.-E. Andersen, R. McGaughey, S. Reutebuch, G. Schreuder, J. Agee, B. Mercer, "Estimating canopy fuel parameters in a pacific northwest conifer forest using multifrequency polarimetric IFSAR," *Proceedings of XXth ISPRS Congress, Commission 3*, vol. XXXV, 12-23 July 2004, Istanbul, Turkey, 2004.
- [154] Y. Bian, Y. Zhou, and C. Li, "Some adaptive filterbank spectral estimation methods based on FLOS," *Acta Electronica Sinica*, vol. 36, No. 6, pp. 1235-1241, June 2008.
- [155] B. Mercer, "DEMs created from airborne IFSAR-an update," *Proceedings of XXth ISPRS Congress, Commission 2*, vol. XXXV, 12-23 July 2004, Istanbul, Turkey, 2004.
- [156] S. Cambanis, "Complex symmetric stable variables and processes," in *Contributions to Statistics, Essays in Honour of Norman L. Johnson*, P. K. Sen (Editor), pp. 63-79, 1983.

- [157] E. F. Fama and R. Roll, "Parameter estimates for symmetric stable distributions," *Journal of the American Statistical Association*, vol. 66, No. 334, pp. 331-338, June 1971.
- [158] J. Gu, J. Yang, H. Zhang, Y. Peng, C. Wang, and H. Zhang, "Speckle filtering in polarimetric SAR data based on the subspace decomposition," *IEEE Transactions on Geoscience and Remote Sensing*, vol. 42, No. 8, pp. 1635-1641, August 2004.
- [159] E. E. Kuruoglu, "Density parameter estimation of skewed α -stable distributions," *IEEE Transactions on Signal Processing*, vol. 49, No. 10, pp. 2192-2201, October 2001.
- [160] E. E. Kuruoglu and J. Zerubia, "Modeling SAR images with a generalization of the Rayleigh distribution," *IEEE Transactions on Image Processing*, vol. 13, No. 4, pp. 527-533, April 2004.
- [161] G. Liu, S. Huang, A. Torre, and F. Rubertone, "The multilook polarimetric whitening filter (MPWF) for intensity speckle reduction in polarimetric SAR images," *IEEE Transactions on Geoscience and Remote Sensing*, vol. 36, no. 3, pp. 1016-1020, May 1998.
- [162] A. Lopes and F. Séry, "Optimal speckle reduction for the product model in multilook polarimetric SAR imagery and the Wishart distribution," *IEEE Transactions on Geoscience and Remote Sensing*, vol. 35, no. 3, pp. 632-647, May 1997.
- [163] A. Lopes, R. Touzi, E. Nezry, "Adaptive speckle filters and scene heterogeneity," *IEEE Transactions on Geoscience and Remote Sensing*, vol. 28, no. 6, pp. 992-1000, November 1990.

- [164] X. Ma and C. L. Nikias, "Parameter estimation and blind channel identification in impulsive signal environments," *IEEE Transactions on Signal Processing*, vol. 43, no. 12, pp. 2884-2897, December 1995.
- [165] X. Ma and C. L. Nikias, "Joint estimation of time delay and frequency delay in impulsive noise using fractional lower order statistics," *IEEE Transactions on Signal Processing*, vol. 44, no. 11, pp. 2669-2687, November 1996.
- [166] G. Miller, "Properties of certain symmetric stable distributions," *Journal of Multivariate Analysis*, vol. 8, issue 3, pp. 346-360, September 1978.
- [167] C. L. Nikias and M. Shao, *Signal Processing with Alpha-Stable Distributions and Applications*, New York: John Wiley & Sons, Inc., 1995.
- [168] J. P. Nolan, STABLE software Website, <http://academic2.american.edu/~jpnolan/stable/stable.html>
- [169] J. P. Nolan, "Numerical calculation of stable densities and distribution functions," *Stochastic Models*, vol. 13, no. 4, pp. 759-774, 1997.
- [170] J. P. Nolan, "Maximum likelihood estimation and diagnostics for stable distributions," in *Levy Processes: Theory and Applications*, edited by Ole E. Barndorff-Nielsen, Thomas Mikosch, and Sidney I. Resnick, Birkhauser, 2001.
- [171] J. P. Nolan, "Multivariate stable densities and distribution functions: general and elliptical case," *Conference on "Heavy tails and stable Paretian distributions in finance and macroeconomics"*, Deutsche Bundesbank's 2005 Annual Fall Conference, November 2005, Eltville. Available from: http://www.bundesbank.de/vfz/vfz_konferenzen_2005.en.php.

- [172] L. M. Novak, M. B. Sechtin, and M. J. Cardullo, "Studies of target detection algorithms that use polarimetric radar data," *IEEE Transactions on Aerospace and Electronic Systems*, vol. AES-25, no. 2, pp. 150-165, March 1989.
- [173] Y. Pi, X. Yang, and G. Liu, "Polarimetric speckle reduction using multi-texture maximum likelihood method," *Electronics Letters*, vol. 39, no. 18, pp. 1348-1349, September 2003.
- [174] S. J. Press, "Estimation in univariate and multivariate stable distributions," *Journal of the American Statistical Association*, vol. 67, no. 340, pp. 842-846, December 1972.
- [175] D. Salas-Gonzalez, E. E. Kuruoglu, and D. P. Ruiz, "Finite mixture of alpha-stable distributions," *Digital Signal Processing*, vol. 9, pp. 250-264, 2009.
- [176] G. Samorodnitsky and M. S. Taqqu, *Stable Non-Gaussian Random Processes: Stochastic Models with Infinite Variance*, New York: Chapman & Hall, 1994.
- [177] M. Schwabisch, S. Gopal, B. Mercer, Q. Zhang, and M. Wei, "Early results using single-pass L-band Pol-InSAR," *IGARSS 2008*, vol. 5, 7-11 July, 2008, pp. V-286-V-289.
- [178] H. Sengar, H. Wang, D. Wijesekera, and S. Jajodia, "Detecting VoIP floods using the Hellinger distance," *IEEE Transactions on Parallel and Distributed Systems*, vol. 19, no. 6, pp. 794-805, June 2008.
- [179] M. Shao and C. L. Nikias, "Signal processing with fractional lower order moments: stable processes and their applications," *Proceedings of The IEEE*, vol. 81, no. 7, pp. 986-1010, July 1993.

- [180] A. A. Swartz, H. A. Yueh, J. A. Kong, L. M. Novak, and R. T. Shin, "Optimal polarizations for achieving maximum contrast in radar images," *Journal of Geophysical Research*, vol. 93, no. B12, pp. 15252-15260, December 10, 1988.
- [181] R. J. A. Tough, D. Blacknell, S. Quegan, "A statistical description of polarimetric and interferometric synthetic aperture radar data," *Proceedings of the Royal Society of London*, A 449, pp. 567-589, 1995.
- [182] P. Tsakalides and C. L. Nikias, "The robust covariation-based MUSIC (ROC-MUSIC) algorithm for bearing estimation in impulsive noise environments," *IEEE Transactions on Signal Processing*, vol. 44, no. 7, pp. 1623-1633, July 1996.
- [183] P. Tsakalides and C. L. Nikias, "High-resolution autofocus techniques for SAR imaging based on fractional lower-order statistics," *IEE Proceedings-Radar, Sonar, and Navigation*, vol. 148, no. 5, pp. 267-276, October 2001.
- [184] G. A. Tsihrintzis and C. L. Nikias, "Fast estimation of the parameters of alpha-stable impulsive interference," *IEEE Transactions on Signal Processing*, vol. 44, no. 6, pp. 1492-1503, June 1996.
- [185] H. Xie, L. E. Pierce, and F. T. Ulaby, "SAR speckle reduction using wavelet denoising and Markov random field modeling," *IEEE Transactions on Geoscience and Remote Sensing*, vol. 40, no. 10, pp. 2196-2212, October 2002.
- [186] S. H. Yueh and J. A. Kong, "K-distribution and polarimetric terrain radar clutter," *Journal of Electromagnetic Waves and Applications*, vol. 3, no. 8, pp. 747-768, 1989.
- [187] S. H. Yueh, J. A. Kong, J. K. Jao, R. T. Shin, H. A. Zebker, T. Le Toan, and H. Ottl, "K-distribution and polarimetric terrain radar clutter," In *Polarimetric Remote Sensing* (ed. J. A. Kong), New York and Amsterdam: Elsevier, 1990.

- [188] V. M. Zolotarev, "Integral transformations of distributions and estimates of parameters of multidimensional spherically symmetric stable laws," in *Contributions to Probability*, pp. 283-305, Academic Press, 1981.
- [189] J. S. Lee, S. R. Cloude, K. P. Papathanassiou, M. R. Grunes, and I. H. Woodhouse, "Speckle filtering and coherence estimation of polarimetric SAR interferometry data for forest applications," *IEEE Transactions on Geoscience and Remote Sensing*, vol. 41, no. 10, pp. 2254-2263, October 2003.
- [190] R. Touzi and A. Lopes, "Statistics of the Stokes parameters and of the complex coherence parameters in one-look and multilook speckle fields," *IEEE Transactions on Geoscience and Remote Sensing*, vol. 34, no. 2, pp. 519-531, March 1996.
- [191] R. Touzi, A. Lopes, J. Bruniquel, and P. W. Vachon, "Coherence estimation for SAR imagery," *IEEE Transactions on Geoscience and Remote Sensing*, vol. 37, no. 1, pp. 135-149, January 1999.
- [192] Yong Bian and Bryan Mercer, "PolInSAR statistical analysis and coherence optimization using fractional lower order statistics," *IEEE Geoscience and Remote Sensing Letters*, vol. 7, no. 2, pp. 314-318, April 2010.
- [193] M. S. Seymour and I. G. Cumming, "Maximum likelihood estimation for SAR interferometry," *IGARSS*, 1994, 2272-2275.
- [194] S. J. Press, "Multivariate stable distributions," *Journal of Multivariate Analysis*, no. 2, pp. 444-462, 1972.
- [195] C. Lopez-Martinez and E. Pottier, "Coherence estimation in synthetic aperture radar data based on speckle noise modeling," *Applied Optics*, vol. 46, no. 4, pp. 544-558, February 2007.

- [196] E. J. M. Rignot and J. J. van Zyl, "Change detection techniques for ERS-1 SAR data," *IEEE Transactions on Geoscience and Remote Sensing*, vol. 31, no. 4, pp. 896-906, July 1993.
- [197] P. Tsakalides, R. Raspanti, and C. L. Nikias, "Angle/doppler estimation in heavy-tailed clutter backgrounds," *IEEE Transactions on Aerospace and Electronic Systems*, vol. 35, no. 2, pp. 419-436, April 1999.
- [198] H. Belkacemi and S. Marcos, "Robust subspace-based algorithms for joint angle/Doppler estimation in non-Gaussian clutter," *Signal Processing*, 87, pp. 1547-1558, 2007.
- [199] Yong Bian, "Polarimetric SAR statistical analysis using alpha-stable distribution and its application in optimal despeckling," *International Journal of Remote Sensing*, Submitted for publication.
- [200] A. Monti Guarnieri and C. Prati, "SAR interferometry: A "quick and dirty" coherence estimator for data browsing," *IEEE Transactions on Geoscience and Remote Sensing*, vol. 35, no. 3, pp. 660-669, May 1997.
- [201] R. Abdelfattah and J.-M. Nicolas, "Inteferometric SAR coherence magnitude estimation using second kind statistics," *IEEE Transactions on Geoscience and Remote Sensing*, vol. 44, no. 7, pp. 1942-1953, July 2006.
- [202] C. Lopez-Martinez, X. Fabregas, and E. Pottier, "Wavelet transform-based interferometric SAR coherence estimator," *IEEE Signal Processing Letters*, vol. 12, no. 12, pp. 831-834, December 2005.

- [203] R. D. Pierce, "Application of the positive alpha-stable distribution," *Proceedings of the IEEE Signal Processing Workshop on Higher-Order Statistics*, pp. 420-424, July 1997.
- [204] F. Pascal, P. Forster, J.-P. Ovarlez, and P. Larzabal, "Performance analysis of covariance matrix estimates in impulsive noise," *IEEE Transactions on Signal Processing*, vol. 56, no. 6, pp. 2206-2217, June 2008.
- [205] V. J. Paulauskas, "Some remarks on multivariate stable distributions," *Journal of Multivariate Analysis*, no. 6, 1976, pp. 356-368.
- [206] M. Santoro, J. I. H. Askne, U. Wegmuller, and C. L. Werner, "Observations, modeling, and applications of ERS-ENVISAT coherence over land surfaces," *IEEE Transactions on Geoscience and Remote Sensing*, vol. 45, no. 8, pp. 2600-2611, August 2007.
- [207] W. F. Perger, A. Bhalla, and M. Nardin, "A numerical evaluator for the generalized hypergeometric series," *Computer Physics Communications*, vol. 77, issue 2, pp. 249-254, October 1993.
- [208] A. M. Achim, C. N. Canagarajah, D. R. Bull, "Complex wavelet domain image fusion based on fractional lower order moments," *2005 8th Int. Conference on Information Fusion*, vol. 1, 25-28 July 2005, 7 pages.
- [209] Source code online available at <http://www.ece.mtu.edu/faculty/wfp/codes.html>.
- [210] Juan J. Martinez-Espla, Tomas Martinez-Marin, and Juan M. Lopez-Sanchez, "An optimized algorithm for InSAR phase unwrapping based on particle filtering, matrix pencil, and region-growing techniques," *IEEE Geoscience and Remote Sensing Letters*, vol. 6, no. 4, pp. 835-839, October 2009.

- [211] Otmar Loffeld, Holger Nies, Stefan Knedlik, and Wang Yu, "Phase unwrapping for SAR interferometry-A data fusion approach by Kalman filtering," *IEEE Transactions on Geoscience and Remote Sensing*, vol. 46, no. 1, pp. 47-58, January 2008.
- [212] J. J. Martinez-Espla, Tomas Martinez-Marin, and Juan M. Lopez-Sanchez, "A particle filter approach for InSAR phase filtering and unwrapping," *IEEE Transactions on Geoscience and Remote Sensing*, vol. 47, no. 4, pp. 1197-1211, April 2009.
- [213] Richard M. Goldstein and Charles L. Werner, "Radar interferogram filtering for geophysical applications," *Geophysical Research Letters*, vol. 25, no. 21, pp. 4035-4038, November 1, 1998.
- [214] Bruno Aiazzi, Stefano Baronti, Massimo Bianchini, Alessandro Mori, Luciano Alparone, "Filtering of interferometric SAR phase images as a fuzzy matching-pursuit blind estimation," *EURASIP Journal on Applied Signal Processing*, vol. 2005, Issue 20, pp. 3220-3230, 2005.
- [215] Nan Wu, Da-Zheng Feng, and Junxia Li, "A locally adaptive filter of interferometric phase images," *IEEE Geoscience and Remote Sensing Letters*, vol. 3, no. 1, pp. 73-77, January 2006.
- [216] Ireneusz Baran, Mike P. Stewart, Bert M. Kampes, Zbigniew Perski, and Peter Lilly, "A modification to the Goldstein radar interferogram filter," *IEEE Transactions on Geoscience and Remote Sensing*, vol. 41, no. 9, pp. 2114-2118, September 2003.

- [217] Carlos Lopez-Martinez and Xavier Fabregas, "Modeling and reduction of SAR interferometric phase noise in the wavelet domain," *IEEE Transactions on Geoscience and Remote Sensing*, vol. 40, no. 12, pp. 2553-2566, December 2002.
- [218] C. L. Martinez, X. F. Canovas, and M. Chandra, "SAR interferometric phase noise reduction using wavelet transform," *Electronics Letters*, vol. 37, no. 10, pp. 649-651, May 2001.
- [219] Xianjie Zha, Rongshan Fu, Zhiyang Dai, and Bin Liu, "Noise reduction in interferograms using the wavelet packet transform and Wiener filtering," *IEEE Geoscience and Remote Sensing Letters*, vol. 5, no. 3, pp. 404-408, July 2008.
- [220] Heresh Fattahi, Mohammad Javad Valadan Zoej, Mohammad Reza Mobasheri, Maryam Dehghani, and Mahmud Reza Sahebi, "Windowed Fourier Transform for noise reduction of SAR interferograms," *IEEE Geoscience and Remote Sensing Letters*, vol. 6, no. 3, pp. 418-422, July 2009.
- [221] Ingrid Daubechies, "The wavelet transform, time-frequency localization and signal analysis," *IEEE Transactions on Information Theory*, vol. 36, no. 5, pp. 961-1005, September 1990.
- [222] David Middleton and Raffaele Esposito, "Simultaneous optimum detection and estimation of signals in noise," *IEEE Transactions on Information Theory*, vol. IT-14, no. 3, pp. 434-444, May 1968.
- [223] Ari Abramson and Israel Cohen, "Simultaneous detection and estimation approach for speech enhancement," *IEEE Transactions on Audio, Speech, and Language Processing*, vol. 15, no. 8, pp. 2348-2359, November 2007.

- [224] Ari Abramson and Israel Cohen, "Single-sensor audio source separation using classification and estimation approach and GARCH modeling," *IEEE Transactions on Audio, Speech, and Language Processing*, vol. 16, no. 8, pp. 1528-1540, November 2008.
- [225] David L. Donoho and Iain M. Johnstone, "Ideal spatial adaptation by wavelet shrinkage," *Biometrika*, vol. 81, no. 3, pp. 425-455, August 1994.
- [226] Anton Fredriksen, David Middleton, and David Vandelinde, "Simultaneous signal detection and estimation under multiple hypotheses," *IEEE Transactions on Information Theory*, vol. IT-18, no. 5, pp. 607-614, September 1972.
- [227] David Middleton and Raffaele Esposito, "New results in the theory of simultaneous optimum detection and estimation of signals in noise," *Problemy Peredachi Informatsii*, vol. 6, no. 2, pp. 3-20, April-June, 1970.
- [228] Oleg Michailovich and Allen Tannenbaum, "Dynamic denoising of tracking sequences," *IEEE Transactions on Image Processing*, vol. 17, no. 6, pp. 847-856, June 2008.
- [229] Aleksandra Pizurica, Wilfried Philips, Ignace Lemahieu, and Marc Acherooy, "A versatile wavelet domain noise filtration technique for medical imaging," *IEEE Transactions on Medical Imaging*, vol. 22, no. 3, pp. 323-331, March 2003.
- [230] Amin G. Jaffer and Someshwar C. Gupta, "Coupled detection-estimation of Gaussian processes in Gaussian noise," *IEEE Transactions on Information Theory*, vol. IT-18, no. 1, pp. 106-110, January 1972.
- [231] David Middleton, *An Introduction to Statistical Communication Theory*, IEEE Press, Piscataway, NJ, 1996.

- [232] C. Lopez and X. Fabregas, "SAR interferometric phase statistics in wavelet domain," *Electronics Letters*, vol. 38, no. 20, pp. 1207-1208, 26th September 2002.
- [233] David L. Donoho, Iain M. Johnstone, Gerard Kerkyacharian, Dominique Picard, "Wavelet shrinkage: Asymptopia?," *Journal of the Royal Statistical Society, Series B (Methodological)*, vol. 57, no. 2, pp. 301-369, 1995.
- [234] Frank R. Hampel, "The influence curve and its role in robust estimation," *Journal of the American Statistical Association*, vol. 69, no. 346, pp. 383-393, June 1974.
- [235] Peter J. Rousseeuw and Christophe Croux, "Alternatives to the median absolute deviation," *Journal of the American Statistical Association*, vol. 88, no. 424, pp. 1273-1283, December 1993.
- [236] Merlise Clyde, Giovanni Parmigiani, and Brani Vidakovic, "Multiple shrinkage and subset selection in wavelets," *Biometrika*, vol. 85, no. 2, pp. 391-401, June 1998.
- [237] I.S. Gradshteyn and I.M. Ryzhik, *Table of Integrals, Series, and Products*, Alan Jeffrey and Dan Zwillinger, Eds., Academic Press, 2000.
- [238] Ronald R. Coifman, Yves Meyer, and Victor Wickerhauser, "Wavelet analysis and signal processing," *Wavelets and Their Applications*, pp. 153-178, Jones and Bartlett Publishers, Inc, Editor Mary Beth Ruskai, et al., 1992.
- [239] Abhijit Karmakar, Arun Kumar, and R. K. Patney, "Design of optimal wavelet packet trees based on auditory perception criterion," *IEEE Signal Processing Letters*, vol. 14, no. 4, pp. 240-243, April 2007.
- [240] B. Walczak, D. L. Massart, "Noise suppression and signal compression using the wavelet packet transform," *Chemometrics and Intelligent Laboratory Systems*, 36, pp. 81-94, 1997.

- [241] Kannan Ramchandran, Martin Vetterli, and Cormac Herley, "Wavelets, subband coding, and best bases," *Proceedings of the IEEE*, vol. 84, no. 4, pp. 541-560, April 1996.
- [242] Hamid Krim, Dewey Tucker, Stephane Mallat, and David Donoho, "On denoising and best signal representation," *IEEE Transactions on Information Theory*, vol. 45, no. 7, pp. 2225-2238, November 1999.
- [243] Stephane Mallat, *A Wavelet Tour of Signal Processing*, Second Edition, Academic Press, 1999.
- [244] Rafael C. Gonzalez and Richard E. Woods, *Digital Image Processing*, second edition, New Jersey: Prentice-Hall, Inc., 2002.
- [245] Fabrizio Argenti and Luciano Alparone, "Speckle removal from SAR images in the undecimated wavelet domain," *IEEE Transactions on Geoscience and Remote Sensing*, vol. 40, no. 11, pp. 2363-2374, November 2002.
- [246] Jean-Luc Starck, Michael Elad, and David Donoho, "Redundant multiscale transforms and their application for morphological component separation," *Advances in Imaging and Electron Physics*, Edited by Peter W. Hawkes, Elsevier Academic Press, San Diego, California, vol. 132, pp. 287-348, 2004.
- [247] R. R. Coifman and D. L. Donoho, "Translation-invariant de-noising," *Wavelets and Statistics*, Edited by Anestis Antoniadis and Georges Oppenheim, Springer-Verlag New York, Inc., pp. 125-150, 1995.
- [248] Mark J. Shensa, "The discrete wavelet transform: wedding the a trous and Mallat algorithms," *IEEE Transactions on Signal Processing*, vol. 40, no. 10, pp. 2464-2482, October 1992.

- [249] Samuel Foucher, Goze Bertin Benie, and Jean-Marc Boucher, "Multiscale MAP filtering of SAR images," *IEEE Transactions on Image Processing*, pp. 49-60, January 2001.
- [250] Mark Nardin, W. F. Perger, and Atul Bhalla, "Algorithm 707 CONHYP: A numerical evaluator of the confluent hypergeometric function for complex arguments of large magnitudes," *ACM Trans. Mathematical Software*, vol. 18, no. 3, pp. 345-349, September 1992.
- [251] Aleksandra Pizurica, Wilfried Philips, Ignace Lemahieu, and Marc Achero, "A joint inter- and intrascale statistical model for Bayesian wavelet based image denoising," *IEEE Transactions on Image Processing*, vol. 11, no. 5, pp. 545-557, May 2002.
- [252] J. J. Martinez-Espla, T. Martinez-Marin, and J. M. Lopez-Sanchez, "Using a grid-based filter to solve InSAR phase unwrapping," *IEEE Geoscience and Remote Sensing Letters*, vol. 5, no. 2, pp. 147-151, April 2008.
- [253] Yong Bian and Bryan Mercer, "Weighted regularized preconditioned conjugate gradient (PCG) phase unwrapping method," *Journal of Optics A: Pure and Applied Optics*, vol. 11, issue 1, Article number: 015504, 11pp, 2009. doi:10.1088/1464-4258/11/1/015504.
- [254] Ingrid Daubechies, "Orthonormal bases of compactly supported wavelets," *Communications on Pure and Applied Mathematics*, vol. XLI, pp. 909-996, 1988.
- [255] Yong Bian and Bryan Mercer, "Using second order residue in PolInSAR phase unwrapping," *Proceedings of the 2008 IEEE Radar Conference*, Rome, Italy, May 26-30, 2008, pp. 1-5.

- [256] S. Grace Chang, Bin Yu, and Martin Vetterli, "Spatially adaptive wavelet thresholding with context modeling for image denoising," *IEEE Transactions on Image Processing*, vol. 9, no. 9, pp. 1522-1531, September 2000.
- [257] Stephane Mallat and Sifen Zhong, "Characterization of signals from multiscale edges," *IEEE Transactions on Pattern Analysis and Machine Intelligence*, vol. 14, no. 7, pp. 710-732, July 1992.
- [258] Aleksandra Pizurica, *Image Denoising Using Wavelets and Spatial Context Modeling*, PhD dissertation, Ghent University, Ghent, Belgium, 2002.
- [259] R. Martin, "Speech enhancement based on minimum mean-square error estimation and supergaussian priors," *IEEE Transactions on Speech and Audio Processing*, vol. 13, no. 5, pp. 845-856, September 2005.
- [260] M. V. Wickerhauser, "INRIA lectures on wavelet packet algorithms," in *Proc. Ondelettes et Paquets d'Ondelettes*, Roquencourt, France, June 17-21, 1991, pp. 31-99.
- [261] Jose L. Marroquin and Mariano Rivera, "Quadratic regularization functionals for phase unwrapping," *J. Opt. Soc. Am. A*, vol. 12, no. 11, pp. 2393-2400, November 1995.
- [262] Mariano Rivera, Jose L. Marroquin, Manuel Servin, and Ramon Rodriguez-Vera, "Fast algorithm for integrating inconsistent gradient fields," *Applied Optics*, vol. 36, no. 32, pp. 8381-8390, 10 November 1997.
- [263] José L. Marroquin, Mariano Rivera, Salvador Botello, Ramón Rodríguez-Vera, and Manuel Servin, "Regularization methods for processing fringe-pattern images," *Applied Optics*, vol. 38, no. 5, pp. 788-794, 10 February 1999.

- [264] Dennis C. Ghiglia and Louis A. Romero, "Robust two-dimensional weighted and unweighted phase unwrapping that uses fast transforms and iterative methods," *J. Opt. Soc. Am. A*, vol. 11, no. 1, pp. 107-117, January 1994.
- [265] Luciano Guerriero, Giovanni Nico, Guido Pasquariello, and Sebastiano Stramaglia, "New regularization scheme for phase unwrapping," *Applied Optics*, vol. 37, no. 14, pp. 3053-3058, 10 May 1998.
- [266] Hiroaki Takajo and Tohru Takahashi, "Least-squares phase estimation from the phase difference," *J. Opt. Soc. Am. A*, vol. 5, no. 3, pp. 416-425, March 1988.
- [267] Hiroaki Takajo and Tohru Takahashi, "Noniterative method for obtaining the exact solution for the normal equation in least-squares phase estimation from the phase difference," *J. Opt. Soc. Am. A*, vol. 5, no. 11, pp. 1818-1827, November 1988.
- [268] Mark D. Pritt, "Phase unwrapping by means of multigrid techniques for interferometric SAR," *IEEE Transactions on Geoscience and Remote Sensing*, vol. 34, no. 3, pp. 728-738, May 1996.
- [269] Aloysius Wehr, Uwe Lohr, "Airborne laser scanning-an introduction and overview," *ISPRS Journal of Photogrammetry & Remote Sensing*, vol. 54, pp. 68-82, 1999.
- [270] Dennis C. Ghiglia and Louis A. Romero, "Minimum L^p -norm two-dimensional phase unwrapping," *J. Opt. Soc. Am. A*, vol. 13, no. 10, pp. 1999-2013, October 1996.
- [271] Jarle Strand, Torfinn Taxt, and Anil K. Jain, "Two-dimensional phase unwrapping using a block least-squares method," *IEEE Transactions on Image Processing*, vol. 8, no. 3, pp. 375-386, March 1999.

- [272] Jarle Strand and Torfinn Taxt, "Performance evaluation of two-dimensional phase unwrapping algorithms," *Applied Optics*, vol. 38, no. 20, pp. 4333-4344, 10 July 1999.
- [273] Guillermo H. Kaufmann, Gustavo E. Galizzi, and Pablo D. Ruiz, "Evaluation of a preconditioned conjugate-gradient algorithm for weighted least-squares unwrapping of digital speckle-pattern interferometry phase maps," *Applied Optics*, vol. 37, no. 14, pp. 3076-3084, 10 May 1998.
- [274] Andriyan Bayu Suksmono and Akira Hirose, "Adaptive noise reduction of InSAR images based on a complex-valued MRF model and its application to phase unwrapping problem," *IEEE Transactions on Geoscience and Remote Sensing*, vol. 40, no. 3, pp. 699-709, March 2002.
- [275] Mario Costantini, Alfonso Farina, and Francesco Zirilli, "A fast phase unwrapping algorithm for SAR interferometry," *IEEE Transactions on Geoscience and Remote Sensing*, vol. 37, no. 1, pp. 452-460, January 1999.
- [276] Salah A. Karout, Munther A. Gdeisat, David R. Burton, and Michael J. Lalor, "Residue vector, an approach to branch-cut placement in phase unwrapping: theoretical study," *Applied Optics*, vol. 46, no. 21, pp. 4712-4727, 20 July 2007.
- [277] Mariano Rivera and Jose L. Marroquin, "Half-quadratic cost functions for phase unwrapping," *Optics Letters*, vol. 29, no. 5, pp. 504-506, March 1, 2004.
- [278] Bernd Gutmann and Herbert Weber, "Phase unwrapping with the branch-cut method: clustering of discontinuity sources and reverse simulated annealing," *Applied Optics*, vol. 38, no. 26, pp. 5577-5593, 10 September 1999.

- [279] Howard A. Zebker and Yanping Lu, "Phase unwrapping algorithms for radar interferometry: residue-cut, least-squares, and synthesis algorithms," *J. Opt. Soc. Am. A*, vol. 15, no. 3, pp. 586-598, March 1998.
- [280] Yong Bian and Yinqing Zhou, "A research on the noise-immune algorithm for the phase unwrapping of InSAR data," *Acta Electronica Sinica*, vol. 31, pp. 2021-2025, 2003.
- [281] A. Baldi, F. Bertolino, and F. Ginesu, "On the performance of some unwrapping algorithms," *Optics and Lasers in Engineering*, vol. 37, pp. 313-330, 2002.
- [282] Yongjian Zhu, Zhu Luan, Qingguo Yang, Dashan Li, Wei Lu, and Liren Liu, "Improved reliability-guided phase unwrapping algorithm based on the fringe modulation and second-order phase difference," *Optik*, vol. 118, pp. 175-180, 2007.
- [283] Mehrdad Soumekh, "Phase reconstruction/unwrapping from amplitude for diffracted waves using a perturbation solution of the wave equation," *IEEE Transactions on Acoustics, Speech, and Signal Processing*, vol. 36, no. 7, pp. 1076-1085, July 1988.
- [284] SooBum Kim and Young-Soo Kim, "Two-dimensional phase unwrapping using wavelet transform," *Electronics Letters*, vol. 38, no. 1, pp. 19-20, 3rd January 2002.
- [285] S. B. Kim and Y.-S. Kim, "Least squares phase unwrapping in wavelet domain," *IEE Proc.-Vis. Image Signal Process.*, vol. 152, no. 3, pp. 261-267, June 2005.
- [286] Yuangang Lu, Xiangzhao Wang, and Xuping Zhang, "Weighted least-squares phase unwrapping algorithm based on derivative variance correlation map," *Optik*, vol. 118, pp. 62-66, 2007.

- [287] J. A. Quiroga, A. González-Cano, and E. Bernabeu, "Phase-unwrapping algorithm based on an adaptive criterion," *Applied Optics*, vol. 34, no. 14, pp. 2560-2563, 10 May 1995.
- [288] D. J. Bone, "Fourier fringe analysis: the two-dimensional phase unwrapping problem," *Applied Optics*, vol. 30, no. 25, pp. 3627-3632, September 1991.
- [289] M. A. Herráez, D. R. Burton, M. J. Lalor, and M. A. Gdeisat, "Fast two-dimensional phase-unwrapping algorithm based on sorting by reliability following a noncontinuous path," *Applied Optics*, vol. 41, no. 35, pp. 7437-7444, 10 December 2002.
- [290] J. A. Quiroga and E. Bernabeu, "Phase-unwrapping algorithm for noisy phase-map processing," *Applied Optics*, vol. 39, no. 29, pp. 6725-6731, 10 October 1994.
- [291] S. Chavez, Q.-S. Xiang, and L. An, "Understanding phase maps in MRI: a new outline phase unwrapping method," *IEEE Transactions on Medical Imaging*, vol. 21, no. 8, pp. 966-977, August 2002.
- [292] G. Nico, J. Fortuny-Guasch, J. M. Lopez-Sanchez, L. Sagues and A. J. Sieber, "Coherence optimization by polarimetric interferometry for phase unwrapping," *IGARSS'2000*, vol. 1, pp. 135-137, 24-28 July 2000.
- [293] M. Qong, "Coherence optimization using the polarization state conformation in PolInSAR," *IEEE Transactions on Geoscience and Remote Sensing*, vol. 2, no. 3, pp. 301-305, July 2005.
- [294] E. Colin, C. Titin-Schnaider, and W. Tabbara, "An interferometric coherence optimization method in radar polarimetry for high-resolution imagery," *IEEE*

- Transactions on Geoscience and Remote Sensing*, vol. 44, no. 1, pp. 167-175, Jan. 2006.
- [295] M. Neumann, L. Ferro-Famil, and A. Reigber, "Multibaseline polarimetric SAR interferometry coherence optimization," *IEEE Geoscience and Remote Sensing Letters*, vol. 5, no. 1, pp. 93-97, January 2008.
- [296] I. Hajnsek and S. R. Cloude, "Pol-InSAR for agricultural vegetation parameter estimation," *IGARSS'04*, vol. 2, pp. 1224-1227, 20-24 September 2004.
- [297] B. Mercer, Q. Zhang, M. Schwaebisch, M. Denbina and S. Cloude, "Forest height and ground topography at L-Band from an experimental single-pass airborne Pol-InSAR system", *Proceedings of PolInSAR2009*, Frascati, January 2009.
- [298] J.-S. Lee, K. W. Hoppel, S. A. Mango and A. R. Miller, "Intensity and phase statistics of multilook polarimetric and interferometric SAR imagery", *IEEE Transactions on Geoscience and Remote Sensing*, vol. 32, no. 5, pp. 1017-1027, September 1994.
- [299] A. Banerjee, P. Burlina and R. Chellappa, "Adaptive target detection in foliage-penetrating SAR images using alpha-stable models", *IEEE Transactions on Image Processing*, vol. 8, no. 12, pp. 1823-1831, December 1999.
- [300] C. López-Martínez and Z. Fàbregas, "Polarimetric SAR speckle noise model", *IEEE Transactions on Geoscience and Remote Sensing*, vol. 41, no.10, pp. 2232-2242, October 2003.
- [301] D. C. Ghiglia, G. A. Mastin, and L. A. Romero, "Cellular-automata method for phase unwrapping," *J. Opt. Soc. Am. A*, vol. 4, no. 1, pp. 267-280, January 1987.

- [302] Yong Bian and Bryan Mercer, "Interferometric SAR extended coherence calculation based on fractional lower order statistics," *IEEE Geoscience and Remote Sensing Letters*, vol. 7, no. 4, pp. 841-845, October 2010.
- [303] Yong Bian and Bryan Mercer, "Interferometric SAR phase filtering in the wavelet domain using simultaneous detection and estimation," *IEEE Transactions on Geoscience and Remote Sensing*, vol. 49, no. 4, pp. 1396-1416, April 2011.
- [304] J. J. van Zyl, H. A. Zebker, and C. Elachi, "Imaging radar polarization signatures: Theory and observation," *Radio Science*, vol. 22, no. 4, pp. 529-543, July-August 1987.
- [305] A. Guissard, "Mueller and Kennaugh matrices in radar polarimetry," *IEEE Transactions on Geoscience and Remote Sensing*, vol. 32, no. 3, pp. 590-597, May 1994.
- [306] W.-M. Boerner, W.-L. Yan, A.-Q. Xi, and Y. Yamaguchi, "On the basic principles of radar polarimetry: the target characteristic polarization state theory of Kennaugh, Huynen's polarization fork concept, and its extension to the partially polarized case," *Proceedings of the IEEE*, vol. 79, no. 10, pp. 1538-1550, October 1991.
- [307] J. J. van Zyl, *On the importance of polarization in radar scattering problems*, PhD thesis, California Institute of Technology, 1986.
- [308] F. Nunziata, A. Gambardella, and M. Migliaccio, "On the Mueller scattering matrix for SAR sea oil slick observation," *IEEE Geoscience and Remote Sensing Letters*, vol. 5, no. 4, pp. 691-695, October 2008.

- [309] M. Qong, "Polarization state conformation and its application to change detection in polarimetric SAR data," *IEEE Geoscience and Remote Sensing Letters*, vol. 1, no. 4, pp. 304-308, October 2004.
- [310] D. L. Evans, T. G. Farr, J. J. van Zyl, and H. A. Zebker, "Radar polarimetry: Analysis tools and applications," *IEEE Transactions on Geoscience and Remote Sensing*, vol. 26, no. 6, pp. 774-789, November 1988.
- [311] K. P. Papathanassiou, *Polarimetric SAR Interferometry*, PhD thesis, Technical University Graz, Austria, January 1999.
- [312] S. R. Cloude, "Target decomposition theorems in radar scattering," *Electronics Letters*, vol. 21, no. 1, pp. 22-24, 3rd January 1985.
- [313] S. V. Nghiem, S. H. Yueh, R. Kwok, and F. K. Li, "Symmetry properties in polarimetric remote sensing," *Radio Science*, vol. 27, no. 5, pp. 693-711, September-October 1992.
- [314] V. Pascazio and G. Schirinzi, "Estimation of terrain elevation by multifrequency interferometric wide band SAR data," *IEEE Signal Processing Letters*, vol. 8, no. 1, pp. 7-9, January 2001.
- [315] J. M. Bioucas-Dias and G. Valadao, "Phase unwrapping via graph cuts," *IEEE Transactions on Image Processing*, vol. 16, no. 3, pp. 698-709, March 2007.
- [316] K. Itoh, "Analysis of the phase unwrapping algorithm," *Applied Optics*, vol. 21, no. 14, pp. 2470-2470, 15 July 1982.
- [317] C. W. Chen, *Statistical-Cost Network-flow Approaches to Two-dimensional Phase Unwrapping for Radar Interferometry*, PhD dissertation, Stanford University, June 2001.

- [318] D. Just and R. Bamler, "Phase statistics of interferograms with applications to synthetic aperture radar," *Applied Optics*, vol. 33, no. 20, pp. 4361-4368, 10 July 1994.
- [319] Ian G. Cumming and Frank H. Wong, *Digital Processing of Synthetic Aperture Radar Data: Algorithms and Implementation*, Artech House 2005, Norwood, MA.
- [320] Chris Oliver and Shaun Quegan, *Understanding Synthetic Aperture Radar Images*, SciTech Publishing, Inc., 2004 Raleigh, NC.
- [321] John J. Kovaly, *Synthetic Aperture Radar*, Artech House, 1976, Dedham, Massachusetts.
- [322] K. Tomiyasu, "Tutorial review of synthetic-aperture radar (SAR) with applications to imaging of the ocean surface," *Proceedings of the IEEE*, vol. 66, no. 5, pp. 563-585, May 1978.
- [323] J.-S. Lee, "Speckle analysis and smoothing of synthetic aperture radar images," *Computer Graphics and Image Processing*, vol. 17, pp. 24-32, 1981.
- [324] L. J. Porcello, N. G. Massey, R. B. Innes, and J. M. Marks, "Speckle reduction in synthetic-aperture radars," *J. Opt. Soc. Am.*, vol. 66, no. 11, pp. 1305-1311, November 1976.
- [325] J. W. Goodman, "Some fundamental properties of speckle," *J. Opt. Soc. Am.*, vol. 66, no. 11, pp. 1145-1150, November 1976.
- [326] D. T. Kuan, A. A. Sawchuk, T. C. Strand, and P. Chavel, "Adaptive restoration of images with speckle," *IEEE Transactions on Acoustics, Speech, and Signal Processing*, vol. ASSP-35, no. 3, pp. 373-383, March 1987.

- [327] R. K. Raney and G. J. Wessels, "Spatial considerations in SAR speckle simulation," *IEEE Transactions on Geoscience and Remote Sensing*, vol. 26, no. 5, pp. 666-672, September 1988.
- [328] S. Fukuda and H. Hirose, "Smoothing effect of wavelet-based speckle filtering: the Haar basis case," *IEEE Transactions on Geoscience and Remote Sensing*, vol. 37, no. 2, pp. 1168-1172, March 1999.
- [329] M. Tur, K. C. Chin, and J. W. Goodman, "When is speckle noise multiplicative?," *Applied Optics*, vol. 21, no. 7, pp. 1157-1159, 1 April 1982.
- [330] Z. Zeng and I. G. Cumming, "SAR image data compression using a tree-structured wavelet transform," *IEEE Transactions on Geoscience and Remote Sensing*, vol. 39, no. 3, pp. 546-552, March 2001.
- [331] J. S. Lee, I. Jurkevich, P. Dewaele, P. Wambacq, and A. Oosterlinck, "Speckle filtering of synthetic aperture radar images: a review," *Remote Sensing Review*, vol. 8, pp. 313-340, 1994.
- [332] C. Wu, K. Y. Liu, and M. Jin, "Modeling and a correlation algorithm for spaceborne SAR signals," *IEEE Transactions on Aerospace and Electronic Systems*, vol. AES-18, no. 5, pp. 563-575, September 1982.
- [333] R. K. Raney, H. Runge, R. Bamler, I. G. Cumming, and F. H. Wong, "Precision SAR processing using chirp scaling," *IEEE Transactions on Geoscience and Remote Sensing*, vol. 32, no. 4, pp. 786-798, July 1994.
- [334] B. Mercer, Q. Zhang, M. Schwaebisch, and M. Denbina, "3D topography and forest recovery from an L-band single-pass airborne PolInSAR system," *IGARSS 2009*, 12-17 July 2009, vol. 3, pp. III-33-III-36.

- [335] M. Schwabisch, B. Mercer, Q. Zhang, and W. Huang, "Accurate focusing of single-pass airborne InSAR data at L-band," *2010 IEEE International Geoscience and Remote Sensing Symposium*, 25-30 July 2010, pp. 2625-2628.
- [336] H.-E Andersen, R. J. McGaughey, W. W. Carson, S. E. Reutebuch, B. Mercer, and J. Allan, "A comparison of forest canopy models from LiDAR and InSAR data in a pacific northwest conifer forest," *Proceedings of the ISPRS working group III/3 workshop "3-D reconstruction from airborne laserscanner and InSAR data"*, Dresden, Germany, vol. XXXIV, Part 3/W13, 8-10 October 2003, online available: http://www.isprs.org/proceedings/XXXIV/3-W13/papers/Andersen_ALSDD2003.pdf
- [337] J. Moreira, "Design of an airborne interferometric SAR for high precision DEM generation," *International Archives of Photogrammetry and Remote Sensing*, vol. XXXI, Part B2, Vienna 1996, pp. 256-260, online available: http://www.isprs.org/proceedings/XXXI/congress/part2/256_XXXI-part2.pdf
- [338] C. Hofmann, M. Schwabisch, S. Och, C. Wimmer, and J. Moreira, "Multipath P-band interferometry-first results," *Proceedings of the Fourth International Airborne Remote Sensing Conference and Exhibition/21st Canadian Symposium on Remote Sensing*, Ottawa, Ontario, Canada, 21-24 1999, Online available: http://www.drmattnolan.org/olderprojects/kuparuk/kupdem/library/paper_pband.pdf